Magnetotransport in novel low-dimensional carbon nanomaterials

DISSERTATION

zur Erlangung des Grades eines Doktors
der Naturwissenschaften
der Fakultät für Mathematik und Physik
der Eberhard-Karls-Universität zu Tübingen

vorgelegt von

Dipl.-Phys. Dirk Obergfell

aus Donaueschingen

2009

Tag der mündlichen Prüfung: 17.02.2009

Dekan: Prof. Dr. W. Knapp
1. Berichterstatter: Prof. Dr. D. Kern
2. Berichterstatter: Dr. habil. S. Roth

Magnetotransport in novel
low-dimensional carbon nanomaterials

Several novel low-dimensional carbon nanomaterials, scilicet graphene mono- and bi-layers, single-walled carbon nanotubes (SWNTs) and SWNTs filled with Dy@C_{82} endohedral metallofullerenes (*metallofullerene peapods*), were deposited onto Si/SiO_2 substrates and provided with metal contacts in order to perform electrical magneto-transport measurements at low temperatures in external magnetic fields of different orientations. The *quantum Hall effect* was measured for graphene mono- and bilayers, results reported on in literature could be reproduced. As anticipated, mono- and bilayers of graphene did not exhibit significant magnetoresistive effects for in-plane magnetic fields, whereas clear *Hall effect* signatures were observed for perpendicular, out-of-plane magnetic fields. Within our experimental resolution, we could not identify reproducible differences between empty SWNTs and metallofullerene peapods in electrical transport and magnetotransport measurements. For both systems, significant negative magnetoresistance (approx. 8 to 14 %) could be observed for axially oriented magnetic fields in some of the samples, where this effect vanished for the perpendicular magnetic field orientation. Other nanotubes did not show this effect at all. According to the theory by E. L. Ivchenko and B. Spivak [Ivc02], the SWNTs exhibiting the negative magnetoresistance for parallel magnetic fields should be chiral, whereas nanotubes not responding electrically to a magnetic field of any orientation should a achiral SWNTs. Moreover, height undulations of the differential conductance Coulomb blockade peaks of SWNTs accompanied by shifts of the respective peak positions along the gate voltage direction were observed, which is attributed to *diamagnetic shifts* and *Zeeman shifts*. Throughout the whole project, great importance was attached to combining the (magneto-)transport measurements with further investigations as high-resolution TEM or AFM on the very same sample in order to cross-check its geometrical and structural properties.

Magnetotransport an neuartigen niederdimensionalen Kohlenstoff-Nanomaterialien

Verschiedene neuartige niederdimensionale Kohlenstoff-Nanomaterialien, nämlich Graphen Mono- und Doppellagen, einwandige Kohlenstoff-Nanoröhren (SWNTs) sowie SWNTs, die mit endohedralen $Dy@C_{82}$ Metallofullerenen gefüllt sind (*Metallofulleren-Peapods*), wurden auf Si/SiO_2-Substraten deponiert und mit metallischen Kontakten versehen, um elektrische Magnetotransport-Messungen bei tiefen Temperaturen in externen Magnetfeldern verschiedener Richtungen durchzuführen. Der *Quanten-Hall-Effekt* wurde an den Graphen Mono- und Doppellagen gemessen, wobei die Ergebnisse aus der Literatur reproduziert werden konnten. Wie erwartet, ergaben sich für Graphen Mono- und Doppellagen keine signifikanten Magnetwiderstands-Effekte bei angelegten in-plane Magnetfeldern, wohingegen jedoch deutliche Anzeichen des *Hall-Effekts* für Magnetfelder senkrecht zu den Graphen-Flocken beobachtet werden konnten. Innerhalb unserer experimentellen Auflösung konnten wir keine reproduzierbaren Unterschiede zwischen leeren SWNTs und Metallofulleren-Peapods im elektrischen Transport und Magnetotransport feststellen. Für beide Systeme konnte an einigen Proben ein deutlicher negativer Magnetwiderstand (ca. 8 bis 14 %) für parallel orientierte Magnetfelder beobachtet werden, dieser Effekt verschwindet jedoch für die senkrechte Magnetfeld-Ausrichtung. Andere Nanoröhren zeigten diesen Effekt nicht. Entsprechend der Theorie von E. L. Ivchenko und B. Spivak [Ivc02] sollten die SWNTs, welche den negativen Magnetwiderstand bei parallelen Magnetfeldern aufweisen, chiraler Natur sein, wohingegen die Nanoröhren, die elektrisch nicht auf ein Magnetfeld beliebiger Richtung reagieren, achiral sein sollten. Weiterhin wurden Höhen-Undulationen der differentiellen Leitwert-Peaks im Coulomb-Blockade-Regime beobachtet, welche einhergehen mit Verschiebungen der entsprechenden Peaks entlang der Gate-Spannungs-Achse. Diese Effekte werden *diamagnetischen Verschiebungen* sowie *Zeeman-Verschiebungen* zugeordnet. Während des gesamten Projekts wurde großer Wert auf die Kombination der (Magneto-)Transport-Messungen mit weiteren Untersuchungen wie hochauflösender Transmissionselektronen-Mikroskopie oder Rasterkraft-Mikroskopie an derselben Probe gelegt, um deren geometrische und strukturelle Eigenschaften zu überprüfen.

Table of Contents

1. Introduction

Within about the last two decades a number of novel carbon modifications have been discovered with a substantial impact in material and solid state sciences. Due to the nanometer scale sizes, the low dimensionality and further extraordinary properties regarding mechanics, electronics, optics and chemistry these novel carbon nanomaterials open up new fields of basic research and start to make their way into first practical applications.

The field of carbon nanostructures was opened in 1985, when the C_{60} buckminister fullerene was discovered by R. E. Curl, H. W. Kroto and R. F. Smalley [Kro85], who later on were awarded the nobel prize in chemistry for this discovery. Five years later, W. Krätschmer succeeded in controlled mass production of C_{60} fullerenes [Kra90]. In 1991, S. Iijima discovered multi-walled carbon nanotubes (MWNTs) in a transmission electron microscopy (TEM) study [Iij91], only 2 years later, the single-walled carbon nanotubes (SWNTs) followed [Iij93, Be93a]. Various high-yield production methods both for SWNTs and MWNTs were developed throughout the forthcoming years [The96, Jou97, Sai98, Cas99, Fan99, Fra00, Set00, Bad05]. Thus, fullerenes and nanotubes became available for researchers in sufficient amounts. Nanotube peapods, which are SWNTs filled with linearly aligned, equidistantly spaced fullerenes (or metallofullerenes), have attracted attention of scientists since 1998, when B. W. Smith and D. E. Luzzi were the first to observe these novel carbon hybrid structures by means of transmission electron microscopy [Smi98]. During the 1990s, many research groups joined the investigations of fullerenes, nanotubes and nanotube peapods, the number of research publications per year on carbon nanotubes has tremendously increased during the last decade [WoS07]. The latest members of the *carbon zoo*, i.e. the different allotropes of carbon, are graphene mono- and double-layers, which were first isolated and experimentally investigated by two research groups around A. K. Geim and P. Kim in 2005 [No05b, Zha05]. These two groups demonstrated independently, that the *quantum Hall effect* can be observed in graphene mono- and bilayers deposited onto Si/SiO_2 substrates, allowing for the first time - in contrast to buried 2-dimensional electron gases (2DEGs) within GaAs heterostructures - free accessibility of a 2DEG in the quantum Hall state. Moreover, due to graphene being a zero-gap semiconductor, the conduction type can be easily tuned from electron to hole condcution by applying the respective gate potential. Further properties of graphene and few-layer graphite flakes are being investigated, inspired by the comprehensive work which had been done internationally in the fields of carbon nanotubes and GaAs heterostructures.

Some carbon nanomaterials nowadays are about to enter mass markets, for instance carbon nanotubes are used as blending material to modify the electrical and thermal properties of polymers, ceramics and metal alloys [Rot07]. Except of nanotubes being excellent electrical [Sai98, Rob07] and thermal [Che00, Fuj05, Yu05] conductors, their extremely high

aspect ratio is favourable for these applications, i.e. thermal and electrical properties are improved already for low loading of the host matrices with carbon nanotubes. Especially the electrical properties of the starting materials can be increased efficiently, electrical conductivity can often be changed by orders of magnitude while mechanical properties do not deteriorate due to the filling. Thermal property improvements so far have been modest only, but they are significant for matrices with low starting values [Rot07]. Furthermore, thin, flexible electrically conducting nanotube networks are prominent candidates for applications as transparent heating elements for car windshields [DPG06, Fra06] or as transparent electrodes in displays [Vas07] or solar cells [Row06, Con07].

Nevertheless, on the level of individual nanotubes, the practical applicability is restricted. For instance, semiconductor industry currently is approaching the physical limits of classical silicon based fabrication techniques (so-called top-down approach, i.e. starting with a large structure and refining it to the final structure by using typical semiconductor processing techniques) and thus urgently looks for new approaches and materials how to meet future challenges in terms of scaling down and speeding up devices. Carbon nanomaterials are amongst the materials being seriously taken into consideration in this respect, especially the nanotubes offering metallic and semiconducting behaviour. Industrial research has been and still is being carried out [Gr05a, Gr05b, Rob07], exploring the possibilities to employ carbon nanotubes as vias[*], interconnects[†] and as transistors. Even though nanotubes outperform up-to-date Cu leads and state-of-the-art Si transistors in several respects [Gr05a, Gr05b, Rob07], there are significant obstacles as lack of sorting[‡] and placing capabilities and lack in reproducibility of device properties[§] [Gr05a, Gr05b, Hoe06], which prevent the large-scale implementation of individual nanotube devices into semiconductor technology at least in near future.

Possible applications of individual graphene sheets are discussed controversially [Gei07, NME07, Bri07]. On the one hand side, graphene offers very high charge carrier mobilities which can exceed 200000 cm^2/Vs [Bol08, Mor08]. The conduction type can continuously be tuned from hole to electron conduction. Furthermore, due to the strong C-C bonds, graphene sheets are of remarkable mechanical stability. On the other hand side, the question how to produce large area graphene sheets in a controlled manner suitable for industrial applications remains unanswered at the moment. Moreover it is questionable, how graphene sheets could be used in microelectronics: due to the zero bandgap, graphene can not be depleted properly which rules out the use as active element. There may be ways to open bandgaps in graphene, e.g. by etching ribbons or by using graphene double-layers [Bri07], but the technology for doing so on large scale has not yet been developed. Apart from these issues, one potential application of individual graphene sheets may become

---

[*]via = **v**ertical **i**nterconnect **a**ccess, i.e. vertical lead connecting layers within a semiconductor chip
[†]interconnect: horizontal lead within one layer of a chip
[‡]for instance, sorting of metallic and semiconducting carbon nanotubes
[§]as, for instance, contact resistance or band-gap

meaningful: the use of graphene as the thinnest conceivable, almost-transparent specimen holder for high-resolution transmission electron microscopy [Mey07, Mey08].

Even though individual carbon nano-objects are hard to utilize for practical applications, for basic research they offer a great variety of highly interesting phenomena, several of which are described in the following references [Sai98, Rei04, Dre04, Dre05, Cot06, Cha07, Shi00, Kit06, Kri06, Zha05, No05b, Nov07, Net07]. As for electronic properties, an intriguing aspect is the question how external magnetic fields influence the motion of the electrons within low-dimensional carbon nanosystems and to which degree the geometrical structures of the different carbon allotropes do matter.

The central topic of this thesis is to study and compare the electrical transport properties of graphene mono-/bilayers, of SWNTs and of SWNTs filled with magnetic $Dy@C_{82}$ metallofullerenes [Hua00] (*metallofullerene peapods*) in dependence of external, differently oriented magnetic fields. Great importance was attached to complementary structural investigations by HR-TEM, HR-AFM and Raman spectroscopy on the same carbon nano-objects which transport has been measured for to make sure that the objects investigated indeed were one/two layer(s) of graphene, individual SWNTs or SWNTs filled with metallofullerenes. For the graphene mono- and bilayer flakes *quantum Hall effect* measurements were performed additionally. This thesis is organized as follows: **Chapter 2** describes the structure of different carbon modifications, **chapter 3** gives detailed information about electrical properties of graphene mono- and bilayers, of SWNTs and of metallofullerene peapods, **chapter 4** comprises all essential technical/experimental information on how to prepare the samples, how to carry out electrical measurements on individual carbon nano-objects and how to combine electrical transport measurements with further structural investigations. In **chapters 5 to 7** the electrical transport and magnetotransport results obtained within this PhD thesis on graphene mono- and bilayers (including QHE) (**chapter 5**), on SWNTs (**chapter 6**) as well as on Dy metallofullerene peapods (**chapter 7**) are presented and discussed. Note that **chapter 7** in addition comprises two sub-chapters on atomic-resolution AFM and TEM studies* on individual Dy metallofullerene peapods which led to *novel and intriguing side results*. **Chapter 8** contains the summary of the thesis, followed by an appendix chapter with more detailed information concerning the data acquisition software developed within this project.

---

*These studies were originally intended to be carried out as complementary studies in order to confirm geometrical aspects of the metallofullerene peapods investigated by electrical transport measurements.

2. The different allotropes of carbon and their structures

Carbon is a unique element - it is the element all life is based upon and it is the only element of the periodic table which can form allotropes of zero, one, two and three dimensions (0D to 3D). The main reason for the large variety of allotropes is that carbon offers many possible configurations of electronic states, which is referred to as the different *hybridizations* of the valence electron orbitals [Sai98]. Hybridization is the mixture of valence electron wave functions and orbitals, respectively. Carbon is the sixth element of the periodic table, it has the electron configuration $1s^2$, $2s^2$ and $2p^2$. The 1s electrons are strongly bound *core electrons*, whereas the four *valence electrons* occupy the 2s and 2p orbitals. Since the energy difference between the 2s and 2p states is small in comparison with the binding energy, the orbitals of a single 2s electron and $n \, \epsilon \, \{1, 2, 3\}$ 2p electrons are mixed, forming $n + 1$ hybrid orbitals, which is called sp^n hybridization. For carbon, sp, sp^2 and sp^3 hybridization exists.

The major two carbon allotropes known before the discovery of fullerenes in 1985, are diamond (3D, sp^3 hybridization), in which the carbon atoms are arranged in tetraeder structures with a carbon-carbon distance of 1.54 Å (Fig. 2.1a) and graphite (3D, sp^2 hybridization), which consists of stacked 2D honeycomb carbon lattices (Fig. 2.1d). The structure of graphite and especially of its individual graphene layers is discussed in chapter 2.1. Another pure carbon allotrope known before the fullerenes is polycarbyne $(C{\equiv}C\text{-})_n$ (sp hybridization), which still nowadays is slightly exotic since it only occurs in interstellar dust and in trace amounts within natural graphite and is not available in amounts needed for experiments [Rot04]. Furthermore, polymers, i.e. 1D carbon chains in which the dangling bonds are saturated by hydrogen (e.g. polyacetylene $(HC{=}CH\text{-})_n$ (sp^2 hybridization)), were known before 1985.

A new class of carbon allotropes emerged in 1985 with the discovery of the spherical C_{60} fullerene molecule (0D, sp^2 hybridization), which consists of 60 carbon atoms arranged in 20 hexagons and 12 pentagons (Fig. 2.1b). There is a large variety of fullerene cages [Dre93] such as fullerenes comprising a larger number of carbon atoms, e.g. C_{70} or C_{84} (etc.) or endohedral fullerenes, e.g. endohedral metallofullerenes (cp. chapter 2.3).

Figure 2.1c depicts a part of a single-walled carbon nanotube (SWNT) (1D, sp^2 hybridization), one of the latest carbon allotropes [Iij93, Be93a]. It can be thought of as a single layer of graphite (i.e. graphene) rolled into a seamless cylinder. The SWNT is terminated by half fullerene caps (Fig. 2.1c). The detailed structure of SWNTs is elucidated in chapter 2.2, whereas multi-walled carbon nanotubes (MWNTs) [Iij91], which are concentrically nested SWNTs of gradually increasing diameters, are not considered further in this thesis.
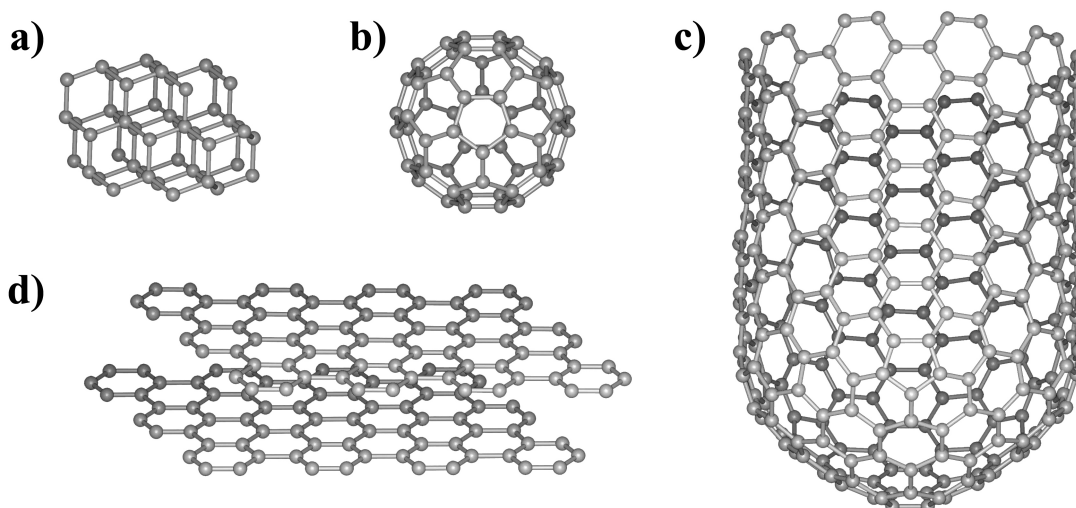
Fig. 2.1: The most important carbon allotropes, differing in dimensionality and hybridization: **a)** diamond (3D, sp^3 hybridization), **b)** a C$_{60}$ fullerene (0D, sp^2 hybridization), **c)** a single-walled carbon nanotube (SWNT) (1D, sp^2 hybridization) and **d)** graphite (3D, composed of stacked 2D graphene sheets, sp^2 hybridization).

2.1 Structure of graphite and graphene mono-/bilayers

In the following, structural aspects of graphite and of graphene mono- and bilayers will be elucidated briefly.

As mentioned before, graphite consists of regularly stacked 2D honeycomb carbon lattices named *graphene layers*. Perfect, crystalline graphite† appears in two different kinds of stacking in nature, which are AB AB AB and ABC ABC stacking, respectively. In literature, AB AB AB stacking is often referred to as *Bernal stacking* as well. In figure 2.2, the two different types of stacking are drawn in a top view, i.e. a view along the z-axis. Figure 2.2a depicts the AB AB AB stacking, in which the 1st, 3rd, 5th... layer (odd-numbered layers, drawn in black) and the 2nd, 4th, 6th... layer (even-numbered layers, drawn in red) each are identical, but the odd-numbered layers are shifted with respect to the even-numbered layers. For the ABC ABC stacking sequence, the 1st, 4th, 7th... layer (drawn in black in Fig. 2.2b), the 2nd, 5th, 8th... layer (drawn in red in Fig. 2.2b) and the 3rd, 6th, 9th... layer (drawn in light blue in Fig. 2.2b) are identical, but shifted towards each other. The AB AB AB and ABC ABC stacking correspond to a *HCP (hexagonal close-packed)* and to a *fcc (face-centered cubic)* lattice, respectively. The spacing of each two graphene layers within a single crystal of graphite equals 3.4 Å, which is due to the *van der Waals* (vdW) forces between the layers.

Getting down with the number of graphene layers to two, obviously only the Bernal stacking is possible, where all possible double-layer configurations of the three layers in figure 2.2b are identical due to symmetry reasons.

---

†in contrast to so-called *turbostratic graphite* which exhibits irregular stacking
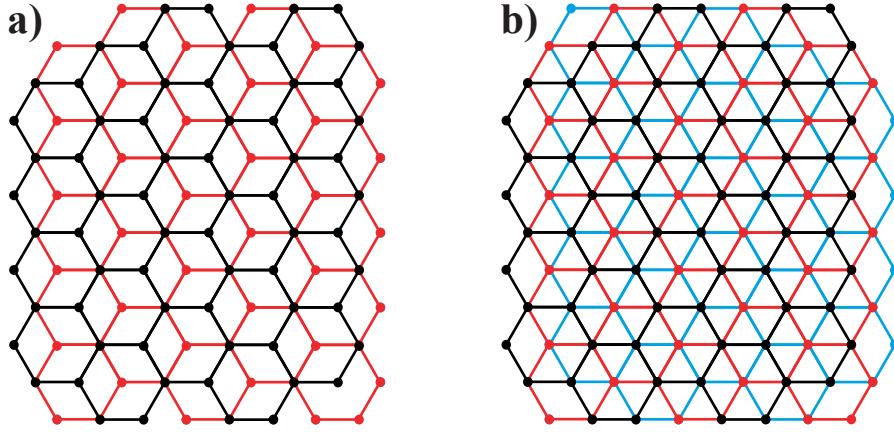
Fig. 2.2: a) graphite AB stacking **b)** graphite ABC stacking.

Considering a graphene monolayer, it remains to be noted, that the next-neighbour distance a_{C-C} equals to 1.42 Å and that the lattice constant a of the hexagonal lattice amounts to $a = \sqrt{3} \cdot a_{C-C} = 2.46$ Å. The graphene lattice and its unit vectors $\vec{a}_1$ and $\vec{a}_2$ (with $|\vec{a}_1| = |\vec{a}_2| = a$) forming the non-primitive unit cell are drawn in figure 2.3.
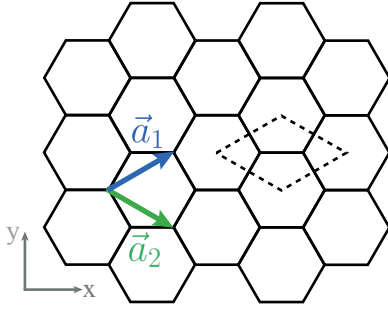
Fig. 2.3: The honeycomb graphene lattice and its unit vectors $\vec{a}_1$ and $\vec{a}_2$ forming the non-primitive unit cell (dashed lines).

The two unit vectors $\vec{a}_1$ and $\vec{a}_2$ can be expressed as:

$$\begin{aligned}
\vec{a}_1 &= \left(\frac{3}{2} a_{C-C}, \frac{\sqrt{3}}{2} a_{C-C} \right) = \left(\frac{\sqrt{3}}{2} a, \frac{a}{2} \right) \\
\vec{a}_2 &= \left(\frac{3}{2} a_{C-C}, -\frac{\sqrt{3}}{2} a_{C-C} \right) = \left(\frac{\sqrt{3}}{2} a, -\frac{a}{2} \right) .
\end{aligned} \tag{2.1}$$

Figure 3.1b depicts the corresponding reciprocal graphene lattice with the reciprocal unit vectors $\vec{b}_1$ and $\vec{b}_2$ and the first Brillouin zone of graphene ($\vec{a}_i \cdot \vec{b}_j = 2\pi \delta_{ij}$, where δ_{ij} is the *Kronecker delta*). The reciprocal lattice constant of graphene is $b = |\vec{b}_1| = |\vec{b}_2| = 4\pi/\sqrt{3}a = 4\pi/3a_{C-C}$. The two unit vectors $\vec{b}_1$ and $\vec{b}_2$ of the reciprocal graphene lattice depend on a_{C-C} and a as follows:

$$\begin{aligned}
\vec{b}_1 &= \left(\frac{2\pi}{3a_{C-C}}, \frac{2\pi}{\sqrt{3}a_{C-C}} \right) = \left(\frac{2\pi}{\sqrt{3}a}, \frac{2\pi}{a} \right) \\
\vec{b}_2 &= \left(\frac{2\pi}{3a_{C-C}}, -\frac{2\pi}{\sqrt{3}a_{C-C}} \right) = \left(\frac{2\pi}{\sqrt{3}a}, -\frac{2\pi}{a} \right) .
\end{aligned} \tag{2.2}$$

2.2   Structure of single-walled carbon nanotubes

In a gedanken experiment, one can think of a single-walled carbon nanotube (ignoring the terminations of the tube) as a graphene sheet being rolled up to a seamless cylinder. Following this idea, it is obvious that the graphene sheet could be rolled up in different ways forming various cylinders which differ from each other in their diameters and in the orientations of the carbon hexagons with respect to the nanotube axis.

If a single-walled carbon nanotube can not be superposed to its mirror image, the SWNT is called *chiral*. If the structure of the nanotube and its mirror image are identical, the SWNT is *achiral*. There are only two cases of achiral SWNTs, which are the high-symmetry cases, called *armchair* and *zigzag* type according to the shape of the imaginary circumferential edges (Figs. 2.4a,b).

a)

b)

c)
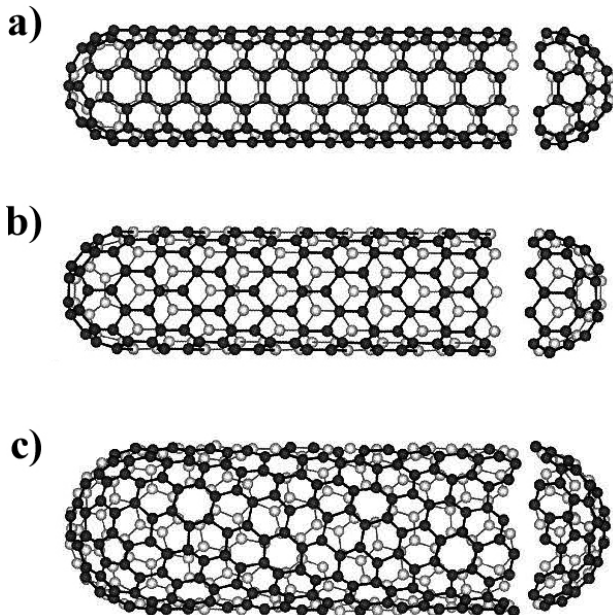
Fig. 2.4: Classification of single-walled carbon nanotubes: **a)** an *armchair*, **b)** a *zigzag* and **c)** a *chiral* SWNT are displayed. Note, that almost any orientation of the carbon hexagons is possible with respect to the nanotube axis [Sai98].

Based on the view of a SWNT as a rolled up graphene sheet, several geometrical properties of single-walled carbon nanotubes are explained in the following [Sai98].

Figure 2.5 displays a section of a graphene sheet. The vector $\vec{c}_{\mathrm{h}}$ named *rolling vector* shall map the chosen origin O onto point A when rolling the graphene to form a cylinder. The absolute value of the rolling vector $|\vec{c}_{\mathrm{h}}|$ corresponds to the circumference of the nanotube. Thus, the vector $\vec{c}_{\mathrm{h}}$ is characteristic for the SWNT structure. The rolling vector can be expressed as a linear combination of the *unit vectors* $\vec{a}_1$ and $\vec{a}_2$ (Fig. 2.5) of the hexagonal graphene lattice:

$$\vec{c}_{\mathrm{h}} = n\vec{a}_1 + m\vec{a}_2 \equiv (n, m) \qquad (n, m \in \mathbb{N};\ 0 \leq |m| \leq n)\ . \qquad (2.3)$$
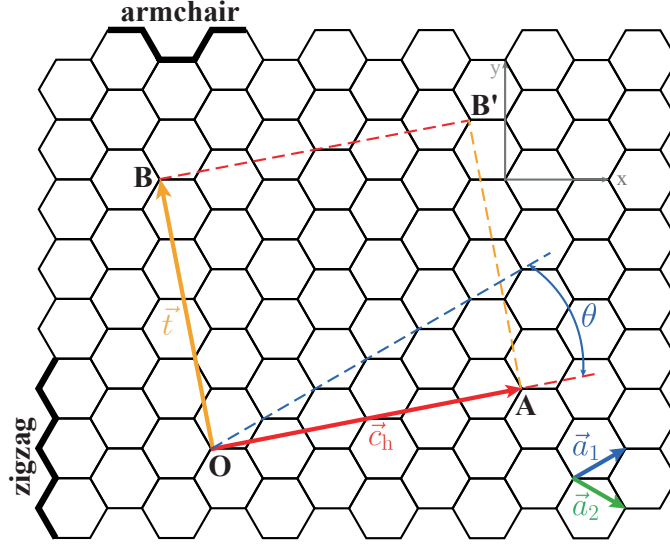
Fig. 2.5: A single-walled carbon nanotube can be thought of as a graphene sheet rolled up along the *rolling vector* $\vec{c}_{\mathrm{h}}$. Furthermore this scheme depicts the unit vectors $\vec{a}_1$ and $\vec{a}_2$ of the hexagonal graphene lattice, the *rolling angle* θ, the translational vector $\vec{t}$ and the unit cell OAB'B of the generated (4,2) SWNT [Sai98].

The pair of integer numbers (n, m) is called *structural indices* of a single-walled carbon nanotube. $(n, 0)$ corresponds to zigzag nanotubes, (n, n) to armchair tubes. All other (n, m) indices result in chiral SWNTs. Due to the symmetry of the hexagonal graphene lattice, it is sufficient to consider the $0 \leq |m| \leq n$ cases for chiral SWNTs. The structural indices of the three SWNTs in figure 2.4 are $(n, m) = (5, 5)$ in figure 2.4a, $(n, m) = (9, 0)$ in figure 2.4b and $(n, m) = (10, 5)$ in figure 2.4c, respectively.

Calculating the diameter of a single-walled carbon nanotube, equations (2.1) are utilized. Thus, the diameter d_{N} of a SWNT is given by:

$$
\begin{aligned}
d_{\mathrm{N}} &= \frac{1}{\pi} |\vec{c}_{\mathrm{h}}| = \frac{1}{\pi} \sqrt{\vec{c}_{\mathrm{h}} \cdot \vec{c}_{\mathrm{h}}} \\
&= \frac{1}{\pi} \sqrt{n^2 \left(\vec{a}_1\right)^2 + m^2 \left(\vec{a}_2\right)^2 + 2nm\vec{a}_1\vec{a}_2} \\
\Rightarrow d_{\mathrm{N}} &= \frac{1}{\pi} a \sqrt{n^2 + m^2 + nm} \; .
\end{aligned}
\tag{2.4}
$$

The *rolling angle* θ (cp. Fig. 2.5) is defined as the angle between the unit vector $\vec{a}_1$ of the hexagonal lattice and the *rolling vector* $\vec{c}_{\mathrm{h}}$. Moreover, θ describes the tilting of the hexagons with respect to the nanotube axis. For a zigzag tube ($\theta = 0°$), the hexagons are oriented parallel to the nanotube axis, whereas they are tilted by $30°$ with regard to the SWNT axis in the case of an armchair tube ($\theta = 30°$). Due to symmetry, θ can be restricted to the angular range $0 \leq |\theta| \leq 30°$. Using equations (2.1), (2.3) and (2.4), θ is

obtained as

$$\theta = \arccos \frac{\vec{c}_\mathrm{h} \cdot \vec{a}_1}{|\vec{c}_\mathrm{h}||\vec{a}_1|} = \arccos \frac{2n + m}{2\sqrt{n^2 + m^2 + nm}} \ . \tag{2.5}$$

The *translational vector* $\vec{t}$ is defined to be the unit vector of a 1D carbon nanotube [Sai98]. The translational vector runs parallel to the nanotube axis, starts in the origin O and ends in the lattice point B of the graphene lattice, which is the closest lattice point to the origin O on the straight line (through O) perpendicular to the rolling vector $\vec{c}_\mathrm{h}$ (Fig. 2.5). Therefore, the unit cell of the single-walled carbon nanotube is given by OAB'B in figure 2.5. The vector $\vec{t}$ can be expressed as a linear combination of the graphene unit vectors $\vec{a}_1$ and $\vec{a}_2$ (Fig. 2.5):

$$\vec{t} = t_1 \vec{a}_1 + t_2 \vec{a}_2 \equiv (t_1, t_2) \qquad\qquad (t_1, t_2 \in \mathbb{N}) \ . \tag{2.6}$$

The coefficients t_1 and t_2 are determined using $\vec{c}_\mathrm{h} \cdot \vec{t} = 0$ and equations (2.1), (2.3) and (2.6), where t_1 and t_2 are required to be as small as possible and where T is the greatest common divisor of $(2m + n)$ and $(2n + m)$ [Sai98]:

$$\begin{aligned} t_1 &= \frac{2m + n}{T} \\ t_2 &= -\frac{2n + m}{T} \ . \end{aligned} \tag{2.7}$$

The length of the translational vector $\vec{t}$ is given by:

$$t = |\vec{t}| = \frac{\sqrt{3}}{T} \cdot a\sqrt{n^2 + m^2 + nm} = \frac{\sqrt{3}}{T} \cdot |\vec{c}_\mathrm{h}| \ . \tag{2.8}$$

Thus, for the area $|\vec{c}_\mathrm{h} \times \vec{t}|$ of the SWNT unit cell one obtains

$$A_\mathrm{SWNT} = |\vec{c}_\mathrm{h} \times \vec{t}| = \sqrt{3}a^2 \left(n^2 + m^2 + nm\right)/T \ . \tag{2.9}$$

Therewith, the number N_hex of hexagons (area of a hexagon: $|\vec{a}_1 \times \vec{a}_2|$) per unit cell of the SWNT can be calculated:

$$N_\mathrm{hex} = \frac{A_\mathrm{SWNT}}{|\vec{a}_1 \times \vec{a}_2|} = \frac{2\left(n^2 + m^2 + nm\right)}{T} = \frac{2|\vec{c}_\mathrm{h}|^2}{a^2 T} \ . \tag{2.10}$$

Since there are 2 carbon atoms in a graphene unit cell, the number of carbon atoms (and also the number of p_z orbitals) per SWNT unit cell is $2N_\mathrm{hex}$.

2.3 Structure of metallofullerene peapods

A *metallofullerene peapod* is a single-walled carbon nanotube the inner hollow of which is filled by equidistantly spaced *endohedral metallofullerenes*. Endohedral metallofullerenes, often called *metallofullerenes* only, are fullerene cages of 60, 70, 72, 74, 80, 82, 84, 90,... [Be93b, Nag96, Shi00] carbon atoms encapsulating one to three metal atoms. Metals which can be included in the inner spaces of (higher) fullerene cages, especially in the C_{82}, are Li, Ca, Sr, Ba, Ti, Zr, Hf, Nb, Mn and Fe and all rare earth metals, namely Sc, Y, La, Ce,..., Er, Tm, Yb and Lu (as of November 2003, see [Yan03]). The denotation of an endohedral metallofullerene is $M_m@C_n$, where m ranges from 1 to 3 (corresponding to a mono-, di- or tri-metallofullerene)(the index m is usually omitted if m = 1), n stands for the number of carbon atoms of the fullerene, and M represents one of the metal elements listed before. Henceforth, only mono-metallofullerenes which are of relevance within this work will be considered. $M@C_{82}$ metallofullerenes are most abundantly formed amongst the mono-metallofullerenes [Nag96] in the arc-discharge process. For the C_{82} cage, there are 9 distinct isomers fulfilling the so-called *isolated pentagon rule (IPR)* [Nag96, Shi00], stating that the most stable fullerenes are the ones in which every pentagon is surrounded by five hexagons. Yet, in practice only one isomer is predominantly occuring, which is C_2 (i.e. the isomer with a vertical 2-fold rotational axis) in the case of empty C_{82} fullerenes and C_{2v} (i.e. the isomer with a vertical 2-fold rotational axis and 2 mirror planes, which are perpendicular to each other and through which the rotational axis is running) for $M@C_{82}$ metallofullerenes [Khl08]. Due to strong metal-cage interactions, the energetically most stable configuration of $M@C_{82}$ metallofullerenes is achieved if the metal atom resides close to the carbon cage, i.e. if it is positioned off-center [Na93a, Na93b, Shi00, Kit07]. The forces responsible for the off-center position of the metal atom with respect to the fullerene cage are the strong charge transfer interactions between e.g. the La^{3+} or Dy^{3+} ion and the negatively charged C_{82}^{3-} after electron transfer from the metal atom to the fullerene cage [Shi00, Kit07]. There are other metal atoms such as Sc which only transfer 2 electrons to the C_{82} cage due to a higher ionization potential in comparison with e.g. La or Dy. The metallofullerenes $M@C_{82}$ are nearly spheroidal and have diameters of approx. 8 Å.

Having opened single-walled carbon nanotubes by oxidation (cp. chapter 4.3), (metallo)fullerenes can enter SWNTs of appropriate diameters through their open ends [Ulb03] and form linear (metallo-)fullerene chains inside the nanotubes. A $(Dy@C_{82})@SWNT$ metallofullerene peapod, which is experimentally investigated in terms of (magneto-)transport measurements within this thesis (cp. chapter 7), is sketched in figure 2.6.
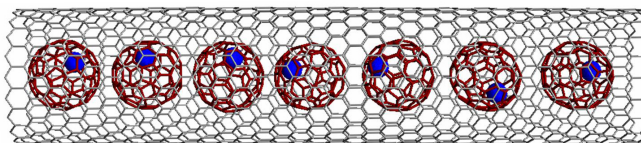
Fig. 2.6: A schematic of a $(Dy@C_{82})@SWNT$ metallofullerene peapod: $Dy@C_{82}$ metallofullerenes are encapsulated in a SWNT forming a linear chain with equidistant spacing.

For the optimum single-walled carbon nanotube diameter $d_{\text{N,opt}}$ there is a net energy
gain of no less than approx. 3 eV per encapsulated fullerene and metallofullerene, respec-
tively [Khl08, Ulb03]. According to theory, this optimum SWNT diameter is $d_{\text{N,opt}} \approx$
$d_{\text{F/MF}} + 0.6$ nm[†] [Yoo05]. With increasing SWNT diameter, the energy gain is minimized,
whereas for narrower diameters filling eventually gets endothermic [Yoo05].

In this thesis, (Dy@C$_{82}$)@SWNT metallofullerene peapods are investigated with regard to
their magnetotransport properties. Experimentally, SWNTs with diameters of 1.3 to 1.7 nm
can be filled with Dy@C$_{82}$ metallofullerenes. In high-resolution TEM and atomic resolution
AFM inspection (cp. chapters 4.3, 4.7.2 and 7.5), we obtained highly regular metalloful-
lerene-metallofullerene distances of 1.05 ± 0.05 nm (Fig. 2.7) and 1.15 ± 0.05 nm (Fig. 2.8d),
respectively[§] [Ash08, As09b], thus we can verify the metallofullerene periodicity displayed
in figure 2.6. Additionally, by atomic resolution AFM we can resolve an axial undulating
pattern of the metallofullerene peapod host nanotube which is due to the Dy@C$_{82}$ filling.
This undulation with an amplitude of 56 ± 5 pm only appears for narrow SWNTs of about
1.3 nm diameter (Fig. 2.8d), whereas large diameter (Dy@C$_{82}$)@SWNT topographies do
not differ significantly from an empty SWNT topography (Figs. 2.8a-c). In summary, many
structural aspects of (Dy@C$_{82}$)@SWNT metallofullerene peapods are known, nevertheless
they differ amongst each other regarding the diameters and helicities of the host SWNTs
and with respect to the nanotube filling (not all SWNTs are perfectly filled, partially filled
tubes *do* exist).
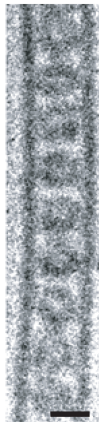
Fig. 2.7: High-resolution trans-
mission electron micrograph of
a (Dy@C$_{82}$)@SWNT metallo-
fullerene peapod. The periodici-
ty of the metallofullerenes in the
SWNT is 1.05 ± 0.05 nm. The
scale bar equals 1 nm [Obe06].
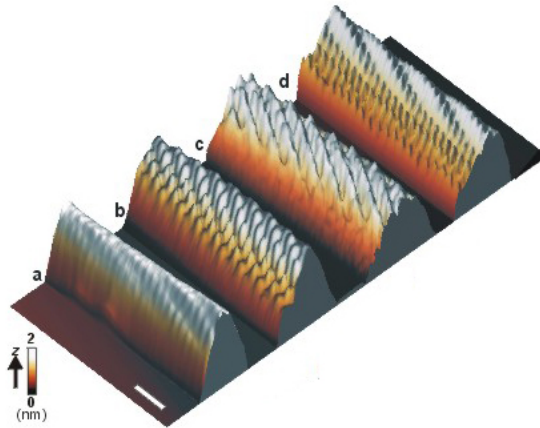
Fig. 2.8: Results obtained by dynamic, atomic resolu-
tion AFM. Scale bar: 1 nm. **a)** Topography of an empty
SWNT with a diameter of 1.30 ± 0.05 nm. **b)-d)** To-
pography images of (Dy@C$_{82}$)@SWNT metallofullerene
peapods with the following diameters: b) 1.62 ± 0.05 nm,
c) 1.50 ± 0.05 nm and d) 1.30 ± 0.05 nm [As09b]. The
periodicity of the nanotube undulations corresponding to
the metallofullerene sites in d) equals 1.15 ± 0.05 nm.
The amplitude of the undulation is 56 ± 5 pm.

[†]$d_{\text{F/MF}}$ is the diameter of the fullerene/metallofullerene
[§]which are in good agreement with each other

3. Electronic properties of graphene, SWNTs and metallofullerene peapods

3.1 Electronic properties of graphene

3.1.1 Bandstructure of graphene mono- and bilayers

By a nearest-neighbour tight-binding approach, the dispersion relation for a graphene monolayer within the graphene Brillouin zone can be calculated [Sai98]. The tight-binding calculation only considers the p_z orbitals forming the delocalized π electron system, which is responsible for electrical conduction of the graphene layer. Figure 3.1b displays the Brillouin zone of the graphene monolayer as a shaded hexagon with the high symmetry points Γ, M, K and K' in reciprocal space. The corresponding graphene honeycomb lattice and its non-primitive unit cell (dotted rhombus) are shown in figure 3.1a. The vectors $\vec{a}_i$ and $\vec{b}_i$ (i = 1,2) are the unit vectors and reciprocal lattice vectors, respectively. Note that the reciprocal lattice points K and K' are inequivalent due to the fact that the graphene honeycomb lattice in real space (Fig. 3.1a) consists of two interpenetrating triangular sublattices A and B.
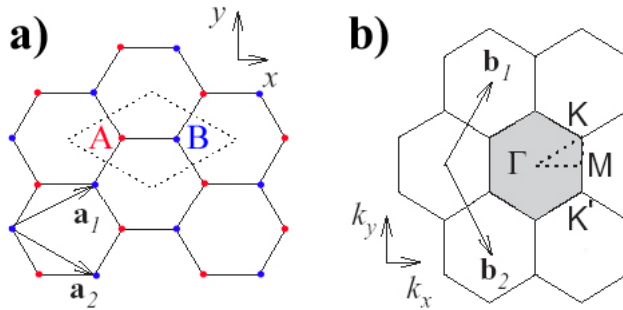
Fig. 3.1: a) The unit cell (dotted rhombus) and **b)** Brillouin zone (shaded hexagon) of graphene. The vectors $\vec{a}_i$ and $\vec{b}_i$ (i = 1,2) are the unit vectors and reciprocal lattice vectors, respectively. The high symmetry points Γ, M, K and K' of the reciprocal lattice are denoted in **b)**. Image adapted from [Dre05].

Performing the tight-binding calculation yields the following expression as the dispersion relation of a graphene monolayer (with $\vec{k} = (k_x, k_y)$, $a = |\vec{a}_1| = |\vec{a}_2|$ and $\gamma_0 \approx 2.5$ eV being the *nearest-neighbour transfer integral* for 2D graphite) [Sai98]:

$$E_{\text{g2D}}(k_x, k_y) = \pm\gamma_0 \left\{ 1 + 4\cos\left(\frac{\sqrt{3}k_x a}{2}\right)\cos\left(\frac{k_y a}{2}\right) + 4\cos^2\left(\frac{k_y a}{2}\right) \right\}^{1/2}. \qquad (3.1)$$

Thus, the respective energies at the high-symmetry points Γ, M and K/K' of the graphene Brillouin zone (cp. Fig. 3.2) are $E_{\text{g2D,}\Gamma} = \pm 3\gamma_0$, $E_{\text{g2D,M}} = \pm\gamma_0$ and $E_{\text{g2D,K/K'}} = 0$ [Sai98].

The graphene dispersion relation within the first Brillouin zone is depicted in figure 3.2. Figure 3.3a displays the graphene dispersion relation along the points of high symmetry M-Γ-K-M. The conduction band ($E > 0$) and the valence band ($E < 0$) form conically

shaped valleys which only touch in the K and K' points, named *Dirac points* as well. The density of states in the Dirac points equals zero. Therefore, a graphene monolayer is classified as a *zero-gap semiconductor*. For an undoped graphene layer, the Fermi energy intersects the dispersion relation exactly at $E = 0$.
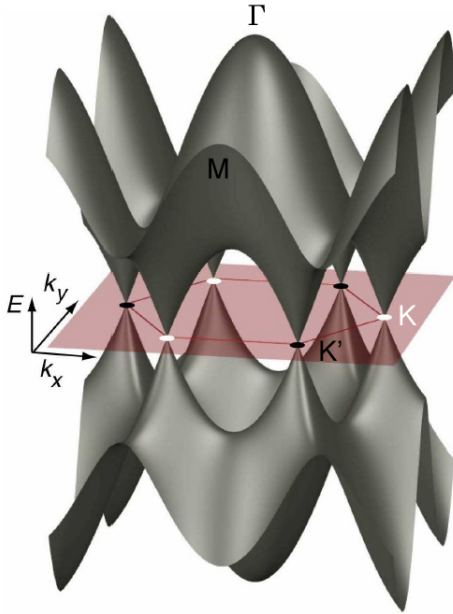
Fig. 3.2: Dispersion relation $E_{\text{g2D}}(k_{\text{x}}, k_{\text{y}})$ of a graphene monolayer plotted for its first Brillouin zone. The conduction band ($E > 0$) and the valence band ($E < 0$) exclusively touch in the K/K' points. Hence, graphene is a *zero-gap semiconductor*. The density of states vanishes in the K/K' points. Further high-symmetry points, namely Γ and M, are indicated (cp. Fig. 3.3). Image adapted from [Bee07].

The charge carriers contributing to transport in a graphene monolayer, i.e. electrons for $E > 0$ and holes for $E < 0$, are energetically close to the Fermi level. These charge carriers are 4-fold degenerate, due to 2 different spin orientations (*spin degeneracy*) and due to the 2 different sublattices within a graphene monolayer (*sublattice* or *valley degeneracy*). Literature often refers to the valley degeneracy with the term *pseudo-spin*, since quantum-mechanically the valley degeneracy can be described similarly to the electron spin. An exceptional property of the charge carriers in graphene monolayers is their *linear dispersion relation*[*] around the K/K' points, i.e. for $|\delta\vec{k}|\,a \ll 1$ ($\delta\vec{k}$ shall be the displacement from the K/K' position in reciprocal space) [Bee07]:

$$E_{\text{g2D}}(\delta\vec{k}) = \hbar v_{\text{F}}\,|\delta\vec{k}|\;. \tag{3.2}$$

In addition, the effective mass m_{eff} does not appear in the dispersion relation of graphene. The charge carriers in graphene behave similarly to light quanta in vacuum, the Fermi velocity $v_{\text{F}} \approx 10^6\,\text{m/s} \approx c/300$ plays an analogous role to the velocity of light. That means, that the charge carriers contributing to transport in a graphene monolayer behave as massless, relativistic quasi-particles theoretically described by the *Dirac equation* instead of the Schrödinger equation.

---

[*]Charge carriers in solids usually obey a parabolic dispersion relation, i.e. $E(\vec{k}) = \hbar^2\vec{k}^2/2m_{\text{eff}}$. The effective mass m_{eff} is introduced to account for the interactions of the charge carriers (described by *Bloch waves*) with the periodic potential of the lattice.
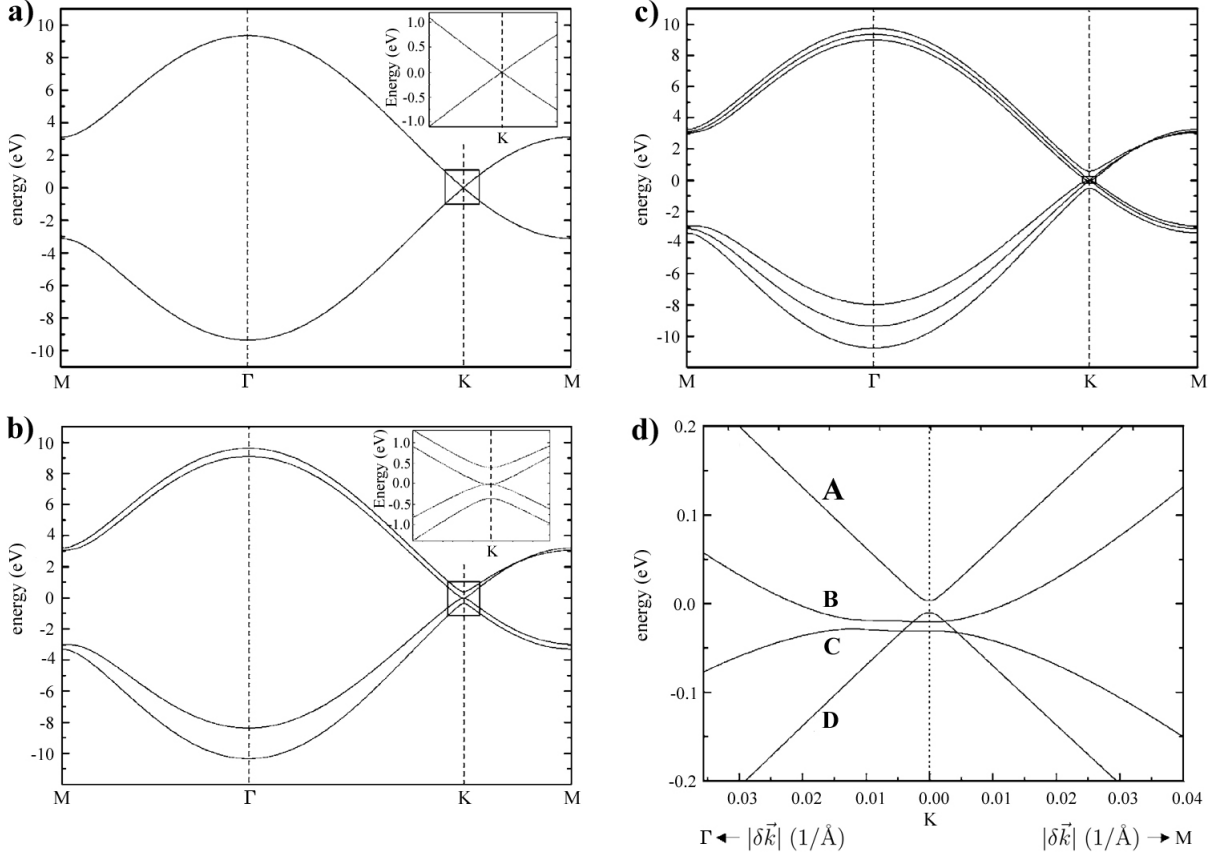
Fig. 3.3: Dispersion relation along the M-Γ-K-M direction of **a)** a graphene monolayer, **b)** a graphene bilayer and **c)** three stacked layers of graphene. Close-ups of the areas around the K points in **a)**, **b)** are given in the respective insets. For a monolayer, the conduction and valence bands touch at the K point at which the density of states (in the monolayer case) is zero. The bands of bilayer graphene overlap by only 1.6 meV at the K point. Panel **d)** displays a close-up of the area around the K point of three stacked graphene layers (cp. **c)**), for which conduction and valence bands overlap significantly by approx. 34 meV (A, B belong to the conduction and C, D to the valence band) [Par06].

Tight-binding calculations of the dispersion relations of graphene bi- and trilayers (displayed along the M-Γ-K-M directions in figures 3.3b,c) reveal, that for two and more stacked graphene layers, the graphene stack behaves as a *semi-metal* instead of a *zero-gap semiconductor* as in the graphene monolayer case. For a graphene bilayer (Fig. 3.3b), the band overlap of 1.6 meV is extremely small, whereas it already is approx. 34 meV for three graphene layers (Fig. 3.3d). For 11 and more stacked layers of graphene, the band overlap is larger than 90% of the value for bulk graphite (41 meV) [Par06].

Finally, figure 3.4 depicts the calculated density of states for a graphene mono- and bilayer [McK93]. The density of states $D_{\mathrm{g2D}}(E)$ of a graphene monolayer (Fig. 3.4a) is symmetric in the energy, this is a consequence of the electron-hole symmetry of the graphene dispersion relation (cp. equation (3.1)). Furthermore, as mentioned before, D_{g2D} becomes zero for $E = 0$. The two *van Hove* singularities in figure 3.4a correspond to the flat regions of the graphene dispersion relation around the M points in reciprocal space (cp. Fig. 3.3a).

Calculation of the density of states $D_{\mathrm{g2D,2l}}(E)$ of a graphene bilayer reveals that $D_{\mathrm{g2D,2l}}(E)$ consists of the sum of two single-layer density of states, where one is slightly shifted to lower and the other one to higher energies (Fig. 3.4b). These energy shifts can be assigned to interactions of atoms positioned directly above each other in different graphene layers [McK93]. The symmetry with respect to $E = 0$ is retained, whereas the density of states gets finite for zero energy.
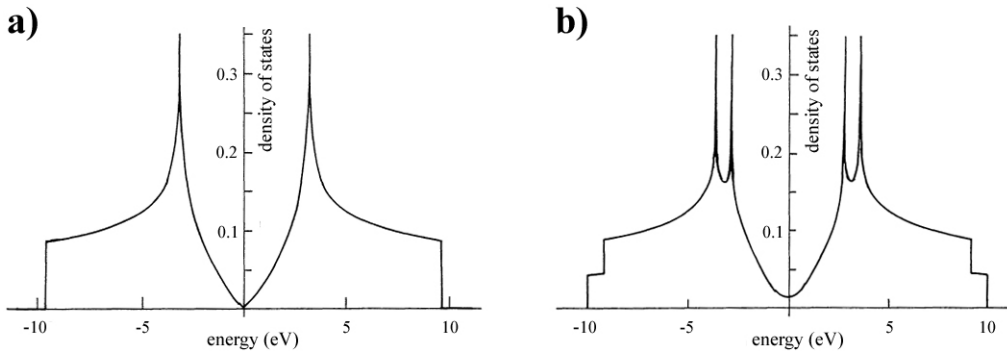
Fig. 3.4: Density of states of **a)** monolayer and **b)** bilayer graphene according to [McK93].

3.1.2   Electric field-effect in graphene mono- and bilayers

As a consequence of their density of states depicted in figure 3.4, graphene mono- and bilayers exhibit a pronounced *ambipolar field-effect*[†]. For both mono- and bilayers, there is high conductance for negative as well as for positive gate voltages, i.e. for the valence and the conduction band, respectively. Since neither a graphene monolayer nor any stacked graphene system of 2 or more layers is a real semiconductor in the sense of having a finite-size bandgap, conduction can not be pinched off in a graphene field-effect transistor device (unless narrow ribbons are etched out of graphene [Che07, Han07] which shall not be considered within this work). If the Fermi level E_{F} is at the *Dirac point*, i.e. at $E = 0$ (for an undoped graphene sample, $V_{\mathrm{g}} = 0$ V in this situation), the resistance and resistivity of the graphene mono- or bilayer are maximum. The gate dependence of the resistivity of an undoped graphene monolayer is shown in figure 3.5, the respective plot for a graphene bilayer can be found in the results chapter 5.
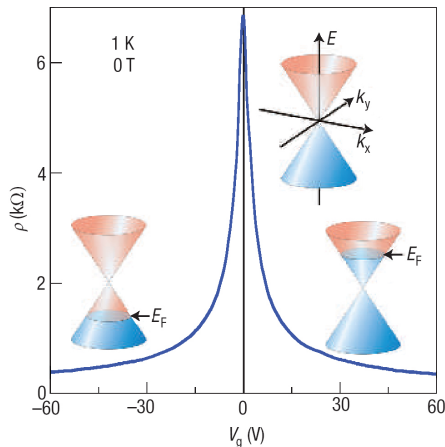
Fig. 3.5: Gate voltage dependence of the resistivity ρ of a graphene monolayer which exhibits a pronounced ambipolar field-effect. The insets illustrate the position of the Fermi level E_{F} with respect to the conical low-energy spectrum $E(k)$ in a schematical way for 3 different gate voltage regimes. The respective graphene monolayer has a mobility of approx. 5000 cm^2/Vs [Gei07].

[†]Some explanations regarding the electrical field-effect in general are given in chapter 3.2.2.

Comparing resistivity vs. gate voltage curves $\rho(V_g)$ of different graphene monolayers (Fig. 3.6a), it is apparent that the *Dirac point*, i.e. the resistivity peak in the gate dependence, can significantly differ from $V_g = 0$ which is a signature of unintentional doping [Tan07]. Since the density of states is sharply zero at $E = 0$ for a graphene monolayer (cp. Fig. 3.4a), one might expect zero conductivity there. Nevertheless, graphene exhibits a *finite minimum conductivity*, which could be due to the fact that graphene flakes are spatially extended samples with varying doping levels even within the same flake [Hal07] eventually inhibiting the precise adjustment of the Fermi level to the Dirac point across the whole flake. Different graphene flakes typically exhibit different resistivity maxima and conductivity minima, respectively (Figs. 3.6a-c), different degrees of disorder in the samples might play an important role in this respect. The data presented in figure 3.6 suggest a sample-dependent minimum conductivity value between 2-12 e^2/h rather than a sharp experimental value of $\sigma_{\min} = 4e^2/h$ [No05b, Gei07] (dotted line in figure 3.6b) or the value of $\sigma_{\min} = 4e^2/\pi h$ proposed theoretically [Nil06, Nom07] (dashed line in figure 3.6b). This *question of minimum conductivity in graphene* is not resolved yet, the reasons for the deviations between the experiments with respect to each other and to theory are still unclear. Figure 3.6d plots the mobility values for the 5 different graphene monolayers from figures 3.6a,c. Note that the used Drude model (cp. equation 3.7) is not applicable for vanishing charge carrier density ($n \to 0$), that is why the mobility curves are dotted lines in the regime around the *Dirac point*. Proper mobility values should be received for high positive or negative values of the charge carrier density n (i.e. of the gate voltage V_g). Comparing figures 3.6d and 3.6a, one further useful information can be gained: the higher the unintentional doping (i.e. the resistivity peak shift in panel a), the lower the mobility μ [Tan07]. Typical mobility values for graphene monolayers are between 3000 and 12000 cm^2/Vs (Fig. 3.6d), the highest mobilities μ reported so far are above 200000 cm^2/Vs [Bol08, Mor08].
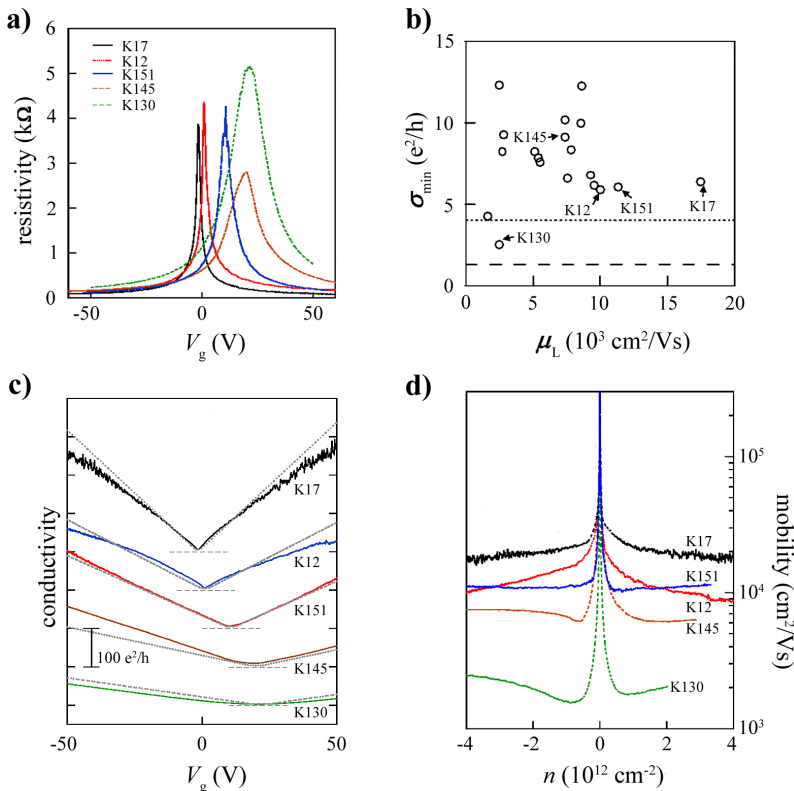
Fig. 3.6: a) Resistivity of 5 different graphene monolayers as function of the applied gate voltage V_g at $T = 1.6$ K. **b)** Minimum conductivity values $\sigma_{\min}$ of 19 different graphene monolayer flakes at $T = 1.6$ K. The 5 flakes of panel **a)** are indicated by arrows. The dotted line corresponds to $\sigma_{\min} = 4e^2/h$, the dashed line to $\sigma_{\min} = 4e^2/\pi h$. **c)** Data from panel **a)** replotted as conductivity curves. **d)** Mobility values extracted for the 5 graphene monolayers from panels **a),c)**. Panels **a)** to **d)** are adapted from [Tan07].

3.1.3 Hall effect and quantum Hall effect

Hall effect, charge carrier density and mobility

A 2-dimensional electron gas (2DEG) confined within a sample in the x-y plane (Fig. 3.7) shall move with constant speed $\vec{v} = (-v_x, 0, 0)$ along the x-axis under the influence of a homogeneous magnetic field $\vec{B} = (0, 0, B_z)$ applied along the z-direction.
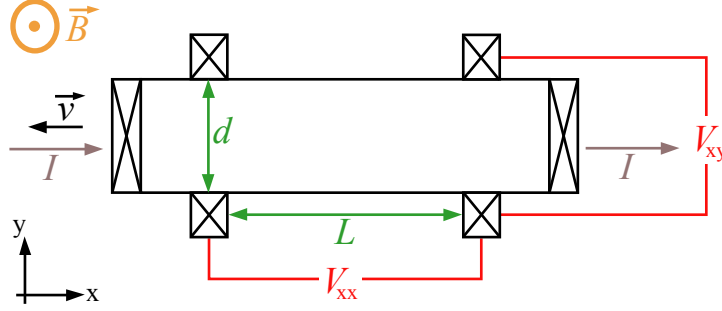
Fig. 3.7: Schematic drawing of the typical hallbar geometry: 6 contacts, i.e. the source and the drain contact as well as 4 voltage probes, are attached to a rectangular stripe of a 2-dimensional electron gas. The magnetic field $\vec{B}$ is applied perpendicularly to the sample along the z-axis. A constant current I is passed along the x-axis. The longitudinal voltage drop V_{xx} is probed with two leads (spacing L) at one edge of the hallbar, whereas the Hall voltage V_{xy} is measured across the hallbar of width d.

In the perpendicular magnetic field $\vec{B}$, the electrons are deflected by the *Lorentz force* $\vec{F}_L$. This gives rise to the formation of an electrical field $\vec{E}_H = (0, -E_y, 0)$ across the hallbar (Fig. 3.7) in such a way, that the resulting force $\vec{F}_{res}$ equals zero (*Hall effect*, E. Hall, 1879):

$$\begin{aligned} \vec{F}_{res} = \vec{F}_L - e\vec{E}_H &= 0 \\ \Rightarrow -e(\vec{E}_H + \vec{v} \times \vec{B}) &= 0 \\ \Rightarrow E_y &= v_x B_z \ . \end{aligned} \tag{3.3}$$

Inserting the definition of the electric field and using the relation between current density $\vec{j}$ and velocity $\vec{v}$ to replace the velocity v_x in equation (3.3) results in the well-known expression for the *Hall voltage* V_{xy} of a 2-dimensional electron gas (with charge carrier density n):

$$\left. \begin{aligned} E_y &= \frac{V_{xy}}{d} \\ \vec{j} = -en\vec{v} \Rightarrow v_x &= \frac{I}{end} \end{aligned} \right\} \Rightarrow V_{xy} = \frac{1}{en} I B_z \ . \tag{3.4}$$

Accordingly, the *Hall resistance* $R_{xy} = V_{xy}/I$ scales linearly with the perpendicular magnetic field B_z and is inversely proportional to the 2-dimensional charge carrier density n:

$$R_{xy} = \frac{1}{en} B_z \ . \tag{3.5}$$

Equation (3.5) provides an easy way how to determine the charge carrier density n of a 2DEG for a given gate voltage V_g experimentally: after measuring the Hall resistance R_{xy}

as a function of the magnetic field B_z at a fixed gate voltage V_g, the charge carrier density n can be directly extracted from the slope.

Another important parameter of a 2-dimensional electron gas (and conductors in general) is the *charge carrier mobility* μ defined as the proportionality factor between an applied electric field $\vec{E}$ and the resulting charge carrier drift velocity $\vec{v}$:

$$\vec{v} = \mu \vec{E} \ . \tag{3.6}$$

The larger μ is, the higher is the final drift velocity the charge carriers can gain due to the applied electric field. The mobility μ and thus the value of the final drift velocity $|\vec{v}|$ is limited by interactions of the charge carriers with phonons or lattice defects. A phenomenon called *ballistic transport* refers to the case in which μ is infinitely large due to the absence of phonons and lattice defects. In practice, phonons and defects can not vanish completely. Nevertheless for certain, nearly-defect-free materials ballistic transport can be observed (up to a certain length of the conductor) at very low temperatures, at which phonons are strongly suppressed. Employing the formula $\vec{j} = -en\vec{v}$ for the current density $\vec{j}$ (semiclassical Drude model) and substituting $\vec{v}$ according to equation (3.6) yields the following expression for the mobility μ of a 2-dimensional electron gas (length L and width d as depicted in figure 3.7, longitudinal resistivity ρ_{xx}):

$$
\begin{aligned}
\vec{j} &= -en\vec{v} = -en\mu\vec{E} \\
\Rightarrow \frac{I}{d} &= \frac{en\mu V_{xx}}{L} \\
\Rightarrow \mu &= \frac{LI}{en\,d\,V_{xx}} = (en\rho_{xx})^{-1} \ .
\end{aligned}
\tag{3.7}
$$

Thus, the mobility μ at fixed gate voltage V_g can be determined experimentally, since the applied current I as well as the hallbar geometry (meaning the values of L and d) is known. The longitudinal voltage drop V_{xx} (at $B = 0$ T) can be measured, the charge carrier density n follows from the Hall effect as described above.

Resistivity and conductivity tensors

Dealing with a hallbar setup as depicted in figure 3.7, the essential voltages or resistances are often given as resistivities and/or conductivities. In this regard, the following formulae apply:

$$\rho_{xx} = R_{xx}\frac{d}{L} \quad , \quad \rho_{xy} = -R_{xy} \ . \tag{3.8}$$

To convert the resistivities into conductivities and vice versa, the subsequent relations are used, with $\rho_{xx} = \rho_{yy}$ and $\rho_{xy} = -\rho_{yx}$ (and $\sigma_{xx} = \sigma_{yy}$ and $\sigma_{xy} = -\sigma_{yx}$) due to the isotropy of the 2-dimensional electron gas:

$$\sigma_{xx} = \sigma_{yy} = \frac{\rho_{xx}}{\rho_{xx}^2 + \rho_{xy}^2} \quad , \quad \sigma_{xy} = -\sigma_{yx} = -\frac{\rho_{xy}}{\rho_{xx}^2 + \rho_{xy}^2} \tag{3.9}$$

$$\rho_{\text{xx}} = \rho_{\text{yy}} = \frac{\sigma_{\text{xx}}}{\sigma_{\text{xx}}^2 + \sigma_{\text{xy}}^2} \quad , \quad \rho_{\text{xy}} = -\rho_{\text{yx}} = -\frac{\sigma_{\text{xy}}}{\sigma_{\text{xx}}^2 + \sigma_{\text{xy}}^2} \; . \tag{3.10}$$

Utilizing the calculated $\rho_{\text{xx}}, \rho_{\text{xy}}, \rho_{\text{yx}}, \rho_{\text{yy}}$ values, the *Ohm's law* (for a 2DEG) can be expressed by the *resistivity tensor* $\boldsymbol{\rho}$:

$$\vec{E} = \boldsymbol{\rho}\vec{j} \Leftrightarrow \begin{pmatrix} E_{\text{x}} \\ E_{\text{y}} \end{pmatrix} = \begin{pmatrix} \rho_{\text{xx}} & \rho_{\text{xy}} \\ \rho_{\text{yx}} & \rho_{\text{yy}} \end{pmatrix} \begin{pmatrix} j_{\text{x}} \\ j_{\text{y}} \end{pmatrix} \Leftrightarrow \begin{cases} E_{\text{x}} = \rho_{\text{xx}} j_{\text{x}} + \rho_{\text{xy}} j_{\text{y}} \\ E_{\text{y}} = \rho_{\text{yx}} j_{\text{x}} + \rho_{\text{yy}} j_{\text{y}} \end{cases} . \tag{3.11}$$

Furthermore, the current density $\vec{j}$ can be expressed through the electric field $\vec{E}$ using the *conductivity tensor* $\boldsymbol{\sigma}$:

$$\vec{j} = \boldsymbol{\sigma}\vec{E} \Leftrightarrow \begin{pmatrix} j_{\text{x}} \\ j_{\text{y}} \end{pmatrix} = \begin{pmatrix} \sigma_{\text{xx}} & \sigma_{\text{xy}} \\ \sigma_{\text{yx}} & \sigma_{\text{yy}} \end{pmatrix} \begin{pmatrix} E_{\text{x}} \\ E_{\text{y}} \end{pmatrix} \Leftrightarrow \begin{cases} j_{\text{x}} = \sigma_{\text{xx}} E_{\text{x}} + \sigma_{\text{xy}} E_{\text{y}} \\ j_{\text{y}} = \sigma_{\text{yx}} E_{\text{x}} + \sigma_{\text{yy}} E_{\text{y}} \end{cases} . \tag{3.12}$$

Quantum Hall effect

The occurrence of the Hall voltage V_{xy} can be described in a semi-classical way, yet for gaining insights in the *quantum Hall effect* and in the (microscopic) behaviour of a 2DEG at high magnetic fields, the energy quantization of electrons into so-called *Landau levels* has to be taken into account.

Without a magnetic field applied, the energy E of mobile electrons in a 2DEG is quasicontinuous, with an effective mass m_{eff} instead of m to account for the electron-lattice interactions (E_0 being a reference energy):

$$E = E_0 + \frac{\hbar^2}{2m_{\text{eff}}} \left(k_{\text{x}}^2 + k_{\text{y}}^2 \right) . \tag{3.13}$$

However, a strong magnetic field $B = (0, 0, B_{\text{z}})$ along the z-direction makes the electrons move in *cyclotron orbits* within the x-y plane with cyclotron radii $l_{\text{c}} = (\hbar c/eB)^{1/2}$. The ideal energy spectrum of these electrons comprises discrete *Landau levels* spaced by the cyclotron energy and the Zeeman energy (if the spins of the electrons are taken into account):

$$E_N = E_0 + \left(N + \frac{1}{2} \right) \hbar\omega_{\text{c}} + m_{\text{s}} g_{\text{s}} \mu_{\text{B}} B \qquad N = 0, 1, 2, ... \tag{3.14}$$

with the cyclotron energy $\hbar\omega_{\text{c}} = \hbar eB/m_{\text{eff}}$, the spin quantum number $m_{\text{s}} = \pm 1/2$, the Landé factor g_{s}, the Bohr magneton μ_{B}, and E_0 being a reference energy [vKl86]. The number of electron states per Landau level and per area (and per spin orientation) is

$$n_{\text{L}} = \frac{B}{\Phi_0} = \frac{e}{h} B \tag{3.15}$$

with the *magnetic flux quantum* $\Phi_0 = h/e$ [vKl05]. Further, the *filling factor* ν of a homogeneous 2DEG with electron density n is given by

$$\nu = \frac{n}{n_{\mathrm{L}}} = \frac{h}{e}\frac{n}{B}\;.\tag{3.16}$$

Measuring the Hall resistance R_{xy} for integer filling factors ν yields the following values, which are theoretically expected according to equations (3.5) and (3.16):

$$R_{\mathrm{xy},\nu} = \frac{h}{\nu e^2}\qquad\qquad \nu = 1,2,3,\dots\;.\tag{3.17}$$

The unexpected discovery by Klaus von Klitzing in 1980 [vKl80, vKl84, vKl86, vKl05] was that the R_{xy} values in equation (3.17) do not solely occur at discrete, integer filling factors ν, but pronounced plateaus with the respective resistance values are observable in the $R_{\mathrm{xy}}(B)$ and $R_{\mathrm{xy}}(n)$ measurements, respectively (the charge carrier density n is tuned by the gate voltage V_{g}). Furthermore, the longitudinal resistance R_{xx} equals zero within the regimes of the R_{xy} plateaus (Fig. 3.8).
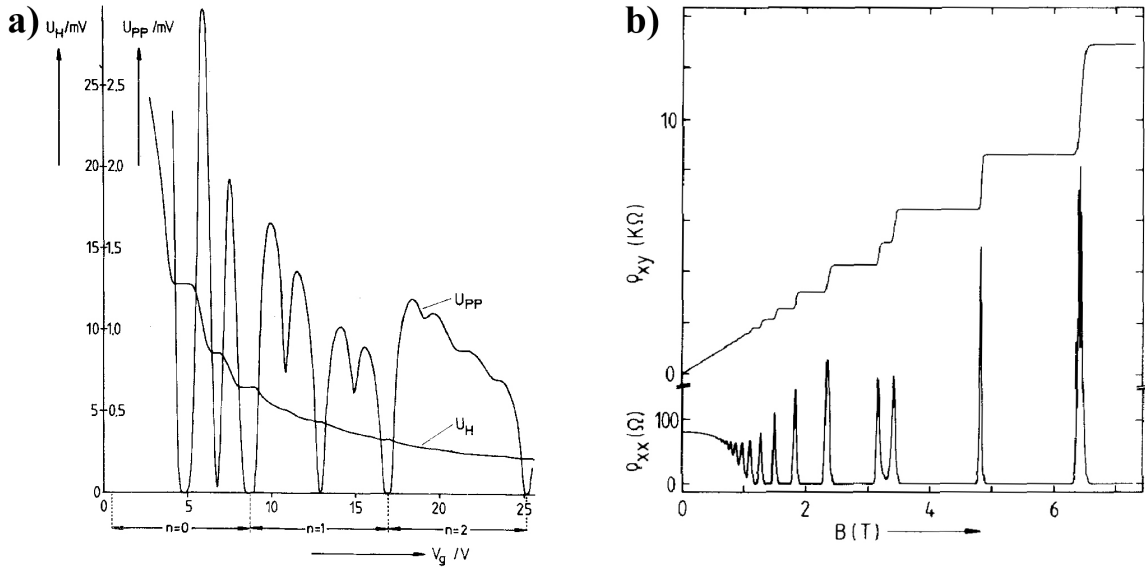
Fig. 3.8: a) Quantum Hall effect measurement on a 2DEG within a MOSFET Si transistor performed at $T = 1.5$ K and $B = 18$ T [vKl80]. U_{PP} corresponds to V_{xx}, U_{H} to V_{xy}, respectively. Longitudinal voltage and Hall voltage are measured as functions of the gate voltage V_{g}, i.e. charge carrier density. **b)** Longitudinal resistivity ρ_{xx} and Hall resistivity ρ_{xy} as a function of magnetic field B measured on a 2DEG within a GaAs/AlGaAs heterostructure at $T = 8$ mK [vKl84].

For filling factor $\nu = 1$, the Hall voltage is $R_{\mathrm{xy},1} = h/e^2 = 25812.807\dots\ \Omega$. Independently of the material, geometry or microscopic details of the sample which contains the 2DEG, experiments yield this value with a precision better than $2 \cdot 10^{-9}$ [vKl05]. That is why in 1990, the *von Klitzing constant* $R_{\mathrm{K}-90} = 25812.807\ \Omega$ was introduced as reference value for resistance calibrations [vKl05]. Moreover, this precise value of $R_{\mathrm{xy},1}$ is proportional to the inverse of the fine-structure constant α (the magnetic constant μ_0 and c have defined and constant values):

$$R_{\mathrm{xy},1} = \frac{h}{e^2} \propto \alpha^{-1} = \frac{h}{e^2}\frac{2}{\mu_0 c} = 137.036\dots\;.\tag{3.18}$$

The latter fact is an important aspect of the quantum Hall effect, namely to relate an effect occurring in solid state and semiconductor physics respectively to such a fundamental physical constant as the fine-structure constant α [vKl80, vKl86, vKl05].

In the following, the *quantum Hall effect*, i.e. the occurrence of plateaus in the Hall resistance R_{xy} and the accompanying disappearance of the longitudinal resistance R_{xx}, shall be explained on the basis of the *edge channel picture*. The description predominantly follows [Hun07], spin-splitting is *not* taken into account.

Due to the *Landau level quantization*, the density of states $D(E)$ of an *ideal* 2-dimensional electron gas no longer is constant (as for $B = 0$, dashed line in Fig. 3.9a), but splits into a series of δ-functions as depicted in figure 3.9a. However, a *real* 2DEG within a hallbar comprises disorder as well as defects which leads to spatial potential fluctuations across the electron gas. That is why the peaks in the density of states of a *real* 2DEG are broadened (in comparison to the ideal case) as shown in figure 3.9b. Furthermore, a *real* 2DEG within a hallbar has edges, along which the electrical potential steeply increases to the vacuum potential.
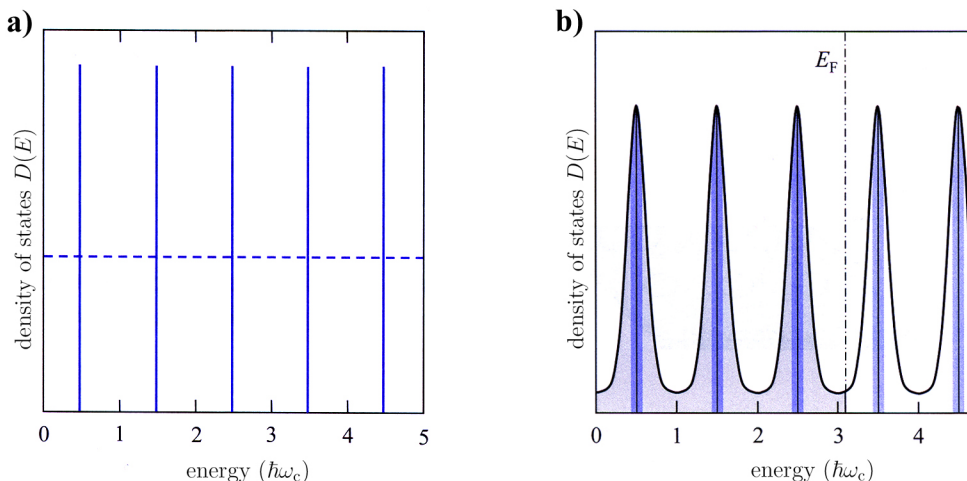
Fig. 3.9: Density of states of **a)** an *ideal* and **b)** a *real* 2-dimensional electron gas (spin splitting is not taken into account). Disorder and defects in the latter case cause potential fluctuations across the 2DEG and thus a broading of the peaks in the $D(E)$ plot [Hun07].

In a first step, only the effects of the hallbar edges on the 2DEG in the quantum Hall regime shall be considered, the implications of defects and disorder will be added later on. Within the 2DEG, the electrons are cycling in cyclotron orbits and do not contribute to the charge transport. The corresponding energy states are the described Landau levels. As already mentioned, the electrical potential along the edges of the 2DEG increases steeply to the vacuum potential, which means that the Landau level energies are bent considerably at the edges. The Fermi energy intersects the Landau levels bent upwards as indicated in figure 3.10a. In this way, 1-dimensional conductance channels, so-called *edge channels*, are formed along the edges of the 2DEG (Figs. 3.10a and 3.11). At the edges of the 2DEG,

the electrons are reflected elastically. The magnetic field suppresses back-scattering and makes the electrons bounce along the sample edges - that is why these trajectories have been named *skipping orbits* (Fig. 3.10b).
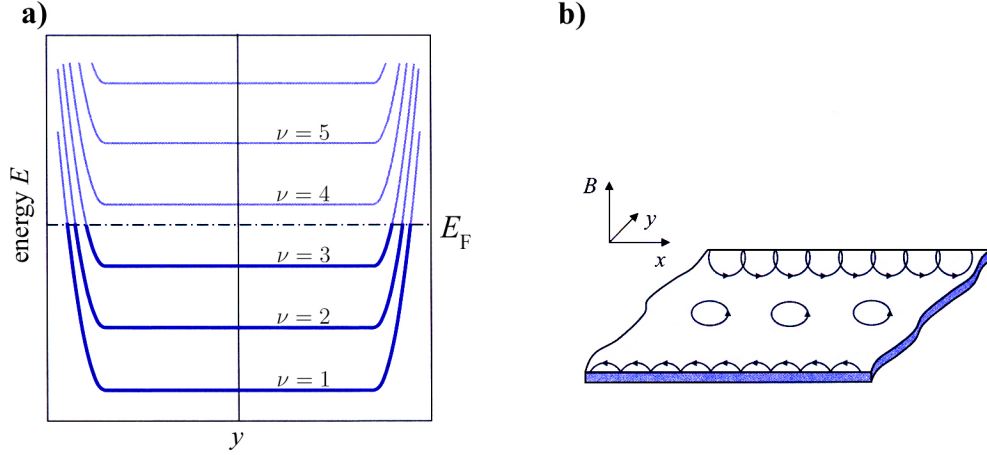

Fig. 3.10: *Edge channels* within a 2-dimensional electron gas in an external perpendicular magnetic field. **a)** Energy plotted versus coordinate y (coordinate along the width of the hallbar, cp. figure 3.7). Within the 2DEG, the Landau level energies correspond to the values described in the main text, the respective filling factors ν are given in the plot. In contrast, the Landau levels are bent upwards to the vacuum potential along the edges of the 2DEG. The Fermi energy intersects the Landau levels bent upwards and forms the so-called *edge channels*. **b)** Schematic illustration of the electron trajectories in the *edge channel picture*: electrons contributing to charge transport bounce along the edges, whereas the electrons within the 2DEG move in closed cyclotron orbits [Hun07].

Due to the Lorentz force, the electrons moving along opposite sample edges move in opposite directions. Every of these quasi-ballistic channels contributes to the electrical transport with one *conductance quantum* $G_{0,\text{s}} = e^2/h$ (per spin orientation).

In the following, the Fermi level E_F shall be between two Landau levels as indicated in figure 3.10a. In this case, there are no states at the Fermi level within the hallbar (Fig. 3.10a), and the charge transport channels for different directions are spatially well separated along the hallbar edges. For these two reasons, inelastic backscattering can be excluded.

Based on this *edge channel picture*, the potentials at the hallbar contacts and the corresponding current, longitudinal and Hall voltage values shall be evaluated (again for the Fermi energy E_F between two Landau levels). For simplicity reasons, perfect transmission between the contacts and no reflection of electrons at the contacts are assumed. Contact 1 shall be at potential $\mu_1 = -\mu$, contact 4 on potential $\mu_4 = 0$ (cp. Fig. 3.11). Thus, the electrons move from contact 1 via contacts 2 and 3 to contact 4 (Fig. 3.11). Since no current is extracted at the contacts 2 and 3, their potentials equal the one of the first contact, i.e. $\mu_1 = \mu_2 = \mu_3 = -\mu$. The same argumentation holds for the opposite way,
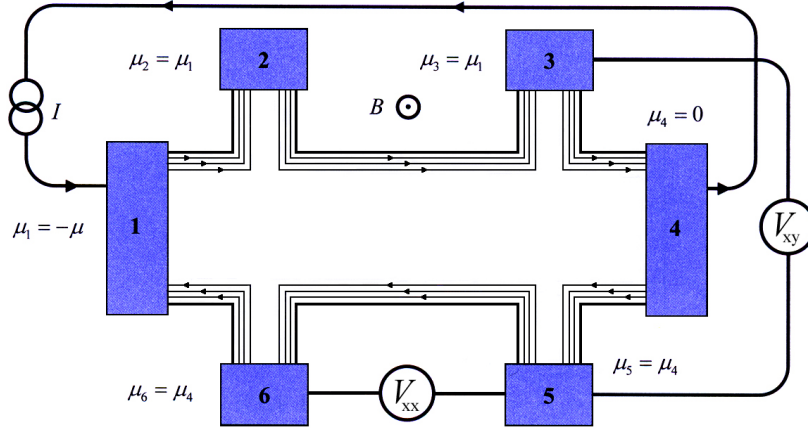
Fig. 3.11: Schematic description of a hallbar in the quantum Hall regime according to the *edge channel picture*. The current I flows from contact 1 to contact 4. The arrows point along the direction of electron motion, *not* along the conventional current direction. Contacts 1 and 4 are at potentials $\mu_1 = -\mu$ and $\mu_4 = 0$, respectively. It is assumed that the Fermi level E_F is between the 3rd and the 4th Landau level (cp. Fig. 3.10a), so that 3 edge channels constitute the electrical transport [Hun07].

along the lower edge of the hallbar in figure 3.11, i.e. $\mu_4 = \mu_5 = \mu_6 = 0$ (which means that the lower channels do not contribute to the current). The resulting current I through the hallbar (per spin orientation) is therefore given by

$$I = \nu \frac{\mu_3 - \mu_4}{e} G_{0,s} = \nu \frac{\mu_3}{e} G_{0,s} = -\nu \frac{\mu}{e} G_{0,s} = -\nu \frac{\mu e}{h} \tag{3.19}$$

with ν being the number of filled Landau levels, i.e. the number of edge channels ($\nu = 3$ in the example depicted in figure 3.10a). With this current I, the Hall resistance R_{xy} reads

$$R_{xy} = \frac{\mu_3 - \mu_5}{eI} = \frac{h}{\nu e^2} \tag{3.20}$$

and the corresponding longitudinal resistance R_{xx} vanishes, since

$$R_{xx} = \frac{\mu_5 - \mu_6}{eI} = 0 \ . \tag{3.21}$$

Finally, the introduced *edge channel picture* of the quantum Hall effect shall be reviewed under the more realistic assumption that real 2DEGs exhibit defects and disorder. As discussed before, defects and disorder in a 2DEG lead to spatial potential fluctuations across the hallbar and thus to broadened Landau level peaks in the 2-dimensional density of states $E(D)$ (Fig. 3.9). The spatial potential fluctuations across the hallbar also have to be considered when plotting the energy of the Landau levels versus the coordinate y along the width of the hallbar. Doing so, figure 3.10a has to be replaced by figure 3.12a taking into account potential fluctuations. These potential fluctuations cause conductance channels within the hallbar as well, which are closed orbits and localized, though, and thus do *not* contribute to charge transport (Fig. 3.12b). Since electrons can not be scattered through these closed orbits within the hallbar, transport still is free of dissipation. The

situation depicted in figure 3.12b corresponds to the energy diagram in figure 3.12a in which the Fermi energy is between the 3rd and 4th Landau level (just touching some peaks from the third Landau level energy). If in this situation the magnetic field B is increased or the charge carrier density n is decreased (by tuning the gate voltage V_g, the Fermi energy gets closer to the lower (in the depicted case 3rd) Landau level, the existing closed orbits gain size and further ones are added. Increasing B (decreasing n) further, the inner two edge channels begin to move away from the hallbar edges (Fig. 3.12c), and backscattering of electrons gets possible (Fig. 3.12d). When finally the Fermi energy is in the Landau level, the two inner channels break into large, localized states within the hallbar (Fig. 3.12e), by which the electrons can be scattered from one edge of the 2DEG to the other. Thus, the longitudinal resistance R_{xx} gets maximum in this state, correspondingly, the Hall resistance R_{xy} changes. In contrast, the quantum Hall effect signatures, i.e. the plateaus of the Hall resistance R_{xy} and the associated disappearance of the longitudinal resistance R_{xx}, are observed if the Fermi energy E_F is between two Landau levels.
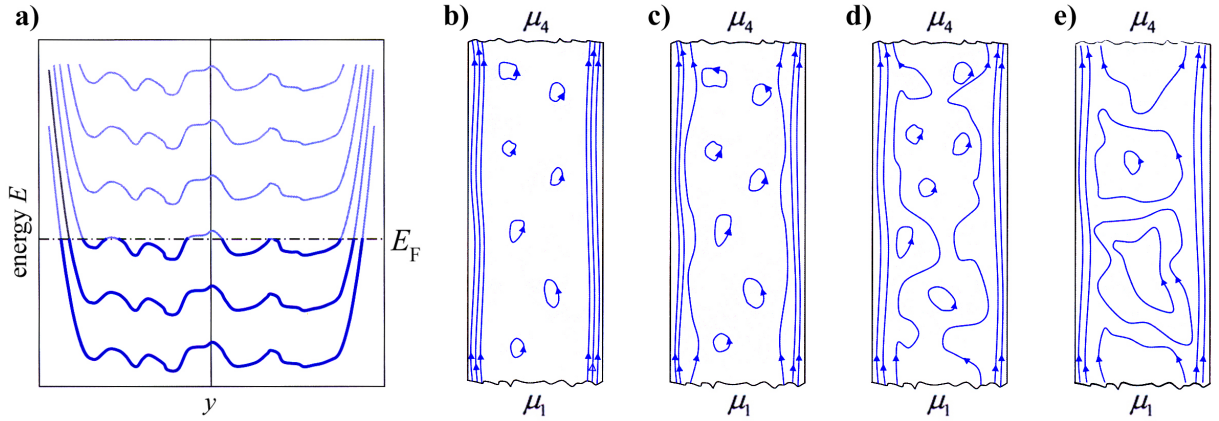
Fig. 3.12: a) Defects and disorder in a 2DEG cause potential fluctuations and therefore Landau level energy fluctuations within the hallbar. **b)-e)** Edge channels in a hallbar (with defects and disorder) at different values of the magnetic field B (or the charge carrier density n). **b)** This situation corresponds to **a)**: the Fermi energy E_F is between the 3rd and the 4th Landau level, so there are 3 edge channels. In addition, due to the local maxima of the Landau level energies, there are closed electron orbits within the hallbar which do not contribute to the charge transport. **c),d)** Increasing B (or decreasing n) minimizes the distance of the Fermi level to the lower, i.e. (in this case) the 3rd Landau level. The inner 2 edge channels move away from the hallbar edges, the inner closed orbits get larger, further closed orbits emerge. Backscattering of the electrons gets possible. **e)** B (n) has been increased (decreased) further, so that the Fermi energy is within the lower Landau level. The inner 2 channels break apart and form large, localized states within the hallbar, through which the electrons can be scattered from one edge to the other. Therefore, inelastic scattering as well as the longitudinal resistance is maximum in this situation, and the Hall voltage R_{xy} is changing [Hun07].

The introduced *edge channel picture* of the *quantum Hall effect* represents a model for basic understanding. Meanwhile theoretical as well as experimental studies refined this picture, especially the microscopic potential distribution in the quantum Hall state, introducing the concept of *compressible and incompressible strips*. Experimentally, researchers got access to the potential distribution in the quantum Hall regime by scanning a hallbar in the quantum Hall state with a low temperature atomic force microscope which is sensitive to electrostatics [We00a, We00b, Ahl01, Ahl02]. Introducing the theory of compressible and incompressible strips would go beyond the scope of this thesis. For further details regarding the *edge channel picture* and especially the concept of *compressible and incompressible strips* of the *quantum Hall effect* refer to the following publications [Bue88, Chk92, Hau93, Lie94, Dat95, Yos02, Gue03, Sid04, vKl05].

3.1.4 Quantum Hall effect in graphene mono- and bilayers

As in a silicon MOSFET or in a GaAs heterostructure (cp. last chapter), 2-dimensional electron gases can be realized as well in graphene mono- and bilayers. In the graphene case, the electron confinement along the z-axis is already given due to geometry and does not need to be induced by application of a gate voltage or by stacking of layers in a heterostructure. A further difference between the 2DEGs in Si MOSFET or a GaAs heterostructure and the ones in a graphene mono- or bilayer is the kind of charge carriers as well as the associated Landau level quantizations. In a Si MOSFET or a GaAs heterostructure, the charge carriers are electrons or holes (unless the *fractional QHE* is considered, where correlation effects play an important role and *composite fermions* are introduced) with the Landau level spectrum given by equation (3.14), in which essentially $E_N \propto N + 1/2$ (cp. Fig. 3.13c), if the spin of the charge carriers is not taken into account. Concerning a graphene monolayer, the charge carriers behave as relativistic, massless Dirac fermions with the following Landau level spectrum [Gei07], plotted in figure 3.13a:

$$E_N = \pm\sqrt{2e\hbar v_F^2 NB} \qquad N = 0, 1, 2, \dots . \qquad (3.22)$$

In the case of a graphene bilayer, the massless Dirac fermions are transformed into a new kind of quasiparticles provided with a finite effective mass $m_{eff} \approx 0.05 m_0$ (m_0 being the electron rest mass) and the parabolic spectrum $E(\vec{k}) = \hbar^2 \vec{k}^2 / 2m_{eff}$ by coupling of the two graphene layers [Nov06]. The Landau level spectrum of these *massive Dirac fermions* in a graphene bilayer is given by

$$E_N = \pm\hbar\omega_c \sqrt{N(N-1)} \qquad N = 0, 1, 2, \dots \qquad (3.23)$$

[Gei07], as displayed in figure 3.13b.

The differences between the Landau level spectra of charge carriers in conventional 2DEGs and in graphene mono- and bilayers lead to significant alterations in the sequence of Hall conductivity values σ_{xy}, at which quantum Hall plateaus occur.
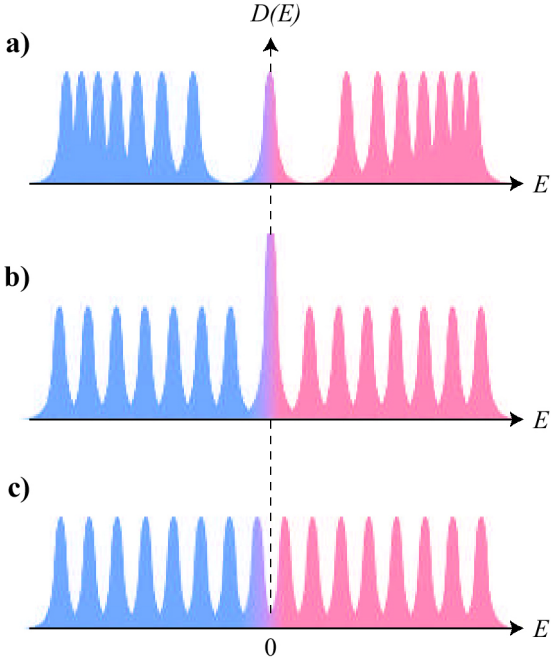
Fig. 3.13: Different types of Landau level quantization. **a)** Landau level spectrum of a graphene monolayer, where $E_N \propto \sqrt{N}$. **b)** Landau level quantization for a graphene bilayer, in which $E_N \propto \sqrt{N(N-1)}$. **c)** The standard Landau level sequence in the density of states as it is known from quantum Hall effect measurements on Si samples or GaAs heterostructures (cp. equation (3.14)): $E_N \propto N + 1/2$. Adapted from [Gei07].

For the conventional *quantum Hall effect*, the σ_{xy} values of quantum Hall plateaus are given by

$$\sigma_{xy} = R_{xy}^{-1} = \nu \frac{e^2}{h} \quad \text{with} \quad \nu = 1, 2, 3, \dots . \tag{3.24}$$

In contrast, the quantum Hall plateaus appear for the following values of σ_{xy} in a graphene monolayer:

$$\sigma_{xy} = R_{xy}^{-1} = \pm\xi \left(N + \frac{1}{2} \right) \frac{e^2}{h} \quad \text{with} \quad \nu = \pm\xi \left(N + \frac{1}{2} \right) \quad \text{and} \quad N = 0, 1, 2, 3, \dots , \tag{3.25}$$

whereas for a graphene bilayer, the respective values are

$$\sigma_{xy} = R_{xy}^{-1} = \pm\xi N \frac{e^2}{h} \quad \text{with} \quad \nu = \pm\xi N \quad \text{and} \quad N = 1, 2, 3, \dots . \tag{3.26}$$

For all three equations (3.24) to (3.26), the longitudinal resistance R_{xx} equals zero, as it always is the case in the quantum Hall regime. For graphene mono- and bilayers, in which only the low-lying Landau levels are occupied (*low-lying* means $|N| < 10^4$ for $B = 10$ T), the Landau level separation ΔE_N is small compared to the Zeeman spin splitting, so that each Landau level has a degeneracy of $\xi = 4$ accounting for spin and sublattice degeneracy [Zha05, Gei07]. Thus, the sequence of filling factors ν at which quantum Hall plateaus occur is $\nu = \pm 2, \pm 6, \pm 10, \dots$ for a monolayer and $\nu = \pm 4, \pm 8, \pm 12, \dots$ for a bilayer of graphene.

Figure 3.14 depicts experimental data on the quantum Hall effect in a graphene monolayer measured by Y. Zhang et al. [Zha05]. The longitudinal resistance R_{xx} and the Hall resistance R_{xy} at $T = 30$ mK and $V_g = 15$ V are drawn as functions of the applied magnetic field B in figure 3.14a. The expected plateaus of the Hall resistance at filling factors
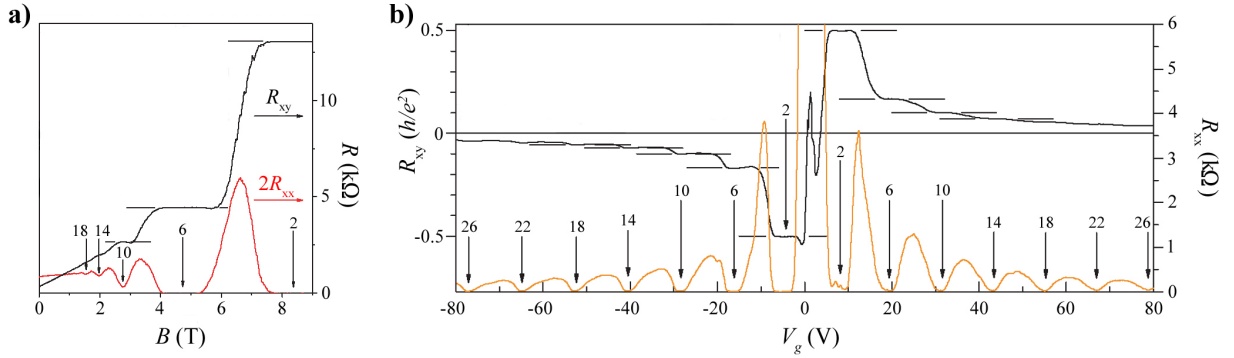
Fig. 3.14: Quantum Hall effect measurements on a graphene monolayer. **a)** Longitudinal resistance R_{xx} (red) and Hall resistance R_{xy} (black) as functions of the perpendicularly oriented, external magnetic field B at $T = 30$ mK and $V_{\text{g}} = 15$ V. The vertical arrows are labeled with the filling factors ν at which the longitudinal resistance vanishes. At the same magnetic field values, the Hall voltage R_{xy} equals $h/\nu e^2$, indicated by horizontal lines. The quantum Hall plateaus at filling factors 2, 6 and 10 are well resolved. **b)** Dependence of R_{xx} (orange) and R_{xy} (black) on the gate voltage V_{g} (and the charge carrier density n, respecively) measured in a graphene monolayer at $T = 1.6$ K and fixed magnetic field $B = 9$ T. Again, the integer numbers above the arrows indicate filling factors ν. Adapted from [Zha05].
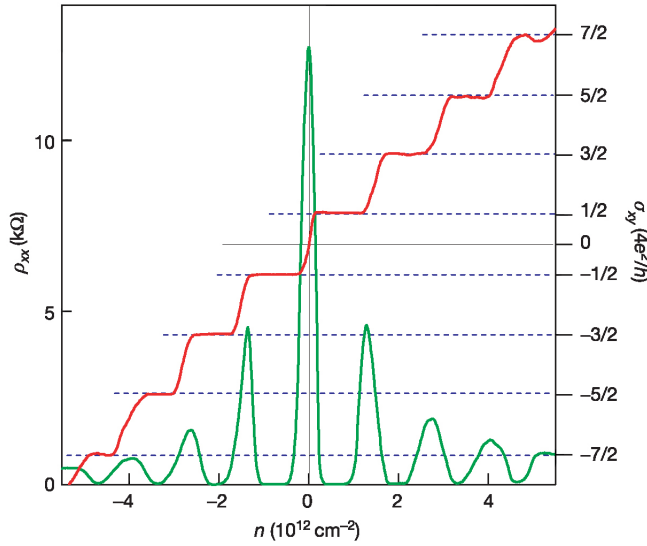

Fig. 3.15: Hall conductivity σ_{xy} and longitudinal resistivity ρ_{xx} of a quantum Hall effect measurement on a graphene monolayer at $B = 14$ T and $T = 4$ K. σ_{xy} and ρ_{xx} are plotted vs. the charge carrier density n (i.e. vs. the gate voltage V_{g}. The corresponding values R_{xy} and R_{xx} of the Hall resistance and the longitudinal resistance have been transformed into conductivity and resistivity values using equations (3.8) to (3.10). Plotting σ_{xy} instead of R_{xy}, the equidistantly spaced quantum Hall plateaus become apparent. Adapted from [No05b].

$\nu = 2, 6, 10$ are clearly resolved, simultaneously the longitudinal resistance R_{xx} is vanishing. Figure 3.14b plots R_{xx} and R_{xy} as functions of the applied gate voltage V_{g} at fixed magnetic field $B = 9$ T, measured at 1.6 K. In this type of measurement, the Landau levels are first filled with holes (for $V_{\text{g}} < V_{\text{Dirac}}$) and finally, for $V_{\text{g}} > V_{\text{Dirac}}$ with electrons. $R_{\text{xx}}(V_{\text{g}})$ exhibits symmetric Shubnikov-de Haas oscillations with vanishing longitudinal resistance for the expected filling factors, whereas the Hall resistance $R_{\text{xy}}(V_{\text{g}})$ together with its well-resolved Hall plateaus is antisymmetric clearly reflecting the polarity change of the charge carriers at the *Dirac point*.

Similar data on graphene monolayers have been acquired at the same time by K. S. No-voselov et al. [No05b] (Fig. 3.15). In this case, instead of resistances, the longitudinal resistivity ρ_{xx} and the Hall conductivity σ_{xy} are plotted vs. the charge carrier density (Fig. 3.15). For calculating resistivities/conductivities from resistances or vice versa, see equations (3.8) to (3.10). The charge carrier density n is tuned by the gate voltage V_g, it can be obtained from V_g by $n = \tilde{\alpha}V_g$ with $\tilde{\alpha} \approx 7.3 \times 10^{10}$ cm^{-2}V^{-1} for the widely used 300 nm SiO$_2$ dielectric [No05b]. The theoretically expected, equidistant plateaus in σ_{xy} (equation (3.25)), which are an uninterrupted sequence also when going through the *Dirac point*, are resolved in the experiment and depicted in figure 3.15 along with the cha-racteristic Shubikov-de Haas oscillations with vanishing ρ_{xx} for the respective filling factors.

As for *quantum Hall effect* measurements on graphene bilayers, K. S. Novoselov et al. published results in 2006 some of which are displayed in figure 3.16. The data have been acquired at 4 K, figure 3.16a plots ρ_{xy} and ρ_{xx} vs. the applied magnetic field B, whereas figures 3.16b,c illustrate σ_{xy} and ρ_{xx} as functions of the charge carrier density n at $B = 12$ T and $B = 20$ T, respectively. The measurements confirm the sequence of quantum Hall plateaus in σ_{xy} according to equation (3.26). The spacings between the Hall conductivity plateaus are again equidistant with one exception at the *Dirac point* at which a double spacing occurs, which - together with the different filling factors - makes up a distinct difference between graphene mono- and bilayers.
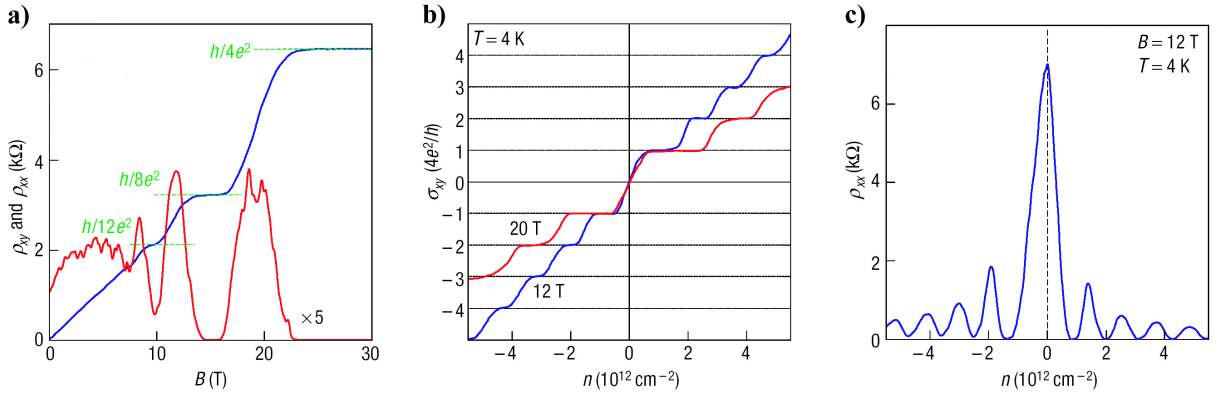
Fig. 3.16: Quantum Hall effect in a graphene bilayer (mobility $\mu \approx 3000$ cm^2/Vs). **a)** Hall resistivity ρ_{xy} and longitudinal resistivity ρ_{xx} as functions of the externally applied magnetic field B at fixed charge carrier concentration $n \approx 2.5 \times 10^{12}$ cm^{-2}. Pronounced Hall plateaus of the graphene bilayer are experimentally found at filling factors $\nu = 4, 8, 12$. **b)** Hall conductivity σ_{xy} plotted vs. charge carrier density n (i.e. vs. gate voltage V_g, see main text) for $B = 12$ T and $B = 20$ T at $T = 4$ K. Note that σ_{xy} crosses zero *without occurence of a zero-level plateau*, which is a peculiarity of the double-layer graphene. **c)** Longitudinal resistivity ρ_{xx} as function of the charge carrier density n for $B = 12$ T at $T = 4$ K. Adapted from [Nov06].

3.2   Electronic properties of single-walled carbon nanotubes

3.2.1   Bandstructure of SWNTs

The calculation of the dispersion relation and bandstructure of SWNTs is closely related to the dispersion relation obtained for a monolayer of graphene (cp. chapter 3.1.1), the *parent material* of single-walled carbon nanotubes. As mentioned in chapter 2.2 where the structure of nanotubes has been discussed, one can imagine a single-walled carbon nanotube* as a graphene sheet rolled up to form a seamless cylinder. The same approach is pursued when dealing with the electronic properties of SWNTs.

Rolling a monolayer of graphene is tackled theoretically by imposing periodic boundary conditions along the circumferential direction of the single-walled carbon nanotube. That means, that quantization of the unrolled reciprocal space of the SWNT along the direction of the reciprocal vector $\vec{K}_1$ is introduced, which corresponds to the direction of the rolling vector $\vec{c}_\mathrm{h}$ in real space. In contrast, the unrolled reciprocal space of the SWNT is continuous along the reciprocal vector $\vec{K}_2$ corresponding to the axial direction of the SWNT in real space.

In detail, the *concept of cutting lines* [Sam03] is applied to acquire the SWNT dispersion relation and its density of states. The main idea is to construct the 1D electronic energy subbands of a SWNT by *cutting* the 2D electronic dispersion relation of a graphene monolayer with a set of parallel, equidistant lines, the *cutting lines*, which are deduced from the quantization of the circumferential reciprocal vector. This method also is referred to as *zone-folding* [Sam03]. For explanation, the (4,2) SWNT is used as *model nanotube*, as already done in chapter 2.2 (cp. Fig. 2.5)[†].

The reciprocal lattice unit vectors $\vec{K}_i$ ($i = 1, 2$) of the SWNT are obtained as follows (N_hex given in equation (2.10)) [Sam03]

$$\left.\begin{array}{l} \vec{c}_\mathrm{h} \cdot \vec{K}_1 = \vec{t} \cdot \vec{K}_2 = \ 2\pi \\ \vec{c}_\mathrm{h} \cdot \vec{K}_2 = \vec{t} \cdot \vec{K}_1 = \ \ 0 \end{array}\right\} \Rightarrow \begin{cases} \vec{K}_1 = -(t_2\vec{b}_1 - t_1\vec{b}_2)/N_\mathrm{hex} \\ \vec{K}_2 = (m\vec{b}_1 - n\vec{b}_2)/N_\mathrm{hex} \ \ . \end{cases} \tag{3.27}$$

Since the number of quantized states of the reciprocal vector $\vec{K}_1$ equals the number of unit cells of the SWNT parent material graphene per SWNT unit cell [Sam03], there are $N_\mathrm{hex} = 2\left(n^2 + m^2 + nm\right)/T$[§] (cp. equation (2.10)) quantized states along the direction of $\vec{K}_1$ corresponding to the circumferential direction of the SWNT in real space. $\vec{K}_1$ is the shortest possible vector along its direction. Thus, the N_hex quantized states are formed by the vectors $\kappa\vec{K}_1$ with κ being an integer between $(1-N_\mathrm{hex}/2)$ and $N_\mathrm{hex}/2$ (note that N_hex is always even) [Sam03]. In the case of the (4,2) model SWNT (cp. Fig. 2.5), N_hex is 28, the respec-

---

*ignoring the terminations of the tube

[†]The (4,2) SWNT can only be regarded as *model nanotube*, since in reality its diameter is too small for this SWNT to be stable.

[§]with T being the greatest common divisor of $(2m + n)$ and $(2n + m)$
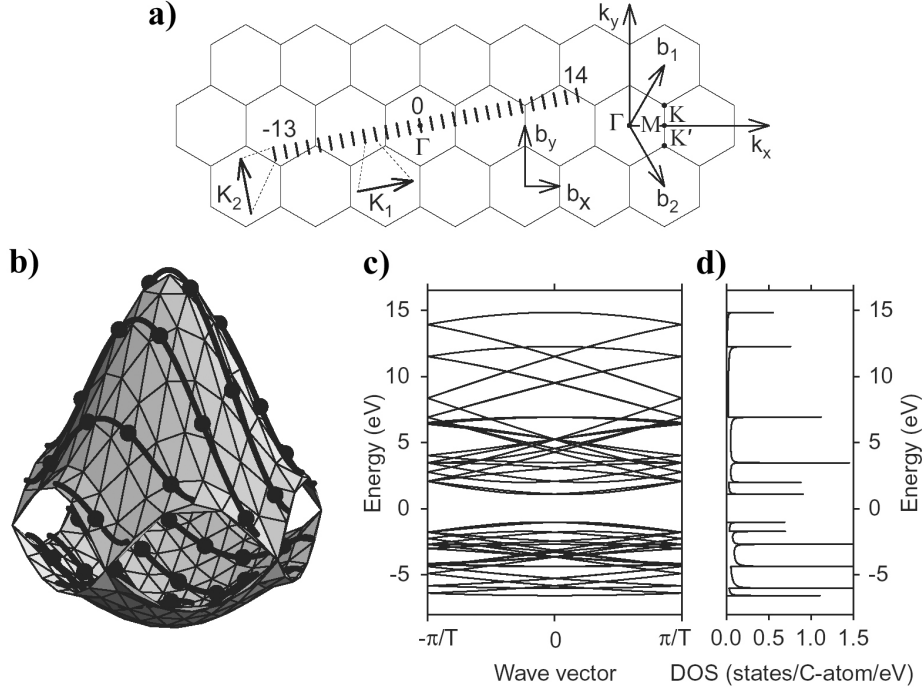
Fig. 3.17: a) Parallel, equidistant *cutting lines* for the (4,2) model SWNT (cp. Fig. 2.5). For the (4,2) SWNT there are $N_{hex} = 28$ *cutting lines* labeled by the cutting line index κ which assumes values between $1 - N_{hex}/2 = -13$ and $N_{hex}/2 = 14$. The *cutting lines* are aligned along the direction of the reciprocal vector $\vec{K}_1$ corresponding to the circumferential direction of a SWNT in real space. Quantization of the unrolled reciprocal space of the SWNT occurs along the direction of $\vec{K}_1$. **b)** The conduction and valence bands of a graphene monolayer in the first Brillouin zone calculated by a nearest-neighbour tight-binding approach, cp. chapter 3.1.1. The solid black lines indicate the *cutting lines* for the considered (4,2) model SWNT in the *fully reduced representation*, i.e. in the representation which maps the *cutting lines* onto the first Brillouin zone. Solid dots along the cutting lines represent the ends of the *cutting lines* in the $\vec{K}_1$-*extended representation* (displayed in **a)**). **c)** Dispersion relation diagram for the (4,2) model SWNT extracted by zone-folding from **a)**. **d)** Density of states of the (4,2) model SWNT obtained for the band digram in **b)**. Adapted from [Sam03, Dre05].

tive 28 *cutting lines* with cutting line index κ ranging from $-13 = 1 - N_{hex}/2$ to $14 = N_{hex}/2$ are displayed in figure 3.17a. The *cutting lines* are arranged in such a way, that the middle one ($\kappa = 0$) runs through the center of the first Brillouin zone of the unrolled reciprocal lattice of the SWNT [Sam03]. The representation of the *cutting lines* depicted in figure 3.17a, in which the *cutting lines* are aligned equidistantly along the $\vec{K}_1$ direction in reciprocal space, is called $\vec{K}_1$-*extended representation*. By shifting the *cutting lines* in reciprocal space by the unit vectors $\vec{b}_1$ and $\vec{b}_2$, this representation can be transformed into the *fully reduced representation*, in which the new, composed *cutting lines* cover the whole first Brillouin zone (for details, see [Sam03]). Figure 3.17b displays the dispersion relation of the delocalized π electron system of a graphene monolayer (cp. chapter 3.1.1) together with superimposed solid black lines corresponding to the graphene dispersion relation values at the *cutting lines* in the *fully reduced representation*. In order to gain the dispersion

relation diagram for the (4,2) model SWNT, the $E(k)$ values along the *cutting lines* from figure 3.17b are transferred into the 1D Brillouin zone of the (4,2) SWNT (Fig. 3.17c) according to the zone-folding scheme [Sam03]. Note, that instead of the $2N_{\text{hex}}$ electrical subbands one would expect to be extracted from the valence and conduction bands of a graphene layer for N_{hex} *cutting lines*, only ($N_{\text{hex}} + 2$) electrical subbands remain due to degeneracy of several subbands. The acquired respective density of states of the (4,2) model SWNT is displayed in figure 3.17d. According to figures 3.17c,d, the (4,2) SWNT exhibits a pronounced bandgap, i.e. it is semiconducting.

Calculating the electronic density of states for a (10,0) SWNT (Fig. 3.18a) and a (9,0) SWNT (Fig. 3.18b) points to the fact that depending on the structural indices (n, m) of a single-walled carbon nanotube, it can be *semiconducting* or *metallic*.
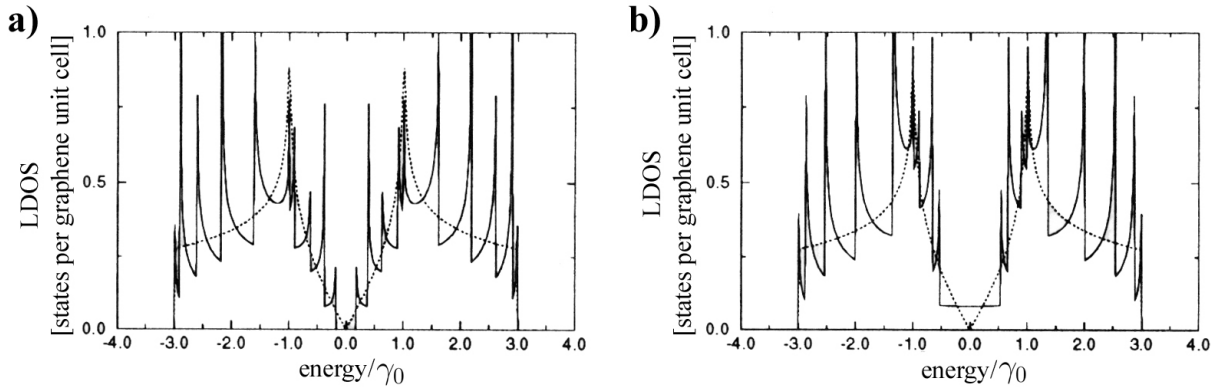
Fig. 3.18: Density of states of **a)** a (10,0) and **b)** a (9,0) single-walled carbon nanotube. Around $E = 0$, the (10,0) SWNT has a pronounced bandgap (i.e. an energy interval with zero density of states), whereas the (9,0) SWNT exhibits a finite density of states also for the energies around $E = 0$. Thus, the (10,0) SWNT is *semiconducting* and the (9,0) SWNT is *metallic*. Note the discrete spikes in the density of states of the SWNTs. They are called *van-Hove singularities* and are characteristic for 1D systems. The dotted lines indicate the density of states of a graphene monolayer (cp. Fig. 3.4a). $\gamma_0 \approx 2.5$ eV is the *nearest-neighbour transfer integral* for 2D graphite [Sai98].

As discussed in chapter 3.1.1, a graphene monolayer is a *zero-gap semiconductor*, i.e. conductance and valence band meet at the K and K' points. The fact determining whether a SWNT is *semiconducting* or *metallic* is the manner how the *cutting lines* are running with respect to the K/K' points of the reciprocal lattice. If one of the *cutting lines* runs through a K or K' point, the respective single-walled carbon nanotube is *metallic*, since the conductance and the valence band meet in the K/K' points. Otherwise, the respective SWNT exhibits *semiconducting* behaviour.

The vector $\overrightarrow{\Gamma K}$ in figure 3.19a can be easily calculated using the unit vectors $\vec{b}_1$ and $\vec{b}_2$ of the reciprocal graphene lattice (cp. Fig. 3.1b) given in equation (2.2):

$$\overrightarrow{\Gamma K} = \left(\frac{2\pi}{\sqrt{3}a}, \frac{2\pi}{3a} \right) \quad . \tag{3.28}$$

Projecting the vector $\overrightarrow{\Gamma K}$ onto the direction of the reciprocal vector $\vec{K}_1$ yields the vector $\overrightarrow{YK}$ in figure 3.19a:

$$|\overrightarrow{YK}| = \frac{\overrightarrow{\Gamma K} \cdot \vec{K}_1}{|\vec{K}_1|} \; . \tag{3.29}$$

If the length of vector $\overrightarrow{YK}$ devided by the length of $\vec{K}_1$ is an integer, i.e. if

$$\frac{|\overrightarrow{YK}|}{|\vec{K}_1|} = \frac{\overrightarrow{\Gamma K} \cdot \vec{K}_1}{\vec{K}_1 \cdot \vec{K}_1} = \frac{2n + m}{3} \, \epsilon \, \mathbb{N} \; , \tag{3.30}$$

the considered single-walled carbon nanotube is *metallic*, since one of the cutting lines runs through the K/K' point in reciprocal space, corresponding to the scenario in figure 3.19b. In the other cases, i.e. if $(2n + m) \bmod 3 \, \epsilon \, \{1, 2\}$, the SWNT is *semiconducting* (Figs. 3.19c,d).
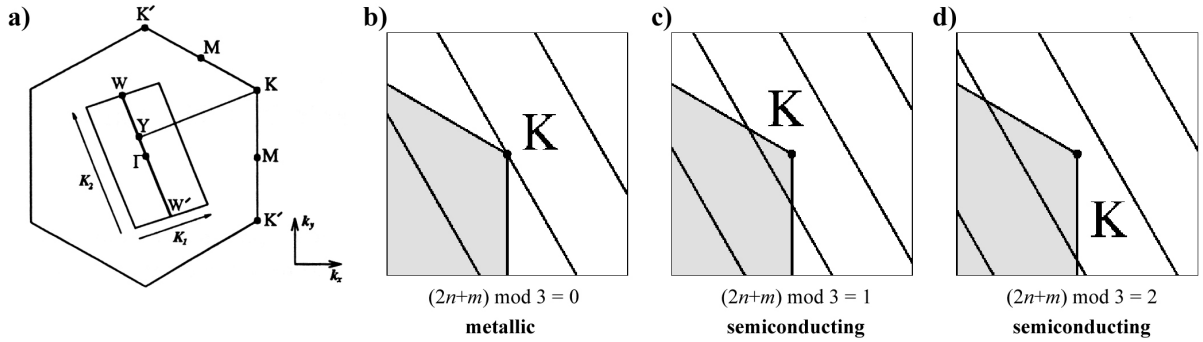
Fig. 3.19: a) Reciprocal lattice of an unrolled SWNT displaying the condition for the SWNT to be *metallic* or *semiconducting*: if the length of the vector $\overrightarrow{YK}$ is an integer multiple of the length of $\vec{K}_1$, the respective SWNT is *metallic*, otherwise *semiconducting*. The ratio of both lengths is $(2n + m)/3$ [Sai98]. **b)-d)** If a *cutting line* is running through a K/K' point in reciprocal space, i.e. $(2n+m) \bmod 3 = 0$, the respective SWNT is *metallic*, otherwise, i.e. $(2n+m) \bmod 3 \, \epsilon \, \{1, 2\}$, it is *semiconducting*. Adapted from [Sam03].

Thus, $2/3$ of all *theoretically possible* (n, m) SWNTs are semiconducting and $1/3$ metallic[†]. Figure 3.20 presents an overview on the distribution of semiconducting and metallic single-walled carbon nanotubes in dependence of their structural indices (n, m). It is obvious that all SWNTs along the high-symmetry *armchair* direction are metallic.

The bandgap E_g of a semiconducting SWNT is inversely proportional to its diameter d_N

$$E_g = \frac{\gamma_0 \cdot a_{C-C}}{d_N} \; , \tag{3.31}$$

independent of the rolling angle θ of the semiconducting SWNT, where $\gamma_0 \approx 2.5$ eV is the *nearest-neighbour transfer integral* for 2D graphite and $a_{C-C} \approx 1.42$ Å the next-neighbour distance in the graphene lattice [Sai98].

[†]In practice, however, this does *not* imply that $2/3$ of any given SWNT sample are semiconducting. The reason for this is that the growth methods as arc-discharge, laser ablation or CVD favour certain (n, m) combinations depending on the chosen growth parameters.
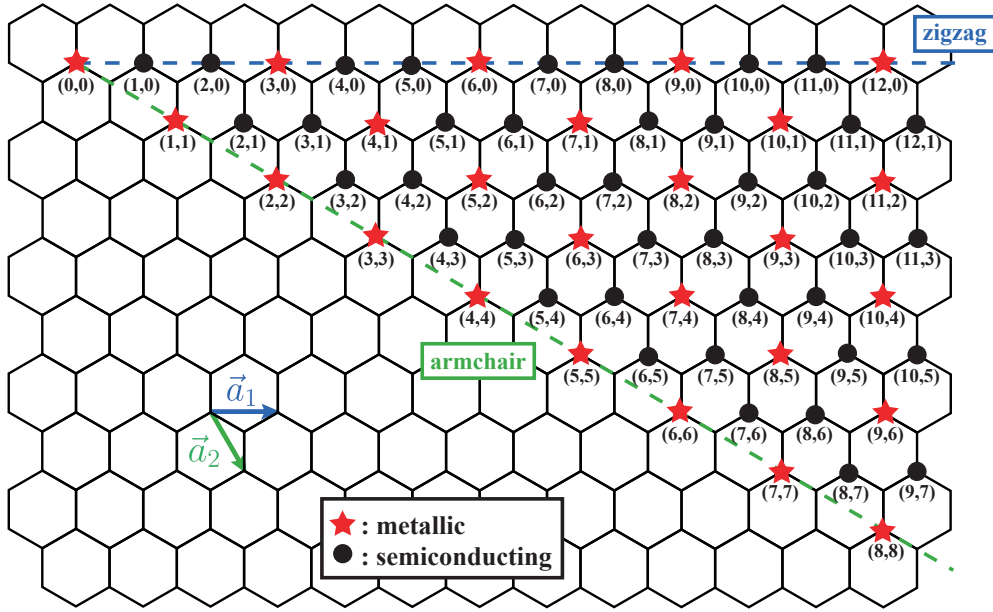
Fig. 3.20: The distribution of *semiconducting* and *metallic* single-walled carbon nanotubes (according to the *concept of cutting lines*). Whether a SWNT is semiconducting or metallic depends on its structural indices (n, m). Of all theoretically conceivable (n, m) combinations $2/3$ are semiconducting and $1/3$ metallic. Adapted from [Sai98].

Finally it has to be pointed out that the concept of *cutting lines* does not account for curvature induced effects on the bandstructure of single-walled carbon nanotubes. These curvature effects are most pronounced for small-diameter SWNTs, the π- and the σ- orbitals of which can overlap, form hybrid orbitals and induce mini-gaps at the Fermi level of metallic SWNTs. The only *truely metallic* SWNTs are the *armchair SWNTs*, because in their case the curvature induced gaps vanish by symmetry [Kan97]. In literature, the single-walled carbon nanotubes with mini-gaps are usually referred to as *narrow-bandgap SWNTs*. The curvature induced mini-gaps scale with d_N^{-2} [Kan97] and are typically of the order of $k_\mathrm{B}T$ at room temperature [Sam03]. Thus, they are significantly smaller than the bandgaps of the inherently semiconducting SWNTs described above when deriving the bandstructure of single-walled carbon nanotubes.

3.2.2 Electrical transport in SWNTs in field-effect transistor configuration

SWNT in field-effect transistor configuration

A single-walled carbon nanotube in *field-effect transistor* configuration is depicted in figure 3.21. The SWNT is deposited on top of a Si/SiO$_2$ substrate where the bulk silicon is highly doped to be electrically conducting even at low temperatures in the mK regime. Furthermore, the nanotube is provided with 2 metal contacts on its top named *source* and *drain* electrodes. Applying a source-drain voltage V_{sd} along the SWNT between the *source* and *drain* contacts leads to a current I_{sd} flowing through the single-walled carbon nanotube. The bulk Si serves as a further electrical contact called *gate* electrode. A gate voltage V_g applied at the gate electrode leads to modulation of the channel current I_{sd} by several orders of magnitude in the case of a semiconducting SWNT (a semiconducting SWNT usually exhibits p-type behaviour), the current through a metallic SWNT is independent of the gate voltage. The arrangement shown in figure 3.21 is called *field-effect transistor* (FET) configuration due to the analogy to the microelectronics counterpart, the Si MOSFET (metal-oxide-semiconductor field-effect transistor) [Sze07].
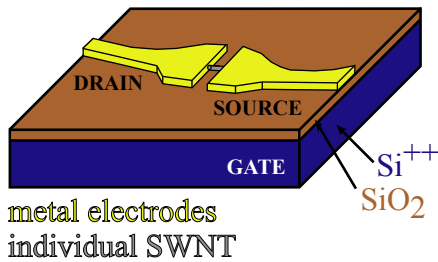
Fig. 3.21: A SWNT *field-effect transistor*: the SWNT, provided with metal *source* and *drain* contacts, is lying on top of a Si/SiO$_2$ substrate. The Si underneath the insulating SiO$_2$ layer is highly doped and serves as a *gate* electrode. The current I_{sd} through the nanotube is measured as a function of the source-drain voltage V_{sd} along the tube and the gate voltage V_g applied to the bulk Si.

The expression *field-effect* refers to the fact that the conductance of a semiconducting channel can be modulated by several orders of magnitude by an electric field imposed by the gate voltage V_g at the gate electrode. The electric field shifts the bands of the conducting channel with respect to the source and drain contacts, which is followed[*] by a flow of charge carriers between the transistor channel and the source/drain contacts, changing the Fermi level and the charge carrier density in the transistor channel. As a consequence, the electrical gate field leads to a relative shift of the Fermi level in the transistor channel with respect to its bandstructure and to a variation of the charge carrier density in the channel[*], respectively.

The preparation of such a nanotube FET device is described in chapter 4.4 in detail, regarding its electric characterisation by measuring $I(V_{sd})$ (*source-drain characteristics* or *output characteristics*) and $I(V_g)$ (*gate voltage characteristics* or *transfer characteristics*) curves refer to chapter 4.6.2[†].

---

[*]if there are available states in the transistor channel, i.e. if its Fermi level is not in a bandgap

[†]For the case of graphene, refer to chapters 4.5, 4.6.2 and 4.6.4. Usually the field-effect in graphene is measured in a 4-probe configuration with two additional leads for the longitudinal voltage drop V_{xx} (cp. chapter 4.6.4).

Ballistic transport in SWNTs

In the ideal case, i.e. if a SWNT does not have defects, a single-walled carbon nanotube behaves as a *ballistic conductor*. The term *ballistic conduction* refers to the situation in which charge carriers travel along the electrical conductor without being scattered (i.e. the mean free path l_s is larger than the channel length L of the ballistic conductor). In the case of *ballistic transport* the conductance G is quantized, i.e. $G = \eta G_0$, where η is the number of conducting channels and $G_0 = 2e^2/h$ is the conductance quantum. For a metallic SWNT, the number of conductance channels η equals 2, thus the conductance of a metallic single-walled carbon nanotube in the ballistic limit is $G_{\mathrm{mSWNT}} = 4e^2/h$ corresponding to the resistance $R_{\mathrm{mSWNT}} = G_{\mathrm{mSWNT}}^{-1} = h/4e^2 \approx 6.5$ kΩ [Sai98]. The same theoretical values hold for semiconducting SWNTs if the Fermi level is within the valence or conduction band [Rot08]. In practice, however, the 2-lead resistances acquired for metallic and semiconducting single-walled carbon nanotubes are (significantly) higher, since in real samples there usually are defects along the SWNTs and there can be unwanted material between the SWNT surface and the electrical contacts forming *tunneling barriers*. In addition, *Schottky barriers* occur at the interface between semiconducting SWNTs and metallic leads which is dealt with briefly in the next section.

Metal-SWNT Schottky barriers

When contacting a semiconducting single-walled carbon nanotube with metallic leads, *Schottky barriers* can be formed [App02, Fre01, Hei02, Nak02] which can be considered as rectifying tunneling barriers. Whether a *Schottky barrier* or an ohmic contact is formed, depends on the work functions Φ_m and $\Phi_{\mathrm{sc-SWNT}}$ of the metal and the semiconducting SWNT. If the SWNT is a p-type semiconductor and $\Phi_m < \Phi_{\mathrm{sc-SWNT}}$ or the SWNT is a n-type semiconductor and $\Phi_m > \Phi_{\mathrm{sc-SWNT}}$, a *Schottky barrier* is formed, otherwise the contact is ohmic. One fact complicating the answer to the question whether a contact between a metal lead and a semiconducting SWNT is a *Schottky barrier* or not is that the work function $\Phi_{\mathrm{sc-SWNT}}$ of a semiconducting SWNT depends on its diameter and the structural indices (n, m), respectively, as shown in figure 3.22 [Zha02]. A comprehensive general review on *Schottky barriers* can be found in [Sze07].
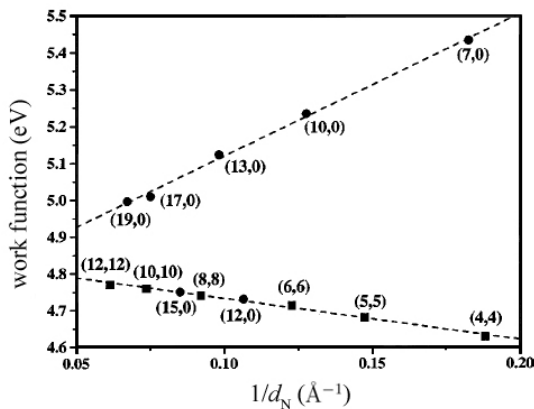

Fig. 3.22: Calculated work function values of individual SWNTs plotted vs. the inverse SWNT diameter d_N^{-1}. The upper line represents semiconducting, the lower one metallic SWNTs. Squares stand for armchair-, circles for zigzag-SWNTs. The limits for $d_N \to \infty$ are 4.73 eV for semiconducting and 4.84 eV for metallic SWNTs [Zha02].

3.2.3   Coulomb blockade oscillations

In the following, *Coulomb blockade oscillations* and the general principles of a *single electron transistor (SET)* shall be discussed based on an electrostatic description [Wei02, Wei05].

Given is an arrangement of a source, a drain and a gate electrode, where an isolated island is surrounded by source, drain and gate as depicted in figure 3.23a. The voltages V_s, V_d and V_g are applied at the source, drain and gate electrode with V_s being the common reference potential. The source-drain voltage V_{sd} is defined as $V_d - V_s$ (cp. Fig. 3.23a). The island is weakly coupled to both the source and the drain electrode by tunneling barriers. Furthermore there is a capacitive coupling of the island with regard to the gate electrode. The capacitances between the island and the source, drain and gate electrode shall be C_s, C_d and C_g. In the corresponding capacitance circuit in figure 3.23b, tunneling barriers between the island and the source and drain electrode are represented by double rectangles.
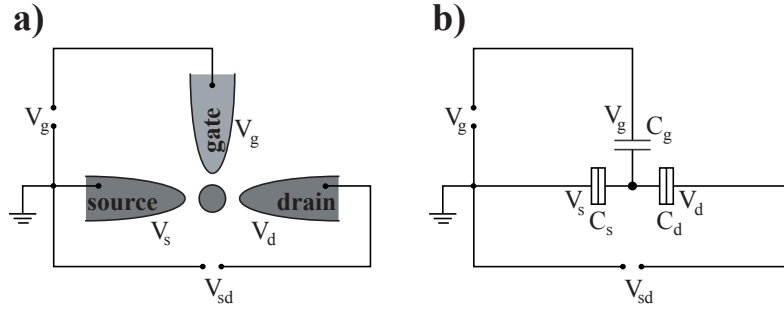
Fig. 3.23: a) Geometrical arrangement of a single-electron transistor: a metallic island is surrounded by a source, a drain and a gate electrode. Tunnel barriers form a weak coupling between the island and the source and drain electrodes whereas the gate electrode is capacitively coupled to the island. The potentials at the electrodes are noted in the figure, common reference potential is V_s. **b)** Equivalent circuit for the arrangement in a). Double rectangles represent capacitances in parallel to the tunnel resistances.

The total capacitance C_Σ of the system in figure 3.23 is

$$C_\Sigma = C_s + C_d + C_g = \sum_{j \in \{s,d,g\}} C_j \ . \tag{3.32}$$

Q_{isl} shall be the electrical charge of the island. Charging the electrically neutral island (i.e. $Q_{isl} = 0$) with N further electrons ($\Rightarrow Q_{isl} = -Ne$) taken from the source electrode with the fixed reference potential $V_s = 0$ results in the electrostatical energy change $E_{el.st.}(N, \{V_j\})$ given by

$$E_{el.st.}(N, \{V_j\}) = -Ne \sum_{j \in \{s,d,g\}} \frac{C_j}{C_\Sigma} V_j + \frac{(Ne)^2}{2C_\Sigma} \ , \tag{3.33}$$

where the first term describes the potential energy of N electrons in the electrostatic potential on the island at $Q_{isl} = 0$. The second term takes the energy into account

which is needed to separate the charge $-Ne$ from the counter charge on the electrodes. Applying equation (3.33) yields the so-called *charging energy* $\Delta E_{\text{el.st.}}(N, \{V_j\})$ required to add a further electron onto the island being charged with $(N-1)$ electrons, so that the charge on the island is $Q_{\text{isl}} = -Ne$:

$$
\begin{aligned}
\Delta E_{\text{el.st.}}(N, \{V_j\}) &= E_{\text{el.st.}}(N, \{V_j\}) - E_{\text{el.st.}}(N-1, \{V_j\}) \\
&= -e \sum_{j \in \{s,d,g\}} \frac{C_j}{C_\Sigma} V_j + \left(N - \tfrac{1}{2}\right) \frac{e^2}{C_\Sigma} \, .
\end{aligned}
\tag{3.34}
$$

Firstly, only the second term of equation (3.34) shall be discussed. According to this second term, the energy $e^2/(2C_\Sigma)$ is needed to charge the island with the first electron, whereas further charging requires the energy e^2/C_Σ per electron. That means that each two adjacent energy levels of the island have a spacing of $2E_{\text{C}}$ with

$$
E_{\text{C}} = \frac{e^2}{2C_\Sigma}
\tag{3.35}
$$

being the *single-electron charging energy*. Considering now the first term in equation (3.34), it is recognized that the *charging energy* $\Delta E_{\text{el.st.}}(N, \{V_j\})$ can be linearly varied by changing the voltage applied at the drain and/or the gate electrode. This circumstance allows the introduced arrangement in figure 3.23 to be used as *single-electron transistor*, i.e. this system can be tuned in such a way that *single* electrons *sequentially* tunnel from the source to the drain electrode.

However, the following three conditions must be fulfilled for the electrode arrangement diplayed in figure 3.23 to work as *single-electron transistor*. Firstly, the voltage V_{d} at the drain electrode has to be set to a very low value so that the condition

$$
|V_{\text{d}} - V_{\text{s}}| = |V_{\text{sd}}| \ll e/C_\Sigma
\tag{3.36}
$$

is fulfilled, where $V_{\text{s}} = 0$ is set. Secondly, the thermal excitation of the electrons must be small compared to the *single-electron charging energy* E_{C}, i.e.

$$
k_{\text{B}}T \ll \frac{e^2}{2C_\Sigma} \, .
\tag{3.37}
$$

Thirdly, the total tunneling resistance R_{T} between the source and drain electrode has to be at least as large as the *von Klitzing constant* $R_{\text{K}-90} = 25812.807 \ \Omega$ for the system to show *single-electron transistor* behaviour:

$$
\left.
\begin{aligned}
\Delta E \, \Delta t &\geq h \\
\Delta t &\approx R_{\text{T}} \, C_\Sigma \\
\Delta E &= 2E_{\text{C}}
\end{aligned}
\right\}
\Rightarrow R_{\text{T}} \geq \frac{h}{e^2} \approx 25.8 \ \text{k}\Omega
\tag{3.38}
$$

The requirement in equation (3.38) is deduced from the *Heisenberg uncertainty relation* regarding the island as discharging capacitor with the time-constant Δt and assuming the

energy uncertainty $\Delta E = 2E_C$.

Figure 3.24 presents the energy scheme corresponding to equation (3.34). The Fermi level of the drain contact is slightly shiftet against the Fermi level of the source contact by $-eV_d = -eV_{sd}$. The island depicted in figure 3.24 is charged with N electrons, the $(N+1)^{st}$ level is not reachable for the electrons of the source electrode due to the low thermal excitation requirement stated above. Thus, no current is flowing across the island in this situation, the transistor is in the state of the so-called *Coulomb blockade*. If now the gate voltage V_g is slowly increased, the *charging energy* of the $(N+1)^{st}$ level will decrease according to equation (3.34). As soon as this $(N+1)^{st}$ energy level reaches the Fermi level of the source electrode, the transistor is in the conducting state, i.e. one electron after the other can tunnel from the source contact to the island and further to the drain contact. If the gate voltage is increased further, the $(N+1)^{st}$ level will be lying lower than the Fermi level of the drain electrode, i.e. the transistor will not conduct any more. Until the next energy level will be reached, there are $N+1$ electrons residing on the island.
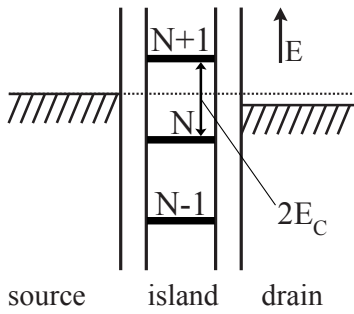

Fig. 3.24: Energy scheme of a single-electron transistor: the vertical double lines represent tunnel barriers. The Fermi level of the drain electrode is slighty shifted with respect to the source electrode Fermi level. Through variation of the gate voltage V_g the energy levels of the island can be shifted. The level spacing is equidistant and equals to $2E_C$.

When sweeping the gate voltage V_g at low bias voltage V_{sd}, peaks of both the current I_{sd} and the differential conductance dI_{sd}/dV_{sd}[†] appear, whereas electrical conductance is suppressed between the spikes. These oscillations are called *Coulomb blockade oscillations*, they are schematically depicted in figure 3.25a. With increasing gate voltage V_g conducting states are passed gradually, where the number of electrons on the island is increased by one per passed conducting state (Fig. 3.25b). According to the introduced theory, the peaks of the current I_{sd} or the differential conductance dI_{sd}/dV_{sd} are equidistant with a peak-to-peak distance of e/C_g. A sequence of energy schemes of the considered system for increasing gate voltages V_g whilst passing through the Coulomb blockade oscillations at a fixed low bias voltage V_{sd} is given in figures 3.25c-g.

[†]The method how to measure the differential conductance dI_{sd}/dV_{sd} along with the current I_{sd} is described in chapter 4.6.3.
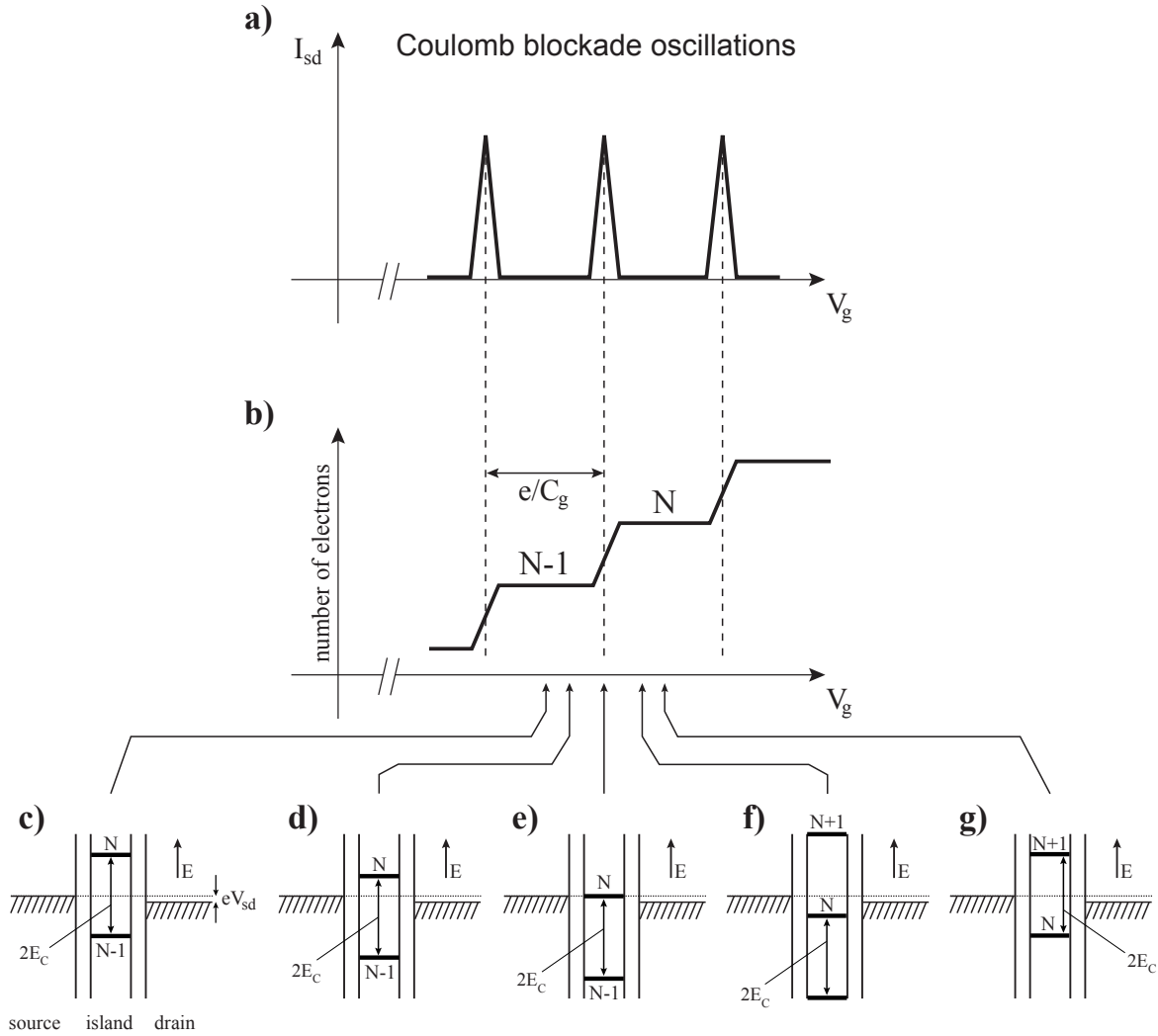
Fig. 3.25: a) Schematics of a $I_{sd}(V_g)$ diagram of a single-electron transistor. Characteristic current peaks occur at certain gate potentials V_g whereas current is suppressed in between two of such peaks. The peak spacing equals to $\Delta V_g = e/C_g$. **b)** After each peak in $I(V_g)$ the number of electrons residing on the island is increased by 1. **c)-g)** Energy schematics of a single-electron transistor for increasing gate voltage values. For increasing V_g the energy levels of the island are being decreased gradually. As soon as one of the island energy levels is identical with the source electrode level (cp. **e)**), the transistor becomes conducting, i.e. the current $I_{sd}(V_g)$ peaks.
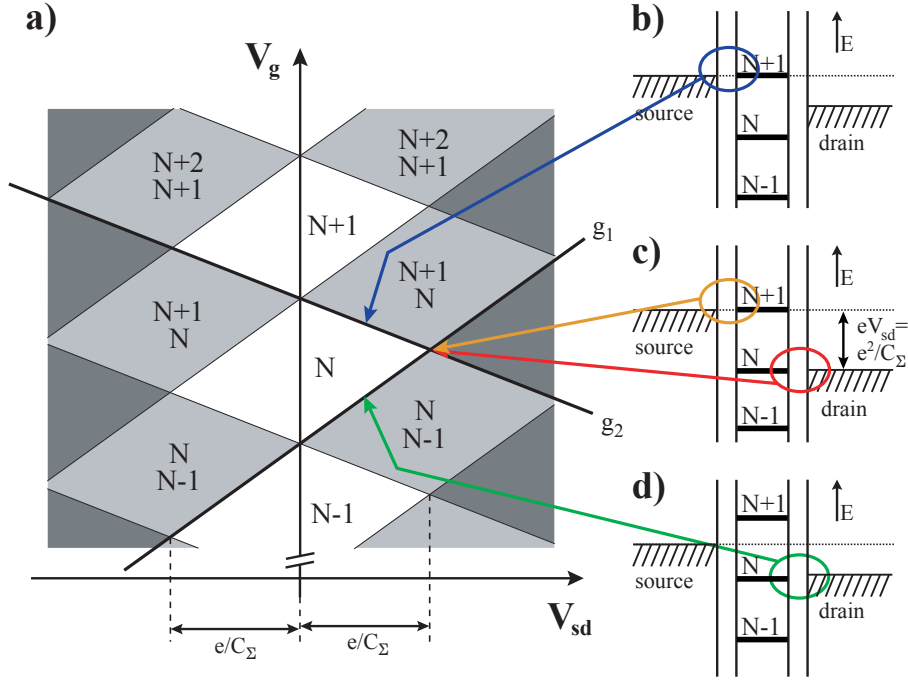
Fig. 3.26: a) The three-dimensional diamond plot of a single-electron transistor plots the differential conductance $dI_{sd}/dV_{sd}(V_g, V_{sd})$. It exhibits diamond shaped areas corresponding to different conduction states. In the white regions the SET is strictly isolating, i.e. here the quantum dot is in Coulomb blockade. Light grey areas stand for single-electron tunneling, dark grey regions for multiple electron conduction. **b)-d)** Energy schemes for dot configurations along the border lines of adjacent diamonds in **a)**.

So far, the voltage $V_{sd} = V_d$ between the source and drain electrode was kept constant at a low value. Measuring the differential conductance dI_{sd}/dV_{sd} as a function of both the gate voltage V_g and the source-drain voltage V_{sd} leads to the so-called *diamond plot* which is schematically illustrated in figure 3.26a. This plot contains various diamonds in the (V_{sd}, V_g) plain in which the transistor is in different states. The total number of electrons on the island in each of these states is printed within the diamonds in figure 3.26a. The white diamonds along the V_g axis correspond to electrically insulating states of the transistor, the number of electrons on the island in these *Coulomb blockade* states is constant as discussed before. The adjacent diamonds coloured light-grey represent (V_{sd}, V_g) values for which *single-electron tunneling* takes place, i.e. the number of electrons on the island varies by one due to electrons which sequentially tunnel onto and off the island. Areas coloured in dark-grey correspond to (V_{sd}, V_g) voltage regimes in which several electrons can tunnel across the island *simultaneously*, since here the source-drain voltage V_{sd} is sufficiently high allowing 2 or more conducting channels to participate in charge transport. Note the energy schemes in figures 3.26b-d which display situations at the boundaries between such diamonds. According to [Wei02, Wei05], the slopes of the lines g_1 and g_2 along the diamond boundaries are

$$\left.\frac{dV_g}{dV_{sd}}\right|_{(V_{sd}, V_g) \in g_1} = \frac{C_\Sigma - C_d}{C_g}, \qquad \left.\frac{dV_g}{dV_{sd}}\right|_{(V_{sd}, V_g) \in g_2} = -\frac{C_d}{C_g}. \qquad (3.39)$$
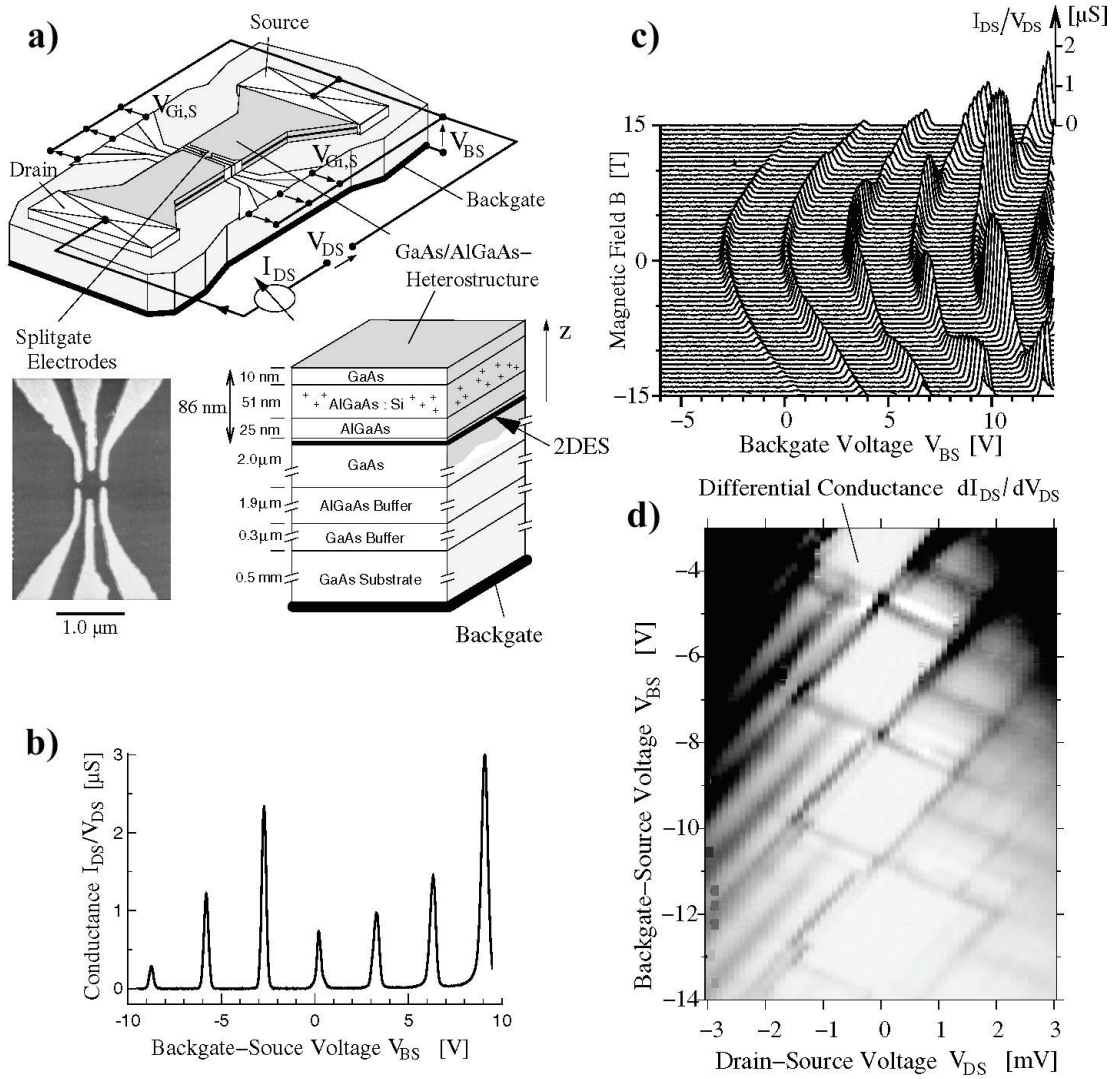
Fig. 3.27: a) A *single-electron transistor (SET)* realized on the basis of a GaAs/AlGaAs hete-rostructure. **b)** Coulomb blockade oscillations as a function of the backgate voltage measured using such a SET device. **c)** Coulomb blockade oscillations for different magnetic fields applied *parallel* to the plane of the 2DEG. **d)** Respective greyscale plot of the differential conductance in dependence of the source-drain and the backgate voltage, cp. figure 3.26a) [Wei05].

The described *single-electron transistor (SET)* can be realized in various ways two of which shall be discussed briefly in the following. The typical way to obtain a SET is to fabricate a *split-gate quantum dot system* based on a GaAs/AlGaAs heterostructure (Fig. 3.27a) [Wei05]. The SET is defined by the following steps: a mesa is etched out of the heterostructure, electrical contacts to the 2DEG buried several 10 nm underneath the mesa surface are formed by alloying metals at certain mesa regions and metal topgates are evaporated. The *quantum dot* (i.e. the *island* in the description above) within the 2DEG is formed by applying negative voltages to the topgates which leads to lateral confinement. In addition, the coupling of the island to the source and drain contacts can be tuned with the topgates. The actual gate voltage V_g is applied at the metallic backgate shifting the electrostatic potential of the system as discussed before (Fig. 3.27a). Measur-

ing the Coulomb blockade, i.e. electrical conductance vs. gate voltage for low bias voltage, of such a device yields a plot as in figure 3.27b with the characteristic conductance spikes. The respective *diamond plot* (cp. scheme in Fig. 3.26a), i.e. the differential conductance as a function of both the gate and the source-drain voltage, is given in figure 3.27d. Investigating the Coulomb blockade oscillations of such a single-electron transistor based on a GaAs/AlGaAs heterostructure (Fig. 3.27a) in dependence of an externally applied magnetic field which is oriented in parallel with respect to the 2DEG leads to shifts of the conductance peaks along the gate voltage axis and furthermore to undulations of the peak heights with the magnetic field as depicted in figure 3.27c. This indicates that the electronic states of the quantum dot (or the *island*) and the coupling of these states to the source and drain electrodes are altered by the in-plane magnetic field.

A further approach to realize a *single-electron transistor* is based on utilizing a single-walled carbon nanotube in *field-effect transistor configuration* as displayed in figure 3.21 and described in chapter 3.2.2. In this case, the confinement of the charge carriers in the x- and y-direction is naturally given by the geometry of the SWNT which typically has a diameter of 1.5 nm. The confinement in the third direction is mediated by the source and drain contacts, which usually do not constitute ideal contacts to the nanotube, but form tunneling barriers, e.g. due to some other material as amorphous carbon between the contacts and the SWNTs. Thus, the *island*, to and from which the charge carriers tunnel, is just given by the SWNT segment between the source and drain contacts without the need for any topgates. The lack of topgates implies that the coupling between the island and the source and drain electrodes can not be changed. Similarly to the prior case of a SET based on a GaAs/AlGaAs heterostructure, a backgate voltage V_g is applied at the highly doped bulk Si in figure 3.21 to tune the electrostatic potential of the *island*.

Coulomb blockade oscillations in individual SWNTs have been reported in literature many times. One example of a high-quality diamond plot of a semiconducting SWNT [Jar04] acquired at 4.2 K is depicted in figure 3.28. In addition to the diamonds, excited electronic states can be recognized manifesting themselves as parallel lines to the diamond boundaries. In contrast to the usual Coulomb blockade phenomena which have been measured and published often, to our best knowledge there are no publications on the development of Coulomb blockade oscillations of a SWNT single-electron transistor with an externally applied magnetic field as displayed in figure 3.27c for a GaAs/AlGaAs quantum dot.
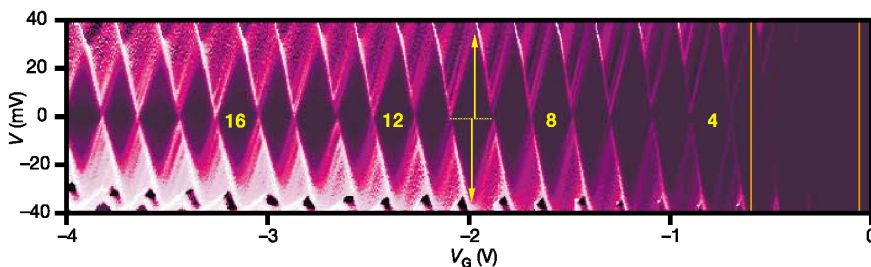
Fig. 3.28: Diamond plot of a single-electron transistor based on a semiconducting SWNT acquired at 4.2 K [Jar04].

3.2.4 SWNTs in axial and perpendicular magnetic fields

The investigation of an electrical device in an externally applied magnetic field $\vec{B}$ by electrical transport measurements is called *magnetotransport*, one of the key terms is the *magnetoresistance MR(B)* defined as

$$MR(B) = \frac{R(B) - R(0)}{R(0)} = \frac{\Delta R}{R} \, ,\qquad(3.40)$$

i.e. the relative change of resistance due to the applied magnetic field with the value B.

In the following, the influences of an external magnetic field on the charge transport in an individual SWNT contacted in field-effect transistor configuration (cp. chapter 3.2.2) shall be discussed. Due to the exceptionally high aspect ratio of a single-walled carbon nanotube, the two cases of axially and perpendicularly aligned magnetic fields with respect to the SWNT axis are considered separately.

Magnetic field oriented parallel to the SWNT axis

Applying an external magnetic field along the axis of a single-walled carbon nanotube introduces an *Aharonov-Bohm phase shift* which can change the electronic properties of the SWNT and convert it from metallic to semiconducting and vice versa [Aji93, Aji96, We05]. The bandgap being inversely proportional to the SWNT diameter (equation (3.31)) is changed significantly as a function of the magnetic flux Φ through the SWNT with a period of $\Phi_0 = h/e$ (Φ_0 is the *magnetic flux quantum*) as displayed in figure 3.29a for a metallic SWNT (there are substructures around half flux quanta for semiconducting SWNTs, see Fig. 3.29b). The maximum field-induced gap E_{M} in the metallic case is
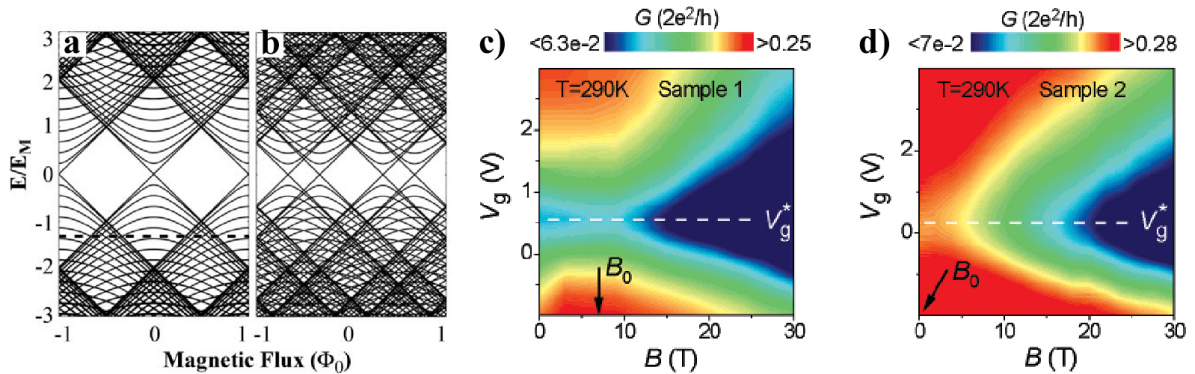
Fig. 3.29: a),b) Calculated energy levels of **a)** a (200,200) armchair and **b)** a (346,0) zigzag SWNT (diameter in both cases $\approx$ 28 nm) plotted vs. the magnetic flux axially threaded through the SWNT. The energy scale is in units of E_{M} (see text), the flux is in units of the flux quantum Φ_0 [We05]. **c),d)** Experimentally measured linear conductance $G = I_{\mathrm{sd}}/V_{\mathrm{sd}}$ of **c)** a narrow-bandgap SWNT (cp. chapter 3.2.1) and **d)** a metallic SWNT at $T = 290$ K as function of the gate voltage V_{g} and the axially oriented magnetic field B. The $G(V_{\mathrm{g}})$ characteristics were recorded for a small bias voltage $V_{\mathrm{sd}} \approx 1$ mV. The white dashed lines indicate the V_{g}^* values which correspond to minimum conductance [Fed07].

$E_{\mathrm{M}} = \sqrt{3}a\,\gamma_0/2d_{\mathrm{N}}$ [We05] with the SWNT diameter d_{N}, the *nearest-neighbour transfer integral* for 2D graphite $\gamma_0 \approx 2.5$ eV and the graphene lattice constant $a = 2.46$ Å. The magnetic flux Φ through the SWNT at a parallel magnetic field $B_{\parallel}$ is $\Phi = \pi B_{\parallel} d_{\mathrm{N}}^2/4$. Hence, the maximum field-induced gap of a metallic SWNT with a (typical) diameter of 1.5 nm equals approx. 355 meV. However, the respective *static* magnetic field to reach this value would be approx. 1170 T, which is far above experimentally accessible magnetic fields. Nevertheless, signatures of the bandgap opening/modification of individual SWNTs due to the Aharonov-Bohm effect can already be seen at around 20 to 30 T as reported for narrow-bandgap semiconducting and metallic SWNTs (Figs. 3.29c,d) in [Fed07].

Magnetic field oriented perpendicularly to the SWNT axis

Considering a magnetic field perpendicular to the SWNT axis, one realizes, that the net magnetic flux through the single-walled carbon nanotube equals zero in this configuration. Detailed theoretical analyses reveal that significant and experimentally accessible changes of electrical resistance in an individual SWNT upon application of a perpendicular magnetic field are not expected [Aji93, Aji96, Sai94, Sai96]. We are not aware of any experimental results published on significant magnetoresistance of an individual single-walled carbon nanotube in perpendicularly oriented magnetic fields.

Effects of SWNT chirality on magnetotransport

The theoretical work of H. Ajiki and T. Ando [Aji93, Aji96], which only covers the behaviour of achiral SWNTs (cp. chapter 2.2) in external magnetic fields, was extended by E. L. Ivchenko and B. Spivak [Ivc02] to account for chirality effects as well.

According to [Ivc02], chirality effects appear due to terms in the electron Hamiltonian describing the coupling between the orbital momentum of the electrons around the circumference of a chiral SWNT and the linear electron momentum along the SWNT. The result is an additional current occuring for a chiral single-walled carbon nanotube in an axially aligned magnetic field. The current density along the axis of the SWNT in this case reads as

$$j_{\parallel} = \sigma E_{\parallel} + \Lambda E_{\parallel}^2 B_{\parallel} \; , \tag{3.41}$$

where σ is the linear *Drude conductivity*, $E_{\parallel}$ and $B_{\parallel}$ are the electric and magnetic field parallel to the SWNT axis and Λ is the *magnetochiral coefficient* only being nonzero for chiral SWNTs. This means that according to this theory, a chiral SWNT in an axially applied magnetic field should exhibit a negative magnetoresistance being linear in B, whereas the same SWNT should not respond to a magnetic field applied perpendicularly to the tube axis. Moreover any achiral SWNT (i.e. an *armchair* or a *zigzag* SWNT) should *not* exhibit magnetoresistance[†] independently of the magnetic field direction.


[†]except for the bandgap modulation due to *Aharonov-Bohm effect* [Aji93, Aji96, We05, Fed07]

3.3   Electronic properties of metallofullerene peapods

Up to the present, no comprehensive theory has been published for transport and magnetotransport in metallofullerene peapod systems. Developing a theory for and/or modelling of such a complex hybrid system as a metallofullerene peapod with its many degrees of freedom (structural indices (n, m) of the host SWNT, diameter-dependent interaction between the metallofullerenes and the host SWNT, different degrees of metallofullerene filling possible with maybe different metallofullerene-metallofullerene spacings, eventually even bundling...) seems to be a very challenging task.

On the experimental side, by means of scanning tunneling microscopy and spectroscopy (STM/STS), results regarding bandgap-modulation of a SWNT due to filling with $Gd@C_{82}$ metallofullerenes have been acquired [Lee02]. As indicated schematically in figure 3.30a, the bandgap of a semiconducting SWNT is narrowed by approximately a factor of 5 at the sites at which the metallofullerenes are inserted [Lee02]. As for electrical transport, two works have been published so far, the first of which claims that $(Gd@C_{82})@SWNT$ metallofullerene bundles behave in an ambipolar way for $23\ \text{K} \leq T \leq 298\ \text{K}$ (Fig. 3.30b), i.e. they always exhibit p- and n-conduction, due to the bandgap narrowing effect mentioned before [Shi02]. In a second publication [Chi01], a temperature dependent change of the transfer characteristics of an individual $(Dy@C_{82})@SWNT$ metallofullerene peapod from p- to n-conduction and further to metallic behaviour is postulated, which is ascribed to ongoing charge transfer from the metallofullerenes to the host nanotube with decreasing temperature due to more intensive overlap of the π-orbitals of the fullerenes and the host SWNT (Figs. 3.30c-e). Up to now, no results regarding magnetotransport in individual metallofullerene peapods have been reported, which might be of interest since several mono-metallofullerenes exhibit imperfect paramagnetism [Hua00].
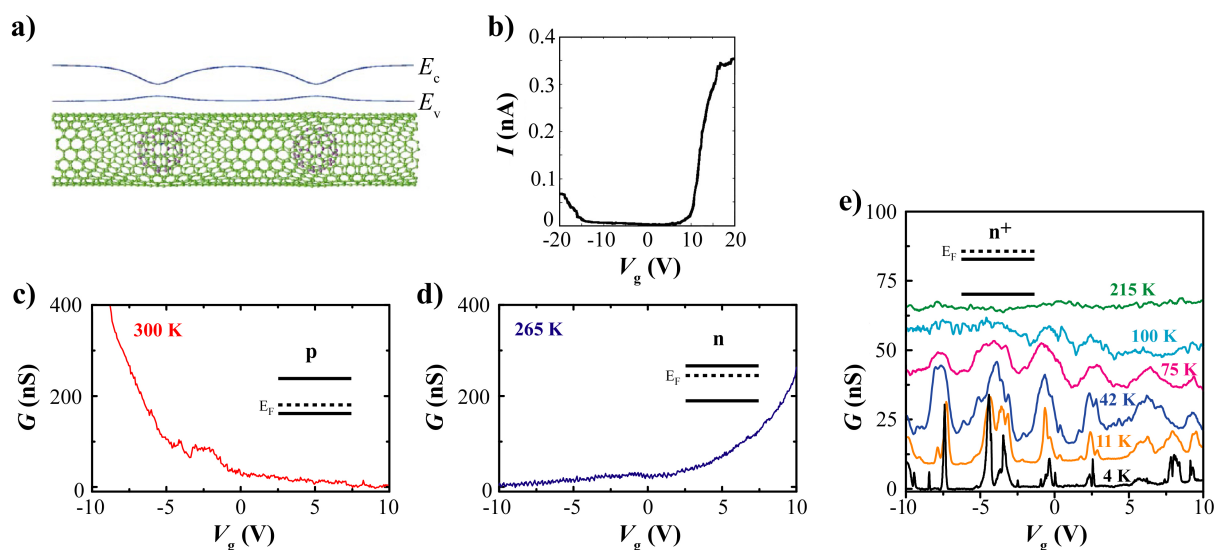
Fig. 3.30: a) Schematic illustration of bandgap narrowing in a semiconducting SWNT due to insertion of metallofullerenes [Lee02]. **b)** Amipolar behaviour of a $(Gd@C_{82})@SWNT$ bundle for $23\ \text{K} \leq T \leq 298\ \text{K}$ and **c)-e)** change from p- to n-conduction to metallicity of an individual $(Dy@C_{82})@SWNT$ with decreasing temperature claimed by [Shi02] and [Chi01], respectively.

4.   Experimental techniques

In this chapter, the experimental techniques applied within this thesis will be discussed in detail. The description covers SWNT and metallofullerene peapod synthesis as well as the preparation of SWNT, metallofullerene peapod and graphene/few-layer graphite transport samples. Furthermore, the setup of the electrical transport rig and the different ways how to electronically characterize samples will be dealt with. The chapter is concluded by pointing out several methods how to combine electrical transport measurements with further structural investigations on the same nanosized object. These novel, combined measurements are of great importance as they provide additional structural information needed to interpret transport data more precisely.

4.1   Synthesis of SWNTs with non-magnetic catalysts and Raman spectroscopy

Empty single-walled carbon nanotubes are needed in two respects within this PhD project: firstly, they are used for the fabrication of nanotube transistors for magnetotransport measurements. Secondly, they serve as host tubes for metallofullerene encapsulation (see chapter 4.3), yielding metallofullerene peapods, which are investigated by electrical magnetotransport measurements as well. This results in the following requirements for the SWNT production process:

1. Catalyst particles cannot be removed completely, neither by chemical purification nor by physical treatment like sonication plus subsequent centrifugation. If magnetic catalyst particles decorate a SWNT or a metallofullerene peapod, they might influence the magnetotransport properties of both empty and filled tubes. Hence one main objective is to utilize non-magnetic catalysts for SWNT production.

2. Despite using non-standard catalysts, the nanotube concentration in the as-produced material has to be high. The contents of amorphous carbon, graphite or catalyst particles should be as small as possible.

3. Since $Dy@C_{82}$ metallofullerenes (mean diameter approx. 8 Å) are to be inserted into single-walled carbon nanotubes, the SWNTs should have a minimum diameter of approx. 1.3 - 1.4 nm [Khl07] combined with a narrow SWNT diameter distribution.

Single-walled carbon nanotube synthesis was carried out using an arc-discharge *Krätschmer* generator [Hal06]. The arc-discharge method has been shown to be capable of SWNT production with non-magnetic catalysts earlier [Kat00, Sai00]. During the arc-discharge process, different carbonaceous deposits are forming. Since the SWNT concentration usually is maximum in the web-like material [Hal06], SWNT webs were the only materials to be considered for detailed characterization and further use for electronic applications.

As the first step, various metal combinations (weight ratio of constituents: 1:1(:1)) were tested concerning applicability as catalysts for SWNT growth. The produced samples were investigated by Raman spectroscopy (Fig. 4.1). The existence of the radial-breathing mode (RBM), being unique for SWNTs [Dre05], in all Raman spectra in figure 4.1 proves that all metal combinations {NiY, FeY, PtRh, PtPd, PtPdRh, PdRh, Pt}* can be used as catalysts to synthesize SWNTs. Figure 4.1a displays the complete Raman spectra with the diameter-dependent RBM mode between 100 cm^{-1} to 300 cm^{-1}, the G mode at about 1580 cm^{-1} and the D and D* modes at approx. 1300 cm^{-1} and 2600 cm^{-1} respectively. The SWNT-specific RBM corresponds to coherent radial atomic vibrations of the single-walled carbon nanotube (as if the tube was breathing), the G mode is due to tangential atomic vibrations, the D mode is defect-induced and the D* mode represents the overtone of the D mode. In general, G, D and D* modes are present in graphite as well. For detailed reviews on Raman spectroscopy on carbon nanotubes refer to [Jor03, Dre05].

The RBMs of the SWNT samples synthesized using different catalyst combinations were evaluated to extract comparative diameter information (Fig. 4.1b). The SWNT diameter distribution in a sample can be described using the relation $\omega_{\mathrm{RBM}} = A/d + B$, where d is the SWNT diameter and the parameters A and B are determined experimentally. For calculating the diameters of the single-walled carbon nanotubes in the web material†, the parameters $A = 234$ cm^{-1}nm and $B = 10$ cm^{-1} were chosen as determined for SWNT bundles [Jor03, Dre05] (Figs. 4.1b, 4.2 [top x-axes]).
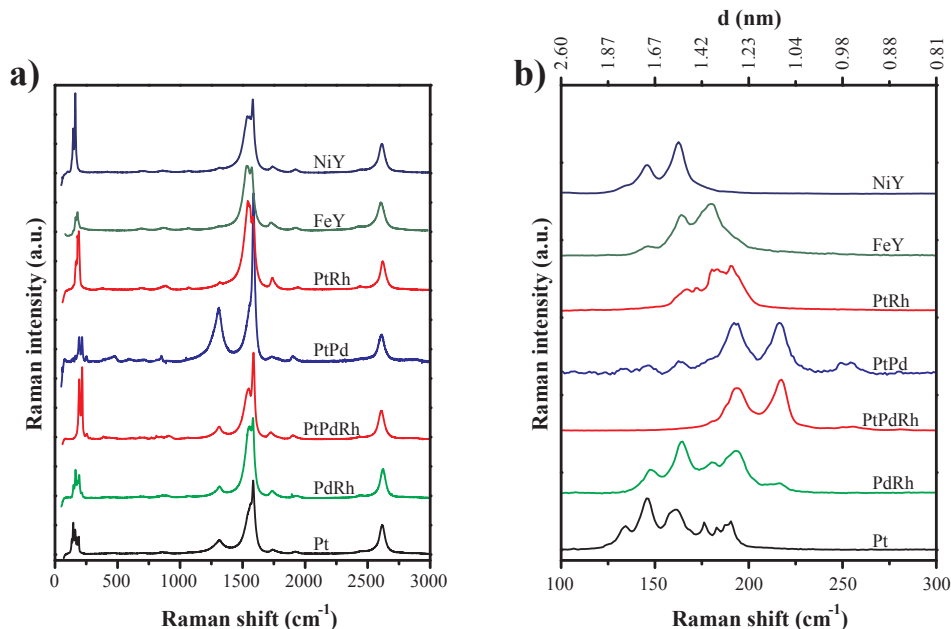
**Fig. 4.1: a)** Raman spectra of SWNTs produced with various combinations of catalysts. **b)** RBM modes of the spectra of **a)**. Amongst the non-magnetic catalysts, PtRh exhibits the narrowest SWNT diameter distribution at large diameters. Laser wavelength in **a),b)**: 633 nm.

---

*The magnetic metal combinations NiY and FeY serve as reference only.

†The SWNTs in web material are predominantly bundled.

Among all tested non-magnetic catalyst combinations, the SWNT web material produced by PtRh catalyst contains single-walled carbon nanotubes with the narrowest diameter distribution at large diameters (Fig. 4.1b). Due to this reason, PtRh was the non-magnetic catalyst combination of choice for the synthesis of single-walled carbon nanotubes to be filled with $Dy@C_{82}$ metallofullerenes [Hal06]. However, the diameter range of the PtRh SWNTs[*] between approx. 1.2 nm and 1.6 nm (Fig. 4.1b) should be slightly increased to obtain more suitable conditions for $Dy@C_{82}$ encapsulation. The estimated minimum SWNT diameter for insertion of $Dy@C_{82}$ metallofullerenes is between 1.3 and 1.4 nm [Khl07], whereas the optimum SWNT diameter[†] is expected to be approx. 1.4 nm according to [Yoo05].

One way to modify the SWNT diameter distribution is to add sulphur to the catalysts used for single-walled carbon nanotube growth [Kia98, Kia00, Hal05]. When varying the sulphur content from 0 at% to 2.6 at% (with respect to the total anode mass), it turns out that a suitable SWNT diameter distribution for tube filling is achieved for 0.9 at% S using PtRh as catalyst (Fig. 4.2) [Hal06].
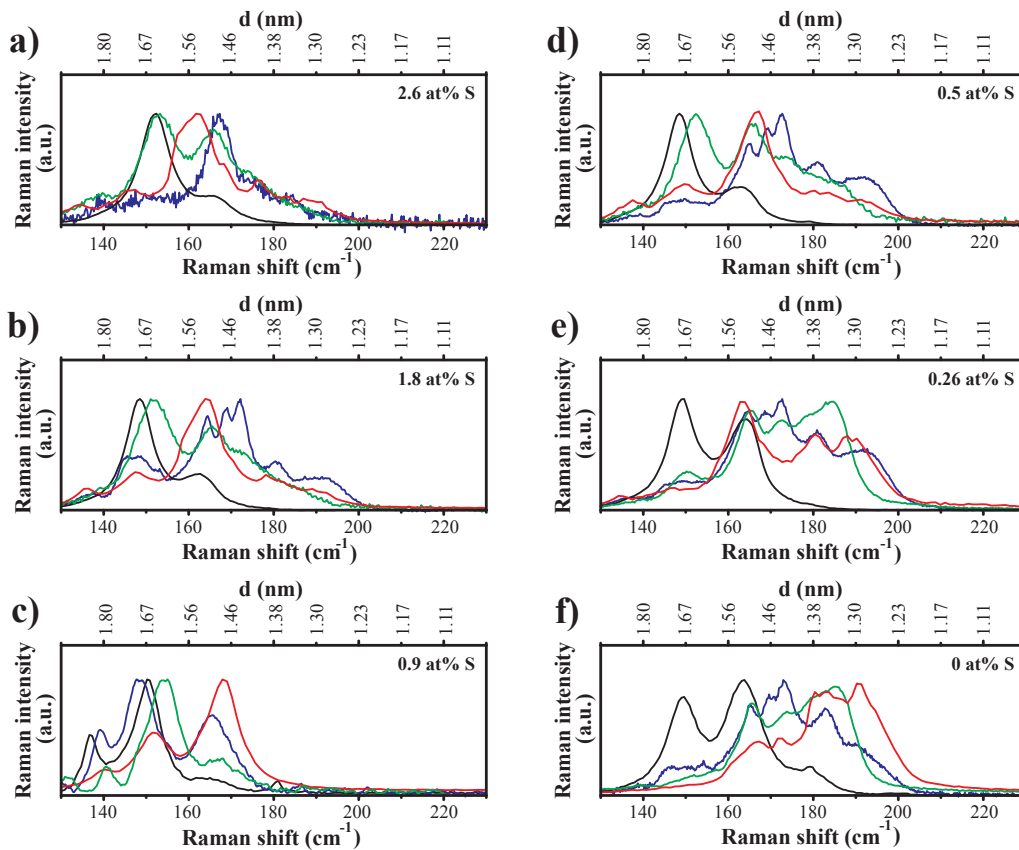
Fig. 4.2: RBM modes of SWNTs produced with PtRh as catalyst and with sulphur as promoter. The relative amount of sulphur with respect to the total anode mass (C, S, PtRh) is indicated in the upper right corners. The four colours {green, red, blue, black} correspond to laser excitation wavelengths of {514 nm, 633 nm, 647 nm, 785 nm} [Hal06].

---

[*]SWNTs being in resonance with the 633 nm laser line, cp. caption of figure 4.1.

[†]i.e. the SWNT diameter at which maximum energy is gained for metallofullerene insertion

According to figure 4.2c, for 0.9 at% S added to the PtRh catalyst, the SWNT diameter distribution (of SWNTs in resonance with the 514 nm, 633 nm, 647 nm, 785 nm laser lines) is approx. 1.4 to 1.9 nm, i.e. all the tubes detected by Raman spectroscopy in this SWNT web-like material are large enough to host Dy@C_{82} metallofullerenes. A further aspect of adding sulphur is the possibility to increase the yield, i.e. the amount of produced SWNTs in relation to the total amount of material evaporated, significantly [Kia98, Kia00, Hal05]. In the case of the PtRh catalyst combination [Hal06], the yield maximum of SWNT webs is achieved for about 0.5 at% S (Fig. 4.3a), it still is acceptable for the 0.9 at% S concentration which was used to produce the SWNTs for this project in order to have a suitable diameter distribution for filling (see above). On a microscopic level it is not clear yet, how the sulphur can enhance the nanotube yield and modify the SWNT diameter distribution. One possibility is that the sulphur changes the surface tension and the melting point of small catalyst droplets [Hal05] and thus modifies features of the SWNTs growing from these metal droplets.

Finally, the relative purity of the SWNTs within the web material (Fig. 4.3b) produced with PtRh catalyst was estimated by thermal gravimetry (TG) and near-IR spectroscopy [Hal06, Itk03]. For 0.9 at% S, the SWNT purity is close to the purity maximum (Fig. 4.3b). The resulting values are relative data since the purity analysis of a SWNT sample based on near-IR spectroscopy of semiconducting SWNTs [Itk03] is relative only.
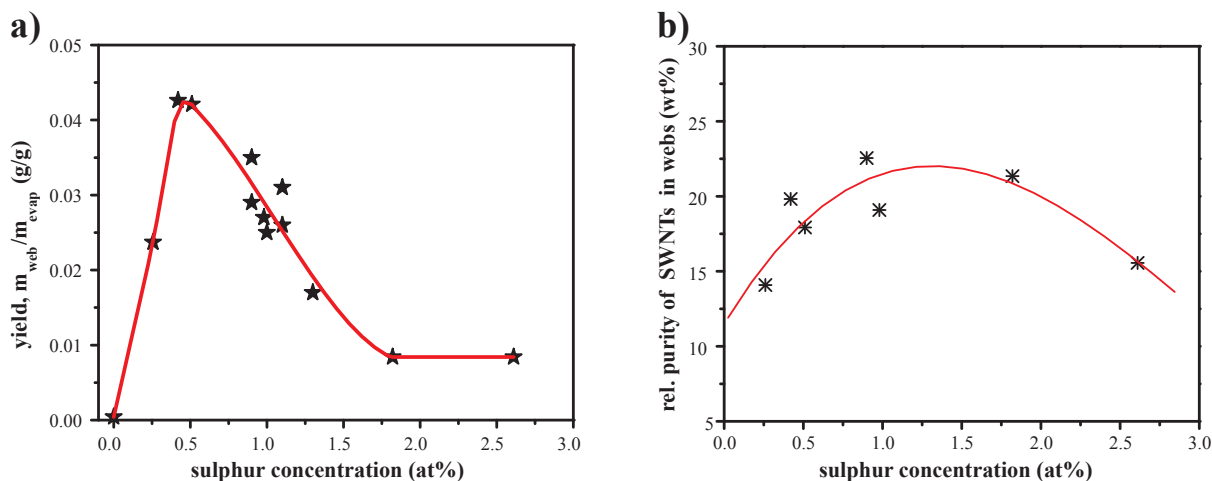
Fig. 4.3: a) Yield and b) estimated relative purity of SWNTs within the web material produced with the PtRh catalyst combination as a function of sulphur concentration [Hal06].

In summary, by using the non-magnetic catalyst combination PtRh together with 0.9 at% of sulphur as promoter, SWNT material with a suitable diameter distribution for Dy@C_{82} encapsulation and with favourable yield and purity values has been produced. Great importance was attached to the use of non-magnetic catalysts in order to avoid magnetic metal clusters along the tubes and tube bundles, which might have effects when performing magnetotransport investigations on SWNT and metallofullerene peapod devices.

4.2 Synthesis and HPLC analysis of Dy@C$_{82}$ metallofullerenes

High purity ($> 99\%$) Dy@C$_{82}$ endohedral metallofullerene samples have been produced by the combination of an arc-discharge process with subsequent extraction/filtration techniques and high-performance liquid chromatography (HPLC) [Yan03].

The anode, which is consumed during the arc-discharge process, was filled with a mixture of graphite powder and Dy$_2$O$_3$ (99.95%, Strem Chemicals) in an atomic ratio of Dy/C equals 0.02 [Yan03]. The product of the arc-discharge process contains several carbon species, i.e. graphite, amorphous carbon and different sorts of fullerenes. The arc-discharge raw soot was dissolved in N,N-dimethylformamide (DMF) and treated by ultrasonic Soxhlet extraction. The remaining powder after DMF evaporation was dissolved in toluene and filtered through a slow-rate filter paper multiple times. After the Soxhlet extraction and filtering, only fullerenes and metallofullerenes are dissolved in the toluene. The Dy@C$_{82}$ metallofullerenes were isolated by HPLC (HPLC system: 600C-400, Waters Inc.) using a COSMOSIL 5PYE column [Yan03].

HPLC chromatograms[†] were taken from a crude extract redissolved in toluene (Fig. 4.4a,A) and from a HPLC purified Dy@C$_{82}$ sample (Fig. 4.4a,B). The product after HPLC was characterized by DCI[‡] negative ion mass spectroscopy [Yan03], in order to check the Dy isotope distribution (Fig. 4.4b) and the purity of the acquired Dy@C$_{82}$ sample.
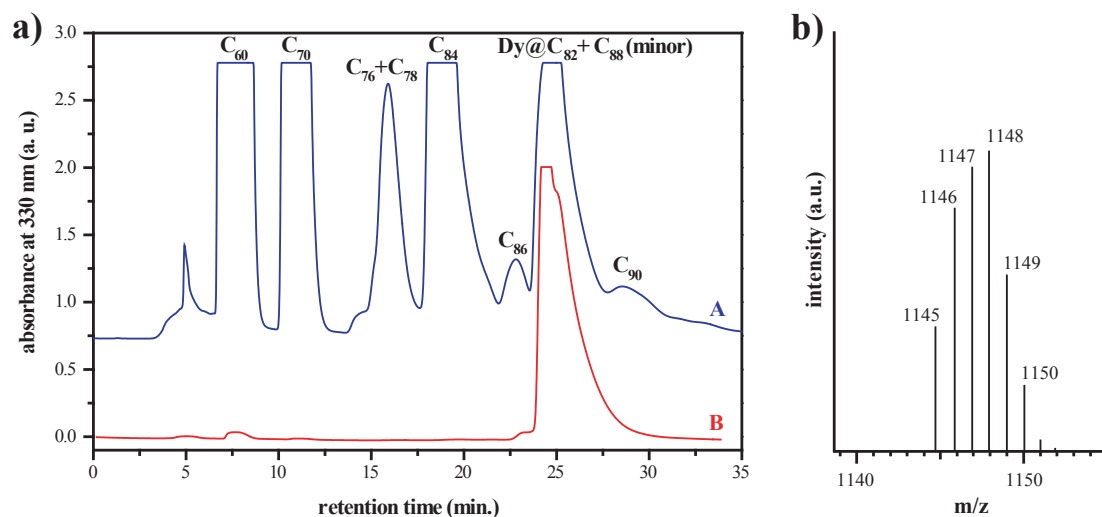
Fig. 4.4: a) HPLC chromatograms of the crude extract redissolved in toluene (A), showing the presence of different sorts of fullerenes in the sample after Soxhlet extraction and filtering, and of the Dy@C$_{82}$ sample after HPLC (B) [Yan03]. **b)** DCI negative ion mass spectrum of a purified Dy@C$_{82}$ sample (after HPLC). The mass differences are due to different Dy isotopes [Yan03].


[†]using absorption of 330 nm UV light
[‡]DCI = desorption chemical ionization

## 4.3   Synthesis and TEM analysis of (Dy@C$_{82}$)@SWNT metallofullerene peapods

Non-magnetic SWNTs produced as described in section 4.1 (1.116 mg) were heated in air at 440°C for 30 min (weight loss 31%) to ensure that the nanotube ends are open and unobstructed by amorphous impurities prior to the filling with metallofullerenes. The SWNTs were then mixed with 0.2 ml of CS$_2$ containing about 0.5 mg of Dy@C$_{82}$ (cp. section 4.2). The solvent was evaporated in air, a dry SWNT + Dy@C$_{82}$ mixture was placed in a platinum crucible, sealed in a quartz tube in 10^{-6} torr vacuum and heated at 440°C for 5 days. Resulting (Dy@C$_{82}$)@SWNT metallofullerene peapods were extensively washed with 10-20 ml of CS$_2$ to remove non-encapsulated fullerenes, filtered on a PTFE porous membrane and dried in air.

A small specimen of (Dy@C$_{82}$)@SWNT powder was dispersed in 1 ml of methanol using an ultrasonic bath, and the grey suspension formed was deposited onto a TEM copper grid coated with amorphous lacy carbon film. High-resolution transmission electron microscopy (HR-TEM, JEOL 4000EX, LaB6, information limit 0.12 nm) was used for imaging. The imaging conditions have been carefully tuned by lowering the accelerating voltage of the microscope to 100 kV and reducing the beam current density to a minimum in order to minimize the beam damage. No beam damage was observed in sp^2-carbon structures under these conditions over a period of 20 min. Figure 4.5a shows a typical image of nanotubes filled with Dy@C$_{82}$ metallofullerenes: most of the nanotubes are aggregated in small bundles consisting of 5-20 nanotubes across with 70-90 % of the nanotubes densely filled with fullerenes. Individual atoms of Dy can be observed as dark spots within the fullerene cages on high magnification images (Figs. 4.5b,c).
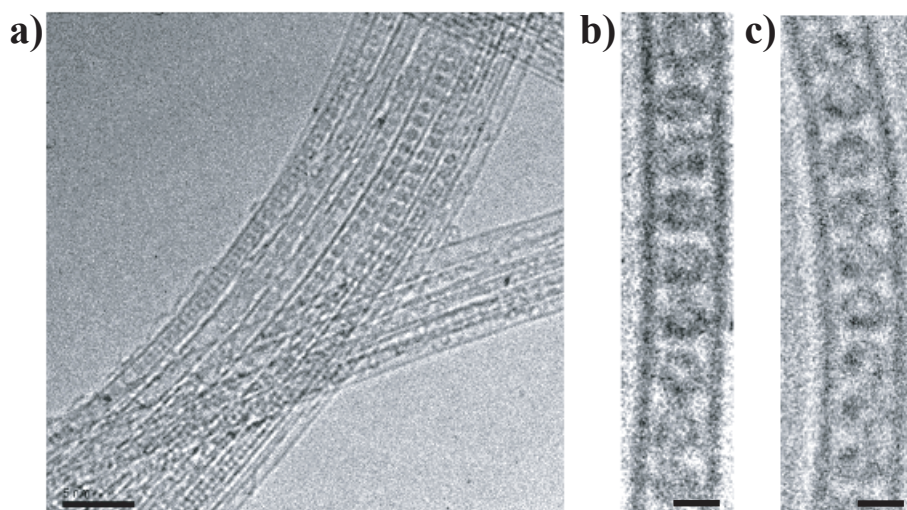
Fig. 4.5: a)-c) TEM micrographs of (Dy@C$_{82}$)@SWNT metallofullerene peapods. The scale bar in **a)** is 5 nm, in **b)** and **c)** 1 nm.

A further metallofullerene peapod sample was investigated by a TITAN 80-300 high-resolution transmission electron microscope [Chu09], for which the spherical aberration of the objective lens is corrected (c_s correction), at accelerating voltage of 80 kV, which is below the knock-on damage threshold for SWNTs and fullerenes. A single $(Dy@C_{82})$@SWNT metallofullerene peapod is depicted in figure 4.6a. Due to the c_s correction, the resolution is enhanced in comparison with figures 4.5b,c, the inner Dy atoms now can be clearly identified. The subsequent HR-TEM images 4.6b,c,d display the same tube as in 4.6a after 9, 32 and 39 minutes of 80 keV electron beam irradiation. The Dy atoms inside the fullerenes gain energy from the incoming electron beam and can open the C_{82} cages, which coalesce (Fig. 4.6b) and establish a second, inner tube (Fig. 4.6c). During this process, the Dy atoms get highly mobile within the whole structure, meet each other and form a metallic cluster [Chu09] (Fig. 4.6c), that manages to break the outer SWNT (Fig. 4.6d) as a result of the acquired energy from the electron beam and the catalytic properties of Dy atoms (cp. chapter 7.6 and [Chu09]).
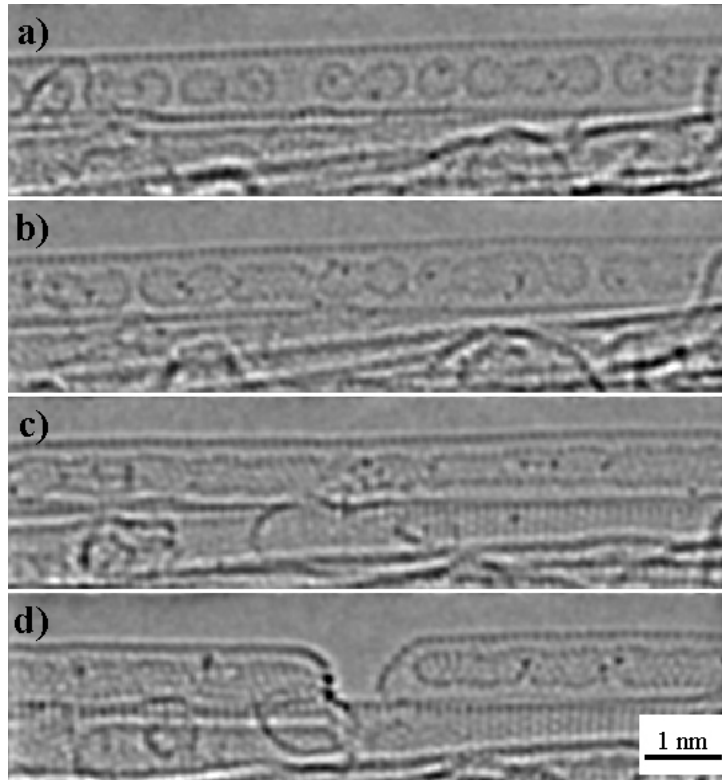
Fig. 4.6: HR-TEM micrographs of an individual $(Dy@C_{82})$@SWNT metallofullerene peapod. The images were obtained with a c_s corrected TITAN 80-300 TEM at 80 kV after **a)** 0 min, **b)** 9 min, **c)** 32 min and **d)** 39 min of electron beam irradiation [Chu09].

In conclusion, $(Dy@C_{82})$@SWNT metallofullerene peapods were produced with non-magnetic SWNTs as host tubes, i.e. SWNTs made by non-magnetic catalysts. After synthesis, HR-TEM analysis has been performed on the metallofullerene peapod sample indicating that approximately 70-90 % of the nanotubes are filled with fullerenes. Moreover the Dy atoms inside the C_{82} fullerene cages were clearly visualized utilizing a c_s corrected high-resolution transmission electron microscope.

4.4   Preparation of SWNT and metallofullerene peapod transport samples

After production and characterization of SWNT and $(Dy@C_{82})@SWNT$ metallofullerene peapod powders, several steps have to be taken to prepare devices for electrical investigation of individual tubes. The nanotubes shall be put onto a substrate and provided with metal contacts to receive single tubes in transistor configuration.

Below, the sequence of steps is listed which was complied with on the way to individual tube devices:

- patterning of marker systems and bondpads onto 4x4 mm^2 Si/SiO$_2$ chips using electron beam lithography
- cleaning the chips by acetone, isopropanol and oxygen plasma treatment
- functionalization of the chip surfaces with silane[*]
- preparation of a sparse dispersion of SWNTs or metallofullerene peapods in SDS[†]
- adsorption of the SWNT or metallofullerene peapod dispersion onto the chips
- AFM to locate individual nanotubes with respect to the marker system
- drawing the designs to electrically contact the selected nanotubes by means of e-beam lithography
- coating the chips with a two-layer e-beam resist system
- e-beam lithography to pattern the design file structures onto the chips
- development of the resists after electron beam lithography
- metallization of the chips by thermal evaporation of the desired contact materials
- lift-off process to remove the resists
- AFM to check the geometry of the individual tube devices
- gluing the chips into non-magnetic chip-carriers using conductive silver
- wire-bonding to electrically connect the nanotubes on the chips with the chip-carriers

In the following, the steps listed above are elucidated in greater detail.

Starting material are highly doped 6" Si wafers with the specific resistance $\rho \leq 6\,m\Omega\,cm$ and with arsenic as electron donor. The high doping level is important to make sure that the conductance does not freeze out at low temperatures. These wafers are provided with a 200 nm thick dry SiO$_2$ dielectric layer, furthermore ohmic backside contacts are established by backside implantation plus backside metallization with an aluminum alloy.

---

[*]The silane N-[3-(Trimethoxysilyl)Propyl]-Ethylen-Diamin (97%) was used within this work.
[†]SDS = sodium dodecyl sulfate, i.e. CH_3-$(CH_2)_{11}$-O-SO_3^- Na^+

Each wafer is cut** into 45x45 mm^2 substrate pieces which are cleaned with methyl pyrrolidone, acetone and isopropanol at 55°C by ultrasonic treatment. Thereafter the substrates are coated with a double-layer e-beam resist system. Onto every 45x45 mm^2 substrate 100 structures (Fig. 4.7a) are patterned by electron beam lithography, each of the structures comprising 20 bondpads with fingers leading towards the inner part of the structure named marker system (Fig. 4.7c). Despite the fact that most of the features of the structure in figure 4.7 are relatively large, i.e. μm scale, the structure is written by electron beam lithography (instead of (standard) optical lithography) since later in the process well-defined corners and edges are needed for alignment purposes.

The marker system is an array of geometrical symbols which serves as coordinate system to refer to when subsequently looking for individual nanotubes. After the development of the structures and the metallization of the substrates with 5 nm Cr (as adhesive layer) and 25 to 30 nm Au, the lift-off process is carried out and every substrate is cut** into 100 4x4 mm^2 chips. Thus, large quantities of chips adequate for nanotube adsorption are manufactured with additionally each chip being labeled with a 4-digit code for easy identification (not shown in Fig. 4.7).

To receive optimum substrates for electrical transport on individual carbon nanotubes, it is of great importance that the substrates undergo an intensive cleaning procedure before adsorption of the nanotubes. Within this work, the chips were cleaned by 10 to 15 minutes ultrasonic treatment at 55°C in acetone and isopropanol, followed by 60 seconds oxygen plasma treatment at 200 W and 0.3 torr. The center of a cleaned chip is depicted in figures 4.7b,d.

Nanotubes do not tend to adhere to clean SiO$_2$ surfaces very well. To enhance nanotube adsorption onto the silicon dioxide surfaces, the Si/SiO$_2$ chips are silanized by steeping the chips into a mixture of 10 μl N-[3-(Trimethoxysilyl)Propyl]-Ethylen-Diamin (97%) and 10 ml pure H$_2$O for 2 minutes, followed by rinsing them in pure water and blowing them dry with argon gas. After this functionalization step the chips are ready for nanotube adsorption.

To disperse SWNTs and (Dy@C$_{82}$)@SWNT metallofullerene peapod powders, 1% aqueous SDS is used as dispersing agent [OCo02]. A small amount of powder is put into 2 to 3 ml SDS. After a 15 to 30 s ultrasonic treatment (ultrasound processor: Dr. Hielscher UP100H), about 1.5 ml of the dispersion is centrifuged for 30 minutes at 14000 rpm with an Eppendorf 5417C centrifuge. The density of nanotubes within the dispersion and the amount of unwanted constituents like amorphous carbon or catalyst particles therein is evaluated by adsorbing the dispersion onto Si/SiO$_2$ test chips. Since the objective is to perform

---

**Before cutting, the substrates are coated with the photoresist S1805 to be protected against scratching and damage during the cutting process.
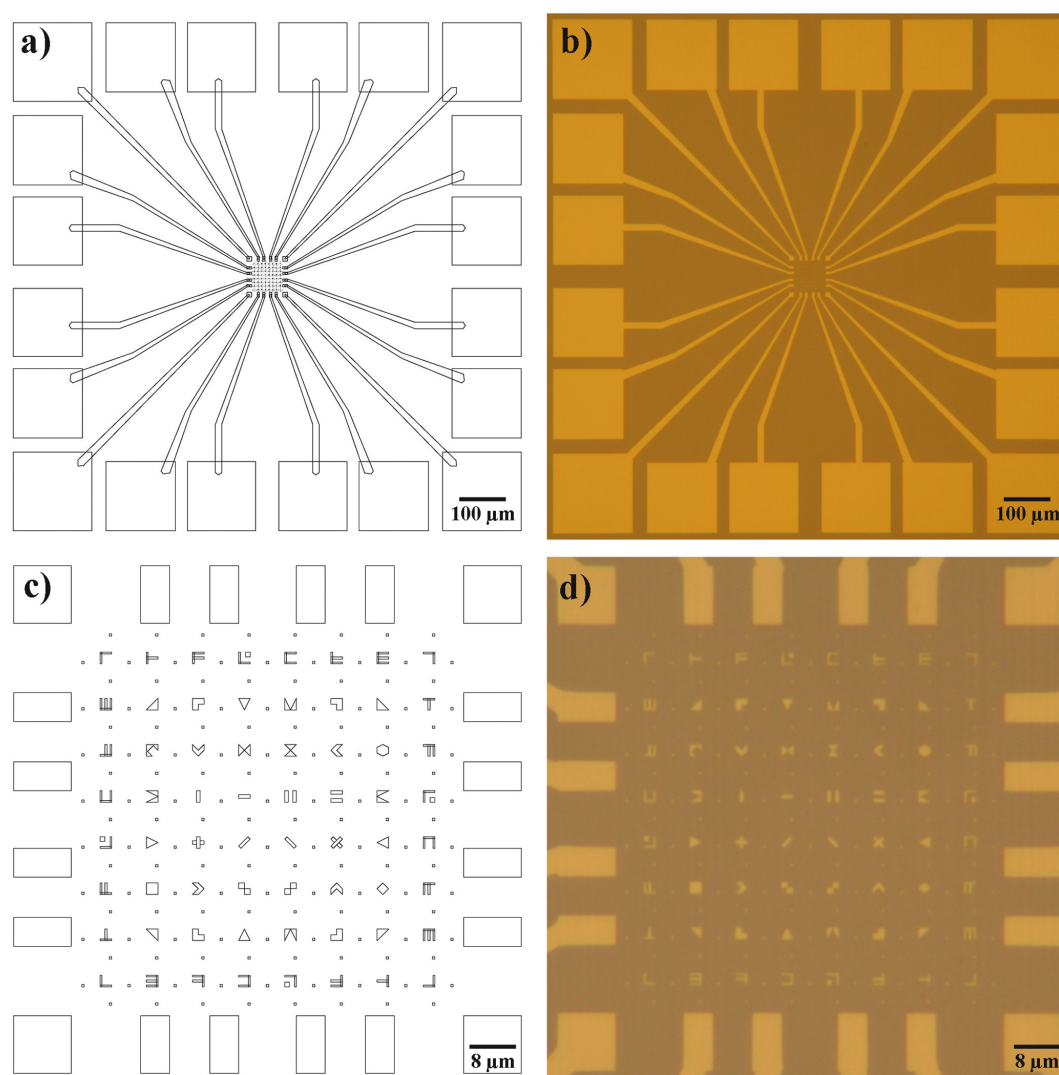
Fig. 4.7: a) Design of the structure which is to be written on every chip before nanotube adsorption. The structure comprises 20 bondpads, fingers leading from the bondpads to the inner part of the structure and the inner part named marker system. **b)** Optical microscopy of the center of a Si/SiO_2 chip which was patterned with the structure on the left handside by e-beam lithography. The chips are metallized with 5 nm Cr (as adhesive agent) and with 25 to 30 nm Au. **c)** Design of the marker system. The marker system consists of 64 symbols called markers, 2 by 2 μm in size, which serve as coordinate system for locating nanotubes later on. In between each two markers there is a 400 by 400 nm large square. The 20 surrounding rectangles are connected to the bondpad fingers (cp. **a)**). **d)** Optical microscopy of a marker system after patterning it onto a Si/SiO_2 substrate by e-beam lithography (metallization 5 nm Cr, 25 to 30 nm Au).

electrical transport measurements on individual tubes, the density of the nanotubes in the dispersion has to be low to avoid touching or adjacent nanotubes on the chips. Lowering the nanotube concentration in the dispersion is achieved by either further dilution with SDS and/or by repeated centrifugation, which reduces dirt concentration as well [OCo02]. In this way it is possible, to get a sparse distribution of isolated SWNTs or metallofullerene

peapods in conjunction with only very little amorphous carbon and remaining catalyst particles.

The prepared dispersion is adsorbed onto the functionalized Si/SiO_2 chips by putting 10 μl dispersion droplets onto the chips. These droplets remain on the chip surfaces for 5-15 min, the duration of adsorption is another handle to influence the final nanotube density on the chip surfaces. After the chosen adsorption time the droplets are blown off the chip surfaces by argon gas, then the chips are cleaned by rinsing them in pure H_2O and finally blown dry, again with argon gas. Note that the deposition of nanotubes from dispersion onto chips is a process resulting in a *random spatial distribution* of nanotubes across the chip. There are other, chemical vapor deposition (CVD) based processes promising better positioning control [Dai02, Yan07], yet these CVD processes are not applicable for metallofullerene peapods and for this reason have not been considered for this study. Despite SDS being a well-suited agent to disperse SWNTs [Yoo07] and metallofullerene peapods and despite the prior application of ultrasonic treatment, the larger fraction of the tubes adsorbed on the chips usually turns out to be nanotube bundles. Thus the next task is to find the positions of individual, straight and isolated SWNTs and metallofullerene peapods respectively by atomic force microscopy within the marker system area (Fig. 4.7d). For later on use, the positions of the individual nanotubes are saved with respect to the markers in AFM images taken at different zoom levels (Fig. 4.8). If the marker system on the chip is always oriented in the same way as depicted in Figs. 4.7c,d, one marker in the AFM image (Fig. 4.8a) is enough to tell the position within the marker system area.
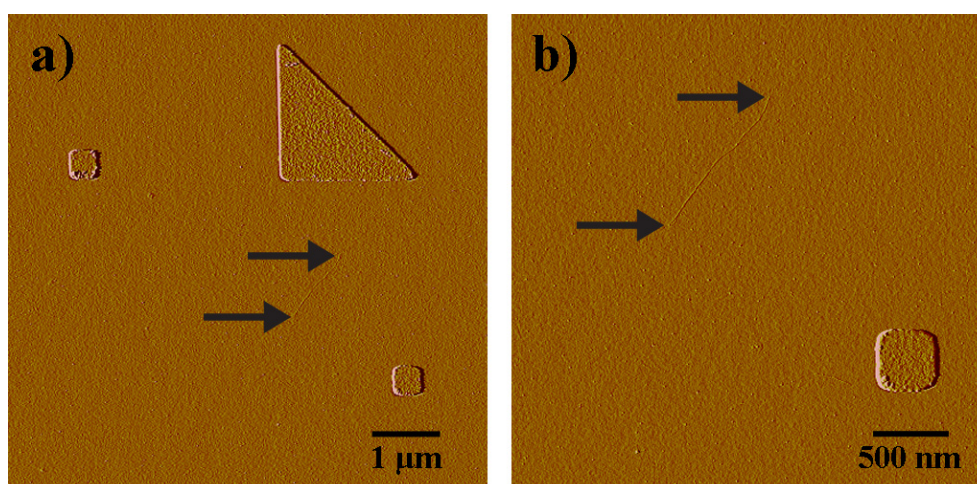
Fig. 4.8: a) Individual SWNT located by AFM with respect to one of the markers. **b)** Blow-up of **a)**. The black arrows in **a),b)** indicate the ends of the carbon nanotube.

The acquired AFM images of individual SWNTs or metallofullerene peapods with different magnifications are imported into the design file (Fig. 4.7c) and rotated and scaled with a graphics software such that the scanned markers match the markers in the design. Thereby the positions of the nanotubes with respect to the design file are known in good precision. Electrical leads are designed according to the positions of the selected individual nanotubes

in the marker system area, providing every nanotube with two contacts, which connect
the chosen nanotubes with the bondpads in the outer structure (Figs. 4.7a,b). A finished
design file, in which the blue polygons will be exposed in the e-beam lithography step to
contact the nanotubes on the chip, is depicted in Fig. 4.9. Typically, 5 to 8 nanotubes are
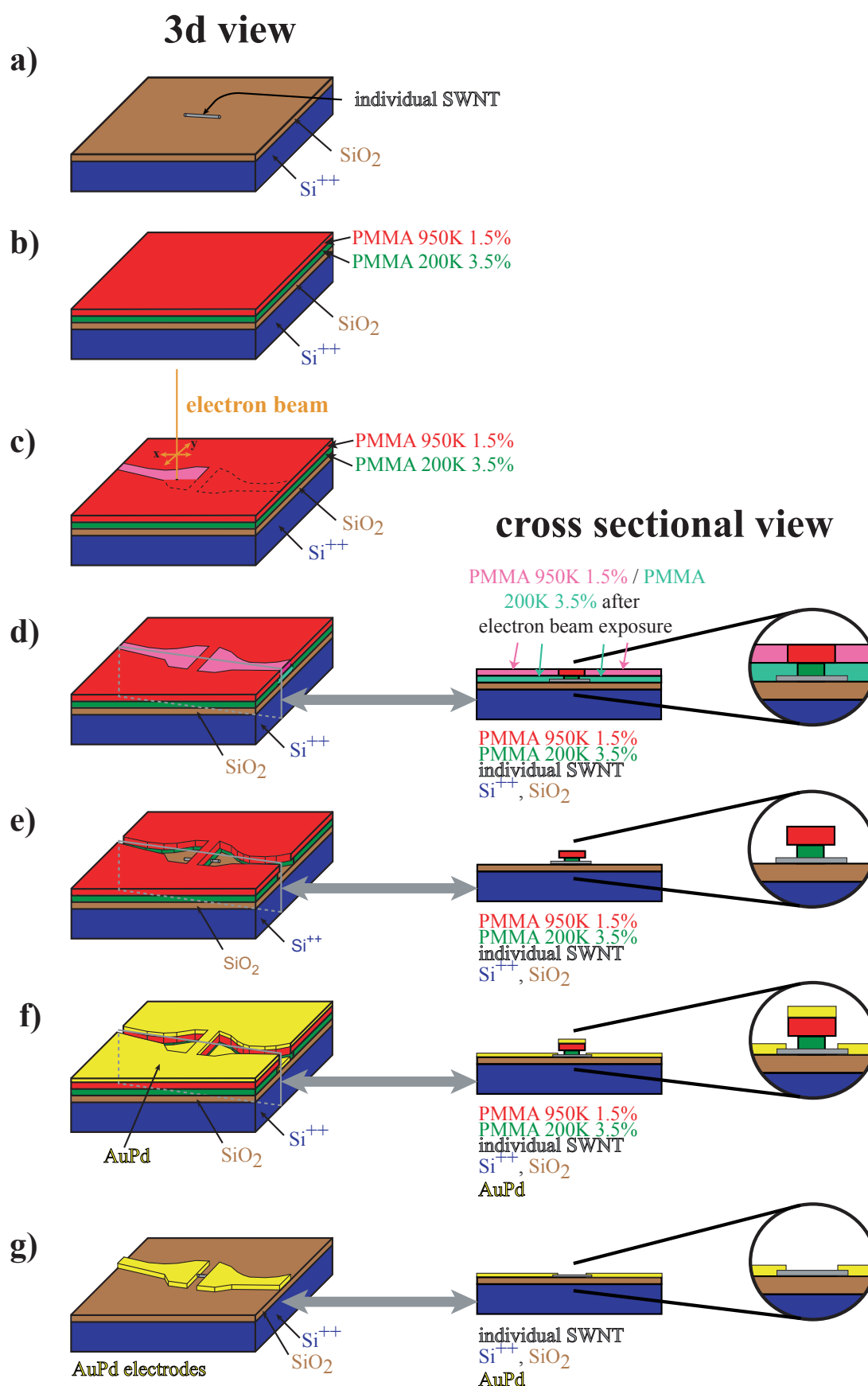contacted per chip.
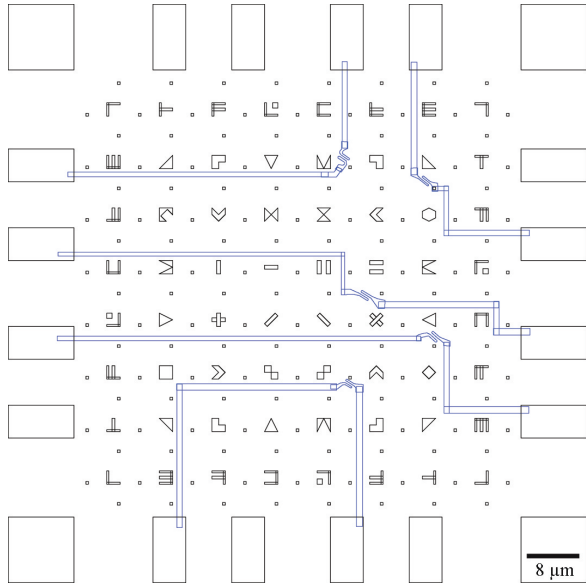
Fig. 4.9: Finished design for electron beam
lithography to contact individual carbon nano-
tubes on top of a Si/SiO$_2$ chip. The black struc-
tures (i.e. the markers) already have been pat-
terned onto the chip before. In the remaining
e-beam step, the blue polygons will be exposed
representing the source and drain contacts for
the chosen carbon nanotubes and connecting the
tubes with the bondpads in the outer structure.

Figure 4.10 schematically guides through the following e-beam process depicting the pro-
cess steps for one representative nanotube on a chip. The chip with the adhering nanotubes
(Fig. 4.10a) is covered with a double-layer of e-beam resist by spin-coating, the 1st layer
is PMMA†† 200K, 3.5%, the 2nd one PMMA 950K, 1.5%, the total thickness is 200 nm
(Fig. 4.10b). The chip is baked out at 160°C for 1 hour after each spin-coating step
to extract the solvent chlorobenzene out of the PMMA. Next, electron beam lithogra-
phy* is perfomed on the coated chip, the electron beam exposing the nanotube contacts
(Fig. 4.10c), e.g. the blue polygons in figure 4.9. Before electron beam exposure the struc-
ture comprising the nanotube contacts has to be aligned by the e-beam system software
with the pre-defined marker system on the chip. By electron beam exposure the poly-
mer chains of the exposed PMMA resists are shortened (bright color areas in Fig. 4.10d)
and such can be selectively dissolved by the development agent isobutyl methyl ketone
(Fig. 4.10e), whereas it does not affect the unexposed PMMA areas (Fig. 4.10e). The main
purpose of the two-layer resist system is to generate an undercut after the development
(Fig. 4.10e, cross sectional view), i.e. the residual PMMA 200K bar crossing the nano-
tube after development (the width of this bar is typically 100 to 400 nm) is thinner than the

---

††PMMA = polymethyl methacrylate
   *Within this work, a Hitachi S2300 SEM upgraded with a Raith Elphy III controller plus the respective
Elphy software and a Raith e-Line were employed for electron beam lithography.

3d view

a)

individual SWNT

SiO_2

Si^{++}

b)

PMMA 950K 1.5%
PMMA 200K 3.5%

SiO_2

Si^{++}

electron beam

c)

PMMA 950K 1.5%
PMMA 200K 3.5%

SiO_2

Si^{++}

cross sectional view

d)

PMMA 950K 1.5% / PMMA
200K 3.5% after
electron beam exposure

Si^{++}

SiO_2

PMMA 950K 1.5%
PMMA 200K 3.5%
individual SWNT
Si^{++}, SiO_2

e)

Si^{++}

SiO_2

PMMA 950K 1.5%
PMMA 200K 3.5%
individual SWNT
Si^{++}, SiO_2

f)

AuPd SiO_2

Si^{++}

PMMA 950K 1.5%
PMMA 200K 3.5%
individual SWNT
Si^{++}, SiO_2
AuPd

g)

Si^{++}
SiO_2

AuPd electrodes

individual SWNT
Si^{++}, SiO_2
AuPd

Fig. 4.10: Schematic of the lithographic process to produce a nanotube in transistor configuration: **a)** nanotube on a substrate; **b)** after spin-coating; **c)** electron beam lithography (EBL); **d)** after EBL; **e)** after development; **f)** after evaporation; **g)** nanotube in transistor configuration after lift-off (*details for a)-g) in the main text*).

PMMA 950K on top of it. After development, the chip is metallized with the desired
contact material (Fig. 4.10f), within this study AuPd 60/40 was used for standard con-
tacts with the typical contact thickness of 25 to 35 nm. The metal is evaporated onto
the whole chip (Fig. 4.10f), filling the trenches which later will be the contacts to the
nanotubes and covering the residual PMMA double-layer. The lift-off process (transition
from Figs. 4.10f-g), which the chemical AR300-70 is used for, removes the residual PMMA
double-layer together with the metal layer on top of the PMMA. The undercut geome-
try (Figs. 4.10e,f, cross sectional view), which has been mentioned before, facilitates a
smooth lift-off since the metal remaining in the trenches is well separated from the metal
on top of the PMMA. After the lift-off procedure, the nanotube
field-effect transistor devices are finished (Fig. 4.10g) and can be inspected by atomic
force microscopy. Figure 4.11 presents AFM images of the same individual SWNT as in
figure 4.8 after the complete lithography process. The typical spacing between the source
and drain electrodes of a contacted nanotube is 100 to 400 nm as depicted in figure 4.11b.
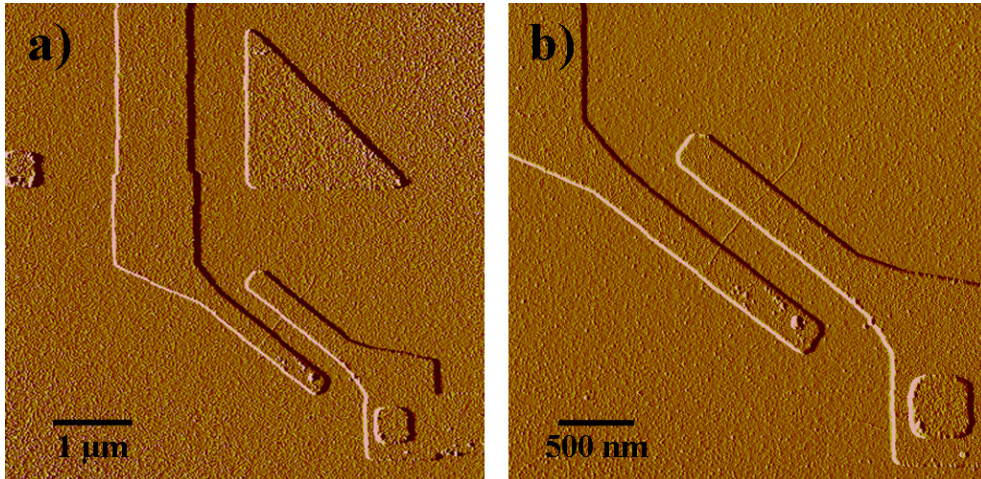
Fig. 4.11: AFM images of the same individual SWNT as in Fig. 4.8 after electron beam litho-
graphy, development, metallization and lift-off. The spacing between the contacts in this case is
about 250 nm.

Finally, the completed chip with 5 to 8 contacted carbon nanotubes or metallofullerene
peapods on top of its SiO_2 layer has to be glued into a chip-carrier and the bondpads
have to be connected to the pins of the chip-carrier by wire-bonding. Gluing the chip into
the chip-carrier is done using conductive silver which establishes an electrical connection
between the metal plate inside the chip-carrier and the highly doped Si serving as back-gate
electrode. One of the pins attached sidewards along the outer edges of the chip-carrier is
electrically connected to the inside metal plate, so the back-gate electrode of the chip can
be addressed by contacting this pin of the chip carrier with the respective counter pin of the
sample stick. Before connecting the bondpads on the chip with the other pins of the chip-
carrier, wire bridges shorting *all* pins of the chip-carrier are bonded in between each two
chip-carrier pins to form a ring of wire bridges along the inner chip-carrier circumference
(Fig. 4.12a). These wire bridges are of great importance since they ensure that after wire-

bonding the real connections to the bondpads (Fig. 4.12a), meaning to the nanotubes, all contacts lie on the same electrical potential and cannot suffer from electrostatic discharge which might appear when handling the sample[§]. Having completed these wire-bonding steps, the sample is ready to be mounted into the sample stick (Fig. 4.19) of the electrical transport measurement rig (Fig. 4.18). Figure 4.12 concludes this chapter by displaying different zoom levels of a finished carbon nanotube transport sample beginning with a photography of the whole chip carrier with the chip glued inside and ending with an AFM image of one of the contacted nanotubes on this chip.
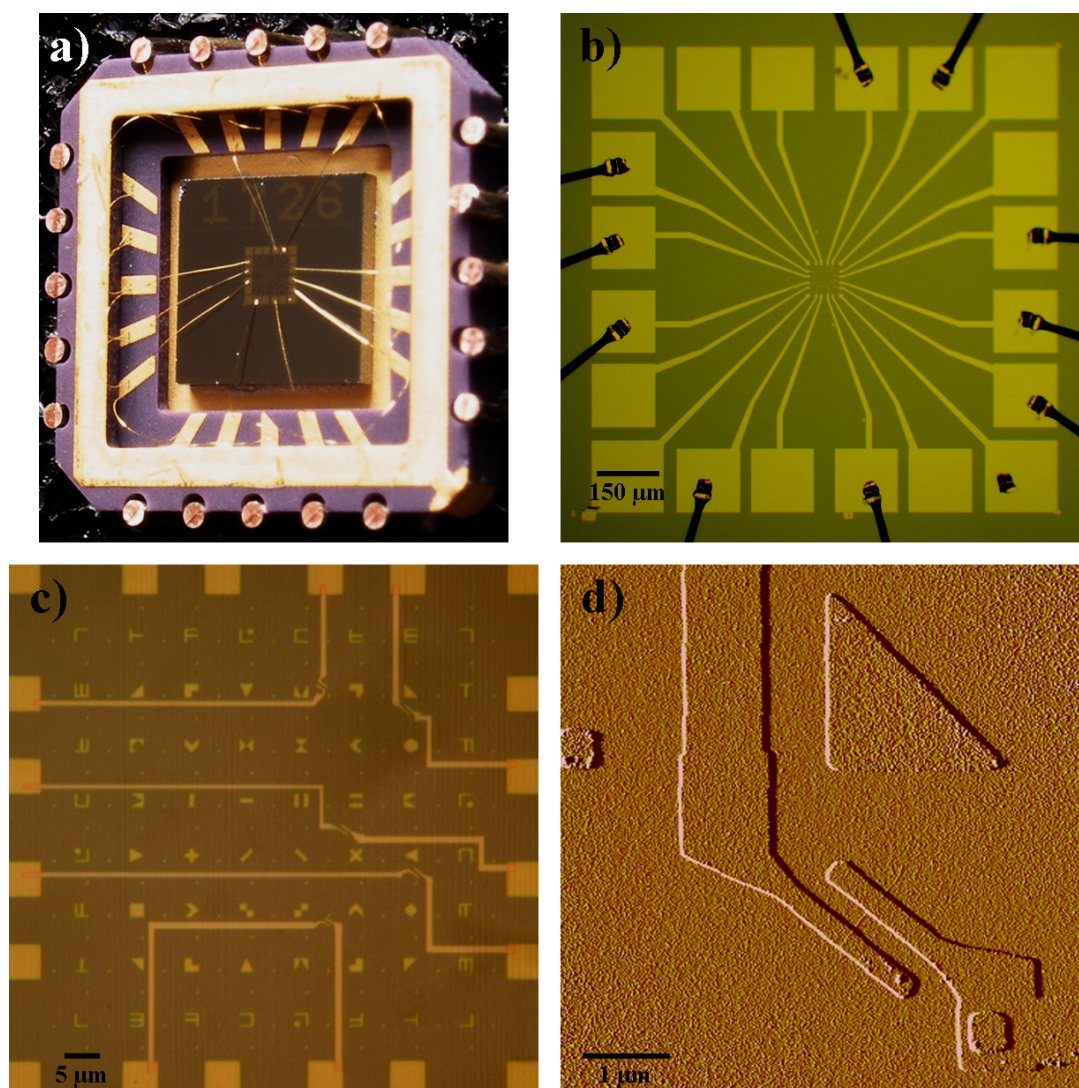
Fig. 4.12: Individual carbon nanotube transport sample ready to be mounted into the sample stick of the electrical transport measurement rig. **a)** Photography of the chip-carrier and the chip after wire bonding. Note the ring of shortcut wire bridges in the chip-carrier preventing the nanotubes on the chip from electrostatic discharge. **b),c)** Optical microscopy images of the bondpads and the marker system. **d)** AFM image of the top right nanotube transistor in **c)**.


[§]The wire bridges are removed directly after mounting the chip-carrier into the sample stick.

4.5   Preparation of graphene and few-layer graphite transport samples

In several basic aspects the production flow of graphene and few-layer graphite transport samples resembles the nanotube transport sample production: in both cases the sample material is deposited onto Si/SiO_2 chips, in both cases this deposition yields a random distribution of sample material on top of the chips, so that both suitable nanotubes and graphite flakes have to be looked for. Marker systems comprising geometrical symbols serve as references to locate the sample material. Furthermore electron beam lithography is used to pattern metal structures on top of the nanotubes/metallofullerene peapods as well as on top of the graphene/few-layer graphite flakes with sharp edges of the exposed structures and - if needed - 100 nm small electrode spacings.

However, there are a few, partially significant differences between preparing individual nanotube and graphene/few-layer graphite transport samples. The most outstanding distinction is the actual sample deposition onto the Si/SiO_2 chips. In the case of SWNTs and metallofullerene peapods, adsorption is done from dispersion, whereas for mono- and multilayers of graphite a dry transfer technique is chosen which literature refers to as *micromechanical cleavage* [No05a, No05b]. For this dry transfer of graphite flakes onto SiO_2 no surface functionalization of the silicon dioxide layer is needed. The deposition of graphene and few-layer graphite is described later in this chapter. Another difference in comparison to the nanotubes is that the shapes, sizes and positions of graphene and few-layer graphite flakes can be observed by optical microscopy, given that an appropriate SiO_2 thickness has been chosen. The visibility of a graphite flake being only one atomic layer thick by means of optical microscopy makes AFM investigation of graphene flakes mostly dispensable (if not details of the flake surface, flake substrate interactions or the electrical contacts subsequently put on the flake are to be investigated). Further, standard AFM is not capable to tell the number of layers of a graphite flake reliably due to water adsorbates between the SiO_2 and the graphite which alters the apparent flake height in the AFM image. Better ways to discriminate between mono-, bi- and multilayers of graphite are to apply HR-TEM (cp. chapter 4.7.1) or Raman spectroscopy (cp. chapter 4.7.3).

As in the nanotube case (cp. chapter 4.4), starting material for graphene transport sample production are highly doped 6" Si wafers, again with dry SiO_2 on top, but with 300 nm oxide thickness instead of 200 nm as for nanotubes. 300 nm silicon dioxide results in a bluish substrate surface color (Fig. 4.13b) favorable for identification of graphite monolayers by standard optical microscopy [Bla07, Abe07]. Like in the case of nanotube sample preparation, the substrates for graphene flake deposition are cut into 45x45 mm^2 substrate pieces, cleaned and provided with 100 graphene marker systems and 100 4-digit codes for identification purposes in the first electron beam lithography step. Thereafter, metallization with 5 nm Cr (as adhesive layer) and 25 to 30 nm Au and the lift-off process are carried out. Finally, the 45x45 mm^2 substrates are cut into
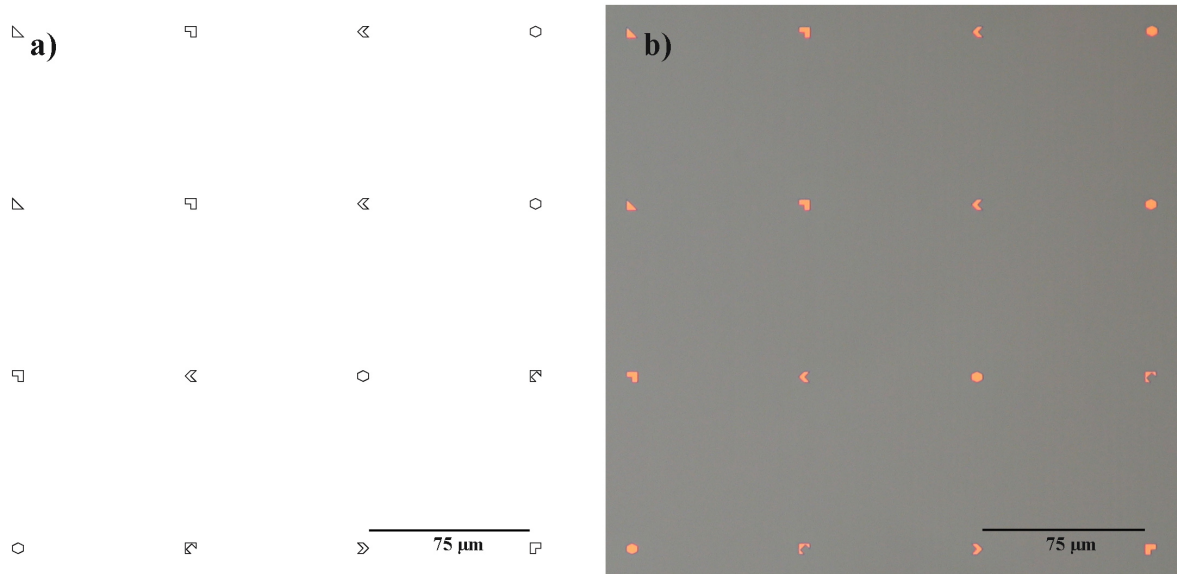
Fig. 4.13: Top right section (i.e. lines 1 to 4, columns 35 to 38) of the marker system for graphene deposition. The markers are 5x5 μm^2 in size and 80 μm apart (center-center distance). The top right section displays the structure of the graphene marker system: the 1st and 2nd line are identical, the 3rd line corresponds to the 2nd line shifted by 1 position to the left, the 4th line is the 3rd line shifted by 2 positions to the left and so on. Note that for each line shifted with respect to lines 1 and 2, the markers on the very left hand side of the chip, i.e. the ones left of column 1 (not displayed in the image), are moved to the very right end of the respective line. Due to this structure, each two markers in the same column and in adjacent lines tell the position within the total 3x3 mm^2 marker system. **a)** Design of the top right marker area section. **b)** Optical microscopy image of the corresponding area after patterning the markers onto a Si/SiO$_2$ chip with 300 nm silicon dioxide, metallization with 5 nm Cr and 25 to 30 nm Au, lift-off and cleaning.

4x4 mm^2 chips and cleaned with acetone, isopropanol and oxygen plasma as described in chapter 4.4. Figure 4.13 depicts the top right section of the approximately 3x3 mm^2 large graphene marker system both as design (Fig. 4.13a) and as optical microscopy image (Fig. 4.13b) after the cleaning process. Graphite flakes can have edge lengths of several 10 μm (Fig. 4.14d), consequently much more space between each two markers of the graphene marker system is needed than in the nanotube case where the respective spacing was only 8 μm (Figs. 4.7c,d). For the graphene marker system, a marker-marker spacing of 80 μm was chosen with each marker being 5x5 μm^2 in size (Fig. 4.13). In order to deposit as many graphene and few-layer graphite flakes within the marker area as possible, the graphene marker system is a 38 by 38 array of markers corresponding to a nearly 3x3 mm^2 marker system centered on each 4x4 mm^2 chip area. Since the graphite flakes are deposited randomly at arbitrary spots within the graphene marker system, there is no point in patterning the bondpads already in the first electron beam lithography step. Instead, suitable flakes are located later on with respect to the marker system and the whole electrode structure including the bondpads is written around the target flakes by electron beam lithography in the second lithography process described later in this chapter.

A desired feature of a marker system, which is fulfilled in the nanotube case (Figs. 4.7c,d), is that one exactly knows the position when observing one marker. This feature is impossible to realize in the case of the 38 by 38 array of graphene markers unless one thinks of 1444 different symbols. Thus the requirements were lowered, the new objective was to know the position when observing two markers in the same column and in adjacent lines of the graphene marker system. This requirement can be met if one picks 38 markers m_k with $k \,\epsilon\, \{1, 2, ..., 38\}$ and defines the array element a_{ij}, where a_{ij} should represent the marker in the ith column and the jth line ($i, j \,\epsilon\, \{1, 2, ..., 38\}$) of the graphene marker system, to be:

$$a_{ij} = m_{(\chi \bmod 39)+\eta} \;\; \text{with} \;\; \chi \;\; = \;\; i + \left\{ \left(\frac{(j-2)(j-1)}{2} \right) \bmod 38 \right\},$$

$$\eta \;\; = \;\; \begin{cases} 0 \text{ for } \chi < 39 \\ 1 \text{ for } \chi \geq 39 \end{cases}. \tag{4.1}$$

Equation 4.1 means the following: the first line of the graphene marker system comprises 38 markers, the second line is identical with the first line. Further, the third line of markers emanates from the second by copying line 2, shifting all markers 1 position to the left and moving the marker of the new third line, which is left of column 1, to the last position (column 38) in the third line. The fourth line results from the third line by copying the third line, shifting the markers of the copied line by 2 positions to the left and subsequentially moving the markers which are left of column 1 to the end of the fourth line (i.e. to columns 37 and 38). This shifting process is repeated for all further lines until line 38, the shift being increased by 1 position to the left per line. As a result of the non-constant left-shift, the combination of any two symbols in the same column and in adjacent lines does not appear twice within the graphene marker system area and such provides a distinct position information.

Having discussed substrate preparation and some special features of the graphene marker system, the rest of the chapter addresses graphene and few-layer graphite flake deposition onto the Si/SiO$_2$ chips as well as patterning electrical contacts on top of the flakes.

Following the route of *micromechanical cleavage* [No05a, No05b], a highly oriented pyrolitic graphite (HOPG) [Bla62, Moo62] block, ZYA grade, is pressed against the sticky side of a *Nitto tape* ribbon and removed, leaving a freshly cleaved, relatively thick graphite layer on top of the tape. By multiple folding, i.e. by repeatedly bringing the sticky tape with the attached HOPG layer into contact with another gluing area of the tape ribbon and detaching the two sticky spots of the same ribbon again, the originally thick HOPG layer glued onto the Nitto tape ribbon is thinned down further and further resulting in relatively thin graphite flakes well spread across the *Nitto tape* surface. The freshly cleaned Si/SiO$_2$ chips with 300 nm thick silicon dioxide layers are firmly pressed against the sticky side of the *Nitto tape* with the well distributed graphite flakes on its top. The density of flakes on the chips depends on the distribution of the graphite flakes on the tape which

had been used for adsorbing flakes on the chips and can be varied to a certain extent by changing the flake density on the tape ribbon. After removing the chips from the tape, the chips are inspected by optical microscopy looking for graphene mono- and bilayers.

Graphite layers of different thicknesses are adsorbed onto the Si/SiO_2 chips with the vast majority of the flakes being many layers thick and appearing as dark bluish areas in optical microscopy. Typically, one can find 1 to 2 graphene flakes per 3x3 mm^2 marker system, which appear as hardly visible, faint structures. Quite often graphite mono- and bilayers are sticking out of larger and thicker graphite aggregations. If these protruding flakes are large enough and positioned in an advantageous angle they might be still electrically contacted for transport and QHE measurements, however, isolated and large graphene mono- and bilayers are optimum for this purpose, but are found only rarely.

Figure 4.14[†] displays exemplary optical microscopy images of graphene monolayers on top of Si/SiO_2 chips (300 nm SiO_2). In the overview images (Figs. 4.14a,c), the faint graphene monolayers are hardly visible. The close-up images of the graphene flakes (Figs. 4.14b,d)[†] with insets with changed contrast/brightness settings for better visibility display the graphene monolayers clearly. The graphene flake in figure 4.14d[†] is fairly large compared to the usually found graphene monolayers, which have typical edge lengths of about 5 μm. After locating suitable graphite flakes, the contacts and bondpads for electrical transport and QHE measurements on the graphene and few-layer graphite samples are patterned within the second electron beam lithography process. Technically this e-beam process is nearly identical with the lithography process introduced in chapter 4.4. The only differences are first, that within the second e-beam lithography in the graphene process, the bondpads have to be written, since - in contrast to the nanotube case - every graphene flake needs a different bondpad configuration and second, instead of AuPd (as for nanotubes), for graphene and few-layer graphite samples Cr/Au is chosen as contact material (approx. 5 nm Cr, 25 to 30 nm Au). Figure 4.15[†] shows a graphene double-layer (at position p4) before the second electron beam lithography process. Optical microscopy images of the same flake after lithography, metallization and lift-off are included in figure 4.16[†] at different magnifications. Six Cr/Au contacts have been patterned onto the flake at position p4 (Fig. 4.16d)[†], two of which serve as source and drain electrodes during transport or QHE measurements, the other four electrodes are used as longitudinal voltage and Hall voltage probes during QHE investigations. The contacts are connected to the bondpads by Cr/Au leads, which increase in width as they come closer to the bondpads (Figs. 4.16c,b,a)[†]. Upon completion of the electron beam lithography processes and the respective metallization and lift-off steps, the transport/QHE graphene devices are glued into chip-carriers and wire-bonded as described in chapter 4.4.
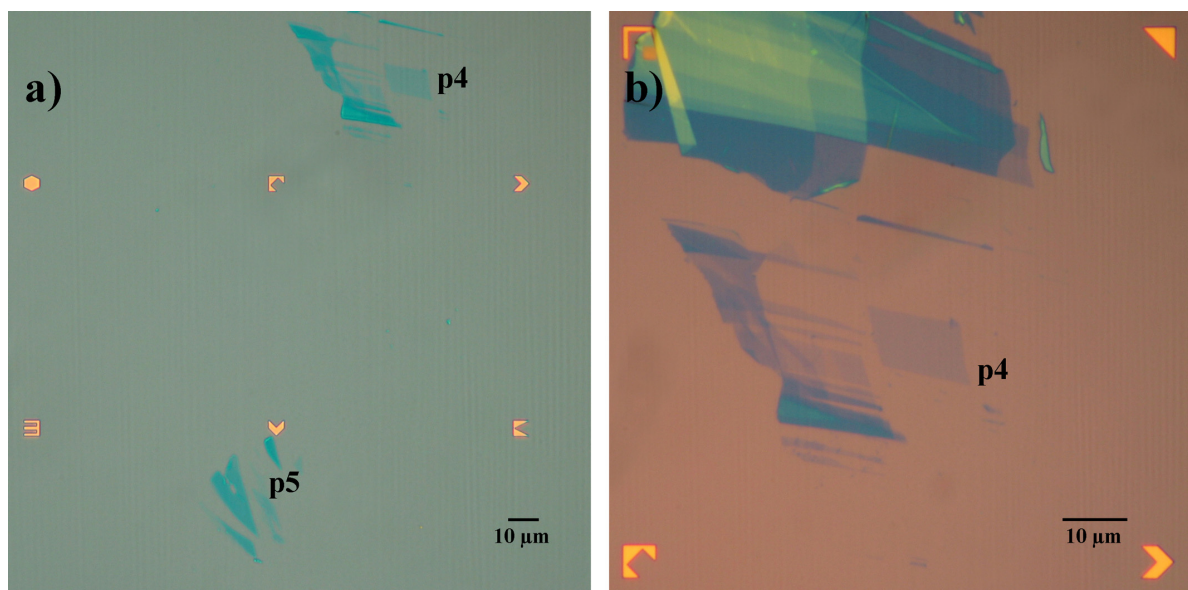

[†]Note that the original color of a Si/SiO_2 chip with 300 nm thick SiO_2 resembles the bluish color in figures 4.13b, 4.14a, 4.14c, 4.15a, 4.16a, 4.16b and 4.16c. The deviations from this color in figures 4.14b, 4.14d, 4.15b and 4.16d are due to automatic parameter settings of the digital CCD camera used to record these images.
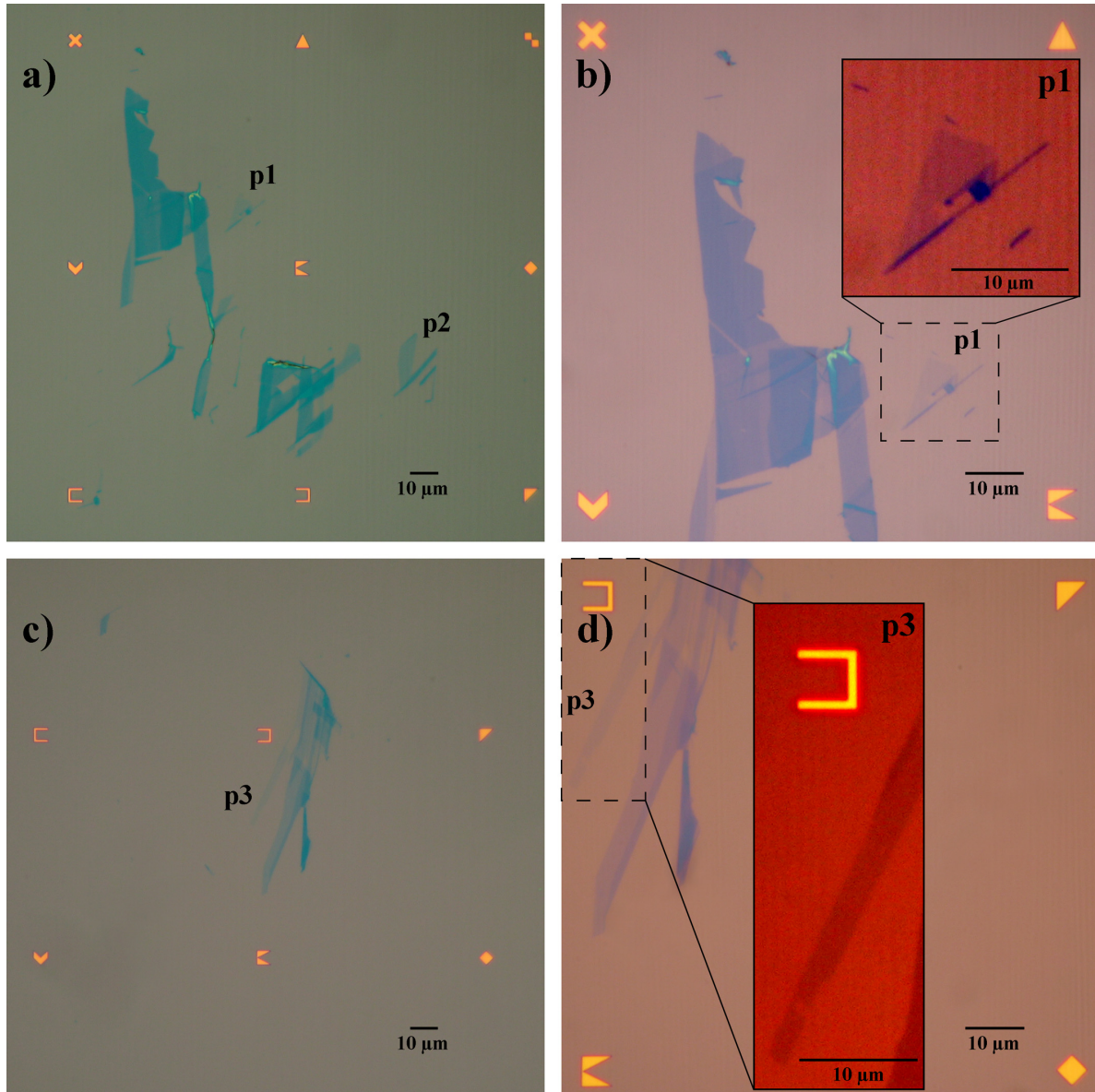
Fig. 4.14: a) Optical microscopy image of graphite flakes on a Si/SiO$_2$ chip (300 nm SiO$_2$) patterned with the graphene marker system. The large, dark blue structures are thick graphite flakes giving rise to strong contrast in optical microscopy. There are thinner graphite layers located at positions p1 and p2. The flake at p1 is a graphene layer appearing only as a faint shadow, whereas the p2 flake is a double-layer generating slightly more contrast. **b)** Close-up of the area around position p1 with the graphene monolayer[†] Inset: a further close-up of position p1 with altered contrast and brightness settings to make the graphene monolayer clearly visible. **c)** Another example of a graphene monolayer, which is positioned at p3 next to some thicker graphite structures. **d)** Close-up of the area in vicinity of position p3. The graphene flake at p3 is approx. 30 μm long in contrast to typically received graphene flake edge lengths of about[†] 5 μm. Inset: magnification of the graphene monolayer at position p3 depicted with different contrast and brightness settings for better visibility.

[†]Note that the original color of a Si/SiO$_2$ chip with 300 nm thick SiO$_2$ resembles the bluish color in figures 4.13b, 4.14a, 4.14c, 4.15a, 4.16a, 4.16b and 4.16c. The deviations from this color in figures 4.14b, 4.14d, 4.15b and 4.16d are due to automatic parameter settings of the digital CCD camera used to record these images.

Fig. 4.15: a) Optical microscopy image of a graphene double-layer at position p4 on a Si/SiO_2 chip with 300 nm SiO_2 before the electron beam lithography process. **b)** Close-up view of **a)**.[†]

[†]Note that the original color of a Si/SiO_2 chip with 300 nm thick SiO_2 resembles the bluish color in figures 4.13b, 4.14a, 4.14c, 4.15a, 4.16a, 4.16b and 4.16c. The deviations from this color in figures 4.14b, 4.14d, 4.15b and 4.16d are due to automatic parameter settings of the digital CCD camera used to record these images.
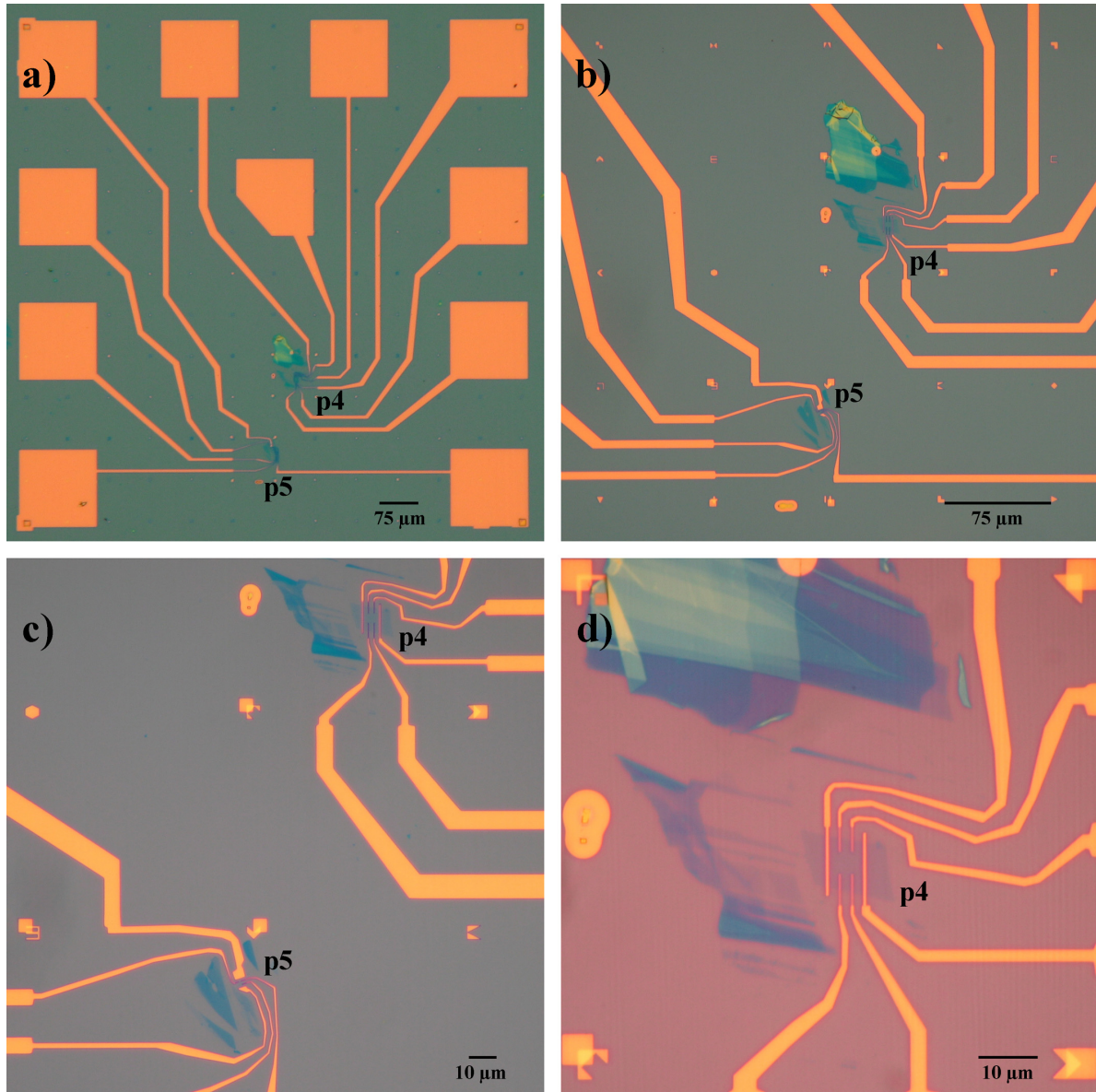
Fig. 4.16: The same double-layer graphene flake (at position p4) as in figure 4.15 after lithography, metallization and lift-off. **a)** Low magnification optical microscopy image of the double-layer flake at position p4 and a further flake at position p5, both being provided with Cr/Au contacts and the respective bondpads for magnetotransport and QHE measurements. **b),c)** Close-ups of the two contacted graphene flakes. **d)** High magnification optical microscopy image of the double-layer graphene flake at position p4. The two electrodes completely crossing the flake are the source and drain electrodes, the other four electrodes are used to probe the longitudinal voltage V_{xx} and the Hall voltage V_{xy}.[†]

[†]Note that the original color of a Si/SiO$_2$ chip with 300 nm thick SiO$_2$ resembles the bluish color in figures 4.13b, 4.14a, 4.14c, 4.15a, 4.16a, 4.16b and 4.16c. The deviations from this color in figures 4.14b, 4.14d, 4.15b and 4.16d are due to automatic parameter settings of the digital CCD camera used to record these images.

4.6 Rig for electrical transport measurements

A rig for electrical transport measurements has been set up in the framework of this PhD project, including the development of a comprehensive data acquisition software.

The electrical transport rig comprises an Oxford ^{4}He bath cryostat, electronic units like voltage sources, multimeters and lock-in amplifiers (details see below) and furthermore two sample sticks. One out of these two sample sticks is a standard sample stick, i.e. the plane in which the sample is mounted is perpendicular to the magnetic field of the cryostat. The second sample stick is equipped with an uniaxial rotational piezo drive[§] which facilitates rotations of the samples at cryogenic conditions with respect to the magnetic field provided by the superconducting solenoid of the cryostat.

In the following, details of the transport rig setup and the rotational sample stick are discussed. The chapters 4.6.1 to 4.6.4 contain further information regarding the data acquisition software *ViDi* and the setup of the electronic units for particular measurements. For detailed information concerning the *ViDi* software also refer to appendix A.1.

The schematic setup of the electrical transport rig is depicted in figure 4.17.

The core piece of equipment is a ^{4}He bath cryostat allowing for electrical transport measurements in the temperature range $1.7\ \text{K} \leq T \leq 295\ \text{K}$ at magnetic fields $B \leq 10\ \text{T}$. The central part of the cryostat is the *variable temperature inset* (VTI), which is thermally isolated from the ^{4}He reservoir[‡] by the VTI vacuum. Adjusting the needle valve between the ^{4}He reservoir and the VTI, the VTI can be provided with helium or completely be separated from the main reservoir. The VTI is attached to a rotary pump by which the He gas pressure in the VTI can be reduced. As well as the ^{4}He reservoir, the rotary pump is connected to the He recovery line. The cryostat and the measurement system are electrically separated from both the rotary pump and the He recovery line by isolating plastic tubes represented by short parallel solid lines interrupting the tubes to the pump and the recovery line in figure 4.17. A superconducting solenoid, depicted in cross section as two black rectangles in figure 4.17, is positioned in the ^{4}He bath, enclosing the end part of the VTI and the VTI vacuum. Thus, the magnetic field of the solenoid is oriented axially to the cylindric *variable temperature inset*, i.e. it is aligned along the axis of a mounted sample stick (Fig. 4.17). A liquid nitrogen volume sandwiched between two vacua [*outer vacuum chamber* (OVC) and *inner vacuum chamber* (IVC)] thermally isolates the ^{4}He reservoir from the ambience.

The superconducting magnet of the cryostat is powered by an Oxford PS120-10 power
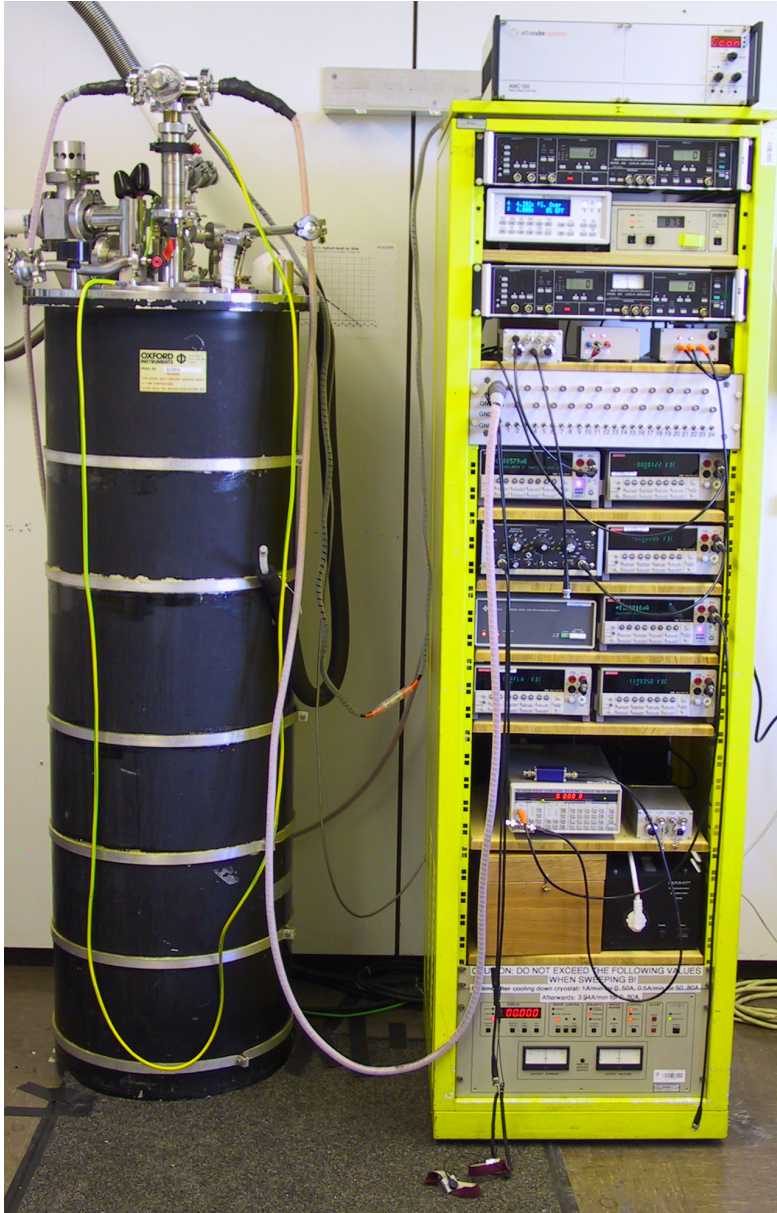

[§]The rotational axis is parallel to the surface normal of the sample and perpendicular to the magnetic field of the cryostat, i.e. the magnetic field is in-plane with respect to the sample surface for any position of the rotational piezo drive.

[‡]The filling level of the ^{4}He reservoir is monitored with an Oxford He level meter.

supply linked via RS-232 bus to the measurement computer of the transport rig. Furthermore, the ground potential, which the magnet power supply is connected to via the own power line, serves as reference potential for the whole electrical transport rig and is denoted by **ref. pot. I** in figure 4.17. It is of utmost importance to connect all components involved in the measurement process to the same reference potential in order to avoid ground loops. To achieve this, all electronic units have to be isolated from their ground potentials provided by the power lines by utilizing isolating transformers (Fig. 4.17). The reference potential **ref. pot. I** is passed from the magnet power supply to the cryostat, from the cryostat to the sample stick and further from the sample stick via the shielding of the data cable to the *central switch box*, which distributes the reference potential to the electronic units involved in the respective measurement process (cp. Figs. 4.21 - 4.24).

The sample stick is inserted into the VTI volume from top as displayed in figure 4.17. During the insertion/removal process, He gas overpressure is put on the VTI to avoid ambient gases entering the VTI volume. The sample stick is fixed at the top of the VTI in a vacuum-tight and electrically isolating way by a specially designed clip collar. Both sample sticks have openings in their cladding tubes to form one volume with the VTI when being inserted. To monitor and change the VTI temperature, a temperature sensor and a heating wire are mounted in each sample stick. For the case that measurements should be done at 4.2 K, the needle valve between VTI and ^{4}He bath is opened and the VTI is completely flooded with liquid ^{4}He. Higher VTI temperatures can be achieved by proper needle valve setting and controlled heating. Temperature readout and temperature control are done by the Lakeshore temperature controller model 332, which is connected to the sample stick via one electrical cable including the leads for the temperature sensor and the heater. The temperature controller is addressed by the measurement computer via GPIB bus (dark blue cable in figure 4.17). Both sample sticks are designed to accommodate a 20 pin chip-carrier (Fig. 4.12a), the holder for which is mounted close to the bottom of each sample stick. The electrical signals of the 20 pins of the chip carrier holder are passed to the sample stick top and further by a 20 channel screened data cable to the so-called *central switch box*. The *central switch box* connects each of the 20 data channels to one out of 20 BNC sockets on its front panel, which can be further connected to the electronic units during the electrical transport measurements (cp. Figs. 4.21 - 4.24). Moreover, each of the 20 channels can be switched to ground (i.e. to the system reference potential **ref. pot. I**) or to floating individually by respective switches mounted on the front panel of the *central switch box* (Fig. 4.17). All 20 pins have to be grounded during mounting/unmounting a new chip-carrier into the chip-carrier holder of the sample stick to prevent damage due to electrostatic discharge. In comparison to the standard sample stick, the rotational sample stick additionally requires a cable connection to the *piezo step controller ANC150 (attocube systems)* and a connection (*stopper signals* in Fig. 4.17) to the measurement computer, which checks whether the rotating plate of the rotational sample stick has reached one of the stoppers. More details concerning the rotational sample stick and the piezo controller are found below in this chapter.

Fig. 4.17: Schematic of the electrical transport rig which was used for the transport investigations within this project. The central component of the rig is a ^{4}He bath cryostat allowing measurements in the temperature range 1.7 K $\leq T \leq$ 295 K at magnetic fields $B \leq$ 10 T. Electronic units like voltage sources, multimeters, lock-in amplifiers and a current preamplifier are used for the electrical transport measurements. Further details regarding the transport rig are given in the main text.

Fig. 4.18: Photograph of the rig for electrical transport measurements (without measurement computer). The rotational sample stick is inserted into the bath cryostat.

As for the electronic units, the transport rig includes two Keithley 2400 voltage/current sources, four Keithley 2000 digital multimeters, one Ithaco 1211 current preamplifier, two EG&G 5210 lock-in amplifiers, one DS 345 function generator, one optocoupler and one voltage adder. As already mentioned before, all these units must be floating, i.e. decoupled from their original reference potential by isolating transformers to ensure that the overall transport rig has one common reference potential. The Keithley units and the temperature controller are connected to the measurement computer via GPIB interface. A *GPIB isolated bus expander* placed in the GPIB line between the electronic units and the measurement computer isolates the measurement computer reference potential **ref. pot. II** from the system reference potential **ref. pot. I**. The function generator is used to generate low-frequency sinusoidal voltage signals for differential conductance measurements (cp. chapter 4.6.3) or QHE measurements (cp. chapter 4.6.4). The lock-in amplifiers utilized

for these measurements need a square wave reference signal (with frequency and phase information) as input, which is delivered by the *ref out* output of the function generator and passed through the optocoupler (Fig. 4.17)[‡‡] to the lock-in amplifiers. The optocoupler branches the reference signal and galvanically separates the function generator from the two lock-in amplifiers.

All measurements are carried out using a measurement computer (Fig. 4.17). It controls/reads all Keithley voltage/current sources, the Keithley multimeters and the temperature controller via GPIB bus (dark blue lines in figure 4.17), furthermore it controls the power supply of the superconducting magnet of the cryostat and the *piezo step controller* via RS-232 bus (green lines in figure 4.17), which is isolated from the computer reference potential **ref. pot. II**. Finally, the measurement computer also reads out the stopper signals of the rotational sample stick.

A photograph of the rig for electrical transport measurements (without measurement computer) is displayed in figure 4.18.

To conclude the first part of this chapter, further details regarding the rotational sample stick shall be discussed. The core piece of the rotational sample stick is a one-axis rotational piezo drive (*inertial rotator ANR50, attocube systems*) mounted close to the bottom of the sample stick as depicted in figure 4.19. The rotational piezo drive consists of a static part with trapezoidal profile, which incorporates the driving piezos, and a rotatable metal disc with the rotational axis being perpendicular to the disc. The external magnetic field is aligned along the sample stick axis, i.e. it is oriented perpendicularly to the rotational axis of the piezo drive. Thus, the magnetic field of the cryostat solenoid is always in-plane with respect to the rotatable disc and the sample, which is mounted in parallel to the disc. A plastic plate, on top of which the holder for the chip-carrier is mounted, is attached to the top of the rotatable metal disc (Fig. 4.19). The chip-carrier holder accommodates 20-pin chip-carriers as displayed in figure 4.12a, the 20 respective thin, isolated electrical leads are twisted to form one 20-lead wire (Figs. 4.19c,d). This 20-lead wire is fixed on top of the green plastic plate mounted on top of the rotatable disc. Hence, the wire has to be bent when the disc is rotated by the piezos. In figures 4.19a-d, the rotatable disc is depicted in $\vartheta = 0°$ position, this is the position, where the 20-lead wire is straight. Two copper stoppers mounted on the bottom side of the green plastic disc (Figs. 4.19b,d) limit the movement of the rotatable disc to $\pm 100°$, i.e. each $100°$ in clock- and counterclockwise rotation. The whole rotatable disc including the two copper stoppers is kept on reference potential **ref. pot. I**. In the case that the maximum angular deflection is reached ($\vartheta = \pm 100°$), one of these two stoppers hits a two-pole copper counter-stopper fixed at the sample stick base plate (Figs. 4.19b,d). The counter-stopper is cylindric, however it is cut axially into two half cylinders electrically isolated from each other forming the two


[‡‡]The double lines (with one brown line) in figures 4.17, 4.21, 4.22, 4.23 and 4.24 represent coaxial cables with the brown lines being the shielding.

electrodes of the counter-stopper. In this way, it can be electrically detected, which of the two stoppers of the rotating plate hits the counter-stopper. The maximum angular deflection of $\pm 100°$ is large enough to align any straight nanotube lying in an arbitrary angle on the sample surface axially or perpendicularly to the in-plane external magnetic field.

The movement of the rotational piezo drive is controlled by the combination of a *piezo step controller ANC150 (attocube systems)* and the measurement computer. The *piezo step controller* generates an AC saw tooth voltage to drive the piezos of the *inertial rotator* based on the *slip-stick principle*. Typical values for the AC peak-to-peak voltage $V_{\mathrm{ANC150,pp}}$ and the frequency f_0 are $V_{\mathrm{ANC150,pp}} = 40$ V and $f_0 = 500$ Hz at T = 4.2 K. The *piezo step controller ANC150* has its own reference potential **ref. pot. III** and is connected with the rotational sample stick via two shielded cables (Fig. 4.17). Note that the reference potential **ref. pot. III** is strictly separated from the rest of the transport rig. Within the rotational sample stick, the power lines for the piezos are running inside a thin metal tube which ensures the shielding against all other components and cables. As already mentioned, the *piezo step controller* can be controlled by the measurement computer via RS-232 bus. Moreover the computer is equipped with a digital input-output card, connected to a TTL (transistor-transistor logic) card reading the electrical potentials of the two semi-cylindrical contacts of the copper counter-stopper. As soon as one of the two stoppers mounted on the bottom side of the green disc (on top of the rotatable disc) touches the corresponding counter-stopper electrode, the respective stopper puts the counter-stopper electrode from floating to reference potential **ref. pot. I**, which is detected by the TTL card. Subsequently the corresponding bit of the input-output card is changed indicating that the respective stopper hit the counter-stopper.

In order to make the *inertial rotator* move to a specific angle at 4.2 K, first the number of piezo steps is counted which corresponds to the rotation from stopper to stopper, i.e. which corresponds to a rotational angle of $200°$. Thereafter the number of steps for the movement from one stopper to the target angle can be calculated easily. However, one has to consider that the rotational piezo drive does not rotate freely, but is connected to the sample stick by the 20-lead wire which exerts external, position-dependent torque onto the rotator during the wire bending. That is why additional calibration runs were needed to check offset angles and the positioning precision of the piezo drive for various target angles. In addition to the remaining uncertainties in the positioning, there can be errors when estimating the offset angle between the edge of the chip and the edge of the chip-carrier which the chip was glued into. Another error source can be the estimation of the angle in which a nanotube, a metallofullerene peapod or a graphene/few-layer graphite flake is lying with respect to the marker system. Taking into account these possible error sources for angle setting, one comes to the conclusion that a realistic error estimation results in $\Delta\vartheta = \pm 5°$ for the typical and $\Delta\vartheta = \pm 10°$ for the worst case. Since the temperature significantly influences the rotational behavior of the *inertial rotator*, all angles were set at 4.2 K.
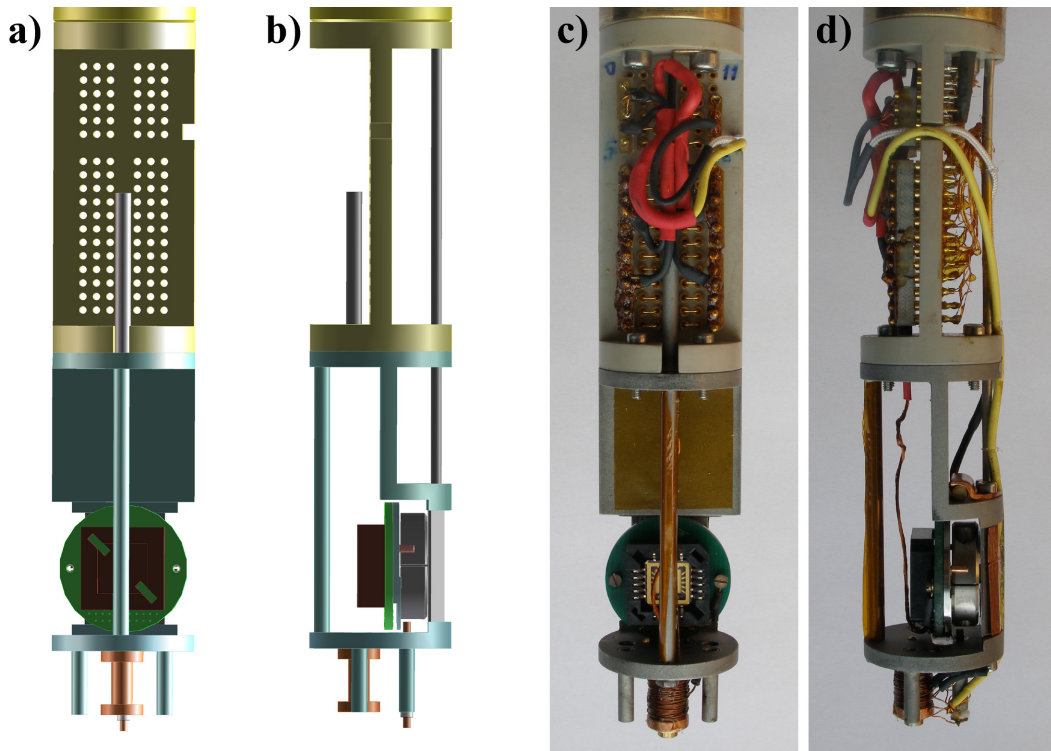
Fig. 4.19: The lower end part of the rotational sample stick without cladding tube depicted as **a)** CAD drawing (top view, without wiring), **b)** CAD drawing (side view, without wiring), **c)** photograph (top view), **d)** photograph (side view). The core piece of the rotational sample stick is the one-axis rotational piezo drive (*inertial rotator ANR50, attocube systems*) consisting of a static part with a trapezoidal profile and a rotatable metal disc. The rotational axis is perpendicular to the metal disc, i.e. perpendicular to the external magnetic field along the sample stick axis. On top of the rotatable disc a further green plastic disc is attached, onto which a 20-pin chip-carrier holder is mounted. The 20 pins are connected to 20 very thin, electrically isolated leads which are twisted to form one 20-lead wire, that can be seen best in the side view photograph **d)**. In **c)**, most of this wire is hidden behind the front pole. If the metal disc begins to rotate, the green disc and the chip-carrier holder rotate along, the 20-lead wire starts to be bent smoothly. In **a)-d)**, the rotatable disc is depicted in $\vartheta = 0°$ position, at this position, the 20-lead wire is straight. Maximum angular deflection is $\pm 100°$. Two copper stoppers are mounted onto the bottom side of the green plastic plate, which stop the movement after $100°$ of clock-/counterclockwise rotation, since one of them touches the two-pole counter-stopper mounted statically to the sample stick base plate (**b),d)**).

4.6.1   Data acquisition software *ViDi*

During this PhD project, a comprehensive data acquisition software named *ViDi* has been developed to conduct electrical transport measurements. The software, which was programmed using *LabView 6i*, is discussed in this chapter and in appendix A.1, which contains more detailed information with respect to the source code.

The *ViDi* software features 33 measurement modes, 16 of which are designed for 2-probe and another 15 for 4-probe measurements. Further 2 measurement modes are dedicated to QHE lock-in investigations. In principle, the measurement modes for 2-probe, 4-probe and QHE measurements work in a similar way, so the following description as well as the complementary discussion in appendix A.1 is restricted to the case of a 2-probe measurement.

The 16 2-probe measurement modes differ from each other by a varied combination of parameters to be swept and to remain constant throughout the measurement process. Moreover there are two kinds of how to sweep a parameter, e.g. the gate voltage V_g can either be swept from a minimum to a maximum value (or vice versa) or it can be swept in a loop, beginning with 0, sweeping to $V_{g,max}$ to $V_{g,min}$ and back to 0 (or vice versa). Performing loop and especially repeated loop measurements reveals potential hysteresis effects which might be present in the sample investigated. In the case of the 2-probe measurement modes, the source-drain current I_{sd} and possibly the differential conductance dI_{sd}/dV_{sd} is/are measured in dependence of the parameters source-drain voltage V_{sd}, gate voltage V_g and magnetic field B (the temperature is not computer-controlled, but adjusted manually).

An example for a standard measurement mode amongst the 2-probe modes is to measure the $I_{sd}(V_{sd})$ characteristics at constant gate voltage V_g, where V_{sd} is swept from minimum to maximum or vice versa. A second mode would be fairly identical with the exception, that V_{sd} is swept in a loop. Another two standard modes are to measure $I_{sd}(V_g)$ at constant V_{sd}, with V_g swept from minimum to maximum (or vice versa) or in a loop. Besides the standard modes there are more complex ones, which combine sweeping of different parameters. One example is the measurement mode required to record Coulomb blockade diamonds (cp. chapter 3.2.3, chapter 6 and chapter 7), where $I_{sd}(V_{sd}, V_g)$ and $dI_{sd}/dV_{sd}(V_{sd}, V_g)$ data are acquired. In this mode, the source-drain voltage V_{sd} is swept from the minimum to the maximum value with the gate voltage V_g being gradually increased after every V_{sd} sweep. Obviously there are several possible combinations how to sweep parameters in these combined measurement modes, details shall be discussed in an exemplary way just for one of these combined modes in the rest of this chapter and mainly in the appendix A.1. The measurement mode which shall be discussed more precisely is mode 13 (cp. Fig. 4.20), in which the channel current I_{sd} at fixed V_{sd} is measured as a function of the gate voltage V_g, which is swept in loops. After each V_g loop, the magnetic field B is stepwise increased from B_{min} to B_{max} (or decreased from B_{max} to B_{min}).

A screenshot of the ViDi measurement software (version 1.70) panel during a run in mode 13 is depicted in figure 4.20. The most important functions and features of the *ViDi* panel will be described in the following. The large green button on the left hand side is the main switch to toggle between the 33 measurement modes - in this case, mode 13 is selected. In the top left hand area, there are multiple input boxes for entry of parameters. In the first line, all parameters concerning V_{sd} should be entered, the second line is assigned to the I_{sd} parameters[†], the third line to the V_g and the fourth line the B parameters. In the case shown in figure 4.20, the source-drain voltage V_{sd} was set to 200 mV, the gate voltage V_g is swept in loops between -5 and 5 V in 1000 steps with a delay of 100 ms and the magnetic field B is gradually increased from B_{min} = -10 T to B_{max} = 10 T in 10 steps with a delay of 20 s. Below the input boxes are further boxes to save user comments, to enter the file name of the output file, to select GPIB addresses of the used measurement units and to adjust the sensitivity of the used current preamplifier. At the middle right hand side there is a *Quicksweep* knob allowing to set the voltage/current sources stepwise to given parameters without recording data and a *STOP* button to stop the measurement process. Approximately in the middle of the bottom side there are output boxes which display the up-to-date temperature and magnetic field values. In the case displayed in figure 4.20, the temperature was 4.148 K (the real temperature was 4.2 K, the small offset is due to a not negligible magnetoresistance of the Cernox temperature sensor) and the current magnetic field was -10 T.

Three graphical output windows are integrated into the *ViDi* panel, namely the temperature vs. time window at the bottom and two output windows for the measured electrical characteristics at the right hand side. For a standard DC 2-probe measurement without recording differential conductance values, only the top output window at the right hand side is used as in figure 4.20, in which the $I_{sd}(V_g)$ characteristics measured for $B = -10$ T is being displayed. Having completed the $I_{sd}(V_g)$ curve for $B = -10$ T, the $I_{sd}(V_g)$ characteristics will be recorded for -8 T, -6 T, ..., 8 T, 10 T, whereat the output window is cleared before going to the next magnetic field value.

The diagram, i.e. the source code of the *ViDi* software comprises a common frame structure for all 33 measurement modes and 33 independent segments each including the specific routines for the respective mode. In appendix A.1, the diagram of *ViDi* 1.70 is representatively plotted[‡] and described for measurement mode 13.

[†]Line 2 is only needed for the 4-probe measurements, in which a current can be set. For 2-probe measurement modes like mode 13, input line 2 is inactive and greyed out.

[‡]except for subroutine diagrams
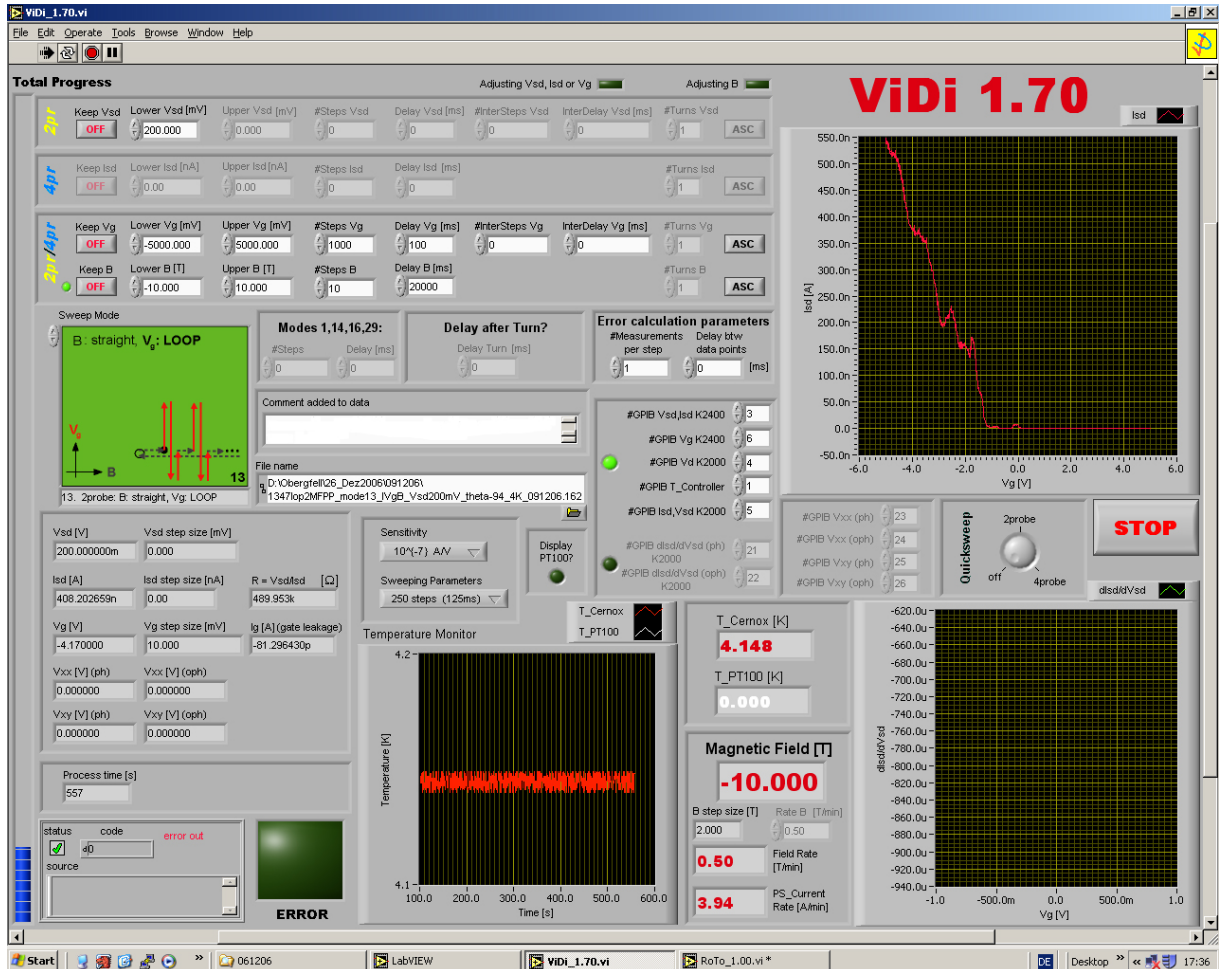
Fig. 4.20: Screenshot of the panel of the data acquisition software ViDi (here: version 1.70), which has been developed within this PhD project and was used for most of the electrical transport measurements presented in this work. ViDi 1.70 features 33 different measurement modes covering 2-probe measurements (with the possibility to run simultaneous differential conductance measurements), 4-probe measurements and QHE lock-in measurements. Details concerning the software can be found in the main text and in appendix A.1.

4.6.2 Setup for 2-probe DC measurements

The overall setup of the transport rig already has been discussed above and displayed in figure 4.17. This chapter describes the configuration of the electronic units to carry out 2-probe DC measurements on an individual SWNT, an individual metallofullerene peapod or a graphene/few-layer graphite flake.

A Si/SiO$_2$ substrate with the bulk Si serving as gate electrode shall be mounted into the sample stick of the measurement rig and a SWNT, a metallofullerene peapod or a graphene/few-layer graphite flake on top of the Si/SiO$_2$ chip shall be provided with a source and a drain contact.
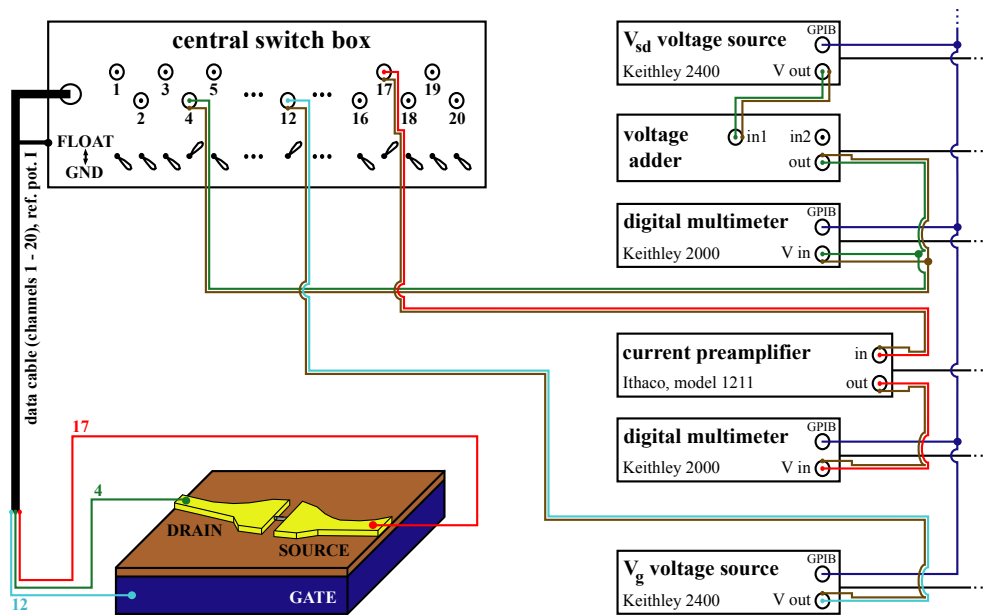
Fig. 4.21: Schematic of the experimental setup for 2-probe DC transport measurements on an individual SWNT, an individual metallofullerene peapod or a graphene/few-layer graphite flake. The double lines (with one brown line) represent coaxial cables with the brown line being the shielding. Further information is given in the main text.

Figure 4.21 depicts the schematic setup of the electronic units for a 2-probe DC measurement. In this example, the gate electrode is connected to pin 12, the drain contact to pin 4 and the source contact to pin 17. The double lines in figure 4.21 represent coaxial cables with the brown lines standing for the shielding. Recall that the *central switch box* is connected to the reference potential **ref. pot. I** of the measurement rig. The reference potential is distributed from the *central switch box* to the attached electronic units by the shieldings of the coaxial cables (i.e. the brown lines in Fig. 4.21). All pins except for pins 4, 12 and 17 are set to the reference potential. Pin 12 is directly connected to the gate voltage source. The source-drain voltage V_{sd} is provided by a second voltage source, passed to a voltage adder and from the voltage adder directly to pin 4, meaning to the drain contact of the mounted device. The applied V_{sd} voltage is monitored with a digital

multimeter. The source contact at pin 17 is connected to a current preamplifier, which measures the current I_{sd} and puts out a voltage, that results in the measured current I_{sd} when multiplied with the adjusted sensitivity μ (in A/V) of the current preamplifier. The voltage proportional to the current is measured with a further digital multimeter. The source contact potential is controlled by the current preamplifier to be identical with the reference potential **ref. pot. I**. Minor offsets (in the order of 100 μV) between the source contact potential and the reference potential **ref. pot. I** can come about due to the current preamplifier electronics. These offsets can be compensated for with the voltage adder. The voltage sources and digital multimeters are connected to the measurement computer by GPIB bus (dark blue lines in Fig. 4.21), the computer controls the electronic units and records the data.

4.6.3   Setup for 2-probe differential conductance measurements

The setup of the electronic units for differential conductance measurements in 2-probe configuration is based on the 2-probe DC measurement setup described in chapter 4.6.2. To measure the differential conductance dI_{sd}/dV_{sd} in addition to the 2-probe DC signals, the configuration depicted schematically in figure 4.21 is extended by a function generator, an optocoupler and a lock-in amplifier together with two digital multimeters to read the phase and out-of-phase channels of the lock-in amplifier.

Figure 4.22 schematically displays the setup of the electronic units in the case of 2-probe differential conductance measurements on an individual SWNT, an individual metallo-fullerene peapod or a graphene/few-layer graphite flake.

As described earlier, the lock-in amplifier receives its reference signal with frequency and phase information from the *ref out* output of the function generator. The reference signal has to be sent through the optocoupler in order to galvanically separate the function generator and the lock-in amplifier. Furthermore the function generator provides an AC sinusoidal voltage V_{AC} at the *signal out* output which is added to the DC source-drain voltage V_{sd} within the voltage adder. Usually the sinusoidal voltage V_{AC} is fed in the voltage adder via a 1/100 input, i.e. it is scaled down by a factor of 100 before being added to V_{sd}. The total voltage signal is passed to the drain contact, i.e. pin 4 in the example depicted in figure 4.22. If needed, the total voltage signal can be scaled down further by a voltage divider in order to reduce the noise level before being passed to the drain contact of the sample investigated (pin 4 in figure 4.22). After scaling down, a typical rms value of the AC excitation voltage for these measurements is $V_{AC,div}^{rms} = 100\,\mu$V. Typically, low frequencies f_{AC} were used, e.g. $f_{AC} = 13.43$ Hz or $f_{AC} = 21.5$ Hz[†]. Like in the case of a standard 2-probe DC measurement (Fig. 4.21), the source contact (pin 17 in figure 4.22) is connected with the current preamplifier, however, the output signal of the

---

[†]Frequencies being a multiple of the electricity network frequency 50 Hz may not be selected in order to keep the noise level low.

current preamplifier is branched to a digital multimeter measuring the DC component and to the lock-in amplifier measuring the AC component. The AC component of the output voltage of the current preamplifier corresponds to the variation of the current induced by the AC voltage $V_{\mathrm{AC,div}}^{\mathrm{rms}}$ superimposed on the DC voltage. In other words, the AC voltage measured by the lock-in amplifier is proportional to the differential conductance $dI_{\mathrm{sd}}/dV_{\mathrm{sd}}$ (for small $V_{\mathrm{AC,div}}^{\mathrm{rms}}$ values). The phase signal of the lock-in amplifier corresponding to the differential conductance of the sample investigated has to be calibrated applying the circuitry in figure 4.22 to several standard resistors (instead of the depicted sample) with precisely known resistance values.
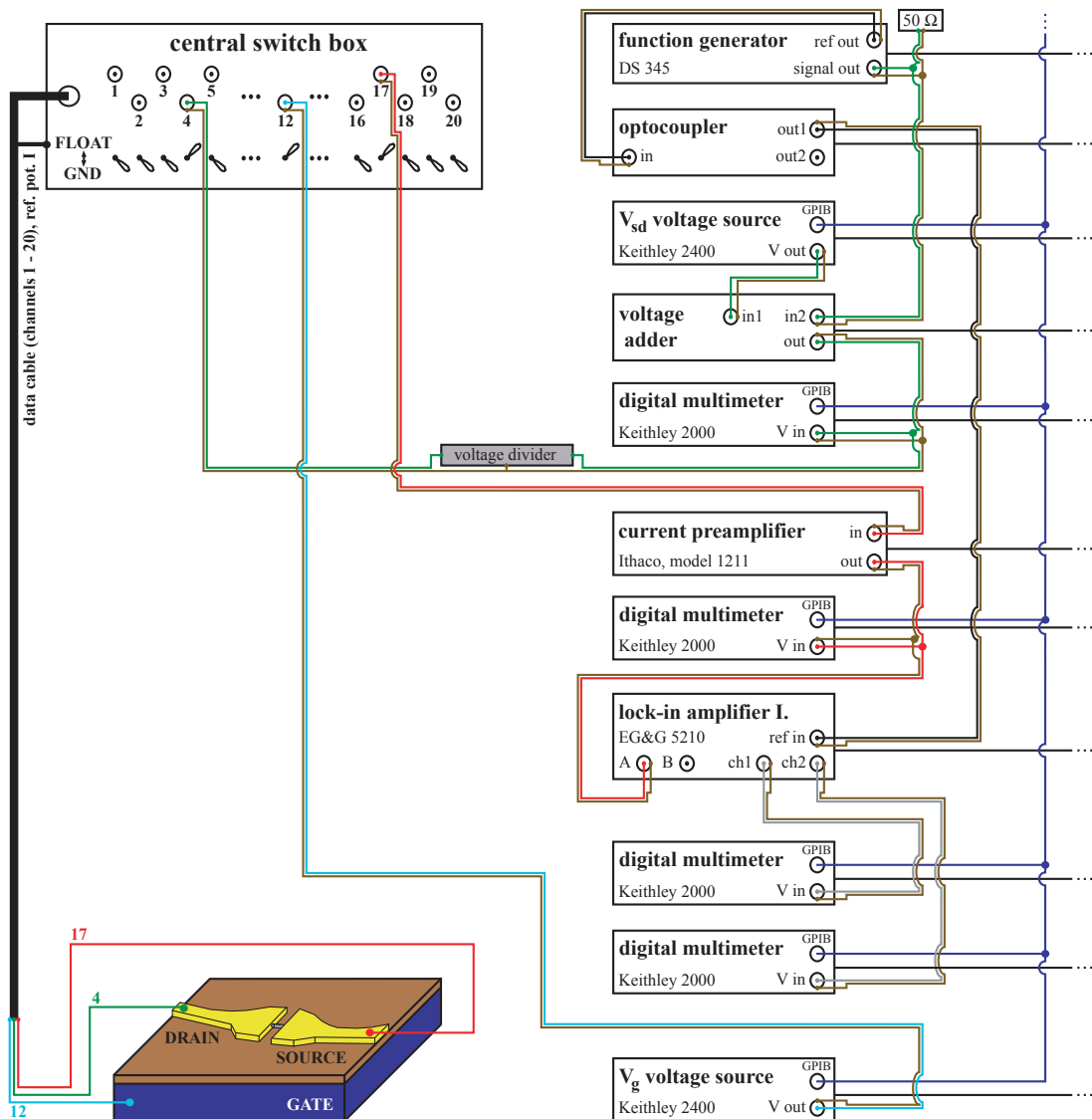
Fig. 4.22: Schematic of the experimental setup for 2-probe DC transport including differential conductance $dI_{\mathrm{sd}}/dV_{\mathrm{sd}}$ measurements on an individual SWNT, an individual metallofullerene peapod or a graphene/few-layer graphite flake. The double lines (with one brown line) represent coaxial cables with the brown line being the shielding. Further information is given in the main text.

4.6.4   Setup for quantum Hall effect measurements

For quantum Hall effect measurements on a graphene/few-layer graphite flake, two lock-in amplifiers are used to record the longitudinal voltage drop V_{xx} and the Hall voltage V_{xy}. The AC current driven through the sample is provided by a function generator (Fig. 4.24).

Before the actual QHE measurement, the AC current I_{AC} passed through the sample is to be adjusted. For doing so, all voltage probes are set to floating and an AC current is sent via a 1 MΩ resistor into the drain contact of a graphene/few-layer graphite flake on top of a Si/SiO$_2$ substrate (Fig. 4.23). The 1 MΩ serial resistance, which will be applied for the actual QHE measurement as well, is large in comparison to the 2-probe source-drain sample resistance and is used to keep the overall resistance and the current I_{AC} constant even if the sample exhibits variations of the longitudinal resistance. The source contact of the graphene/few-layer graphite flake is connected to the lock-in amplifier, which measures the AC current. The output current of the function generator is varied until the lock-in amplifier reads the desired AC current value. As mentioned before, the lock-in amplifier obtains its square wave reference signal from the *ref out* output of the function generator with the optocoupler in between the function generator and the lock-in amplifier.
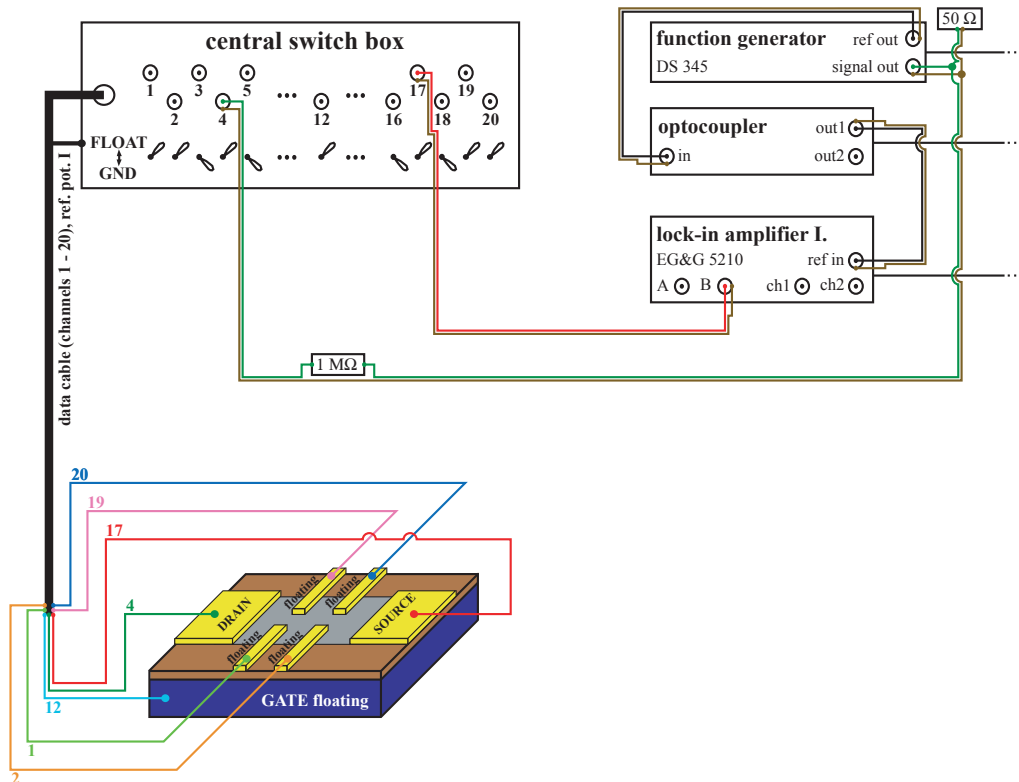
Fig. 4.23: Schematic of the experimental setup to adjust the AC current I_{AC} through a graphene/few-layer graphite flake before QHE measurements. The double lines (with one brown line) represent coaxial cables with the brown line being the shielding. Further information is given in the main text.
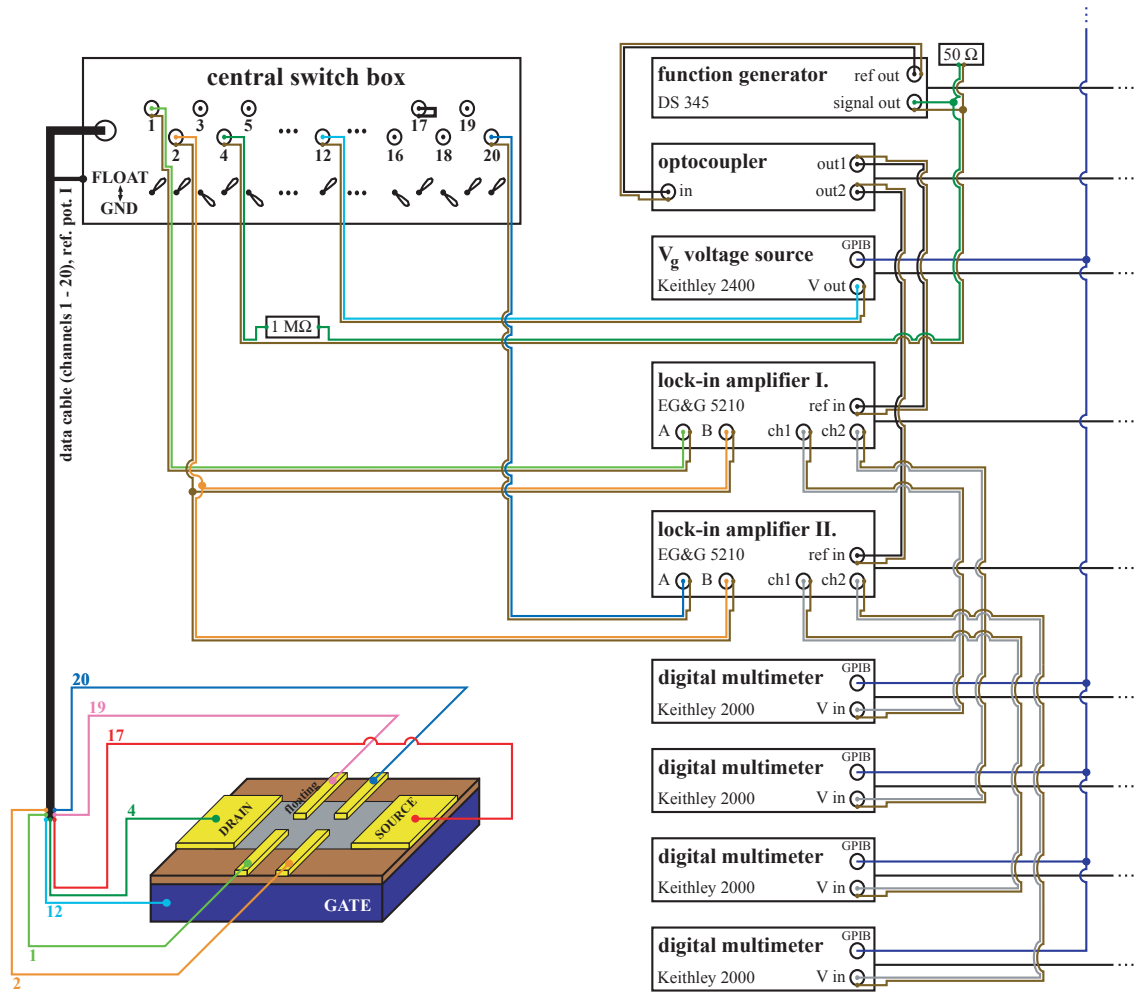
Fig. 4.24: Schematic of the experimental setup to measure the quantum Hall effect on a graphene/few-layer graphite flake. The double lines (with one brown line) represent coaxial cables with the brown line being the shielding. Further information is given in the main text.

Having adjusted the current to typically $I_{AC} = 100$ nA (rms) at the frequency $f_{AC} = 13.43$ Hz or $f_{AC} = 21.5$ Hz[†], the actual quantum Hall effect measurements on the graphene/few-layer graphite flake are carried out in the configuration schematically depicted in figure 4.24.

In the example in figure 4.24, the back gate electrode is connected with pin 12, the drain electrode of the graphene/few-layer graphite flakes is connected with pin 4, the source electrode with pin 17 and the electrodes to probe the longitudinal and the Hall voltage with pins 1, 2, 19 and 20. The double lines with one brown line stand for coaxial cables (the brown line represents the shielding). The *central switch box* is connected to the reference potential **ref. pot. I** of the measurement rig and distributes it to the attached electronic units via their coaxial cable shieldings. As described earlier, the two lock-in amplifiers are provided with square wave reference signals for the AC measurements by

---

[†]Frequencies being a multiple of the electricity network frequency 50 Hz may not be selected in order to keep the noise level low.

the *ref out* output of the function generator. The reference AC signals are galvanically separated between the function generator and the lock-in amplifiers by the optocoupler. The back gate contact is directly connected to the DC voltage source. The AC sinusoidal current I_{AC} is passed into the drain contact via a 1 MΩ resistor, the source contact is kept on the reference potential **ref. pot. I**. For the V_{xx} and V_{xy} measurements, two pairs of electrodes are needed, which share one common contact (pin 2 in figure 4.24). In this case, one of the four voltage probes remains floating (pin 19 in figure 4.24). The voltage signals from the two pairs of potential probes, i.e. from pin 1/pin 2 and pin 2/pin 20, are passed to the input sockets of the two lock-in amplifiers with the shared pin 2 being split. In figure 4.24, lock-in amplifier I. measures the longitudinal voltage V_{xx}, whereas lock-in amplifier II. reads the Hall voltage V_{xy}. Two digital multimeters are attached to each of the lock-in amplifiers reading out the lock-in phase and out-of-phase signals. Taking into account the sensitivity settings of the lock-in amplifiers, the V_{xx} and V_{xy} values can be deduced. The measurement computer, linked to the devices by GPIB bus (dark blue cable in figure 4.24), controls the V_{g} voltage source and reads the four digital multimeters.

4.7   Combination of electrical transport and further experiments on the same sample

Electrical transport experiments on individual single-walled carbon nanotubes have been carried out for about a decade (first publications: [Mar98, Tan98]), yet most of the research done in this respect focuses only on the transport measurements themselves and does not check whether the asserted individual SWNT serving as transistor channel indeed is an individual tube or not a bundle of SWNTs. Nanotube bundling due to van der Waals forces is a well known phenomenon and despite of using surfactants like SDS to de-bundle SWNTs, it happens easily that thin bundles are adsorbed on chip surfaces. Standard AFM, which mostly is used to image SWNTs on top of substrates, is incapable to tell whether the inspected tube is individual or e.g. a thin bundle of two tubes lying next to each other. That is because standard AFM provides rather good precision in z direction whereas the apparent size of a nanoscale object in the x-y plane is not precise since the AFM in-plane imaging severly depends on the tip diameter.

In the case of peapods an additional problem arises, namely to be sure that the tube investigated by electrical transport measurements indeed is filled with fullerenes. Usually similar filling procedures as the one explained in chapter 4.3 are used, however these methods typically do not to deliver 100% tube filling. Again, standard AFM measurements can not tell whether a tube is filled with fullerenes or metallofullerenes or whether it is empty.

As for graphene and few-layer graphite flakes, one question posed is how many graphene layers the flakes consist of. Here, already the evaluation of the apparent flake contrast in optical microscopy gives hints, whether one deals with a mono- or a bilayer of graphene (cp. Fig. 4.14d and Fig. 4.15b), but this information gained by optical microscopy is not absolutely reliable. The same is true for standard AFM, in this case water layers residing between the silicon oxide and the graphite flakes falsify the height information.

These facts underline the need for reliable methods how to resolve the geometry and the detailed structure of the object on which transport measurements are performed. Only if one knows the structure of the investigated object well one can come to proper conclusions when evaluating the electrical transport data. To address these issues, we came up with several approaches: the underetching method developed by J. C. Meyer [Mey04, Mey06] was utilized to prepare SWNT and metallofullerene peapod samples for TEM investigation after having carried out the electrical transport measurements on the very same SWNTs/metallofullerene peapods (details see in chapter 4.7.1). Furthermore the very same technique was applied to calibrate Raman investigations to judge the thicknesses of graphene flakes (chapter 4.7.3). Finally, a high-resolution AFM approach was developed in cooperation with M. Ashino and R. Wiesendanger (University of Hamburg) (chapters 4.7.2 and 7.5) to overcome yield problems of the underetching technique and to differentiate between SWNTs and metallofullerene peapods in a non-invasive way.

### 4.7.1 Combination of transport and HR-TEM on the same sample

By now, several research groups have come up with techniques to combine transport experiments and TEM studies on the same individual carbon nanotubes [Sag04, Kas99, Koc02, Gol03, Kim05, Mey04, Cha06]. However, all approaches except of ours [Mey04] either do not allow for measuring gate dependences of the conductance $G(V_g)$ of the nanotubes with a well-defined gate architecture [Sag04, Kas99, Koc02, Gol03] or the gate electrodes are such far away [Kim05] that the gate coupling factor α can be expected to be very small in comparison to the usual field-effect transistor configuration. One of the latest approaches to carry out TEM on the same nanotube which electrical transport is done on is a mechanical transfer technique [Cha06] which does not implicate the restrictions mentioned above. Nevertheless this method is dedicated for nanotubes grown across a slit by chemical vapor deposition and it remains unclear whether it would be applicable for metallofullerene peapods as well.

In our approach, we adsorb SWNTs or metallofullerene peapods onto a Si/SiO_2 substrate as described in chapter 4.4. Directly after adsorption, the chip with the marker system (cp. Fig. 4.7b,d) is scribed such, that the scratch in the SiO_2 surface runs horizontally through the marker system in figure 4.7d. Since Si can not be cleaved in a very controlled way, it is important that the scratch is running through the marker system as close as possible to its center so that after cleaving on each part of the chip approx. half a marker system resides together with the respective contacts and bond-pads. In order to place the scribing line as close as possible to the horizontal center line of the marker system in figure 4.7d, we equipped a commercially available silicon scriber with an optical system and an optically transparent saphire tip (instead of the standard non-transparent tip), which allows to position the scribing line with a high precision. Subsequently, the two half chips were glued together onto a small piece of substrate stabilizing and supporting the two half Si chips. At this step it is of great relevance to match the two half chips along the cleaved edges very well in order to have only a tiny gap between the chip pieces.

The stripes along the cleaved edge are inspected by AFM in order to select suitable SWNTs or metallofullerene peapods which are located in close proximity to the edge (max. 20 μm away). Subsequently, the electron beam lithography process (cp. Fig. 4.10) is carried out to contact the chosen SWNTs/metallofullerene peapods with source and drain contacts. Note, that the two half chips have been glued together before AFM and e-beam lithography for the following two reasons: firstly, scanning a substrate close to its edge by AFM could result in breaking the tip. Secondly, electron beam lithography can not be carried out properly at the edge of a chip due to very inhomogeneous resist thickness (bead) close to the edge. If the chip halves are glued together with only a very thin gap remaining in between, the glued chip can be spin-coated homogeneously allowing for structuring patterns by electron beam as close as 500 nm to the edge. After running through the usual lithography process depicted in figure 4.10, the chip halves are separately measured by electrical transport measurements in the cryostat (cp. chapter 4.6).

Having carried out the electrical investigations, the two chip halves are glued together again, another electron beam lithography run is performed to define a metallic scaffold on top of the structures which should stabilize the electrodes and the contacted nanotubes during the etching process and later on. The chip halves are cleaved to fit into the sample holder of the transmission electron microscope, i.e. the sizes of the chip halves after cleaving are about 0.5 mm x 1 mm.

After these preparatory steps, the chip halves are etched in 30% aqueous KOH solution at about 60°C for about 7 hours (Fig. 4.25). KOH attacks both the highly doped Si chip and the thermally grown, 200 nm SiO_2 covering the Si substrate. The highly doped Si is etched approximately 100 times faster than the SiO_2, which means that one can etch about 20 μm Si edgewise until the 200 nm SiO_2 have been etched away completely and thus the etching gets uncontrolled. By this method one can underetch all nanotube devices being maximum 20 μm away from the cleaved chip edges.
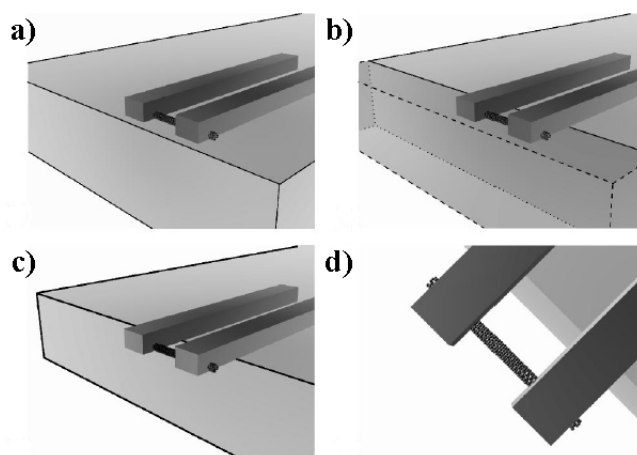
Fig. 4.25: Sequence of images depicting the underetching process of a nanotube field-effect transistor schematically [Mey04]. The stabilizing metal scaffold is omitted in this schematical drawing. **a)** A nanotube provided with a source and a drain contact close to the cleaved edge of a Si/SiO_2 chip. **b)** The same device after etching the indicated volume from the side by KOH etching. **c)** The same device after KOH etching. **d)** Top view of the device after etching: the nanotube is freestanding and can be imaged by high-resolution transmission electron microscopy.

To finalize the TEM sample preparation, the chips are dried by *critical point drying* which prevents the freestanding nanotube transistors from being destroyed by forces that would act on the fragile structures during a usual drying process in which the phase boundary between the liquid and the gaseous phase has to be crossed. After critical point drying, the same nanotube transistors which have been investigated by electrical transport measurements before and which are now freestanding can be investigated by means of high-resolution transmission electron microscopy. HR-TEM tells the number of nanotubes in a field-effect transistor channel and about possible filling of the tubes with metallofullerenes.

An example of an underetched nanotube device is depicted in figure 4.26 [Mey04]. The Si/SiO$_2$ substrate after KOH etching and critical point drying is shown in figure 4.26f as a scanning electron microscopy image: the two black arrows indicate the edge of the substrate after etching, i.e. on the left side, the bulk of the chip can be seen, whereas the structures on the right side are sticking out across the edge of the chip and hence are freestanding. The AuPd contacts formerly used for the transport measurements (cp. chapter 4.4 and Fig. 4.11) are denoted by dashed, black lines. The massive structure on top of the contacts on the right side is the stabilizing metal scaffold. Figures 4.26d,e display TEM images of the area around the nanotube between the contacts marked by dashed lines in different magnifications. The high-resolution TEM micrographs of three segments of the respective nanotube in figures 4.26a,b,c exhibit that it is a thin bundle of two empty SWNTs instead of the expected metallofullerene peapod (cp. [Mey04]) which underlines the importance of combined measurements.

A major drawback of this very method is that it involves a considerable risc to destroy a sample after time-intensive electrical transport investigations.
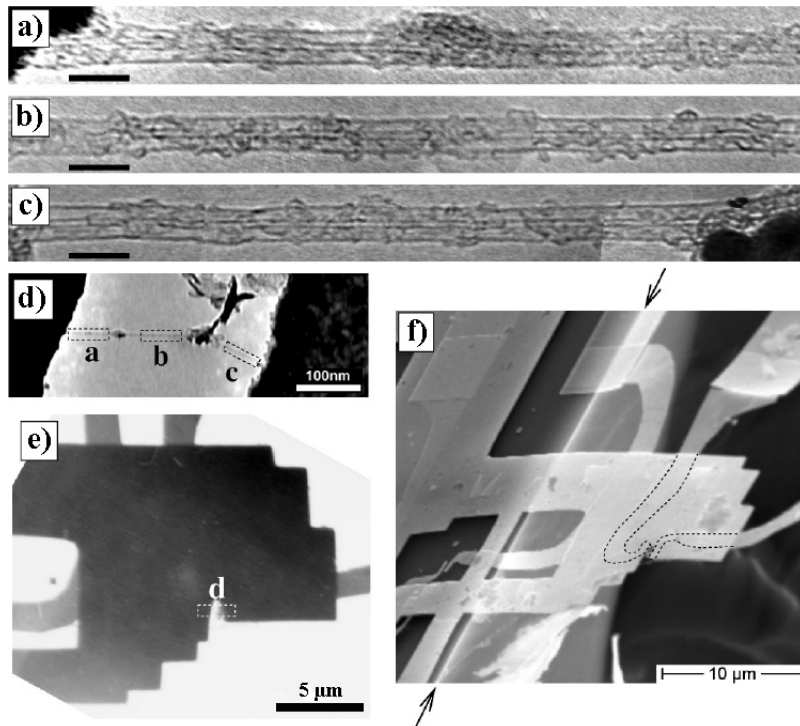
Fig. 4.26: A Si/SiO$_2$ chip after underetching. **a)-c)** High-resolution TEM micrographs of three sections of the nanotube bundle between the contacts displayed as dashed lines in f). Scale bars: 5 nm. **d),e)** Low resolution TEM images of the freestanding nanotube bundle. **f)** Scanning electron microscopy image of the chip. The black arrows indicate the border between the remaining Si/SiO$_2$ chip (left side) and the freestanding structures (right side). The electrodes marked by dashed lines have been used for electrical transport measurements before. The massive structure on top is the metal scaffold stabilizing the arrangement [Mey04].

4.7.2   Combination of transport and HR-AFM on the same sample

To avoid the risc of loosing samples throughout the underetching process, atomic-resolution dynamic atomic force microscopy (AFM) was employed[*] to gain detailed structural information on the same nanotube or metallofullerene peapod sample, electrical transport measurements have been performed on. The only drawback of this method is the low sample throughput, the atomic-resolution AFM is a highly challenging and time-intensive way of sample characterization. Within this short chapter, the basic technology is introduced, whereas the imaging results regarding Dy metallofullerene peapods are presented in the results chapter 7.5. An example for the combination of transport and high-resolution AFM on a SWNT sample can be found in chapter 6 (cp. Fig. 6.5).[†]

In dynamic AFM operation, a cantilever mounted on a piezo actuator is oscillated at its eigenfrequency f_0 by a self-excitation resonance loop [Ash08]. Two feedback loops are operated simultaneously (Fig. 4.27) to keep the frequency shift $\Delta f = f - f_0$ and the amplitude A of the cantilever oscillation constant. The frequency shift Δf comes about by long- and short-range forces acting between the resonating AFM tip apex and the sample surface. The feedback loop keeping Δf constant provides the sample topography using the frequency modulation technique [Alb91]. Increasing sensitivity of the Δf detection together with minimizing long-range contributions as electrostatic forces allows for atomic resolution [Ash08]. The amplitude A of the AFM cantilever oscillation changes if energy is transferred between the resonating AFM tip and the sample, i.e. by mapping the energy put into the AFM cantilever oscillation by the amplitude regulation feedback loop, an atomically resolved ΔE energy dissipation image of the sample can be acquired. The dynamic AFM experiments were carried out with a home-built UHV low-temperature AFM of Wiesendanger's group (University of Hamburg) optimized for atomic-scale studies [All98] at a background pressure $P < 10^{-8}$ Pa and $T < 13$ K.
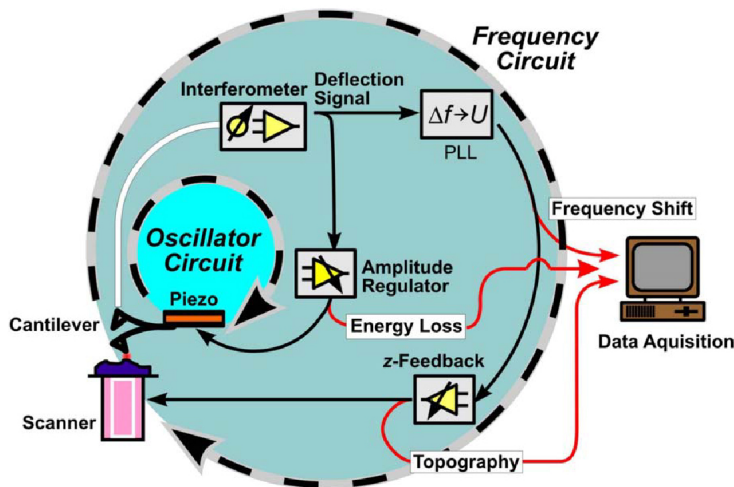
Fig. 4.27: Schematic diagram of a dynamic AFM system. Two feedback loops are used to maintain the frequency shift Δf and the amplitude A of the AFM cantilever oscillation constant. Thus, the atomically resolved sample topography and sample energy dissipation ΔE are acquired. $\Delta f / A$ is kept constant by tuning the voltage applied to the z piezo of the scanner/the piezo actuator driving the cantilever oscillation [Ash08].

---

[*]in cooperation with M. Ashino and R. Wiesendanger, University of Hamburg

[†]In this case, the AFM imaging quality was significantly below atomic resolution due to adsorbates on the sample and eventually non-optimum tip conditions.

4.7.3   Combination of transport and Raman spectroscopy on the same sample

Looking for an independent method how to resolve the structure of a graphene flake (especially the number of graphene layers), which has been investigated by electrical transport measurements, the first method applied was the underetching method[†] in a similar way to underetching of nanotube/metallofullerene peapod transport samples as described in chapter 4.7.1. Figure 4.28 displays that the underetching and subsequent high-resolution TEM of a graphene transport sample after carrying out the transport measurements can tell the number of layers within the graphene flake. The flake in figure 4.28a is provided with a metal scaffold and underetched so that it is freely suspended and stabilized by the metal structures on top of it (Fig. 4.28b). Note, that the bright areas correspond to the metal leads having been used for transport (cp. Fig. 4.28a), whereas the dark metal stripes constitute the stabilizing metal scaffold. A part of this graphene flake has been detached from the metal structures during the underetching process and was flipped over to the left hand side (Fig. 4.28b). Inspecting the edges of such suspended graphene flakes, areas are found in which the edges are bent upwards and intersect the focal TEM plane perpendicularly so that the incident electron beam locally parallels the graphene flake. This allows to directly observe the number of graphene layers of the flake, which appear in high-resolution TEM as dark parallel lines (Fig. 4.28c). The flake depicted in figure 4.28 is a double-layer graphene.
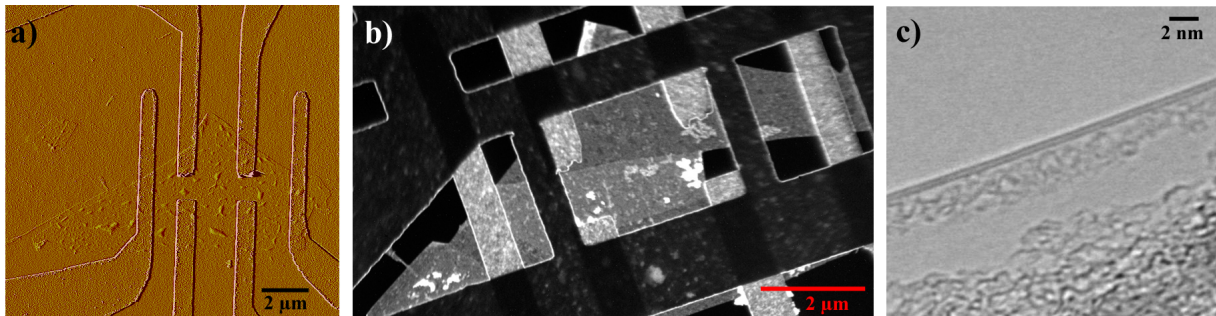
Fig. 4.28: Sequence of images illustrating underetching a contacted graphene sample and performing high-resolution TEM to identify the number of graphene layers the flake consists of. **a)** A graphene flake contacted by Cr/Au contacts to carry out electrical transport measurements. **b)** Low-resolution TEM image of the same flake as in a) after underetching and critical point drying. Before underetching, the graphene flake has been stabilized by a metal scaffold. **c)** High-resolution TEM micrograph of an edge of the freestanding graphene sample depicted in b). This edge is bent upwards and crosses the TEM focal plane perpendicularly so that locally the electron beam is parallel to the flake. In this case, one can directly count the number of graphene layers in the flake which appear as dark parallel lines with the van der Waals distance of 3.4 Å as spacing. According to c), the flake depicted here is a graphene bilayer.


[†]underetching and TEM investigations done by J. C. Meyer

Since the preparation of suspended graphene flakes after transport measurements is laborious and risky in terms of damaging the flakes, again - as in the nanotube/metallofullerene peapod case - a non-invasive method is looked for by which the number of layers in a graphene flake can be gained. Meanwhile, Raman spectroscopy is the established method to differentiate between a monolayer, a bilayer and a few-layer graphene flake [Fer06, Hal07]. Raman spectroscopy on graphene flakes is a high-throughput and a non-destructive method to differentiate the number of graphene layers based on significant differences between the D^* band of a monolayer, a bilayer and a few-layer graphene. Due to changes in the electron bands, the D^* peak changes its shape, width and position with increasing number of graphene layers [Fer06]. The main differences between the Raman spectrum of a graphene monolayer and a double-layer is that the monolayer exhibits one sharp D^* peak, whereas the corresponding D^* signal for a double-layer is wider and is composed of 4 components (Figs. 4.29, 4.30) [Fer06] leading to a kind of shoulder left of the main peak, furthermore the D^* peak of a double-layer is up-shifted in wavenumber in comparison to the monolayer [Fer06, Hal07]. These changes are sufficient criteria to keep one, two and few layers (> 2) of graphene apart (these are the most important cases), however, some caution is needed interpreting the results since pure D^* peak shifts can also originate from doping of the graphene layers by physisorbed oxygen or water [Hal07].
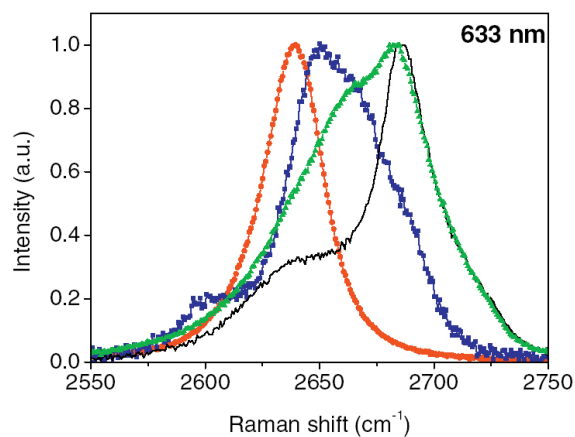
Fig. 4.29: Raman spectra of monolayer graphene (red), bilayer graphene (blue), few-layer graphene (green) and HOPG (black) [Hal07].
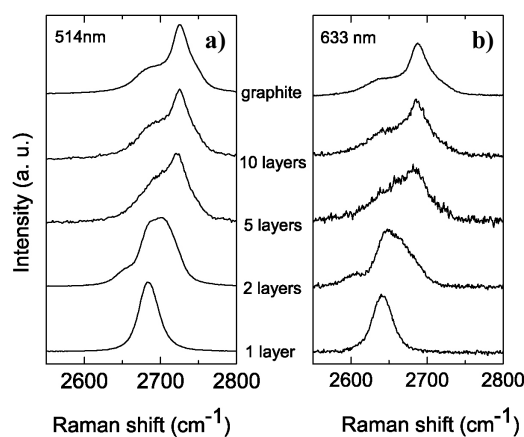
Fig. 4.30: Evolution of the Raman spectra at **a)** 514 nm and at **b)** 633 nm with the number of graphene layers [Fer06]).

# 5. Results on electrical transport in graphene mono- and bilayers

This chapter includes the (magneto-)transport results acquired for graphene mono- and bilayers. As already pointed out in chapter 4.7, one important aspect of this thesis is to combine the transport measurements with structural investigations on the same object transport is measured on. That is why the Raman spectroscopy and HR-TEM data which clarify whether the prepared flakes are mono- or bilayers of graphene are introduced before entering the first sub-chapter on *quantum Hall effect* measurements on the flakes. The (magneto-)transport data of four flakes named G1 to G4 will be presented. Optical microscopy images of these four flakes before and after providing the electrical contacts are given in figures 5.1 to 5.4. The D* peaks in Raman spectroscopy of the four flakes are illustrated in green in figures 5.1c, 5.2c, 5.3c and 5.4d and compared to the D* peaks for mono- and bilayer graphene from literature [Hal07]. The conclusion is that the flakes G1 and G2 are monolayers, whereas G3 and G4 are bilayers of graphene.
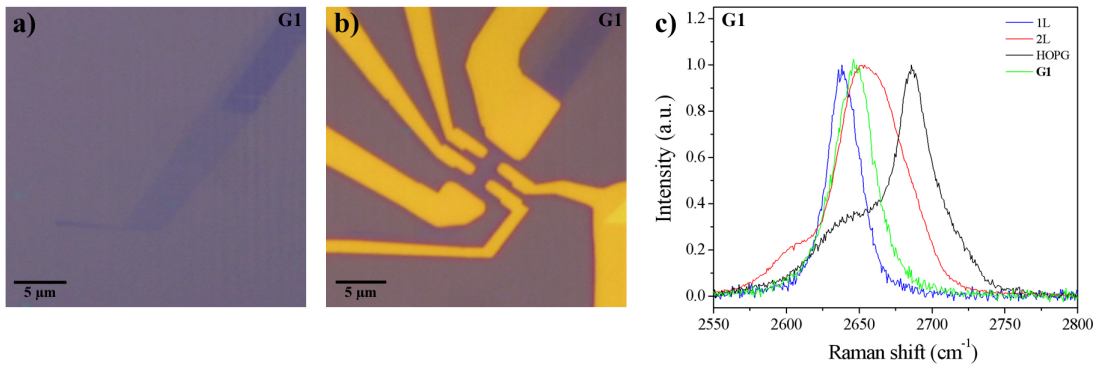
Fig. 5.1: Optical microscopy image of sample G1 **a)** before and **b)** after putting the electrical contacts. **c)** The D* peak of G1 (green) in Raman spectroscopy indicates that G1 is a graphene monolayer (cp. chapter 4.7.3 and [Hal07]).
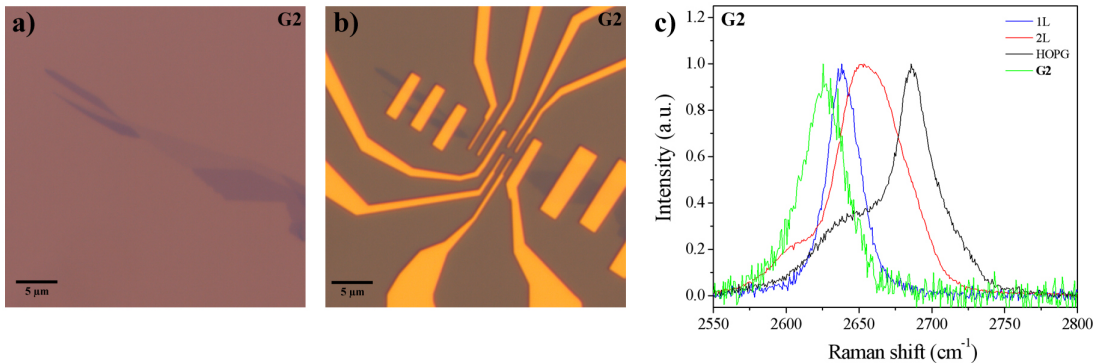
Fig. 5.2: Optical microscopy image of sample G2 **a)** before and **b)** after putting the electrical contacts. **c)** The D* peak of G2 (green) in Raman spectroscopy indicates that G2 is a graphene monolayer as well (cp. chapter 4.7.3 and [Hal07]).
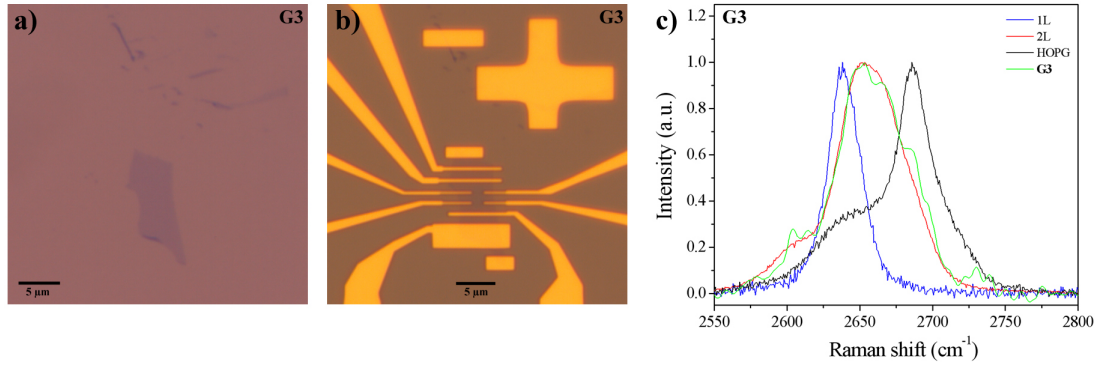
Fig. 5.3: Optical microscopy image of sample G3 **a)** before and **b)** after putting the electrical contacts. **c)** The D* peak of G3 (green) in Raman spectroscopy indicates that G3 is a graphene bilayer (cp. chapter 4.7.3 and [Hal07]).
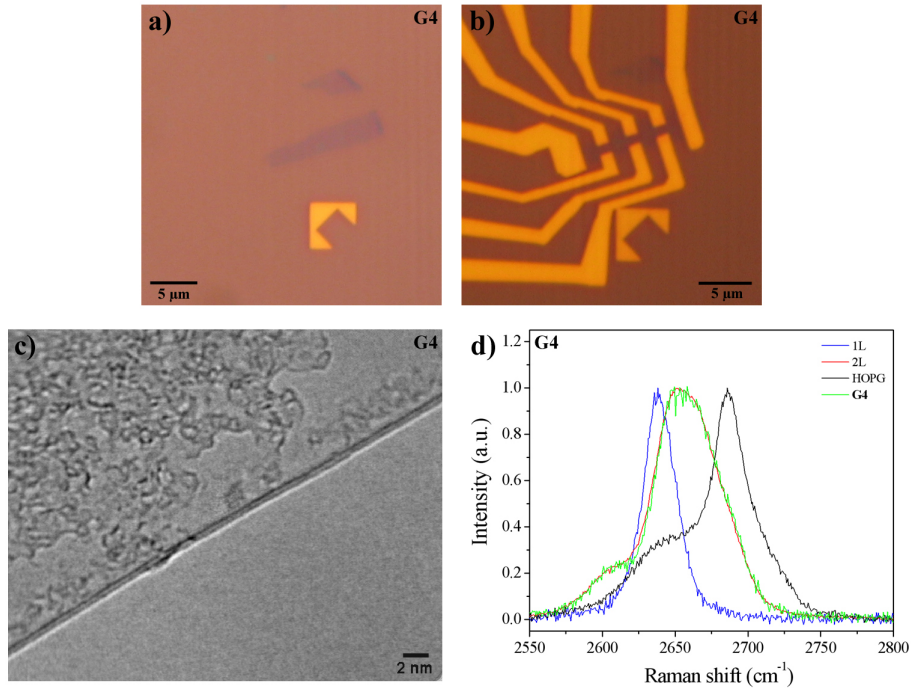

Fig. 5.4: Optical microscopy image of sample G4 **a)** before and **b)** after putting the electrical contacts. **c)** High-resolution transmission electron microscopy image of an edge of G4 being parallel to the incident electron beam. Two parallel black lines are clearly visible, i.e. sample G4 is a graphene bilayer. **d)** The D* peak of G4 (green) in Raman spectroscopy confirms that G4 is a double-layer flake (cp. chapter 4.7.3 and [Hal07]).

In addition, figure 5.4c displays a high-resolution transmission electron microscopy image* of an edge of sample G4 which is bent upwards in such a way that it is parallel to the incoming electron beam and one can thus directly count the number of graphene layers in real space. It can be clearly seen that G4 comprises two layers of graphene. This sample was one of the samples used to calibrate the Raman data for [Hal07].

---

*TEM image by J. C. Meyer

5.1 Quantum Hall effect measurements on graphene mono- and bilayers

In order to characterize the graphene flakes G1 to G4 further, their charge carrier mobilities μ (cp. equation (3.6)) at different gate voltages V_g are approximated using equation (3.7). For doing so, the geometries of the flakes after providing them with electrical contacts, i.e. the lengths L, d in figure 3.7, as well as the charge carrier densities n are needed. L, d are well known from designing the contacts and imaging the flakes after processing. The charge carrier densities n at different gate voltages V_g have been determined by measurements of the Hall resistance R_{xy} at low magnetic fields for $T = 1.5$ K (samples G1, G4) and $T = 4.2$ K (samples G2, G3). The variations of the charge carrier mobility, of the longitudinal resistance R_{xx} and of the Hall resistance R_{xy} in graphene flakes are negligible between 1.5 K and 4.2 K [Ulb08], so that the received mobility values of G1 to G4 are well comparable. The values of the charge carrier densities of the two monolayers G1, G2 and the two bilayers G3, G4 for different gate voltages V_g are compiled in figure 5.5. There is a clear distinction between the mobilities of the mono- and the bilayer graphene flakes: the mobilities of the graphene monolayers G1 and G2 are approximately between 4000 and 6000 cm^2/Vs and systematically exceed the ones of graphene bilayers G3 and G4 for which the mobility is between approx. 1500 and 3000 cm^2/Vs.
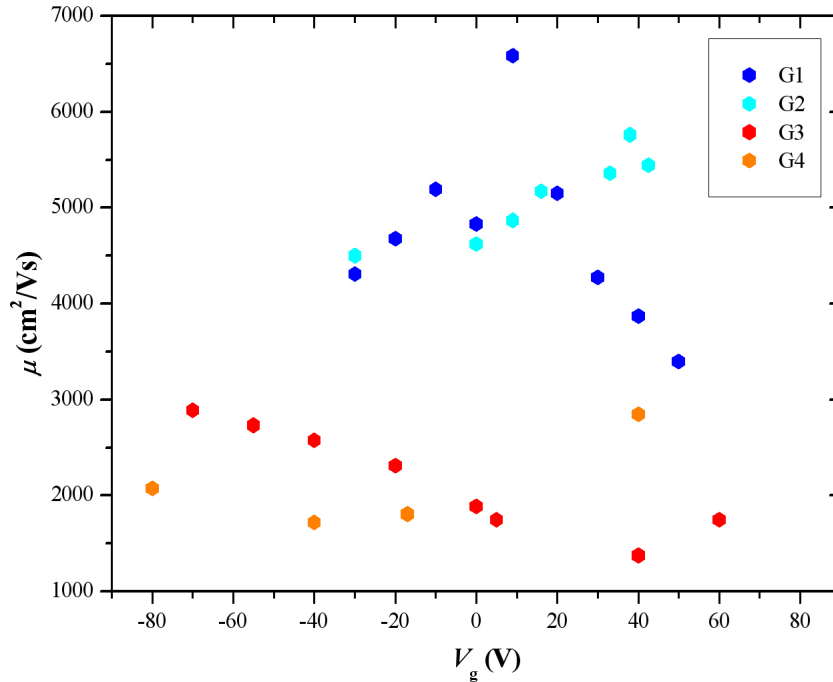
Fig. 5.5: Mobility values μ of the four graphene samples G1 to G4 at T = 1.5 K (G1, G4) and T = 4.2 K (G2, G3). Since the variation of R_{xx} and R_{xy} in graphene samples is insignificant when changing the temperature from 1.5 K to 4.2 K [Ulb08], the mobility values at these two temperatures can be well compared. The mobilities are received using equation (3.7), which requires knowledge of the geometries of the graphene flakes and their charge carrier densities n at the respective gate voltages V_g gained by Hall effect measurements at low magnetic fields.

In the following, the actual results of the *quantum Hall effect* measurements performed on the graphene samples G1 to G4 will be discussed. The $R_{xx}(V_g)$ and $R_{xy}(V_g)$ data received for the graphene monolayer G1 at $T = 1.5$ K for different magnetic fields B are displayed in figure 5.6. The next figure 5.7 plots R_{xx} and R_{xy} of G1 as functions of the magnetic field B for different gate voltages V_g. The corresponding data for the graphene monolayer G2 at $T = 4.2$ K are given in figures 5.8 and 5.9. Similarly, the results obtained for the two graphene bilayers G3 (at $T = 32$ mK and $T = 4.2$ K)[†] and G4 (at $T = 1.5$ K) are presented in figures 5.10 to 5.13.

The overall observations are that firstly the expected plateau values of R_{xy}, namely $\pm h/2e^2, \pm h/6e^2, \pm h/10e^2,...$ for graphene monolayers and $\pm h/4e^2, \pm h/8e^2, \pm h/12e^2,...$ for bilayers[‡] (cp. chapter 3.1.4), are met by G1 to G4 for sufficiently high magnetic fields. Secondly, the plateaus in R_{xy} and the accompanying drops of R_{xx} to zero are reached by the graphene double-layers G3 and G4 only for considerably higher magnetic fields in comparison with the monolayers G1 and G2. This is obviously related to the lower mobility of the bilayer graphene samples (Fig. 5.5) which can be attributed to additional scattering centers, e.g. hardly removable impurities between the two layers. Thirdly, it seems that in contrast to GaAs hallbars, the mobility values μ of the mono- and bilayer graphene samples are only a limited measure for how well the *quantum Hall effect* will be developed. The monolayer flakes G1 and G2 have comparable mobilities, yet the *quantum Hall effect* is much better resolved for sample G1 at comparably high magnetic fields. The reason for this limitation of the mobility as a parameter to describe the quality of the *quantum Hall effect* measurements in graphene mono- and bilayers may be that in contrast to GaAs hallbars having well-defined edges, graphene mono- and bilayers (being not etched into hallbar shape as in our case) have undefined edges strongly determining the quality of the *quantum Hall effect* but being not necessarily taken into account by the charge carrier mobility μ acquired by equation 3.7.

Now the *quantum Hall effect* data of the graphene flakes G1 to G4 are analyzed in more detail on the basis of figures 5.6 to 5.13. The graphene monolayer G1 shows very pronounced *quantum Hall effect* characteristics (Figs. 5.6, 5.7) comparable to data published in literature [No05b, Zha05]. Considering the gate dependences of R_{xx} and R_{xy} in figure 5.6, it can be seen that for $B = 12$ T (Figs. 5.6a,b), the *quantum Hall effect* is very well resolved with the R_{xy} plateaus at the correct resistance values and the *Shubnikov-de Haas oscillations* in R_{xx} dropping to zero for the respective gate voltages. The Dirac point (cp. chapters 3.1.1, 3.1.2, 3.1.4) is at $V_{g,\text{Dirac}}^{\text{G1}} \approx 10$ V reflecting some degree of doping. For decreasing magnetic fields (Figs. 5.6c-f), the plateau regimes get smaller and are shifted towards smaller gate voltages (i.e. to gate voltages closer to the gate voltage of the Dirac point $V_{g,\text{Dirac}}^{\text{G1}} \approx 10$ V). Correspondingly, the $R_{xx} = 0$ regimes get smaller, but larger in

---

[†]The shifts of the G3 curves taken at $T = 32$ mK and $T = 4.2$ K along the V_g axes in figures 5.10e-g are predominantly due to unintentional doping of sample G3 when being transferred into another cryostat.

[‡]dotted lines in the R_{xy} plots in figures 5.6 to 5.13

number and shift towards the Dirac point as well. According to equation (3.16), which relates the filling factor ν with the charge carrier density n and the applied magnetic field B, this can be understood as follows: the filling factor at a fixed gate voltage V_g, i.e. a constant charge carrier density n, increases with decreasing magnetic field B. That means that in the figure sequence 5.6 a → c → e and b → d → f, respectively, more and more $R_{xx} = 0$ regimes and more R_{xy} plateaus with increasing values of the filling factor ν should be visible which indeed matches the experimental observations in figure 5.6a-f. At zero magnetic field only a peak in the R_{xx} curve remains which corresponds to maximum resistance at the Dirac point, whereas the Hall resistance vanishes as expected (Figs. 5.6g,h). A similar line of argumentation based on equation (3.16) can be followed when considering figure 5.7 which displays R_{xx} and R_{xy} as functions of the magnetic field B at different gate voltages V_g (or charge carrier densities n). The closer V_g is to the gate voltage $V_{g,\text{Dirac}}^{\text{G1}}$ corresponding to the Dirac point (i.e. the smaller the charge carrier density n), the smaller is the filling factor ν for a given magnetic field, which means that fewer $R_{xx} = 0$ regimes and fewer R_{xy} plateaus are visible. There is a further remarkable feature of the graphene monolayer G1 in figure 5.7d which shall be mentioned: when increasing the magnetic field B from -10 T towards 0 T, the Hall resistance R_{xy} does not increase from the $-h/2e^2$ plateau to the $-h/6e^2$ plateau directly, but overshoots before. We attribute this behaviour to either charge carrier scattering at the graphene flake edges or to a R_{xx} contribution to R_{xy}. For graphene samples which have been etched into hallbar geometries, these over-/undershoots do not appear any more, whereas they can occur in as-adsorbed and unetched graphene flakes as the ones presented here. The *quantum Hall effect* measurements on the second monolayer graphene flake G2 (Figs. 5.8, 5.9) *in principle* resemble the G1 data, however the doping is higher (Dirac point $V_{g,\text{Dirac}}^{\text{G2}} \approx 25$ V) and the quality is much worse despite of nominally comparable mobility values as already pointed out above. Even at $B = 10$ T, the R_{xy} plateaus are not fully developed (Fig. 5.8b). Note that there is an asymmetry in figure 5.8b, namely over-/undershoots of R_{xy} for $V_g < 10$ V, but precise R_{xy} plateaus without these features for $V_g > 40$ V. With decreasing magnetic field the *quantum Hall* features of the monolayer flake G2 are rapidly decaying (Fig. 5.8). As for the bilayer graphene samples G3 and G4, clear signatures of the *quantum Hall effect* were measured as displayed in figures 5.10 to 5.13, yet high magnetic fields, namely $B = 18$ T for G3 (Fig. 5.10a,b) and $B = 16.5$ T for G4 (Fig. 5.12a,b) were needed. Despite of these high magnetic fields, the *Shubnikov-de Haas oscillations* in most cases did not drop to zero in the *quantum Hall* states.

More recent studies demonstrate that the quality of *quantum Hall effect* measurements on graphene mono- and bilayers increases if the flakes are etched in order to avoid edge effects and to obtain a well-defined hallbar geometry and furthermore if the flake-substrate interactions are minimized by surface functionalization [Laf08] or by etching away the substrate underneath the flake resulting in freestanding graphene devices [Bol08, Mor08].
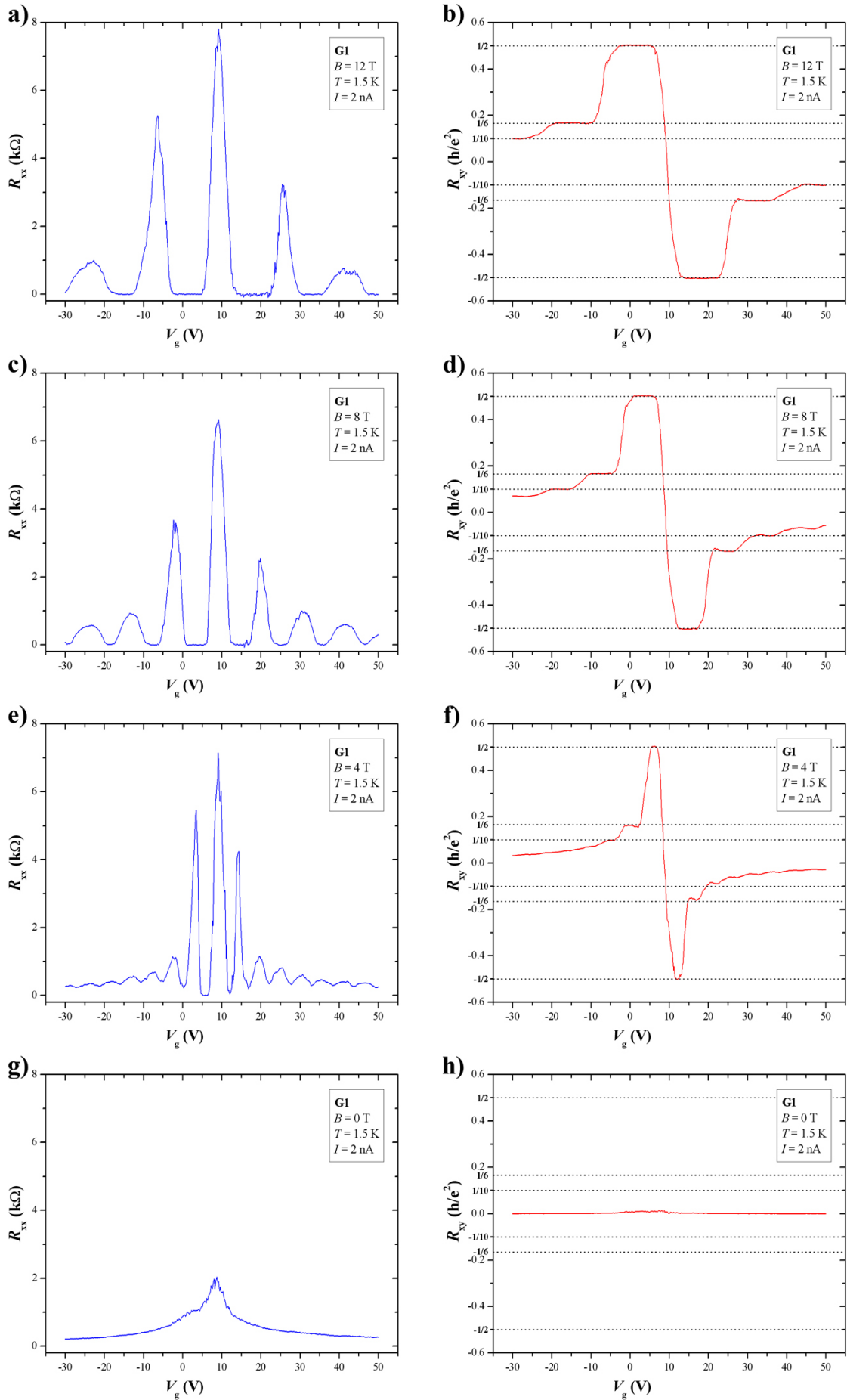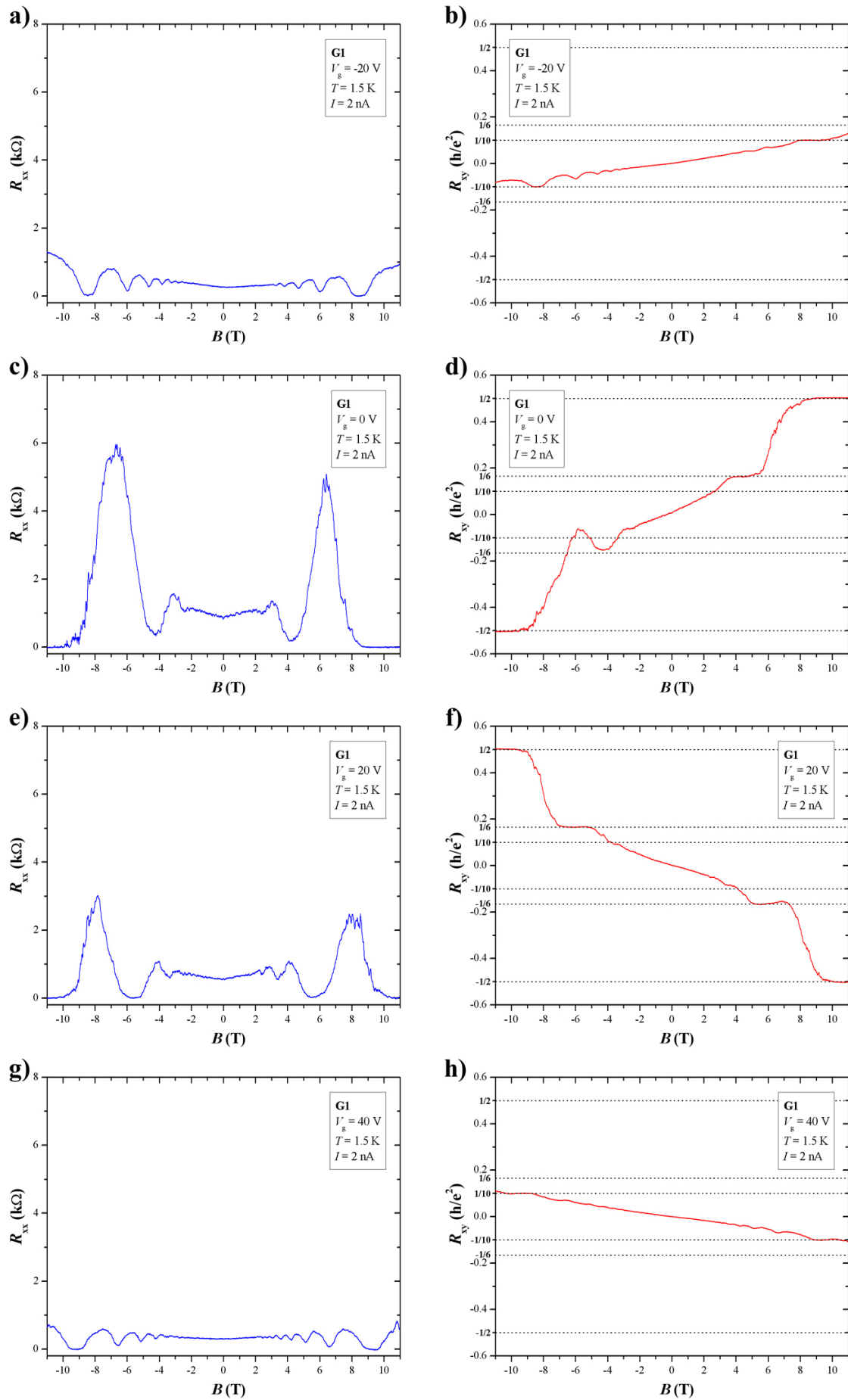
Fig. 5.6: Quantum Hall effect measurements performed on sample G1 at 1.5 K and $I = 2$ nA. **a),c),e),g)** $R_{xx}(V_g)$ at $B = 12, 8, 4$ and 0 T. **b),d),f),h)** $R_{xy}(V_g)$ at $B = 12, 8, 4$ and 0 T.
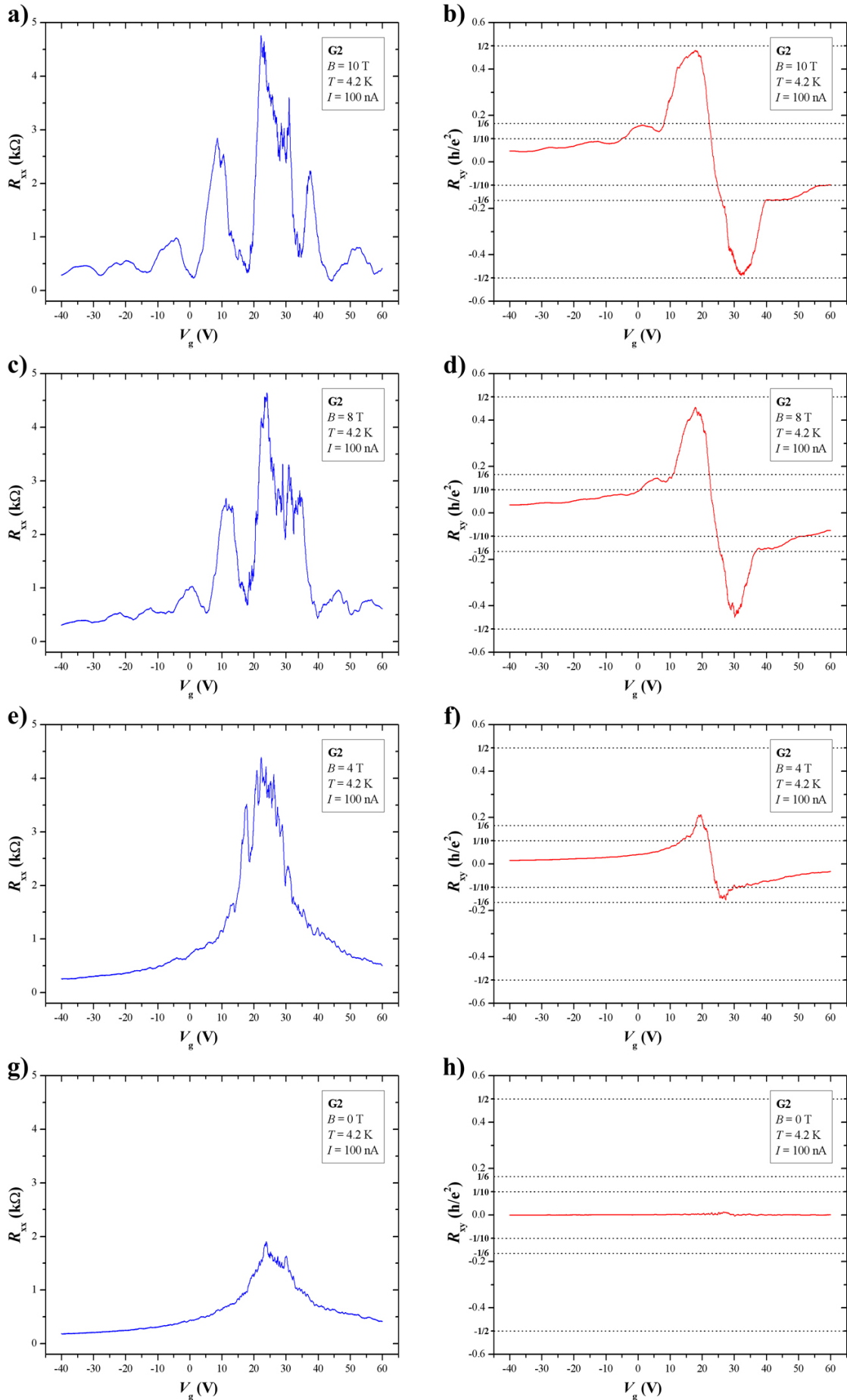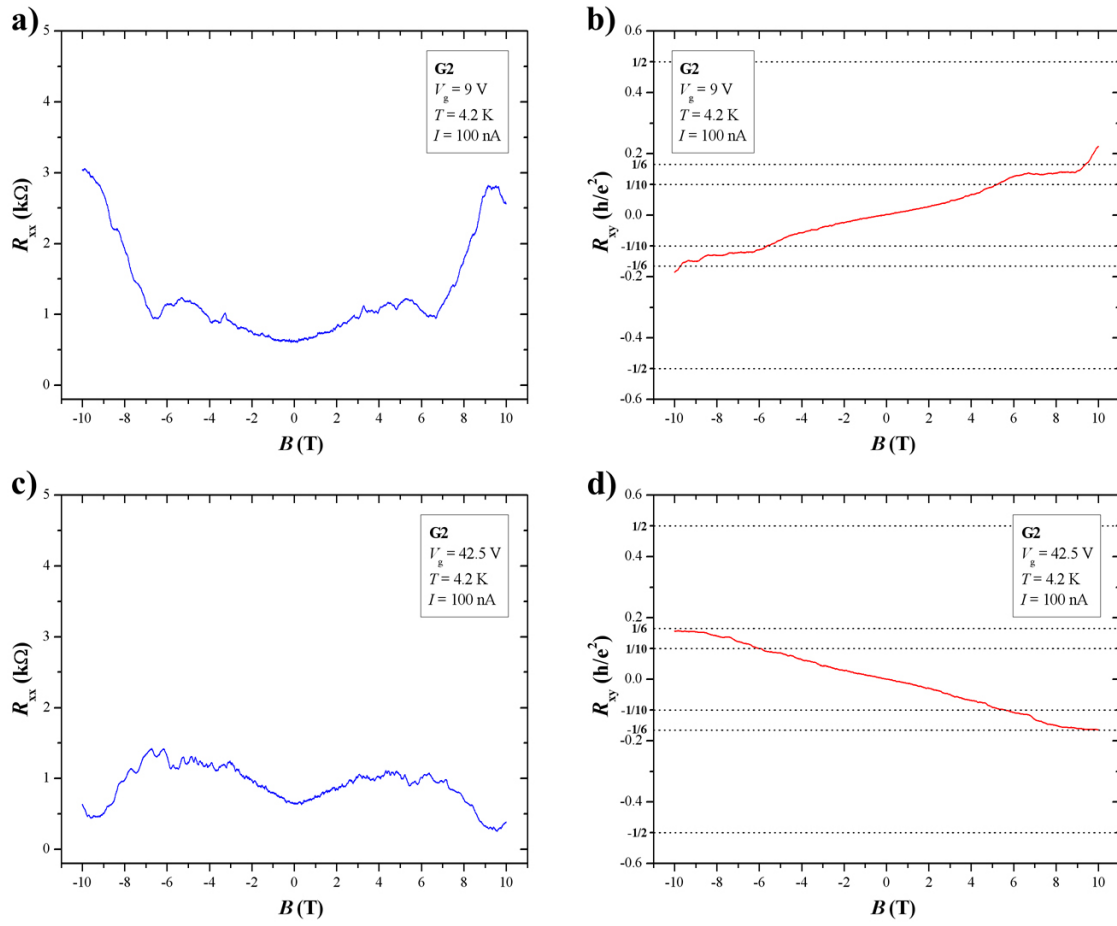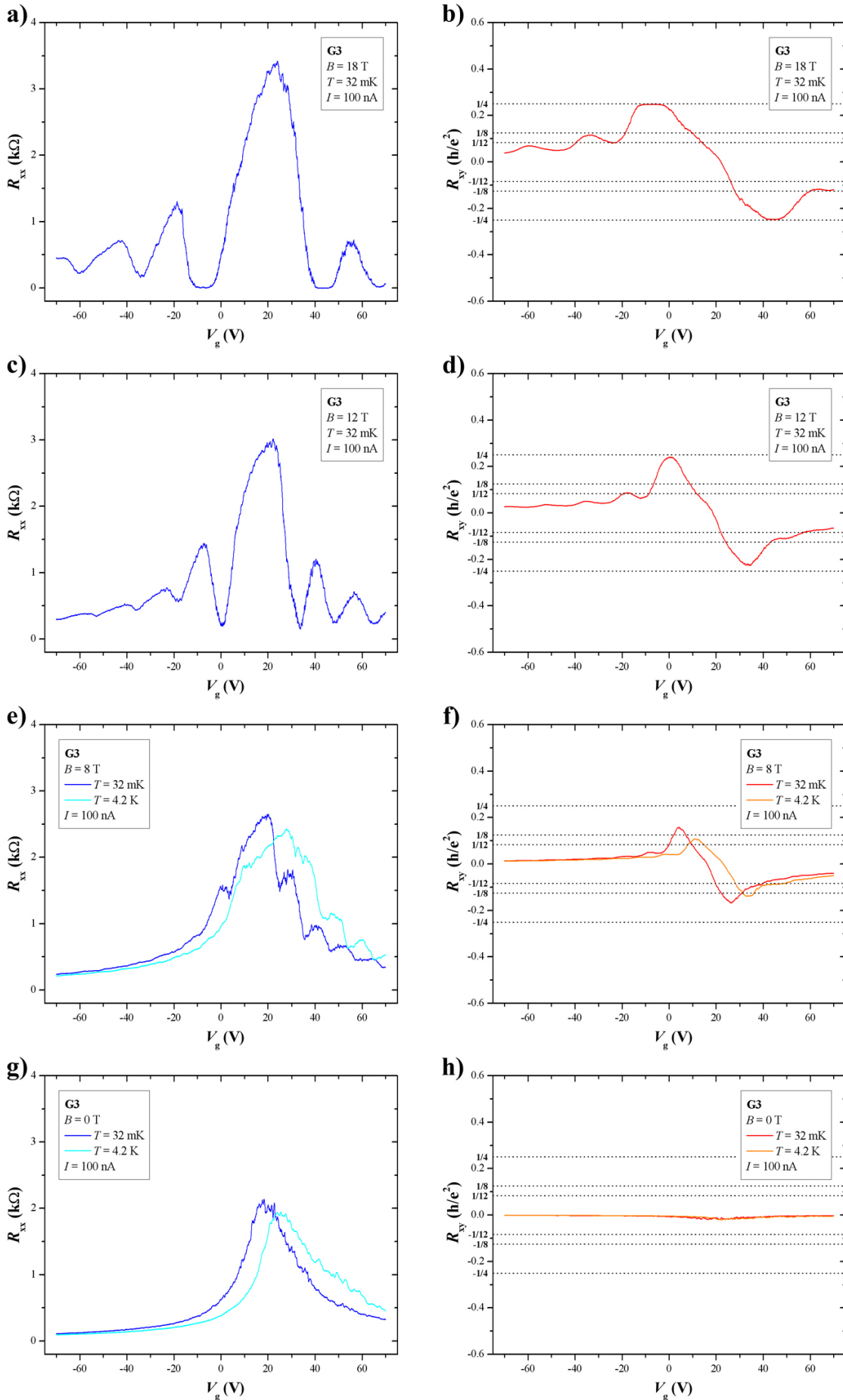
Fig. 5.7: Quantum Hall effect measurements performed on sample G1 at 1.5 K and $I = 2$ nA. **a),c),e),g)** $R_{xx}(B)$ at $V_g = -20, 0, 20, 40$ V. **b),d),f),h)** $R_{xy}(B)$ at $V_g = -20, 0, 20, 40$ V.
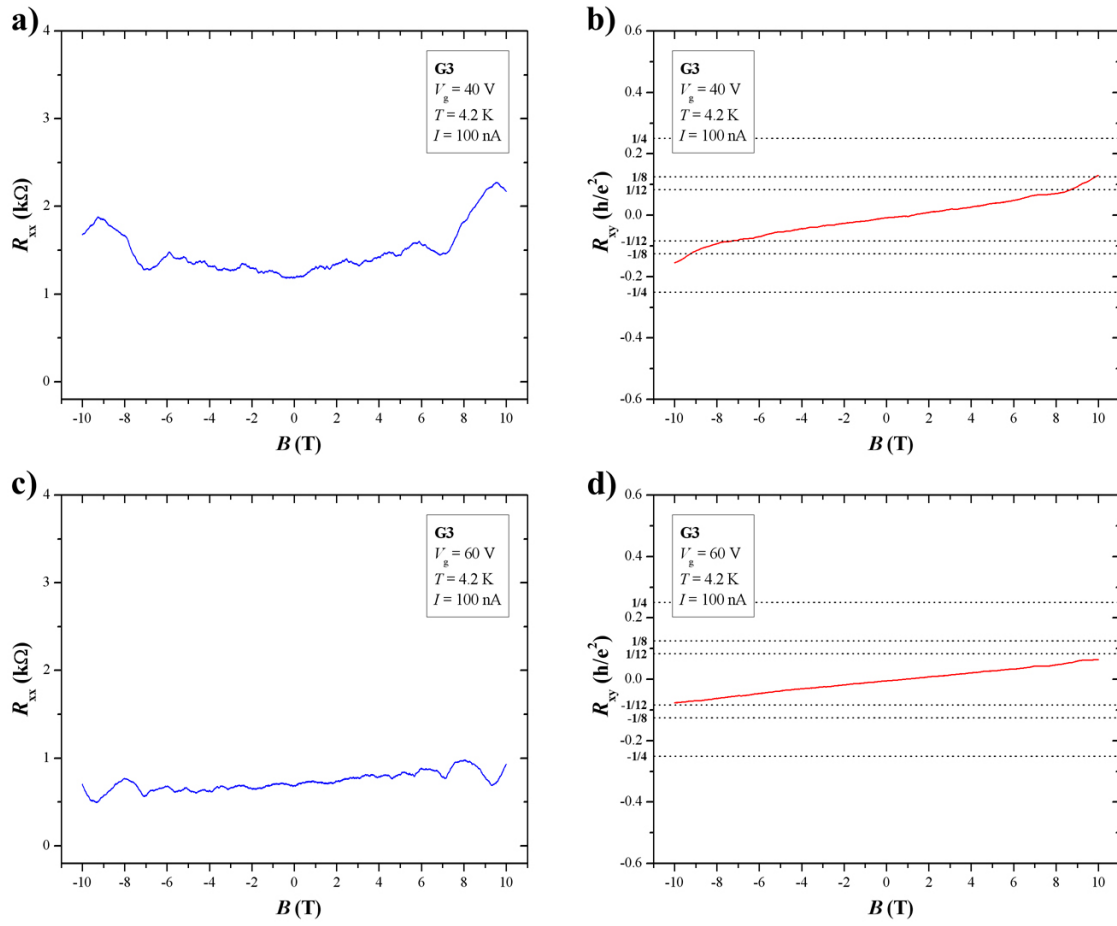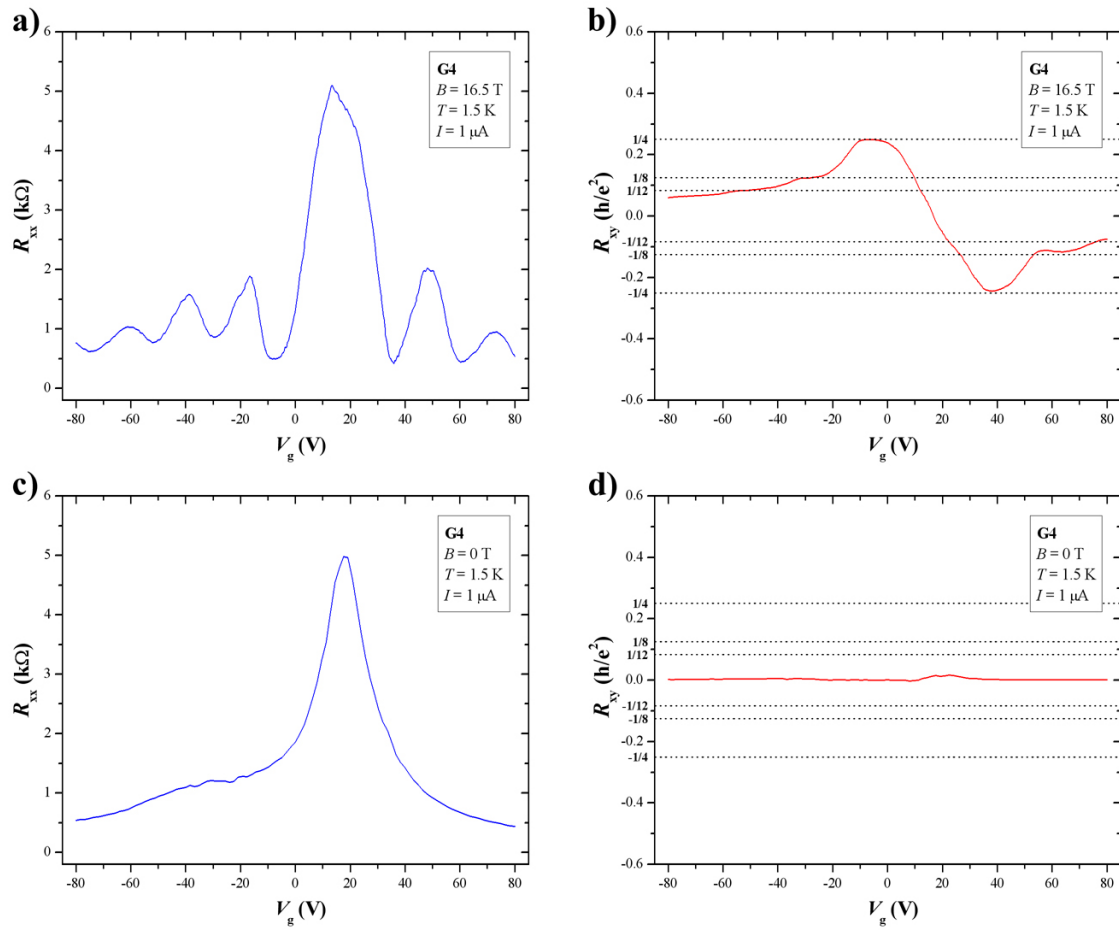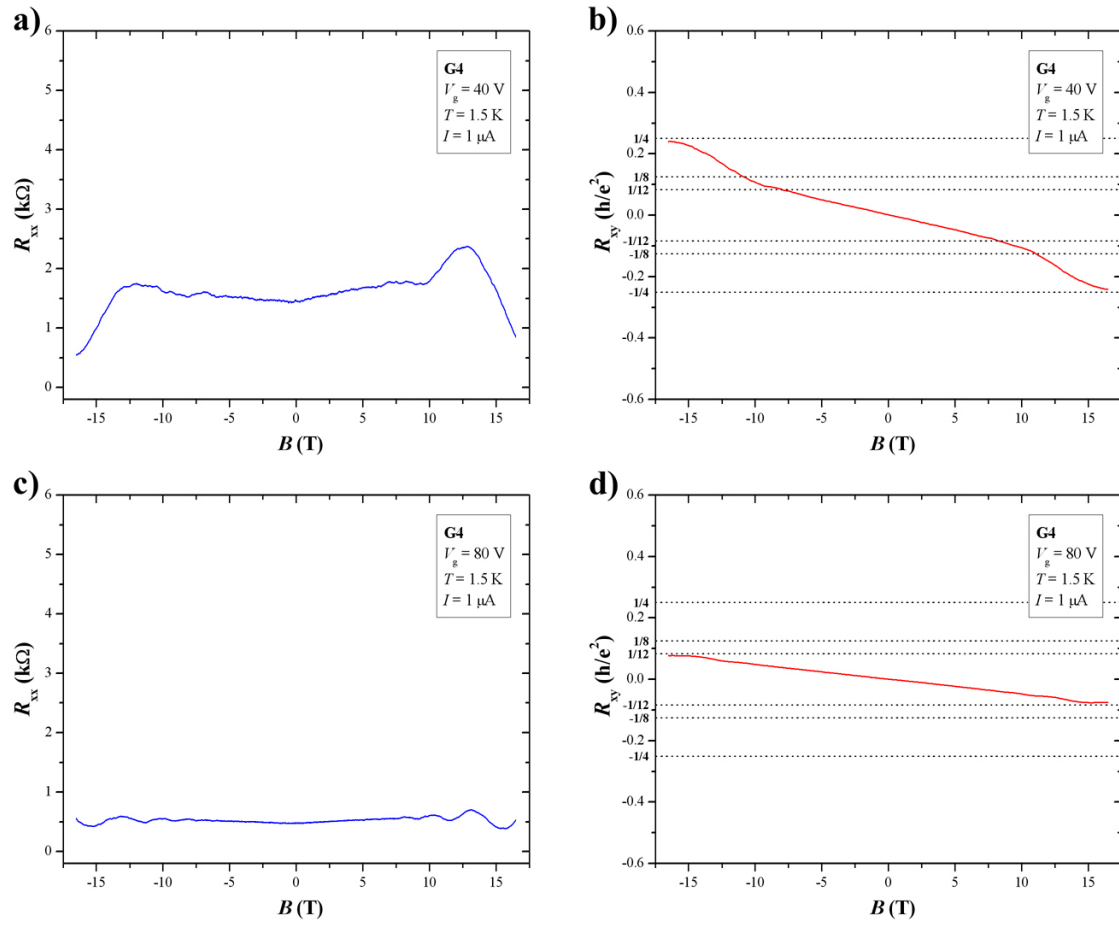
Fig. 5.8: Quantum Hall effect measurements performed on sample G2 at 4.2 K and $I = 100$ nA. **a),c),e),g)** $R_{xx}(V_g)$ at $B = 10, 8, 4$ and 0 T. **b),d),f),h)** $R_{xy}(V_g)$ at $B = 10, 8, 4$ and 0 T.

Fig. 5.9: Quantum Hall effect measurements performed on sample G2 at 4.2 K and $I = 100$ nA. **a),c)** $R_{xx}(B)$ at $V_g = 9$ and 42.5 V. **b),d)** $R_{xy}(B)$ at $V_g = 9$ and 42.5 V.

Fig. 5.10: Quantum Hall effect measurements performed on sample G3 at 32 mK/4.2 K and $I = 100$ nA. **a),c),e),g)** $R_{xx}(V_g)$ at $B = 18, 12, 8$ and 0 T. **b),d),f),h)** $R_{xy}(V_g)$ at $B = 18, 12, 8$ and 0 T.

Fig. 5.11: Quantum Hall effect measurements performed on sample G3 at 4.2 K and $I = 100$ nA. **a),c)** $R_{\mathrm{xx}}(B)$ at $V_{\mathrm{g}} = 40$ and 60 V. **b),d)** $R_{\mathrm{xy}}(B)$ at $V_{\mathrm{g}} = 40$ and 60 V.

Fig. 5.12: Quantum Hall effect measurements performed on sample G4 at 1.5 K and $I = 1\ \mu$A. **a),c)** $R_{\mathrm{xx}}(V_{\mathrm{g}})$ at $B = 16.5$ and 0 T. **b),d)** $R_{\mathrm{xy}}(V_{\mathrm{g}})$ at $B = 16.5$ and 0 T.

Fig. 5.13: Quantum Hall effect measurements performed on sample G4 at 1.5 K and $I = 1\ \mu$A. **a),c)** $R_{xx}(B)$ at $V_g = 40$ and 80 V. **b),d)** $R_{xy}(B)$ at $V_g = 40$ and 80 V.

5.2   Transport and magnetotransport in graphene mono- and bilayers at 4.2 K

In addition to the *quantum Hall effect* measurements described in the last sub-chapter, 2-probe magnetotransport measurements were carried out on the monolayer G2 and the graphene bilayer G3 at $T = 4.2$ K in analogy to the 2-probe magnetotransport investigations on SWNTs and metallofullerene peapods discussed in chapters 6.1 and 7.1. For doing so, the flakes G2 and G3 were provided with further electrical contacts crossing the whole flakes as depicted in the optical microscopy images in figures 5.2b and 5.3b.

The results of the 2-probe magnetotransport measurements (averaged from multiple runs) are summarized in figures 5.14 to 5.16 for the graphene monolayer G2 and in figures 5.17 to 5.19 for the bilayer G3. Each figure consists of an image which indicates the magnetic field orientation with respect to the sample (a), the current I_{sd} as a function of the gate voltage V_g for $B = -10, 0, 10$ T (b), the respective magnetoresistance curves (c), the current I_{sd} plotted vs. the magnetic field B in the range from -10 to 10 T at a fixed gate voltage V_g (d), the respective magnetoresistance data (e) and finally the current I_{sd} as a function of the source-drain voltage V_{sd} at the same fixed gate voltage V_g for $B = -10, 0, 10$ T (f) and the respective magnetoresistance plots (g). The flakes have been investigated in three different magnetic field orientations, namely with the magnetic field $B_{\perp,opl}$ being out-of-plane and perpendicularly oriented to the substrate and the graphene flakes (Figs. 5.14, 5.17), with the magnetic field $B_{\parallel,ipl}$ being in-plane and parallel to the metal contacts (Figs. 5.15, 5.18) and finally with the magnetic field $B_{\perp,ipl}$ in-plane and perpendicularly aligned to the metal contacts (Figs. 5.16, 5.19). After the out-of-plane measurements the samples had to be transferred into another sample stick for the in-plane measurements and thus had to be taken out of the helium atmosphere, which can cause additional doping as happened for G2 (compare the gate dependences in Figs. 5.14b and 5.15b). Qualitatively the flakes G2 and G3 despite being a mono- and a bilayer behave in a similar manner in 2-probe magnetotransport. At in-plane magnetic fields $B_{\parallel,ipl}$ and $B_{\perp,ipl}$ the effects of the magnetic field are negligible as anticipated. Note that the change of the magnetoresistance MR for $V_{sd} \to 0$ in figures 5.14g, 5.15g, 5.16g, 5.17g, 5.18g and 5.19g is meaningless, it is due to a known artefact of the used current-voltage amplifier occurring for small voltages in the range of 100 μV. That is the reason why the parts of the magnetoresistance curves between $V_{sd} = -200\,\mu$V and $V_{sd} = 200\,\mu$V have been excluded in the respective diagrams. In contrast, there is huge positive magnetoresistance for both flakes if the magnetic field is oriented perpendicularly to the substrate/flake (Figs. 5.14, 5.17), obviously due to the *Hall effect*. The maximum magnetoresistances are $MR_{max}^{G2} \approx 600\,\%$ for G2 and $MR_{max}^{G3} \approx 250\,\%$ for G3. Further remarkable features are the humps in the $I_{sd}(V_g)$ curves in figures 5.14b and 5.17b induced by the magnetic field leading to corresponding peaks in the associated $MR(V_g)$ plots in figures 5.14c and 5.17c. We attribute these humps to additional phase shifts due to the magnetic field which influence charge carrier interference effects.
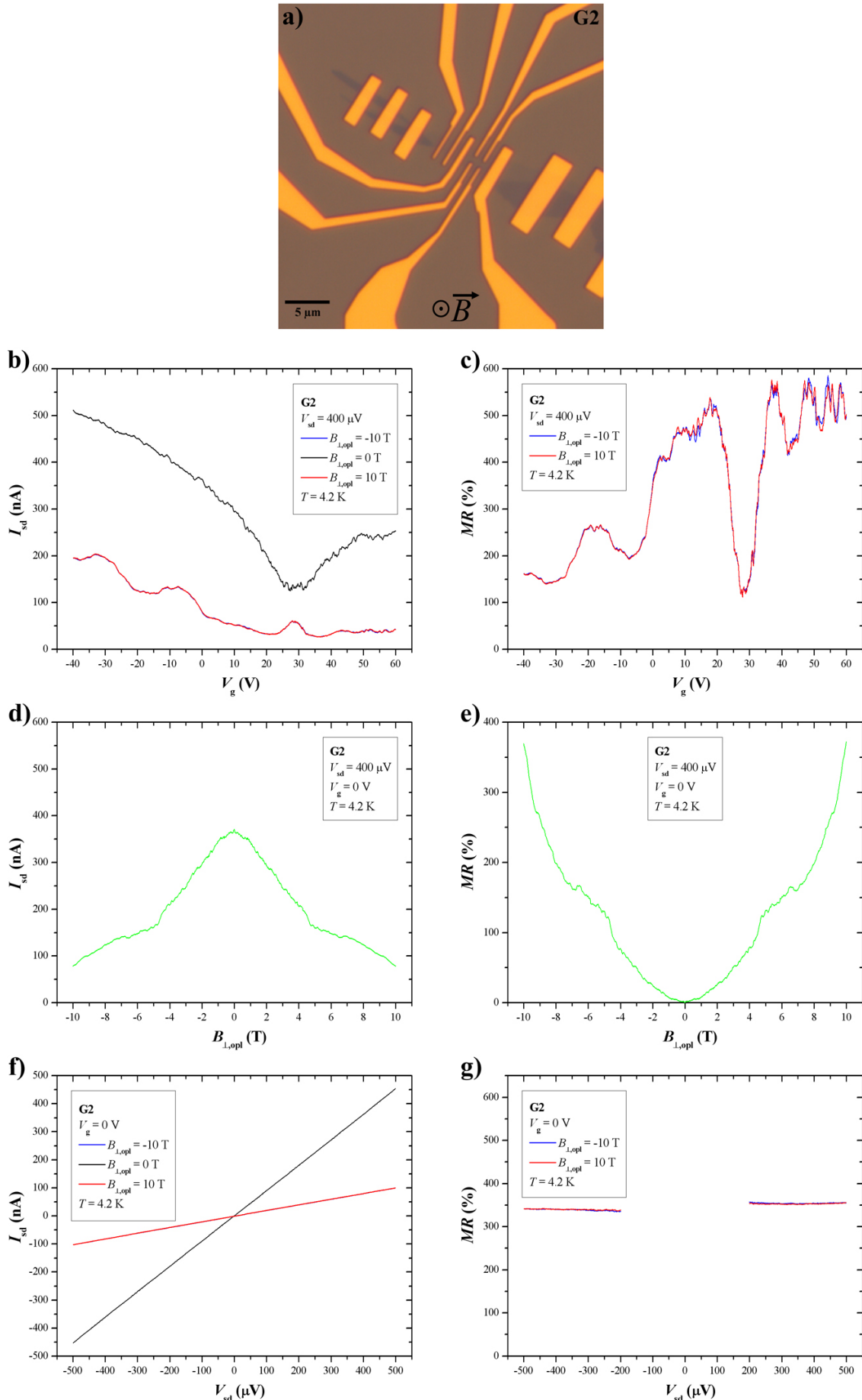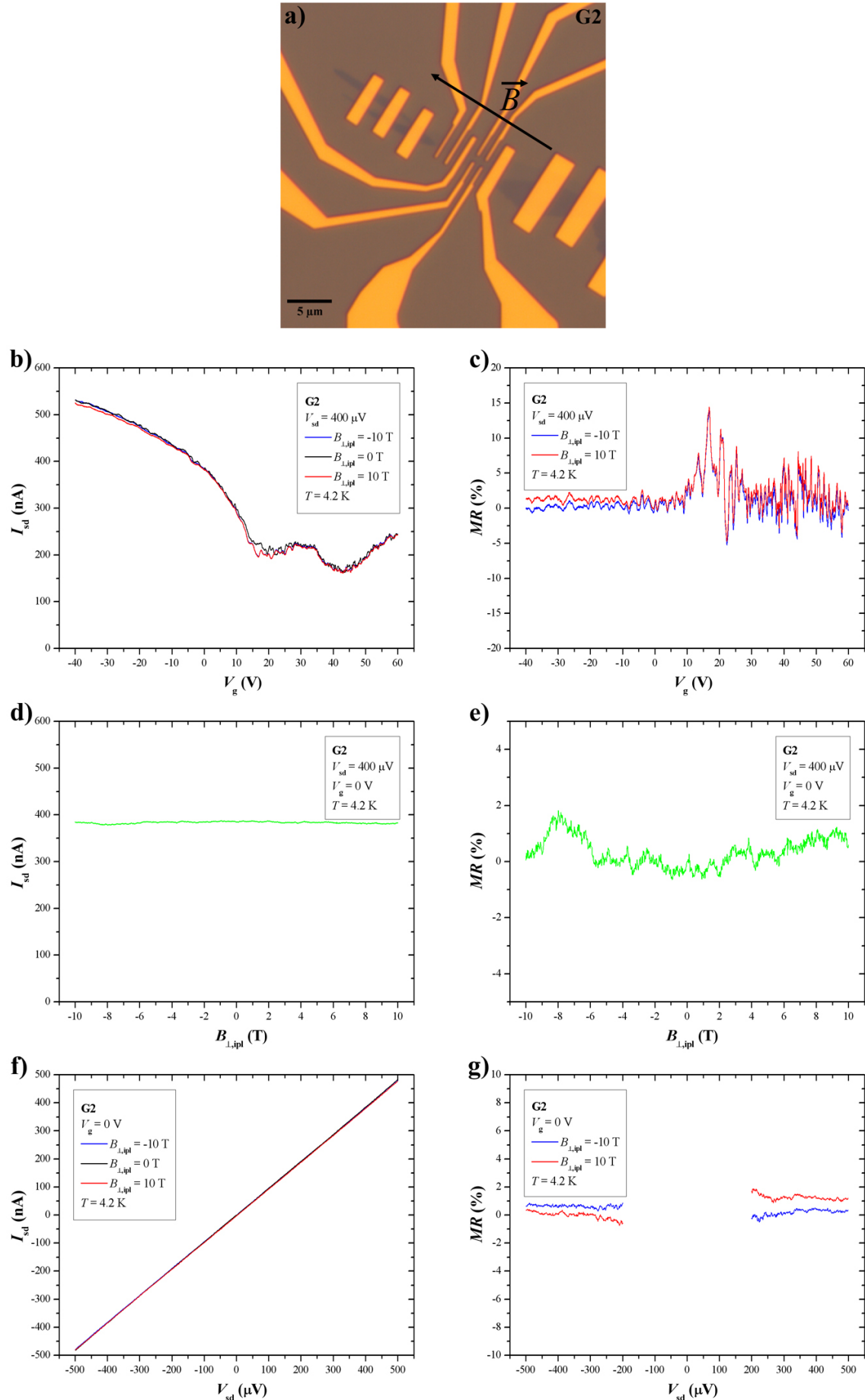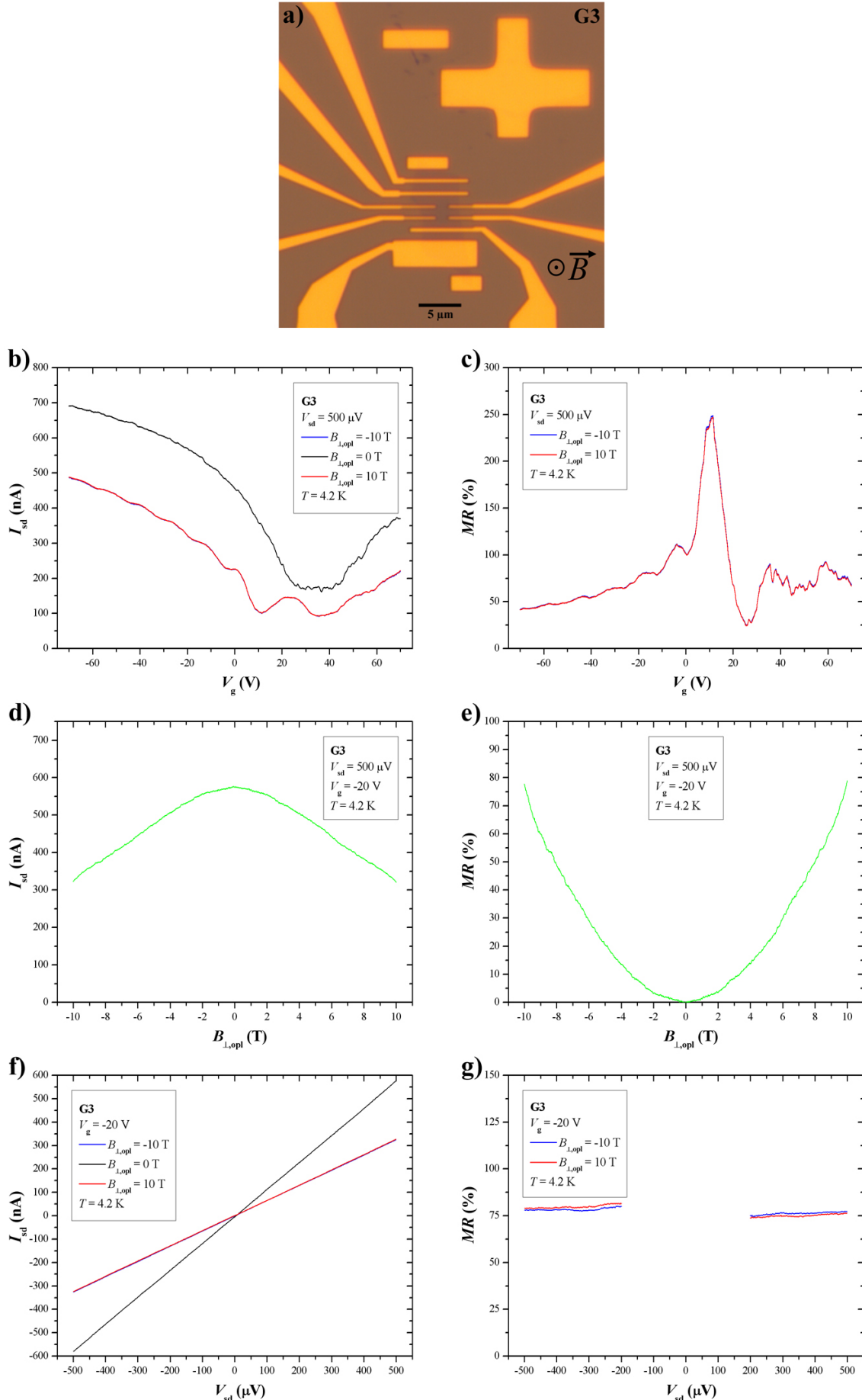
Fig. 5.14: 2-probe magnetotransport measurements performed on sample G2 at 4.2 K with the magnetic field $B_{\perp,\mathrm{opl}}$ perpendicular to the graphene flake. **a)** Magnetic field orientation. **b),d),f)** I_{sd} as function of V_{g}, $B_{\perp,\mathrm{opl}}$ and V_{sd}. **c),e),g)** Magnetoresistance data corresponding to **b),d),f)**.
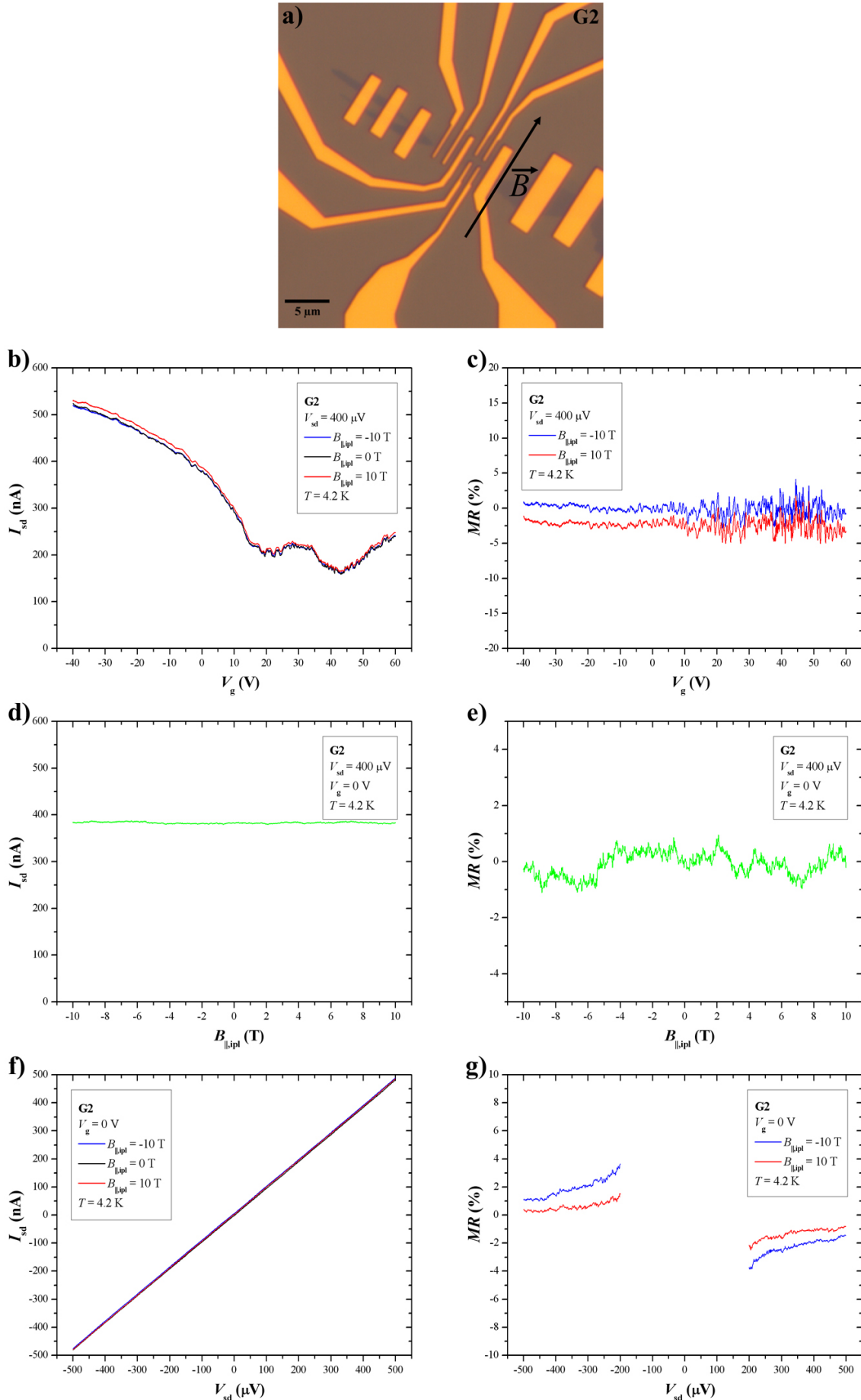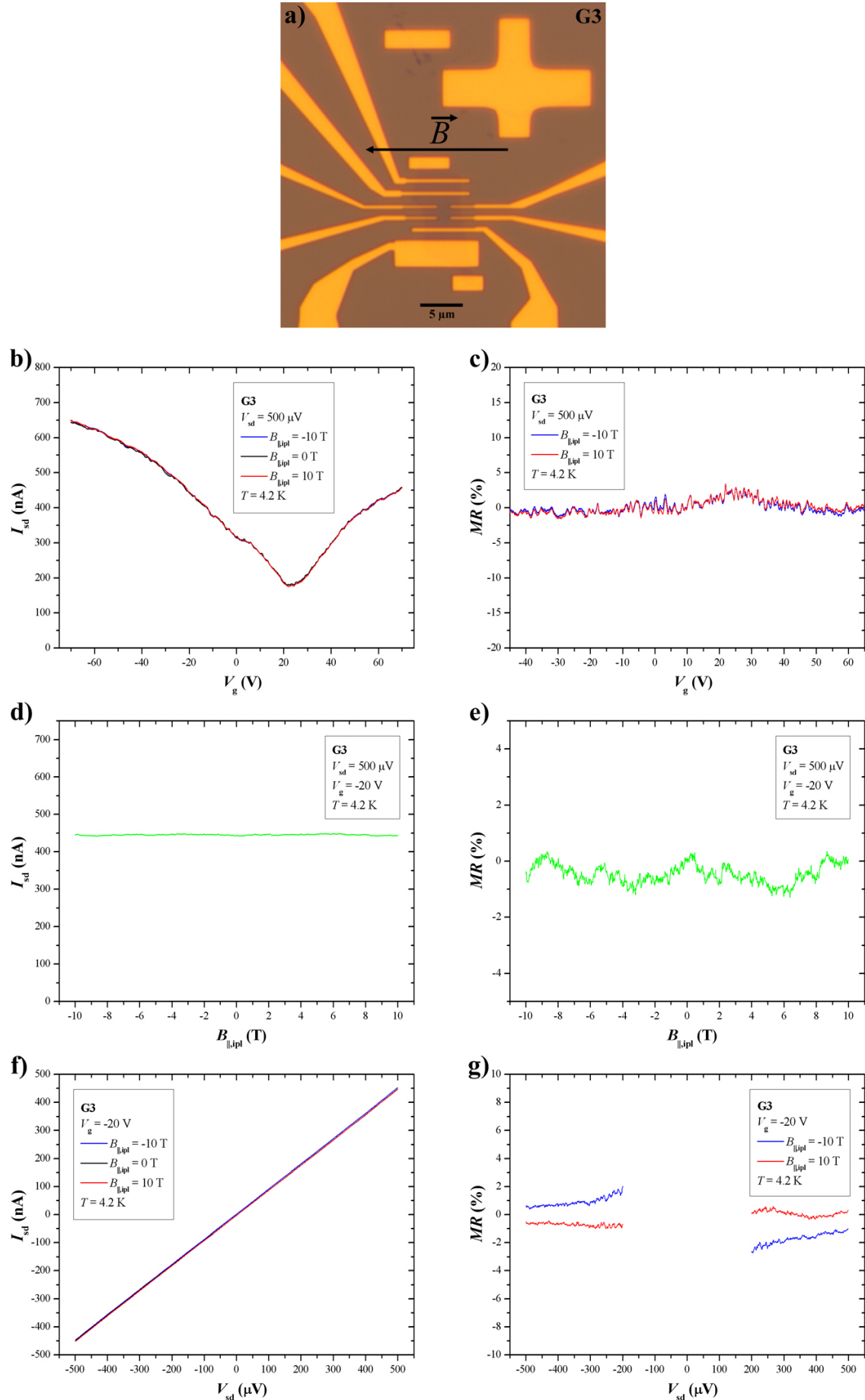
Fig. 5.15: 2-probe magnetotransport measurements performed on sample G2 at 4.2 K with the in-plane magnetic field $B_{\parallel,\text{ipl}}$ parallel to the contacts of G2. **a)** Magnetic field orientation. **b),d),f)** I_{sd} as function of V_{g}, $B_{\parallel,\text{ipl}}$ and V_{sd}. **c),e),g)** Magnetoresistance data corresponding to **b),d),f)**.
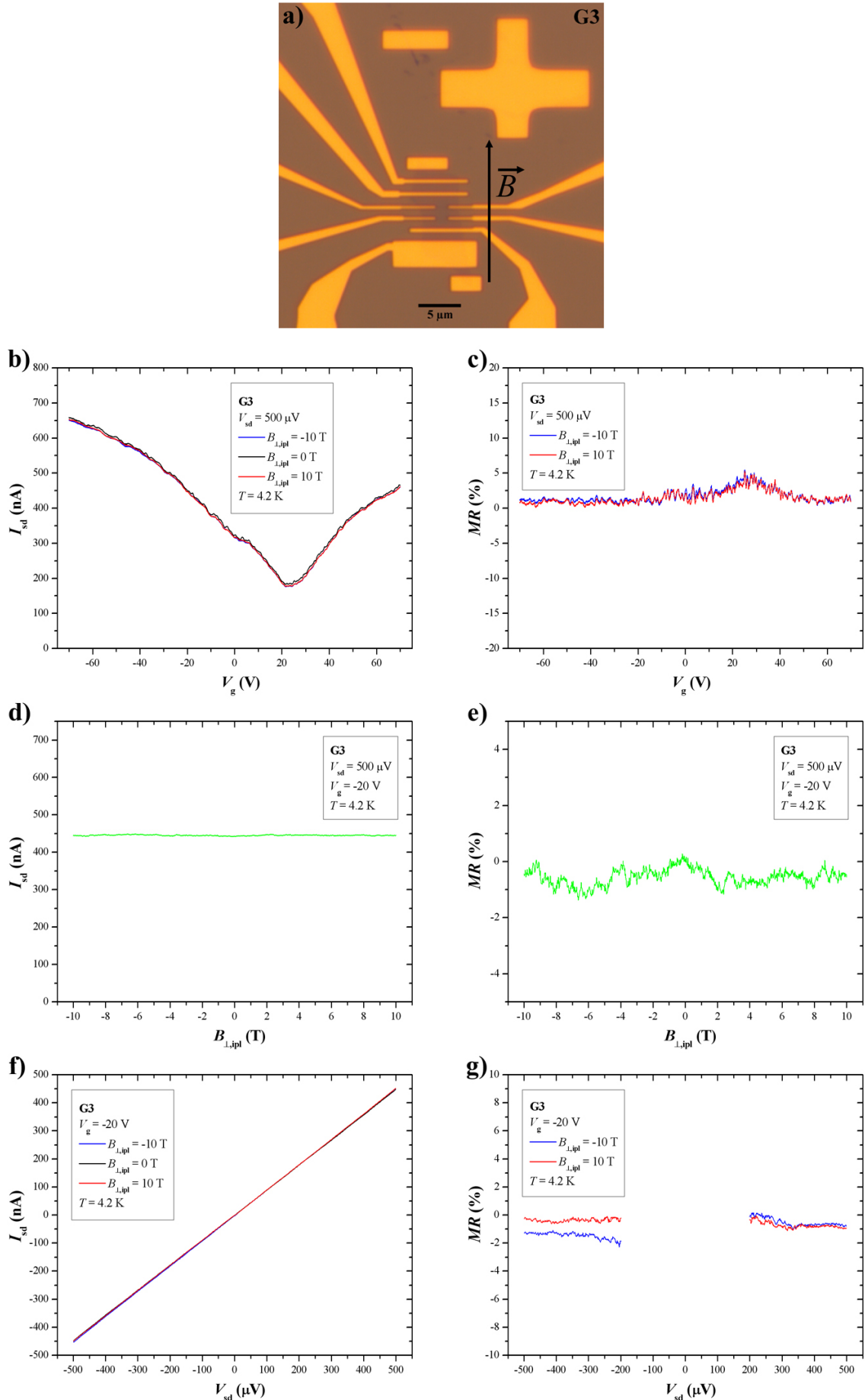
Fig. 5.16: 2-probe magnetotransport measurements performed on sample G2 at 4.2 K with the in-plane magnetic field $B_{\perp,\mathrm{ipl}}$ perpendicular to the contacts of G2. **a)** Magnetic field orientation. **b),d),f)** I_{sd} as function of V_{g}, $B_{\perp,\mathrm{ipl}}$ and V_{sd}. **c),e),g)** Magnetoresistance data corresponding to **b),d),f)**.

Fig. 5.17: 2-probe magnetotransport measurements performed on sample G3 at 4.2 K with the magnetic field $B_{\perp,\text{opl}}$ perpendicular to the graphene flake. **a)** Magnetic field orientation. **b),d),f)** I_{sd} as function of V_{g}, $B_{\perp,\text{opl}}$ and V_{sd}. **c),e),g)** Magnetoresistance data corresponding to **b),d),f)**.

Fig. 5.18: 2-probe magnetotransport measurements performed on sample G3 at 4.2 K with the in-plane magnetic field $B_{\parallel,\mathrm{ipl}}$ parallel to the contacts of G3. **a)** Magnetic field orientation. **b),d),f)** I_{sd} as function of V_{g}, $B_{\parallel,\mathrm{ipl}}$ and V_{sd}. **c),e),g)** Magnetoresistance data corresponding to **b),d),f)**.

Fig. 5.19: 2-probe magnetotransport measurements performed on sample G3 at 4.2 K with the in-plane magnetic field $B_{\perp,\text{ipl}}$ perpendicular to the contacts of G3. **a)** Magnetic field orientation. **b),d),f)** I_{sd} as function of V_{g}, $B_{\perp,\text{ipl}}$ and V_{sd}. **c),e),g)** Magnetoresistance data corresponding to **b),d),f)**.

5.3 Temperature dependence of electrical transport in graphene mono- and bilayers

Transfer characteristics $I_{sd}(V_g)$ and output characteristics $I_{sd}(V_{sd})$ of the graphene mono-layer G2 and the bilayer G3 were measured in 2-probe configuration at three temperatures $T = 4.2$ K, $T = 102/103/106$ K and $T = 289/290$ K, the results are displayed in figures 5.20 and 5.21. The general conclusion is that there is only a weak temperature dependence for both mono- and bilayer graphene systems in the temperature regime 4.2 K $\leq T \leq 290$ K. Except for the gate voltage regime around the Dirac point where both types of charge carriers contribute to the transport, the current decreases with increasing temperature by approx. 5 % from 4.2 K to 106 K for G2, by approx. 7 % from 4.2 K to 102/103 K for G3 and by approx. 15 % for G2 and approx. 25-30 % for G3 when heating from 106/(102/103) K to 289/290 K, probably due to phonon scattering.
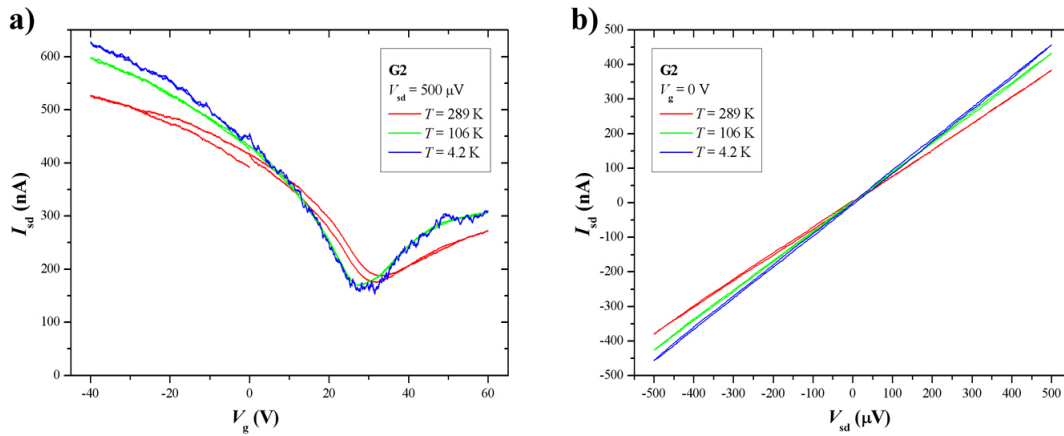
Fig. 5.20: Temperature dependence of 2-probe transport performed on the monolayer graphene sample G2. **a)** Transfer characteristics $I_{sd}(V_g)$ at $V_{sd} = 500\mu$V and $T = 4.2$ K, 106 K, 289 K. **b)** Output characteristics $I_{sd}(V_{sd})$ at $V_g = 0$ V and $T = 4.2$ K, 106 K, 289 K.
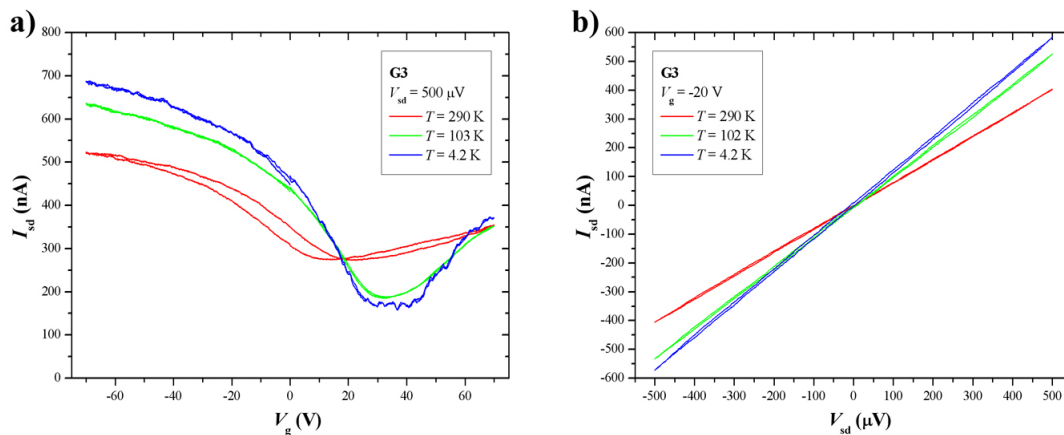
Fig. 5.21: Temperature dependence of 2-probe transport done on the bilayer graphene sample G3. **a)** Transfer characteristics $I_{sd}(V_g)$ at $V_{sd} = 500\mu$V and $T = 4.2$ K, 103 K, 290 K. **b)** Output characteristics $I_{sd}(V_{sd})$ at $V_g = -20$ V and $T = 4.2$ K, 102 K, 290 K.

Apart from the weak temperature dependence of the graphene flakes G2 and G3, other prominent features are observable in the $I_{sd}(V_g)$ characteristics taken at different temperatures: the transfer characteristics exhibit highly reproducible wiggles at 4.2 K which might be associated with the phenomenon of *universal conductance fluctuations* [Ber06], whereas the respective curves are smooth for 103/106 K. At room temperature the curves are still smooth, nevertheless hysteresis effects are clearly visible (Figs. 5.20a, 5.21a) which we attribute to trapped charge carriers at the interface between the transistor channel and the dielectric as in the case of SWNTs and metallofullerene peapods (cp. chapters 6.3 and 7.3).

5.4 Summary of electrical transport in graphene mono- and bilayers

Graphene mono- and bilayers have been investigated by means of electrical transport and magnetotransport measurements. *Quantum Hall effect* measurements have successfully been performed at low temperatures ($T = 32$ mK, 1.5 K and 4.2 K). The R_{xy} values, namely $\pm h/2e^2, \pm h/6e^2, \pm h/10e^2,...$ for graphene monolayers and $\pm h/4e^2, \pm h/8e^2, \pm h/12e^2,...$ for graphene bilayers, which plateaus should occur at according to literature, were reproduced. In order to acquire well resolved *quantum Hall effect* features as the plateaus in the Hall resistance R_{xy} and *Shubnikov-de Haas oscillations* of the longitudinal resistance R_{xx}, reflecting successive filling of Landau levels and dropping to zero in the *quantum Hall regime*, high magnetic fields of up to 18 T had to be employed for graphene bilayers. In contrast, typically 10 to 12 T were required for graphene monolayers for doing so. Interestingly, the quality of the observed *quantum Hall effect* features significantly differed for monolayers with nominally comparable mobility values. Obviously, except of the charge carrier mobility μ, the properties of the edges of the (unetched) graphene flakes are decisive for the *quantum Hall effect* quality.

Moreover, 2-probe magnetotransport measurements have been carried out on graphene mono- and bilayers with the external magnetic field applied in different directions. As anticipated, large magnetoresistance values of up to 600 % have been observed for magnetic fields oriented perpendicularly to the graphene flakes which is attributed to the *Hall effect*. The graphene flakes did not exhibit significant magnetoresistive effects for in-plane magnetic fields.

Finally, $I_{sd}(V_g)$ and $I_{sd}(V_{sd})$ curves taken in 2-probe configurations at different temperatures ($T = 4.2$ K, 102/103/106 K and 289/290 K) point to the weak temperature dependence of electrical transport in graphene mono- and bilayers in this temperature regime.

For all graphene flakes investigated electronically the number of graphene layers they consist of could be identified by complementary studies as high-resolution transmission electron microscopy and Raman spectroscopy.

6. Results on electrical transport in SWNTs

Within this chapter, the results of electrical transport and magnetotransport measurements on empty single-walled carbon nanotubes† will be presented. The main investigations have been to carry out 2-probe magnetotransport experiments on SWNTs with the external magnetic field oriented in different directions, i.e. once aligned along and once perpendicularly to the SWNT axis. To study the behaviour of the contacted SWNTs in the magnetic field we chose to have a closer look into two regimes, first, the *high-current regime* with I_{sd} being several hundreds of nA and second, the *Coulomb blockade regime* with current spikes at particular gate voltages V_g as reviewed briefly in chapter 3.2.3.

Despite more SWNT devices have been measured throughout the project time, only two representative devices named SWNT1 and SWNT2 will be discussed in the following. Standard AFM images of these two devices are given in figures 6.1a and 6.3a.

6.1 Transport and magnetotransport in SWNTs at 4.2 K

Both devices SWNT1 and SWNT2 exhibit p-type semiconducting behaviour at $T = 4.2$ K and $B = 0$ T as displayed by the black $I_{sd}(V_g)$ transfer characteristics in figures 6.1b and 6.3b. The gate dependences $I_{sd}(V_g)$ of both devices show highly reproducible humps which we attribute to electron interference effects. Figures 6.1f and 6.3f depict the output characteristics of the two devices for $B = 0$ T as black lines. In the case of SWNT1 the suppression of the current I_{sd} for small bias voltages is more pronounced than for SWNT2, furthermore SWNT1 has approximately a factor of 2 higher 2-probe resistance than device SWNT2. However, both devices in general exhibit quite comparable electronic features as long as the magnetic field B is zero.

The behaviour of the devices SWNT1 and SWNT2 upon application of a magnetic field is displayed in figures 6.1 to 6.4. As in the chapter on 2-probe magnetotransport measurements on graphene flakes, figures 6.1 to 6.4 are organized such that firstly, an image of the device (in the case of SWNTs, an AFM image) with the direction of the magnetic field is shown (a) followed by the $I_{sd}(V_g)$ transfer characteristics at $B = -10, 0, 10$ T (b), the $I_{sd}(B)$ plot for fixed bias and gate voltages (d) and the output characteristics $I_{sd}(V_{sd})$, again for $B = -10, 0, 10$ T (f). Secondly, the magnetoresistance data calculated utilizing equation (3.40) and corresponding to the b,d,f panels are displayed in the c,e,g panels. Note that in the $MR(V_g)$ plots (c) and the $MR(V_{sd})$ plots (g) values have been omitted for which the calculation of the magnetoresistance is not possible since $I_{sd} \to 0$ or (I_{sd} and $V_{sd}) \to 0$. Finally it should be mentioned that the curves in figures 6.1b,d,f to 6.4b,d,f are averaged curves from multiple runs.

---

†we aimed to perform the measurements on *individual* SWNTs

When applying an external magnetic field perpendicularly to the axes of SWNT1 and SWNT2, in principle the electronic properties of both devices SWNT1 and SWNT2 remain unaffected (Figs. 6.2, 6.4). Considering the transfer characteristics $I_{sd}(V_g)$ in figures 6.2b and 6.4b as well as the output characteristics $I_{sd}(V_{sd})$ in figures 6.2f and 6.4f, one sees that the curves measured for $B = -10, 0, 10$ T very well lie on top of each other, with some deviations in detail appearing in the respective MR plots in figures 6.2c,g and 6.4c for small values of V_g and V_{sd}, respectively. The origin of these deviations is unknown at the moment. Nevertheless, the matching of the $I_{sd}(V_{sd})$ and $I_{sd}(V_g)$ curves for both SWNT1 and SWNT2 is reasonably good to state that there are only negligible electronic changes upon application of a magnetic field perpendicular to the SWNT axes. This is confirmed by the direct measurements of the currents I_{sd} as functions of the magnetic field for fixed bias and gate voltages in figures 6.2d and 6.4d.

Major differences between SWNT1 and SWNT2 become apparent when the external magnetic field B is oriented along the SWNT axes (Figs. 6.1 and 6.3). In device SWNT2, the changes of the electrical characteristics with the application of a parallel magnetic field $B_{\parallel}$ in general are minor, as indicated by figures 6.3b-e. For large gate voltages V_g in the transfer characteristics and large bias voltages V_{sd} in the output characteristics, respectively, the magnetoresistance is between 0 and 4 % (Figs. 6.3c,g). The $MR(B)$ plot at $V_g = -4.0$ V exhibits between 0 and 2 % magnetoresistance between -10 and 10 T (Fig. 6.3e). However, there are significant deviations of unknown origin from this *minor magnetoresistance* in the $I_{sd}(V_g)$ characteristics for small gate voltages (Fig. 6.3c) and especially in the $I_{sd}(V_{sd})$ characteristics for small bias voltages (Fig. 6.3g).

In contrast to the *minor magnetoresistance* of SWNT2 for a magnetic field oriented along the SWNT axis, device SWNT1 shows strong and systematic change of its electrical characteristics upon application of a parallel magnetic field $B_{\parallel}$ (Fig. 6.1). With exception of the small negative gate voltages $V_g > -2$ V, the magnetoresistance at $B_{\parallel} = -10$ T or 10 T is approx. -8 to -14 % (Fig. 6.1c) for the $I_{sd}(V_g)$ transfer characteristics in figure 6.1b. Similarly, except for the small bias voltage regime, $MR(V_{sd})$ is between -5 and -10 % for the output characteristics $I_{sd}(V_{sd})$ (Figs. 6.1f,g). Measuring the current I_{sd} through SWNT1 in dependence of the parallel magnetic field $B_{\parallel}$ at $V_{sd} = 100$ mV and $V_g = -3.9$ V (Fig. 6.1d) results in a *linear negative magnetoresistance* as a function of $B_{\parallel}$ with $MR \approx$ -12 and -9 % for $B_{\parallel} = \pm 10$ T (Fig. 6.1e)[†].

This specific and well pronounced behaviour of SWNT1 in a parallel magnetic field can be ascribed to the coupling of the orbital momentum of the electrons around the circumference of a chiral SWNT and the linear momentum of the electrons along the SWNT axis as discussed in the theoretical work by E. L. Ivchenko and B. Spivak [Ivc02] (cp. chapter 3.2.4). As claimed in the theory, we see a linear increase of the current through the SWNT device with the applied magnetic field $B_{\parallel}$ in axial direction (Fig. 6.1d), i.e. a

---

[†]The reason for the magnetoresistance asymmetry between -10 and 10 T is unclear.

linear *negative* magnetoresistance MR as function of the magnetic field $B_\parallel$. Furthermore, this effect vanishes after rotating device SWNT1 such that the magnetic field is aligned perpendicularly to the SWNT axis - again, this is in agreement with the theory in [Ivc02], which does not expect an effect of a perpendicular magnetic field on the current through a chiral SWNT.

So our conclusion would be that SWNT1 is an individual, chiral SWNT (cp. Fig. 2.4c), whereas SWNT2 not showing significant electrical response upon application of a magnetic field along or perpendicular to its axis should be an achiral SWNT following the theory in [Ivc02].

Non-contact, high-resolution AFM investigations which ultimately can deliver atomic resolution and give information on the helicity of a SWNT [Ash04] were applied to gain information on the geometry of the SWNT1 and SWNT2 devices. SWNT1 was imaged along the whole length between the contacts in a series of eleven 20 by 20 nm AFM micrographs which were put together to figure 6.5b. The most important information one can extract from this figure is that SWNT1 - contrary to our expectations - is a bundle of single-walled carbon nanotubes. In addition, the high-resolution AFM image in figure 6.5b, especially the upper part of the image series, shows that the nanotubes within the bundle are twisted around each other. Due to adsorbates and probably amorphous carbon on the bundle atomic resolution as in [Ash04, Ash08] was not possible and it is hard to say, whether this twist continues along the whole bundle or not. Furthermore, due to the same reasons, one can not even tell the exact number of tubes within the bundle. From the standard tapping-mode AFM images of SWNT1 taken at ambient conditions (Fig. 6.1a) it is known that its height is approx. 1.6 nm, which - together with experiences we made correlating standard AFM and TEM on the same sample (cp. chapter 4.7.1 and Fig. 7.9) - leads to the conclusion that the bundle should not comprise more than 3 SWNTs. A high-resolution AFM image of SWNT2 (not shown here) confirms that SWNT2 is an individual SWNT, however, the structural indices (n, m) could not be resolved due to the adsorbates mentioned already.

Therefore our explanation for the pronounced, negative magnetoresistance of SWNT1 for a parallel magnetic field $B_\parallel$ is altered by the AFM investigation as follows: either the negative magnetoresistance of SWNT1 in the case of an axially oriented magnetic field is due to electrons moving along a chiral SWNT within the bundle (according to the theory in [Ivc02]) where this individual tube would dominate the transport in the bundle or the interaction with the magnetic field arises from electrons following the twist of the SWNTs around each other. In general, a pronounced magnetoresistance is not a typical signature of SWNT bundles, as one can learn from [Hun03], where 8 out of 9 SWNT bundles do not show any magnetoresistance in an axially aligned magnetic field $B_\parallel$. In the case of SWNT2, we keep to the explanation that it does not exhibit significant magnetoresistance


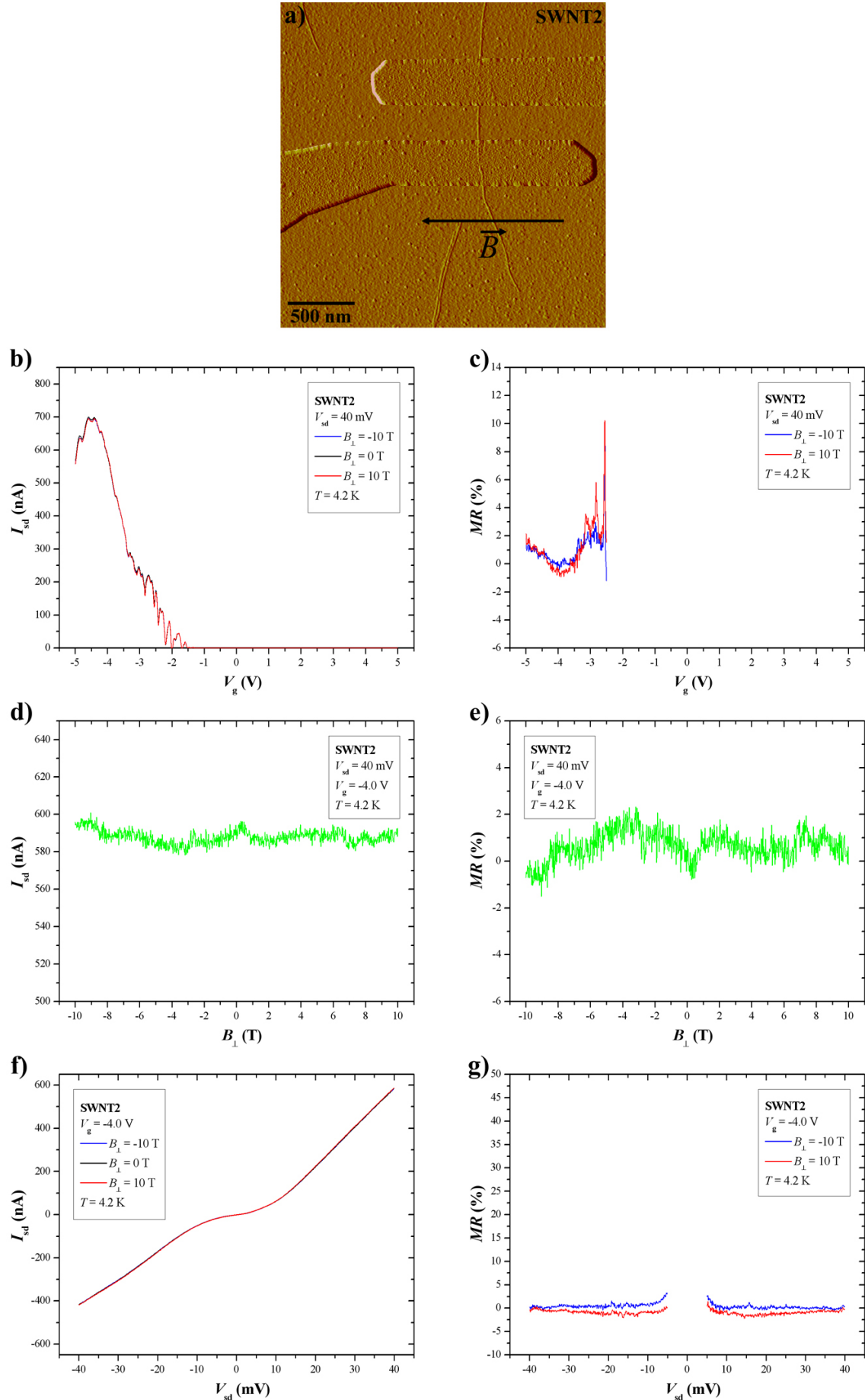[†]which is more likely in a SWNT bundle due to the larger cross-section
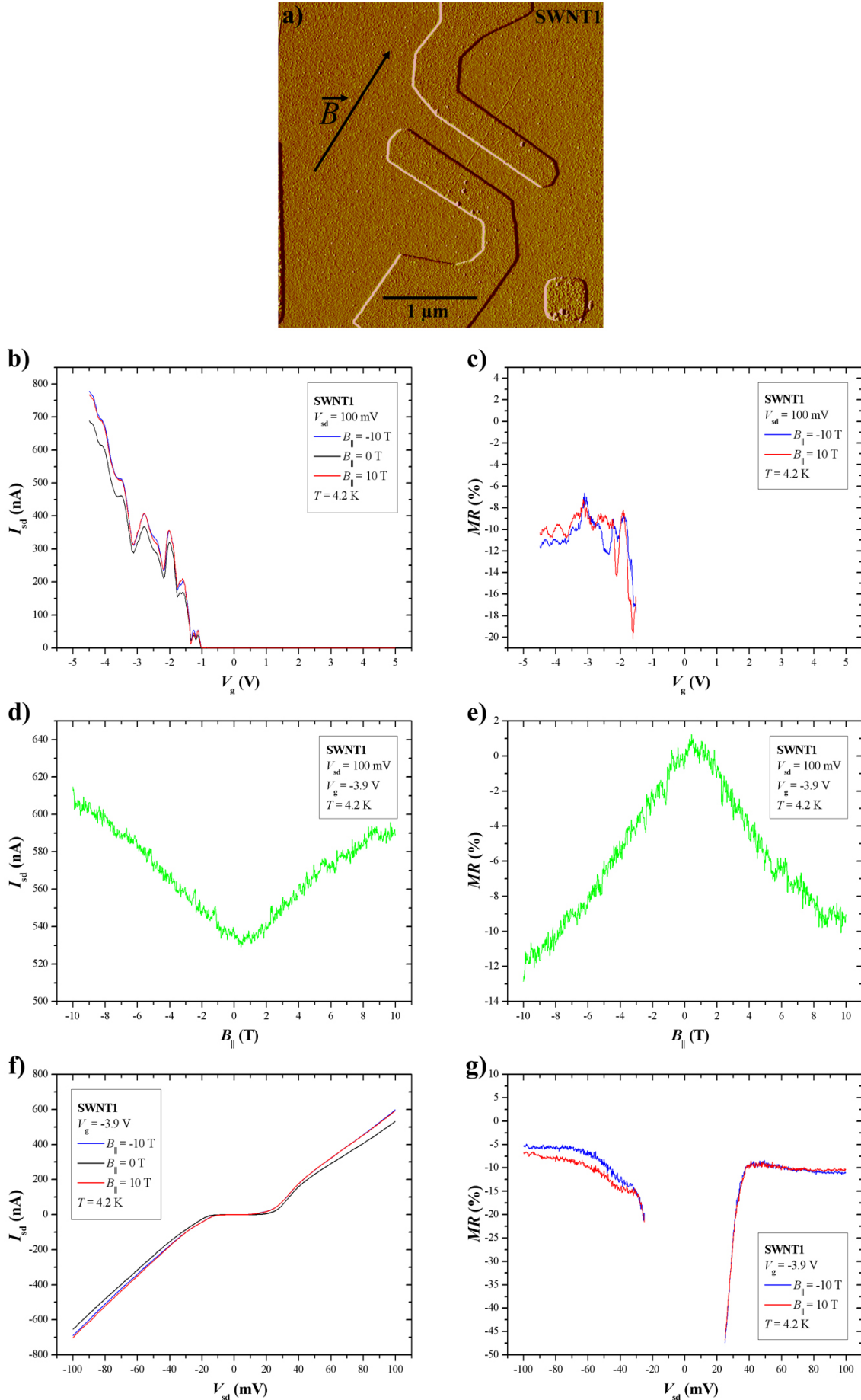
Fig. 6.1: 2-probe magnetotransport measurements performed on sample SWNT1 at 4.2 K with the magnetic field $B_{\parallel}$ parallel to the SWNT axis. **a)** Magnetic field orientation. **b),d),f)** I_{sd} as function of V_g, $B_{\parallel}$ and V_{sd}. **c),e),g)** Magnetoresistance data corresponding to **b),d),f)**.
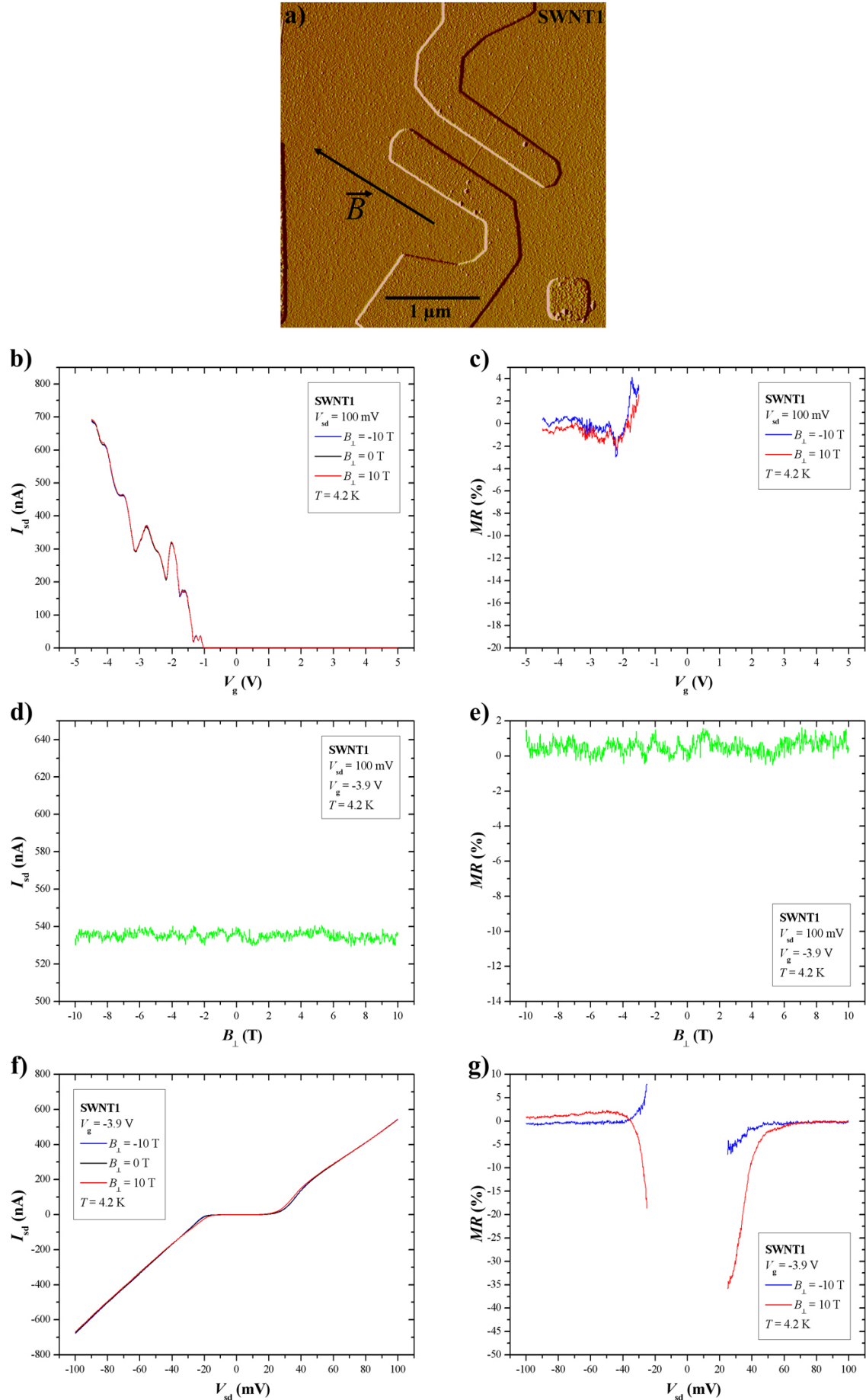
Fig. 6.2: 2-probe magnetotransport measurements performed on sample SWNT1 at 4.2 K with the magnetic field $B_\perp$ perpendicular to the SWNT axis. **a)** Magnetic field orientation. **b),d),f)** I_{sd} as function of V_g, $B_\perp$ and V_{sd}. **c),e),g)** Magnetoresistance data corresponding to **b),d),f)**.
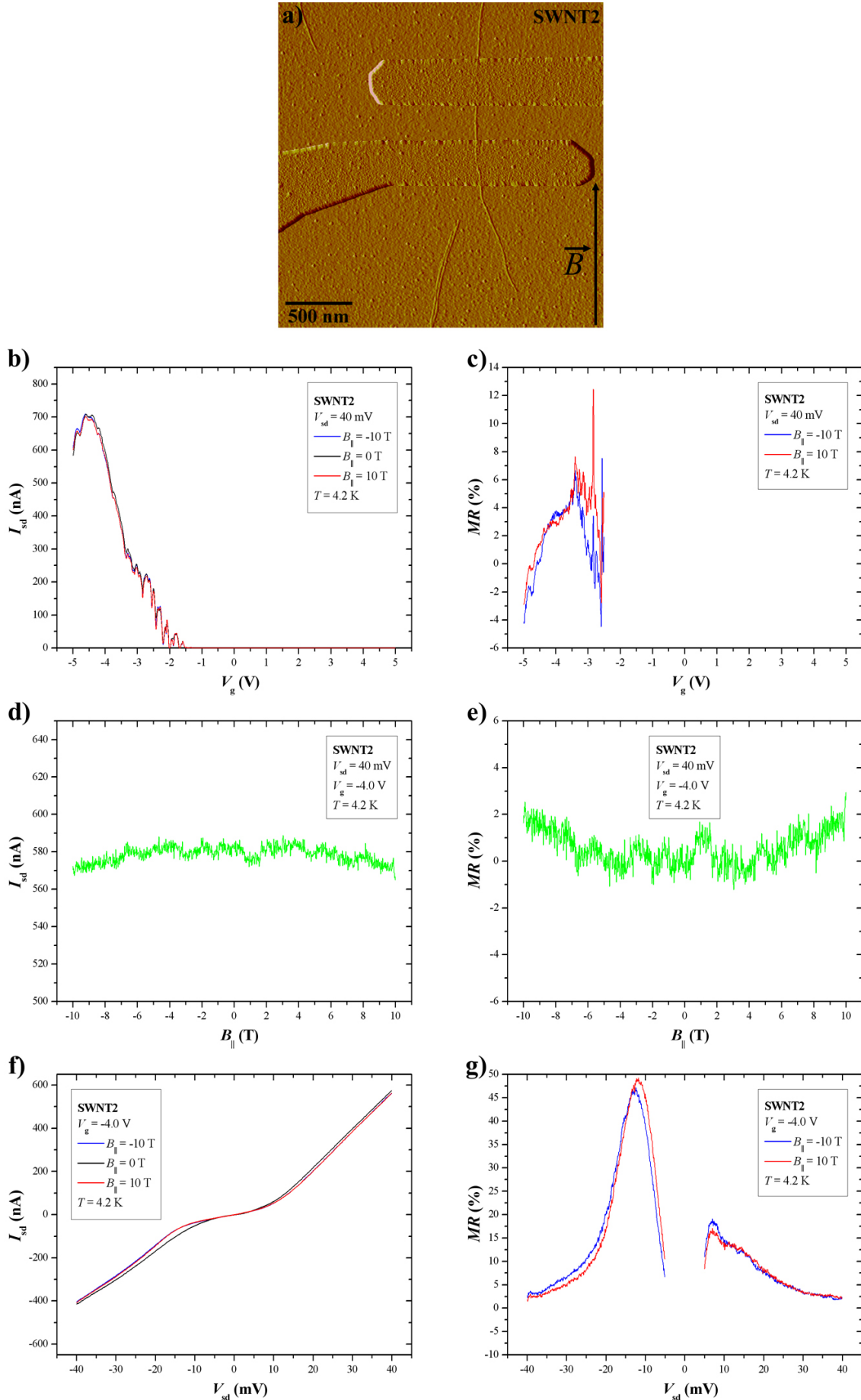
Fig. 6.3: 2-probe magnetotransport measurements performed on sample SWNT2 at 4.2 K with the magnetic field $B_\parallel$ parallel to the SWNT axis. **a)** Magnetic field orientation. **b),d),f)** I_{sd} as function of V_g, $B_\parallel$ and V_{sd}. **c),e),g)** Magnetoresistance data corresponding to **b),d),f)**.

Fig. 6.4: 2-probe magnetotransport measurements performed on sample SWNT2 at 4.2 K with the magnetic field $B_\perp$ perpendicular to the SWNT axis. **a)** Magnetic field orientation. **b),d),f)** I_{sd} as function of V_g, $B_\perp$ and V_{sd}. **c),e),g)** Magnetoresistance data corresponding to **b),d),f)**.
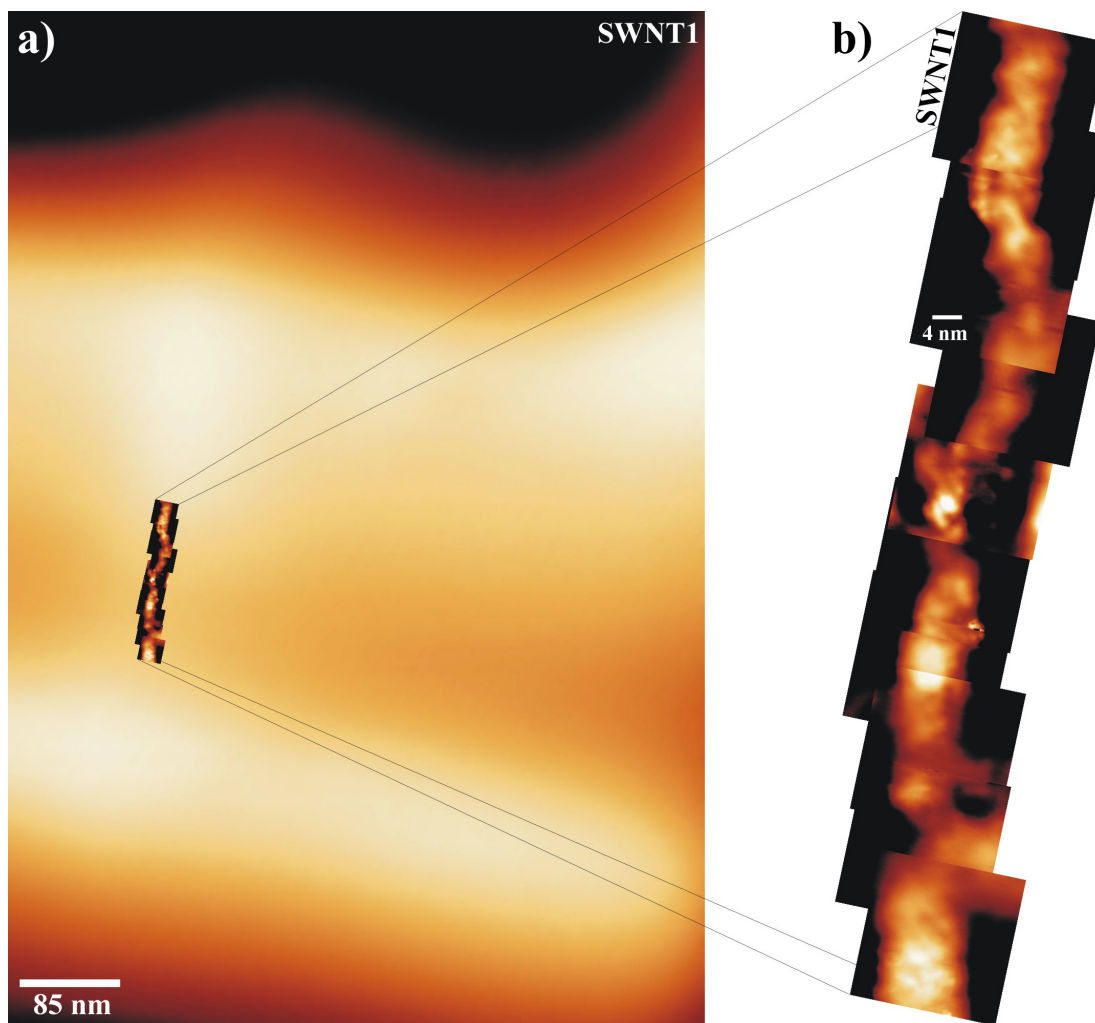
Fig. 6.5: a) Low-resolution AFM image of the contact region of device SWNT1. The bright areas correspond to the metal contacts. **b)** A series of 20 by 20 nm high-resolution AFM images put together to depict SWNT1 completely. Contrary to the expectations, SWNT1 is not an individual SWNT but a SWNT bundle, in which the SWNTs seem to be twisted around each other (see upper section of the image). Due to adsorbates and potentially amorphous carbon on top of the bundle, neither the number of tubes can be identified, nor the structural indices can be obtained. Images by Makoto Ashino, University of Hamburg, 2008.

in either parallel or perpendicular magnetic field direction since it should be an achiral SWNT according to [Ivc02]. High-resolution AFM both on SWNT1 and SWNT2 will be redone after removing as many adsorbates as possible. To clarify experimentally, whether the negative magnetoresistance of SWNT1 is due to the twisted SWNTs within the bundle or to a chiral SWNT dominating the transport and exhibiting magnetoresistance according to [Ivc02], a further series of combined experiments (magnetotransport plus high-resolution AFM) is suggested using CVD SWNTs which are known to occur as individual tubes predominantly.

6.2   Magnetotransport in SWNTs in the Coulomb blockade regime

Both samples SWNT1 and SWNT2 show *Coulomb blockade* behaviour at $B = 0$ T, $T = 4.2$ K and small bias voltages $V_{sd} = 1$ and 2 mV, respectively. The characteristic dI_{sd}/dV_{sd} vs. gate voltage plots are given in figures 6.6a and 6.9a. The different peak heights reflect different couplings of the discrete energy states to the source and drain leads (cp. chapter 3.2.3). Measuring the differential conductance as a function of both the bias and the gate voltage, the *diamond plots* depicted in figures 6.6b and 6.9b are obtained. Finally, the current I_{sd} through the devices SWNT1 and SWNT2 in this regime of Coulomb blockade and few-electron tunneling is plotted as function of V_{sd} and V_g for $B = 0$ T and $T = 4.2$ K (Figs. 6.6c, 6.9c).

Having a look at the overall structures of the diamond plots in figures 6.6b and 6.9b, it can be realized that the diamonds representing the suppressed current regime of SWNT1 in figure 6.6b are partially blurred and surrounded by much more noise than in the case of SWNT2, for which the diamond shapes are sharp and well defined and nearly no noise occurs (Fig. 6.9b). This could be due to the fact that SWNT1 consists of bundled and twisted SWNTs[†] according to the high-resolution AFM image in figure 6.5, whereas SWNT2 is an individual SWNT. However, there is a disruption in the diamond plot of SWNT2 (Fig. 6.9b) manifesting itsself as a sharp line along the V_g direction at $V_g \approx 2.85$ V after which a part of the diamond pattern re-appears. This artefact arises from a *(de-)charging event* in the vicinity of the device (e.g. in the oxide layer), i.e. charges get trapped or released which changes the effective gate potential.

Evaluating the slopes of the diamonds in figures 6.6b and 6.9b according to equation (3.39) and taking into account that the gate voltage spacing ΔV_g^{p-p} between each two current or differential conductance peaks equals e/C_g (Fig. 3.25) allows to calculate the capacitances C_s, C_d, C_g and C_Σ as well as the *single-electron charging energy* E_C (cp. chapter 3.2.3) for the devices SWNT1 and SWNT2. Being aware of C_g and C_Σ, one is able to convert a difference in the gate voltage ΔV_g into the respective energy difference ΔE using the *gate efficiency factor* $\beta = C_g/C_\Sigma$, where

$$\Delta E = \beta \, \Delta V_g \, e \, , \tag{6.1}$$

which is a direct consequence of $2E_C = e^2/C_\Sigma$ and $\Delta V_g^{p-p} = e/C_g$. Performing these calculations for SWNT1 and SWNT2 results in $C_{s,SWNT1} = 0.03$ aF, $C_{d,SWNT1} = 3.9$ aF, $C_{g,SWNT1} = 2.1$ aF, $C_{\Sigma,SWNT1} = 6.0$ aF, $E_{C,SWNT1} = 13.4$ meV, $\beta_{SWNT1} = 0.35$, $C_{s,SWNT2} = 0.5$ aF, $C_{d,SWNT2} = 5.6$ aF, $C_{g,SWNT2} = 2.5$ aF, $C_{\Sigma,SWNT2} = 8.7$ aF, $E_{C,SWNT2} = 9.2$ meV and $\beta_{SWNT2} = 0.29$.

[†]with a much less well defined structure than an individual SWNT

After investigating the samples SWNT1 and SWNT2 in the *Coulomb blockade* and *the few-electron tunneling regime* at $T = 4.2$ K and $B = 0$ T, we now turn to the behaviour of the Coulomb blockade peaks in the differential conductance $dI_{sd}/dV_{sd}(V_g)$ in externally applied axial and perpendicular magnetic fields. The results of the corresponding magnetotransport measurements at $T = 4.2$ K are displayed in figures 6.7 and 6.8 for SWNT1 and in figures 6.10 and 6.11 for SWNT2, respectively.

Figures 6.7c,e and 6.10c,e show how the Coulomb blockade peaks of SWNT1 and SWNT2 change upon application of a magnetic field $B_{\parallel}$ along the SWNT axes as 3-dimensional plots[†]. The most significant changes for both SWNT1 and SWNT2 are the obvious height undulations of the differential conductance peaks which are symmetric in the magnetic field and are typically different for different states. To compare the shapes of the various differential conductance peaks as functions of the parallel magnetic field $B_{\parallel}$, 2D-sections out of the 3-dimensional graphs in figures 6.7c,e and 6.10c,e have been extracted for fixed gate voltages V_g and displayed in figures 6.7a and 6.10a. Finally, in order to judge eventual shifts of the differential conductance peaks along the gate voltage direction due to the applied magnetic field $B_{\parallel}$, greyscale plots of the same datasets, figures 6.7c,e and 6.10c,e are based on, are shown in figure 6.8a for SWNT1 and figure 6.11a for SWNT2. Indeed, slight shifts of the dI_{sd}/dV_{sd} peaks along the V_g are observable for different values of the parallel magnetic field $B_{\parallel}$ in both samples SWNT1 and SWNT2. In contrast, the corresponding greyscale plots for perpendicularly aligned magnetic fields $B_{\perp}$ (Figs. 6.8b for SWNT1 and 6.11b for SWNT2) only display straight vertical bright lines, i.e. the differential conductance peaks do not shift their positions significantly with regard to V_g in the case of a perpendicular magnetic field. Moreover there are only very minor height undulations of the Coulomb blockade peaks for a magnetic field aligned perpendicularly to the axes of SWNT1 and SWNT2 as one can see in the corresponding figures 6.7b,d,f and 6.10b,d,f.

The observed effects of a parallel magnetic field $B_{\parallel}$ on the Coulomb blockade peaks in the differential conductance $dI_{sd}/dV_{sd}(V_g)$ of samples SWNT1 and SWNT2 are attributed to *diamagnetic shifts* ($\propto B^2$) and *Zeeman shifts* ($\propto B$) of the energies of the quantum dot states. The shifts of the Coulomb blockade peaks along the gate voltage direction in figures 6.8a and 6.11a for parallel magnetic fields $B_{\parallel}$ are due to combined diamagnetic and Zeeman shifts, where the different directions of curvature occuring in the respective diagrams of SWNT1 and SWNT2 represent energy gain/loss and arise from the Zeeman shift of the electron spin which can have positive or negative sign. In comparison to similar results gained for quantum dots defined within GaAs heterostructures (Fig. 3.27c) [Wei94, Wei05], the curvature in figures 6.8a and 6.11a is rather shallow, indicating weaker energy shifts in the single-walled carbon nanotubes. Nevertheless, it is possible to observe crossing of ground states and the respective excited states as points at which the curvature of Coulomb blockade peak shifts reverses, e.g. for SWNT2 at $V_g \approx$ -3.185 V and $V_g \approx$ -3.068 V in figure 6.11a. In this case, a ground state and its ex-


[†]the difference between c and e is the different perspective at the 3-dimensional graph

cited state are getting equal in energy, the excited state becomes the new ground state and vice versa. In general, it is assumed, that ground states and excited states move towards each other as experimentally shown for GaAs based quantum dots in [Wei94, Wei05]. In this model of energy shifts of the quantum dot states due to *diamagnetic shifts* and *Zeeman shifts*, also the height undulation of the differential conductance Coulomb blockade peaks can be understood. The height of a Coulomb blockade peak is a measure for the current through the dot in this state and for the coupling of the state to the metal leads. Now we consider a ground state and an excited state, the widths of which are given by thermal broadening and by their lifetimes[†], in proximity to each other, so that they are overlapping partially. If both states are close enough so that at least a part of each broadened peak is within the bias energy window eV_{sd}, both states contribute to the overall coupling to the leads. The mentioned *diamagnetic shifts* and *Zeeman shifts* move the states energetically with respect to each other and thus lead to a different weighting of their contributions to the overall coupling. This results in a continuous variation of the overall coupling to the leads reflected as Coulomb blockade peak height undulations in figures 6.7c,e and 6.10c,e. If one of the states is well aligned to the center of the bias energy window eV_{sd} (cp. chapter 3.2.3) and thus dominates the coupling to the leads, there is a peak in the undulating pattern. If subsequentially the state is shifted out of the center of the bias energy window, the overall coupling decreases gradually until the next state is moving towards the center. The chosen bias voltages $V_{sd} = 2$ mV for SWNT1 and $V_{sd} = 1$ mV for SWNT2 favour the observability of this continuous transition, since the bias energy window is fairly large allowing more than one state to lie within. Applying a narrow bias window plus adjusting small linewidths (low temperature, low coupling) would lead to a more discrete switching between high and low coupling, i.e. pronounced plateaus would occur in the undulating pattern instead of sine-like undulation.

It is not fully understood yet, why a magnetic field $B_\perp$ oriented perpendicularly to the axes of SWNT1 and SWNT2 does not have very significant effects regarding Coulomb blockade peak shifts or height undulations. Nevertheless, it is obvious that the single-walled carbon nanotube geometry plays a dominant role. One suggestion to explain this behaviour is that the diamagnetic moments in the case of an axial magnetic field $B_\parallel$ are induced in such a way that the electrons move along the circumference of the SWNT, regardless of its helicity. Such diamagnetic moments could not be induced by a perpendicular magnetic field, however.


[†]The lifetime of a state in a quantum dot is given by the time an electron resides in this state in the conducting regime. For large tunneling barriers, i.e. weak coupling, this residing time Δt is large as well leading to a sharp Coulomb blockade peak with a small lifetime broading ΔE according to the Heisenberg uncertainty relation.
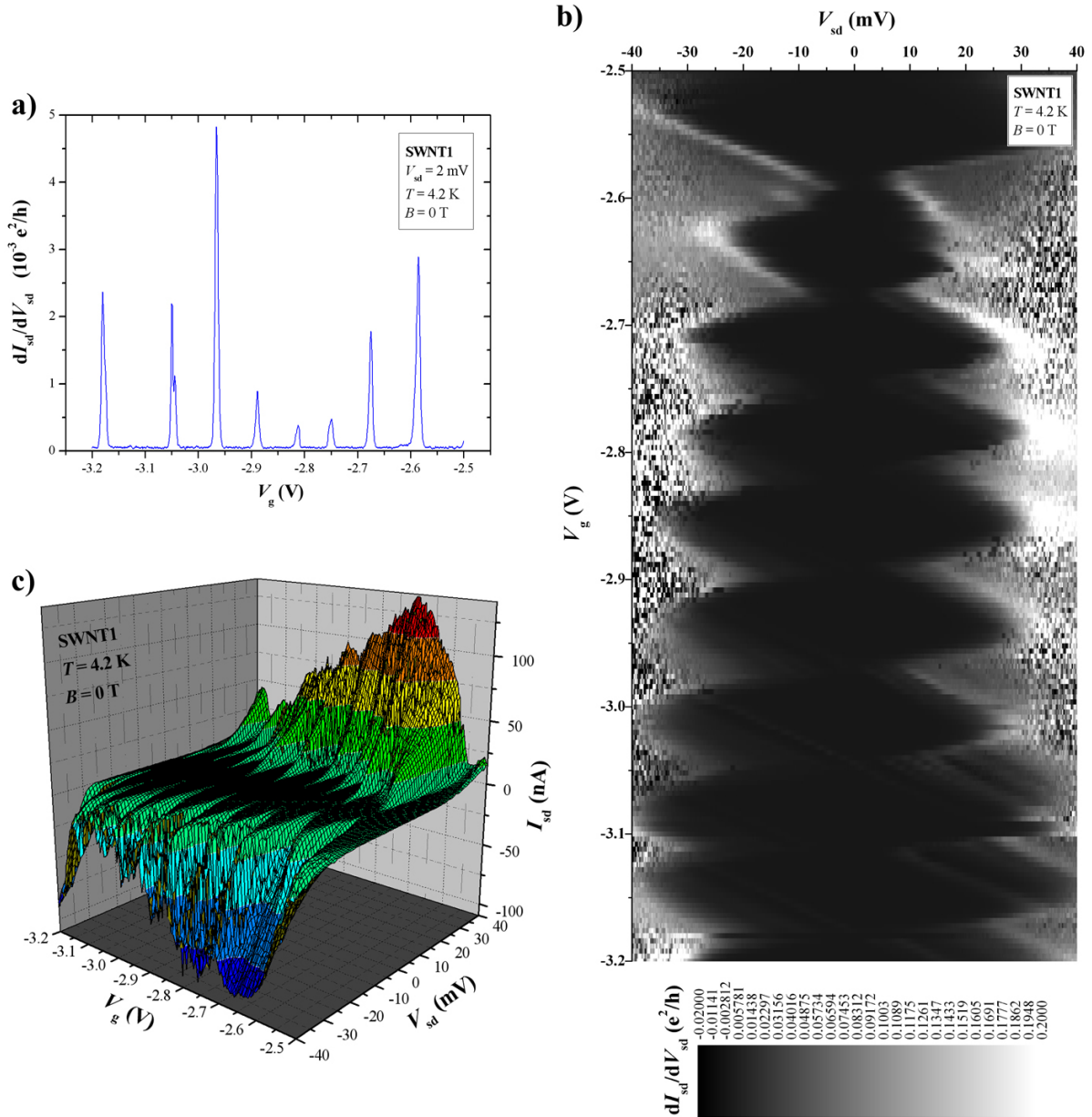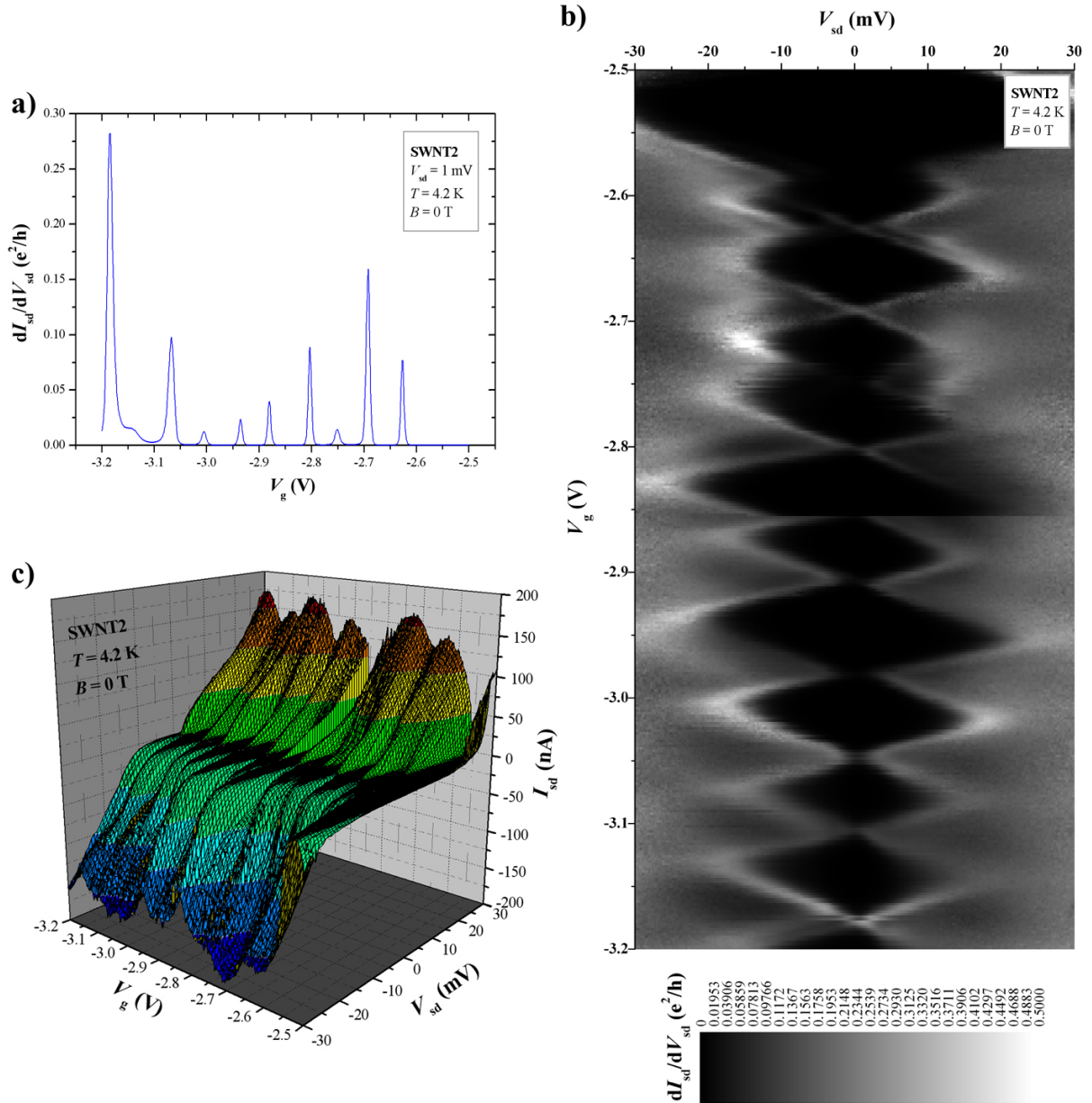
Fig. 6.6: a) Coulomb blockade oscillations of the differential conductance $\mathrm{d}I_\mathrm{sd}/\mathrm{d}V_\mathrm{sd}$ of sample SWNT1 plotted vs. the applied gate voltage V_g at $V_\mathrm{sd} = 2$ mV, $T = 4.2$ K and $B = 0$ T. **b)** Diamond plot of SWNT1, i.e. $\mathrm{d}I_\mathrm{sd}/\mathrm{d}V_\mathrm{sd}$ as a function of the bias voltage V_sd and the gate voltage V_g at $T = 4.2$ K and $B = 0$ T. **c)** 3-dimensional graph of the current I_sd through device SWNT1 in the regime of Coulomb blockade and few-electron tunneling as a function of V_sd and V_g at $T = 4.2$ K and $B = 0$ T.
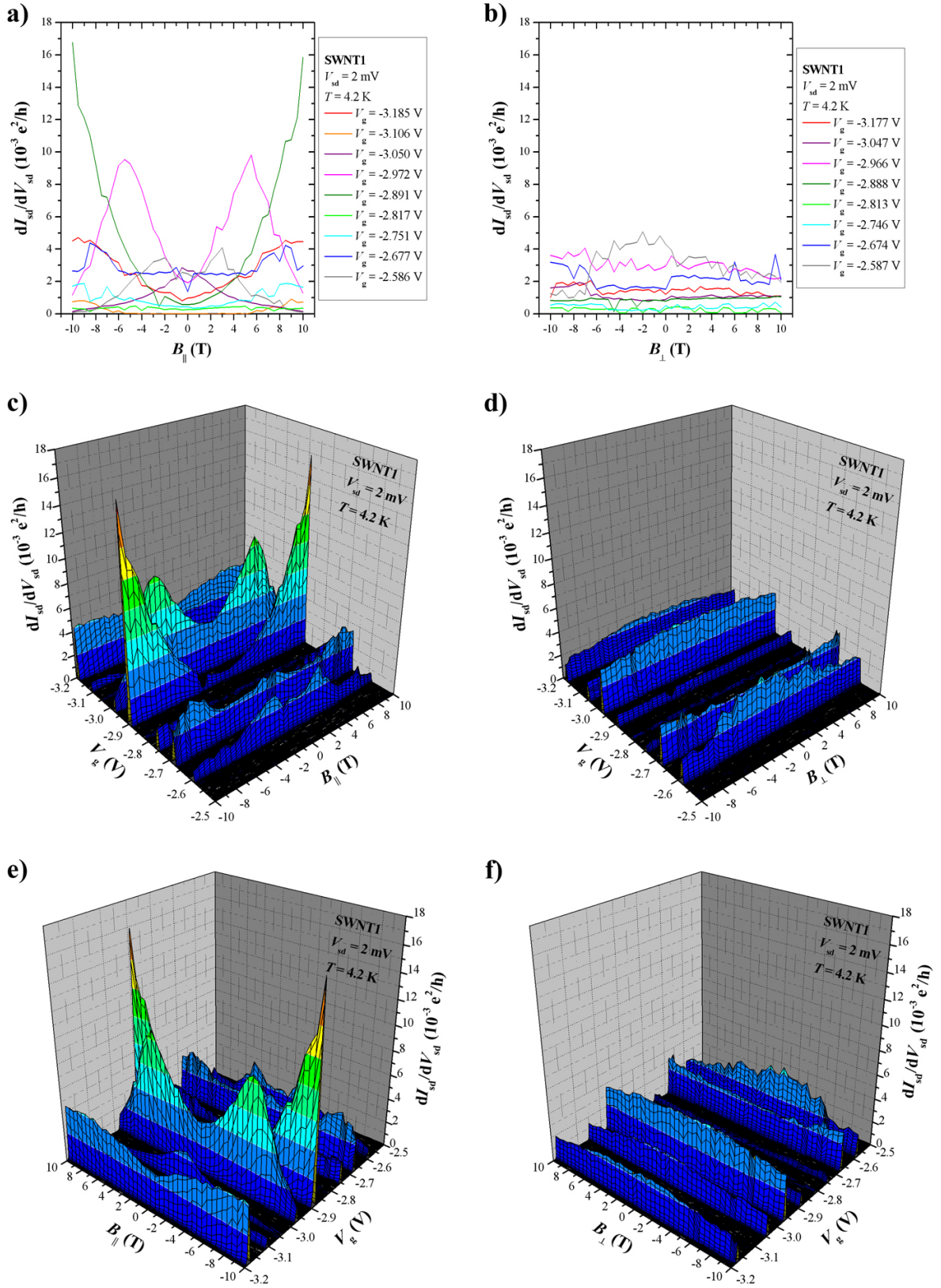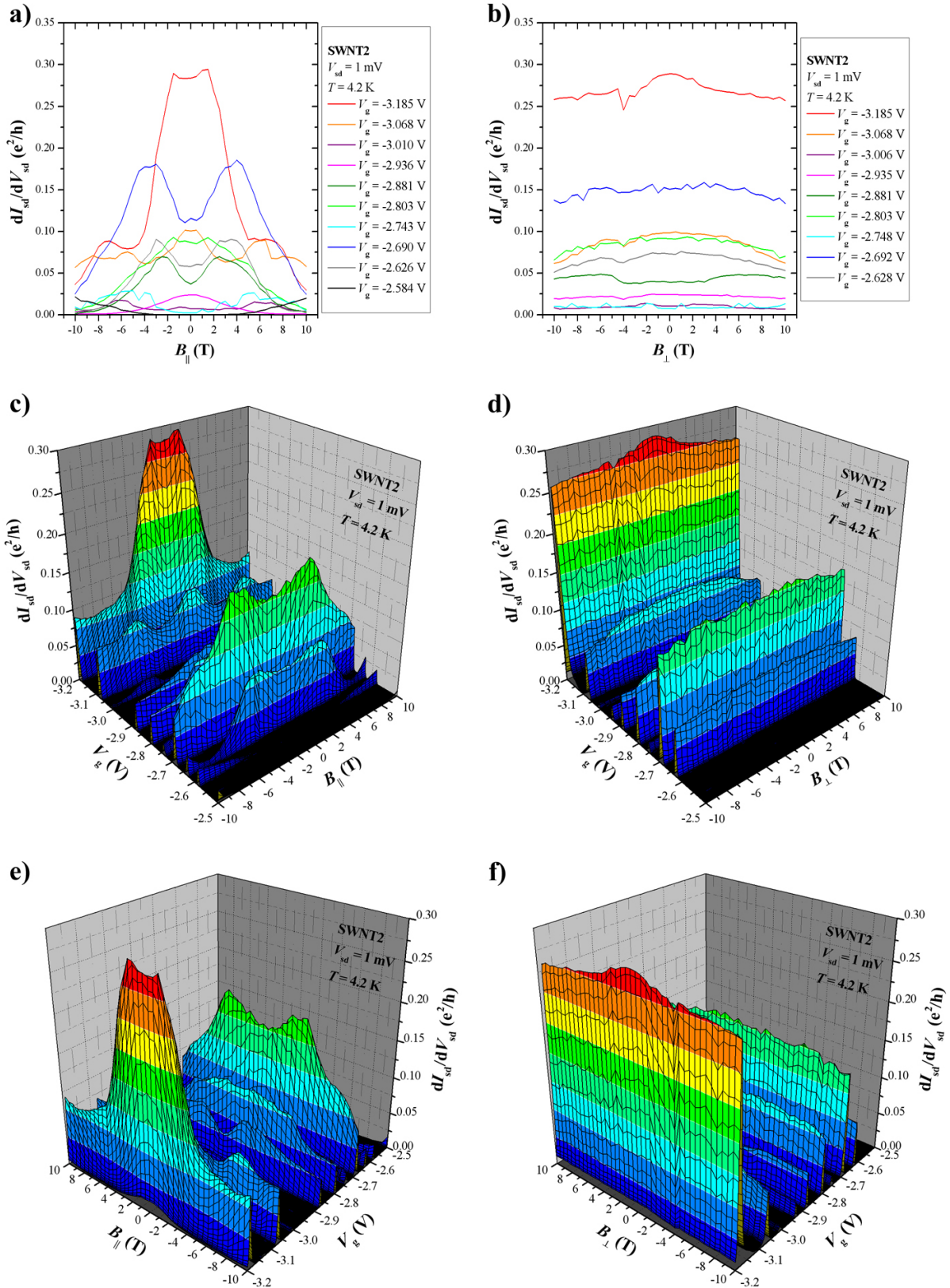
Fig. 6.7: Development of the Coulomb blockade peaks of device SWNT1 with applied magnetic field $B_{\parallel}$ parallel to the axis of SWNT1 (left column) or $B_{\perp}$ perpendicular to the axis of SWNT1 (right column) at $V_{\mathrm{sd}} = 2$ mV and $T = 4.2$ K. **a),b)** Differential conductance $\mathrm{d}I_{\mathrm{sd}}/\mathrm{d}V_{\mathrm{sd}}$ as a function of the **a)** parallel magnetic field $B_{\parallel}$ or the **b)** perpendicular magnetic field $B_{\perp}$ for different fixed gate voltages V_{g}. **c),d),e),f)** 3-dimensional plots of the differential conductance $\mathrm{d}I_{\mathrm{sd}}/\mathrm{d}V_{\mathrm{sd}}$ as function of the gate voltage V_{g} and the **c),e)** parallel magnetic field $B_{\parallel}$ or the **d),f)** perpendicular magnetic field $B_{\perp}$ from different perspectives.
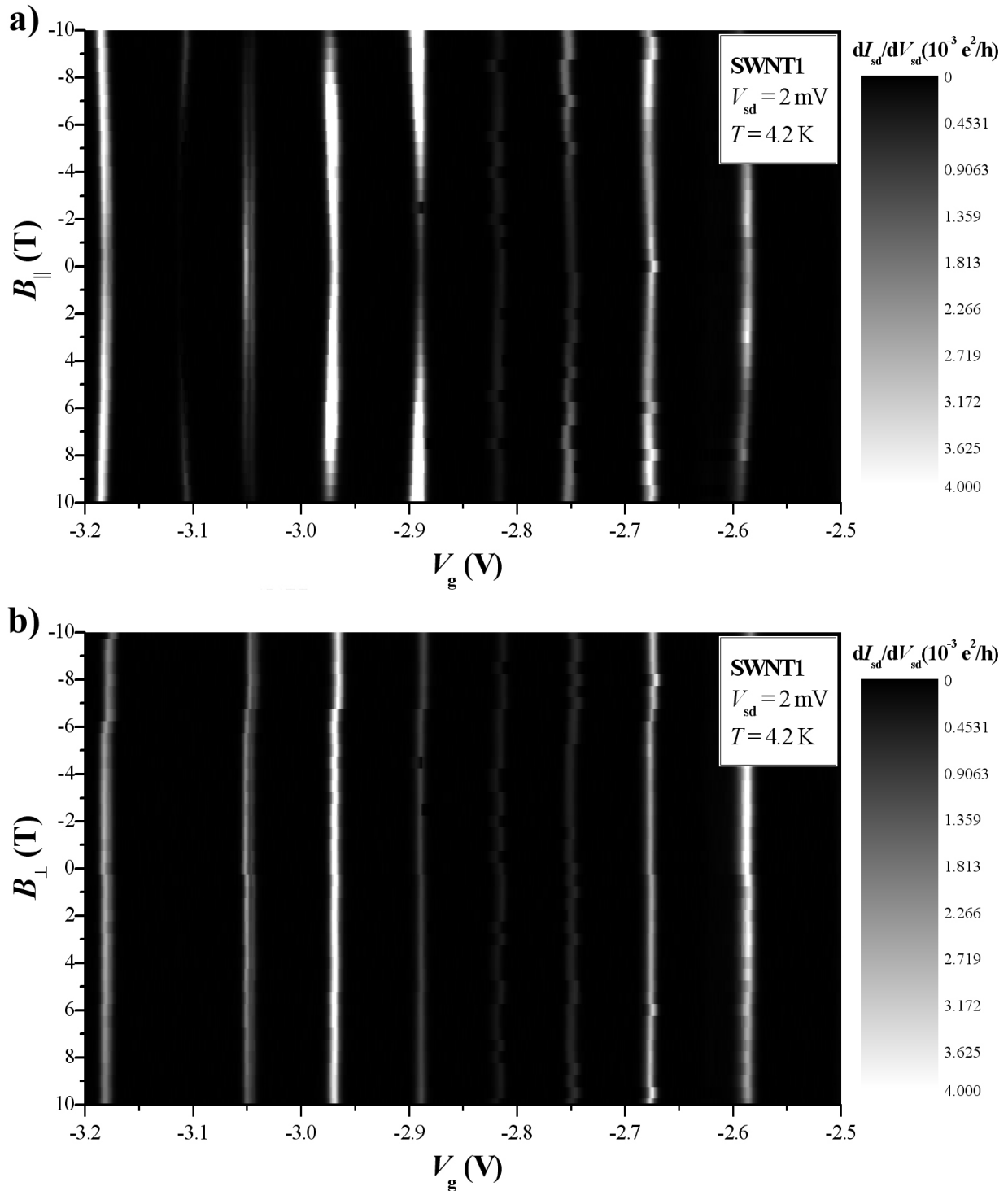
Fig. 6.8: Presentation of the differential conductance $\mathrm{d}I_{\mathrm{sd}}/\mathrm{d}V_{\mathrm{sd}}$ of SWNT1 at $V_{\mathrm{sd}} = 2$ mV and $T = 4.2$ K as function of the gate voltage V_{g} and the **a)** parallel magnetic field $B_{\parallel}$ or the **b)** perpendicular magnetic field $B_{\perp}$ as greyscale plots, in order to evaluate shifts of the Coulomb blockade peaks along the gate voltage axis induced by the magnetic field. The greyscale plots are based on the same datasets as used for figure 6.7.
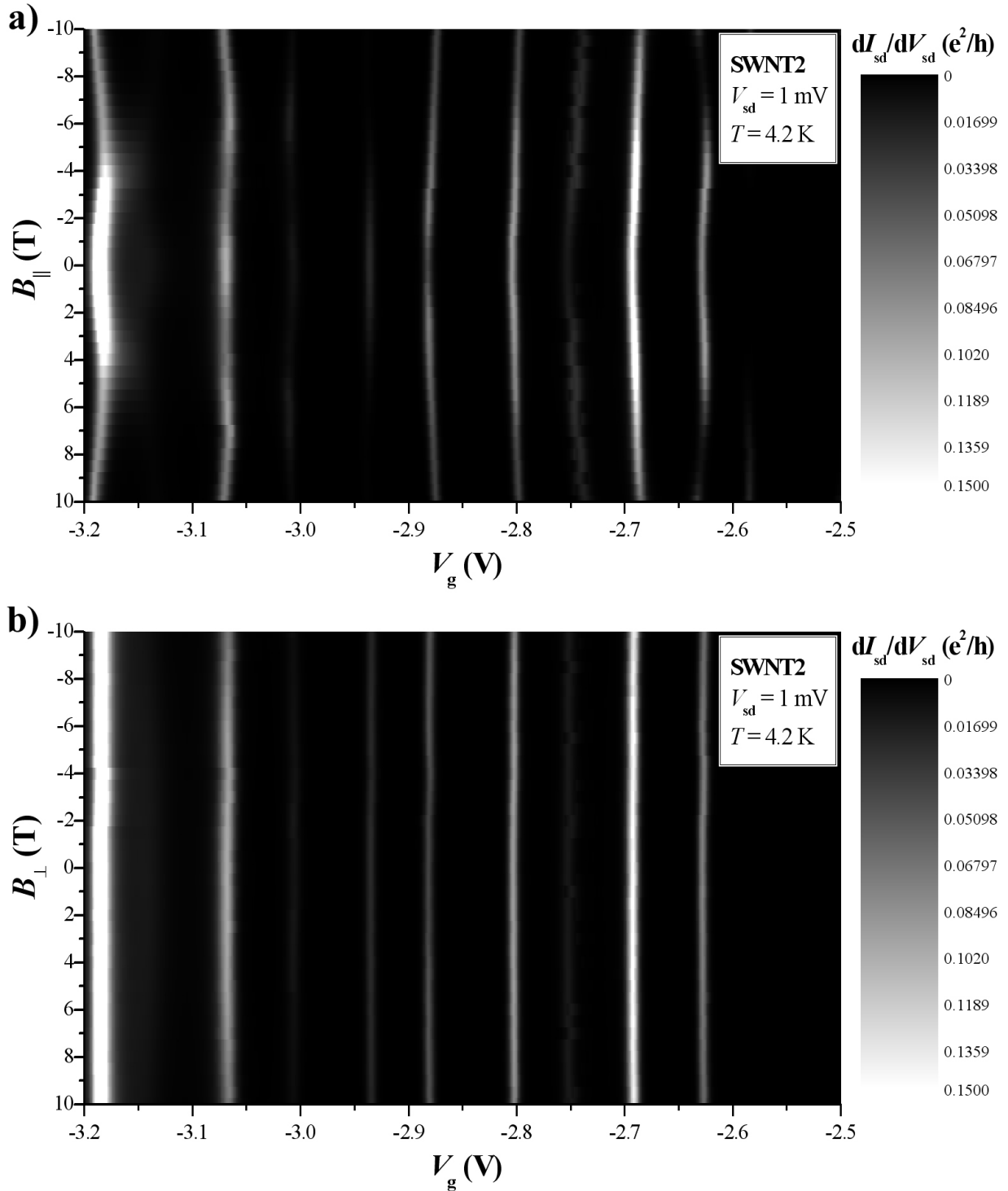
Fig. 6.9: a) Coulomb blockade oscillations of the differential conductance dI_{sd}/dV_{sd} of sample SWNT2 plotted vs. the applied gate voltage V_g at $V_{sd} = 1$ mV, $T = 4.2$ K and $B = 0$ T. **b)** Diamond plot of SWNT2, i.e. dI_{sd}/dV_{sd} as a function of the bias voltage V_{sd} and the gate voltage V_g at $T = 4.2$ K and $B = 0$ T. **c)** 3-dimensional graph of the current I_{sd} through device SWNT2 in the regime of Coulomb blockade and few-electron tunneling as a function of V_{sd} and V_g at $T = 4.2$ K and $B = 0$ T.

Fig. 6.10: Development of the Coulomb blockade peaks of device SWNT2 with applied magnetic field $B_{\parallel}$ parallel to the axis of SWNT1 (left column) or $B_{\perp}$ perpendicular to the axis of SWNT1 (right column) at $V_{sd} = 1$ mV and $T = 4.2$ K. **a),b)** Differential conductance dI_{sd}/dV_{sd} as a function of the **a)** parallel magnetic field $B_{\parallel}$ or the **b)** perpendicular magnetic field $B_{\perp}$ for different fixed gate voltages V_g. **c),d),e),f)** 3-dimensional plots of the differential conductance dI_{sd}/dV_{sd} as function of the gate voltage V_g and the **c),e)** parallel magnetic field $B_{\parallel}$ or the **d),f)** perpendicular magnetic field $B_{\perp}$ from different perspectives.

Fig. 6.11: Presentation of the differential conductance dI_{sd}/dV_{sd} of SWNT2 at $V_{sd} = 1$ mV and $T = 4.2$ K as function of the gate voltage V_g and the **a)** parallel magnetic field $B_{\parallel}$ or the **b)** perpendicular magnetic field $B_{\perp}$ as greyscale plots, in order to evaluate shifts of the Coulomb blockade peaks along the gate voltage axis induced by the magnetic field. The greyscale plots are based on the same datasets as used for figure 6.10.
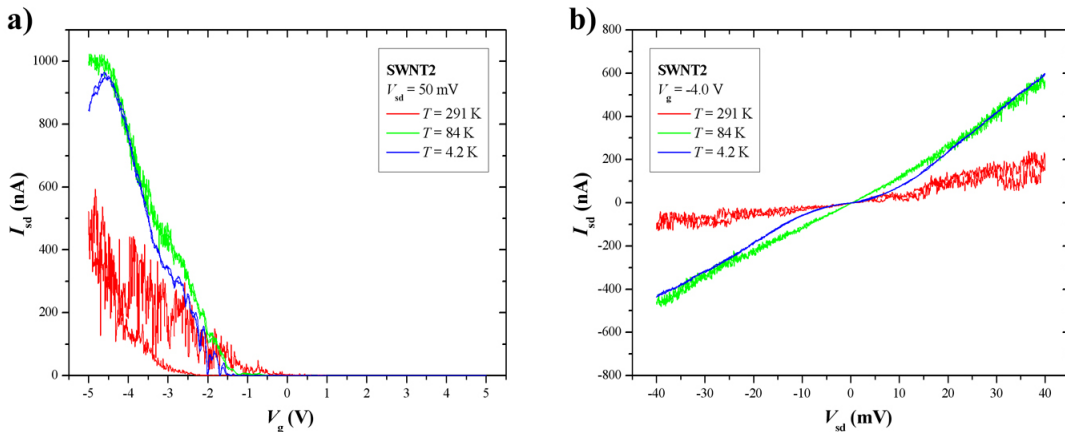
6.3   Temperature dependence of electrical transport in SWNTs

After the samples SWNT1 and SWNT2 have been characterized electrically at $T = 4.2$ K
for $B = 0$ and for magnetic fields axially and perpendicularly oriented to the SWNTs, the
final measurements performed on these samples were 2-probe transport measurements at
three different temperatures comparing the output characteristics $I_{sd}(V_{sd})$ and the trans-
fer characteristics $I_{sd}(V_g)$ for $T = 4.2$ K, $T = 82/84$ K and $T = 291$ K (Figs. 6.12 and 6.13).

As already shown before, both the nanotube bundle SWNT1 and the individual nanotube
SWNT2 are p-type semiconductors. Upon heating to 82 K/84 K, the transfer character-
istics do not change significantly in comparison to $T = 4.2$ K (Figs. 6.12a and 6.13a),
however, the barriers being apparent as regime in which the current I_{sd} is suppressed
for small bias voltages in the output characteristics $I_{sd}(V_{sd})$ of SWNT1 and SWNT2 are
overcome for elevated temperatures, i.e. the region of suppressed current has vanished for
$T = 82$ K and $T = 84$ K, respectively (Figs. 6.12b and 6.13b).
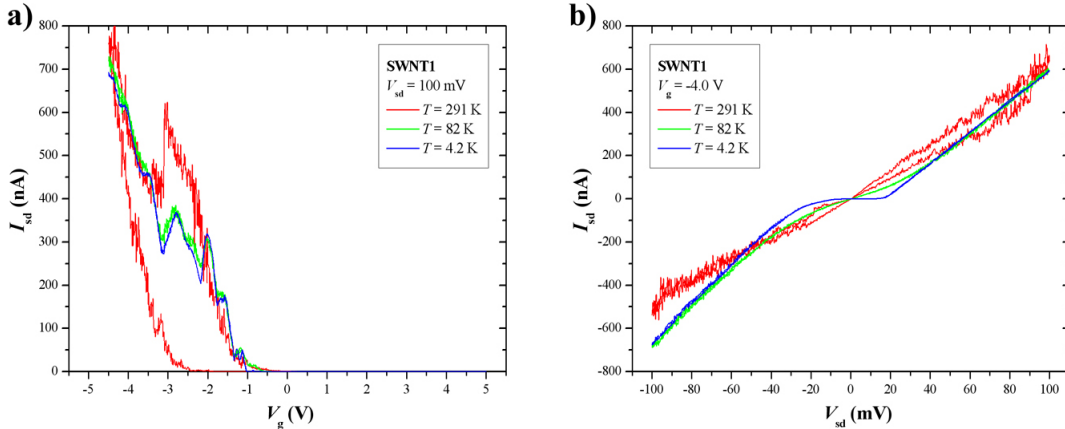
Fig. 6.12: Temperature dependence of 2-probe transport performed on the sample SWNT1.
a) Transfer characteristics $I_{sd}(V_g)$ at $V_{sd} = 100$ mV and $T = 4.2$ K, 82 K, 291 K. **b)** Output
characteristics $I_{sd}(V_{sd})$ at $V_g = $ -4.0 V and $T = 4.2$ K, 82 K, 291 K.

Fig. 6.13: Temperature dependence of 2-probe transport done on sample SWNT2. **a)** Transfer
characteristics $I_{sd}(V_g)$ at $V_{sd} = 50$ mV and $T = 4.2$ K, 84 K, 291 K. **b)** Output characteristics
$I_{sd}(V_{sd})$ at $V_g = $ -4.0 V and $T = 4.2$ K, 84 K, 291 K.

At room temperature, a very typical feature for SWNT transistors comes up, namely strong hysteresis in the gate dependence of the current through the SWNTs, which is associated with charges in the oxide layer or at the oxide-SWNT interface getting trapped and released again changing the effective gate potential (Figs. 6.12a and 6.13a). As for the output characteristics $I_{\mathrm{sd}}(V_{\mathrm{sd}})$ at room temperature, they get much noisier than at lower temperatures due to thermal excitation of processes in the SWNTs themselves or at the SWNT-contact interfaces. Whereas the conductance of SWNT1 at $T = 291$ K stays well comparable to the ones at lower temperatures, the current through SWNT2 drops significantly at room temperature which might be due to enhanced charge carrier scattering.

6.4   Summary of electrical transport in SWNTs

Transport and magnetotransport measurements in 2-probe transistor configuration (cp. chapter 3.2.2) have been carried out on single-walled carbon nanotube samples, where the data acquired for two representative devices SWNT1 and SWNT2 have been presented. Great importance was attached to the combinatorial investigations of these devices, firstly, by the (magneto-)transport measurements and secondly by an imaging method applied on the very same sample in order to clarify its geometry, in this case in order to tell whether the sample is an individual SWNT or a SWNT bundle and eventually the helicity/-ies of the SWNT(s). The imaging method of choice was high-resolution AFM (cp. chapters 4.7.2 and 7.5), the advantage of which is that it is non-destructive, though with the drawback of being a very time-intensive method. High-resolution AFM was successfully done on SWNT1 and SWNT2 revealing SWNT1 to be a bundle of SWNTs in which the single SWNTs seem to be twisted around each other and SWNT2 being an individual SWNT.

Regarding the transport results of SWNT1 and SWNT2, both samples are p-type semiconducting devices with highly reproducible output and transfer characteristics at $T = 4.2$ K. When applying a magnetic field $B_{\perp}$ perpendicularly to the axes of SWNT1 and SWNT2, there is no significant response neither in the high-current regime with I_{sd} being several 100 nA nor in the Coulomb blockade regime. However, when orienting the magnetic field along the axis of the sample SWNT1, it exhibits a large and highly reproducible magnetoresistive effect in the high-current regime with approx. 8 to 14 % negative magnetoresistance which can be explained either by one SWNT within the SWNT1 bundle being chiral (cp. theory of E. L. Ivchenko and B. Spivak [Ivc02], see chapter 3.2.4) and dominating the transport or by the twist of the SWNTs around each other. Sample SWNT2 does not show significant magnetoresistance in the high-current regime at parallel magnetic fields $B_{\parallel}$ and - according to [Ivc02] - should be an achiral SWNT. Applying low bias voltages of 1 or 2 mV and investigating the Coulomb blockade peaks of SWNT1 and SWNT2 at different parallel magnetic fields $B_{\parallel}$, one realizes significant undulations of the Coulomb blockade peak heights as well as small, yet observable shifts of the Coulomb blockade peaks along the V_{g} direction for different values of $B_{\parallel}$. We attribute these effects to *diamagnetic*

shifts and *Zeeman shifts* of the ground states and the respective excited states towards each other due to $B_\parallel$ which leads to gradual change of the weighting of ground and excited stated regarding their contribution to the overall coupling to the metallic leads and thus to a continuous undulating pattern of the Coulomb peak heights. Such a behaviour is known from GaAs quantum dots [Wei94, Wei05] but according to our knowledge has not yet been reported for SWNT transistors so far.

7. Results on electrical transport in Dy metallofullerene peapods

The main objective of this chapter is to compare the transport and magnetotransport results obtained on SWNT samples (cp. chapter 6) with the similar investigations performed on samples which have undergone a filling procedure with Dy@C_{82} metallofullerenes according to chapter 4.2. One intriguing aspect is whether the paramagnetic nature of the Dy@C_{82} metallofullerenes [Hua00] is of relevance for the results of magnetotransport measurements performed on (Dy@C_{82})@SWNT metallofullerene peapods and whether special effects which could be ascribed to the tube filling can be seen within the given experimental resolution.

All metallofullerene peapod samples investigated by (magneto-)transport measurements are envisaged to be scanned by high-resolution AFM (as sample SWNT1, cp. Fig. 6.5) in order to confirm that they comprise nanotubes filled with Dy@C_{82} metallofullerenes (cp. chapter 7.5), however, the project time was not sufficiently long for the time-intensive high-resolution AFM studies to be done. Two metallofullerene peapod samples, the transport results of which are introduced within this chapter, were successfully underetched and imaged by high-resolution TEM (cp. chapter 4.7.1).

In addition to the description of the results of the transport and magnetotransport investigations carried out on the (Dy@C_{82})@SWNT metallofullerene peapods, two further sub-chapters (chapters 7.5 and 7.6) are appended covering novel aspects of high-resolution microscopy on the metallofullerene peapod samples, which have been found in cooperations throughout the period of this research project.

7.1 Transport and magnetotransport in Dy metallofullerene peapods at 4.2 K

In the following, magnetotransport results acquired for four metallofullerene peapod devices named MFPP1 to MFPP4 (MFPP ↔ **m**etallo**f**ullerene **p**ea**p**od) will be introduced. The measurements were carried out in the very same manner as the ones done on SWNTs and described in chapter 6.1, again, it was important to rotate the sample in situ, i.e. in helium atmosphere, to adjust the new magnetic field orientation without the risc of doping the sample at ambient conditions. As in the case of the empty SWNTs, all measurements described in this section were carried out in the 2-probe configuration at $T = 4.2$ K and the curves displayed have been averaged from multiple runs. The magnetotransport data gained for MFPP1 to MFPP4 are presented in figures 7.1 to 7.8 in the same way as the ones of the SWNTs: two figures display the results for each MFPP device, the first of

which is covering the parallel magnetic field orientations (Figs. 7.1, 7.3, 7.5 and 7.7) and the second one the perpendicular magnetic field direction (Figs. 7.2, 7.4, 7.6 and 7.8). As in chapter 6.1, each of these eight figures is devided into seven panels, where the top one shows a standard AFM image of the MFPP device and the orientation of the magnetic field (a), the three panels in the left column display the measured data, namely the current I_{sd} at $B = -10, 0, 10$ T as a function of the gate voltage (b), the bias voltage (f) and of the magnetic field B (d). The right column with the panels c,e,g includes the magnetoresistance data corresponding to the panels b,d,f. Again, some magnetoresistance data is omitted since the magnetoresistance is not defined for $I_{sd} \rightarrow 0$ or $(I_{sd}$ and $V_{sd}) \rightarrow 0$.

Looking at figures 7.2, 7.4, 7.6, 7.8, one can state that there is no significant change of the electrical characteristics of the metallofullerene peapod devices MFPP1 to MFPP4 upon application of magnetic fields $B_{\perp}$ aligned perpendicularly to the peapod axes. The transfer characteristics $I_{sd}(V_g)$ and output characteristics $I_{sd}(V_{sd})$ for $B_{\perp}$ are identical to a great extent with the exception of small gate and bias voltages. The reason of these deviations is unclear. However, the saturating values of the magnetoresistance MR for large gate voltages V_g and large source-drain voltages V_{sd} is always zero in the case of perpendicularly applied magnetic fields $B_{\perp}$. The $MR(B_{\perp})$ plots in figures 7.2e, 7.4e, 7.6e and 7.8e which are flat and around zero magnetoresistance support the statement that magnetoresistive effects due to perpendicularly oriented magnetic fields $B_{\perp}$ are negligible for the samples MFPP1 to MFPP4.

After changing the magnetic field orientation to parallel magnetic field $B_{\parallel}$ regarding the metallofullerene peapod axes, samples MFPP1 and MFPP2 reproducibly exhibit significant magnetoresistance whereas devices MFPP3 and MFPP4 do not[†]. MFPP1 shows approx. 8 to 12 % negative magnetoresistance for large V_{sd} and V_g at $B_{\parallel} = -10, 10$ T (Fig. 7.1c,e,g), the same is true for device MFPP2 (Fig. 7.3c,e,g). In this way, MFPP1 and MFPP2 very much resemble device SWNT1, which showed strong negative magnetoresistance for $B_{\parallel}$ as well (Fig. 6.1). Furthermore one could compare the metallofullerene peapod devices MFPP3 and MFPP4 with sample SWNT2 being an individual empty single-walled carbon nanotube without significant electronic response to a parallel magnetic field $B_{\parallel}$ (Fig. 6.3).

In conclusion, we can not find extraordinary properties of the investigated metallofullerene peapod samples MFPP1 to MFPP4 in magnetotransport measurements with parallel and perpendicular magnetic fields $B_{\parallel}$ and $B_{\perp}$ in the *high-current regime*, in which the current is several 100 nA. The acquired magnetotransport data are well comparable to the ones obtained from empty SWNT samples. There is no hint in our data that the filling of the nanotubes with $Dy@C_{82}$ metallofullerenes would affect the magnetotransport measurements. Obviously the reason for a nanotube to exhibit magnetoresistance is rather the structure of the host SWNT than the filling with metallofullerenes. Following the theory

---

[†]if one does not consider the deviations for small V_{sd} and V_g in figures 7.5c,g and 7.7c,g

by E. L. Ivchenko and B. Spivak [Ivc02], we think that both MFPP1 and MFPP2 comprise chiral host SWNTs, whereas the ones of MFPP3 and MFPP4 are achiral.

As already mentioned, we do not have high-resolution AFM on the metallofullerene peapod samples MFPP1 to MFPP4 yet, so we can not be sure that MFPP1 to MFPP4 are indeed filled nanotubes, however, the overall fraction of nanotubes filled throughout the process described in chapter 4.3 is approx. 70 to 90 % according to high-resolution TEM studies of the batches after synthesis [Khl06, Obe06], so there is a reasonable chance that at least two of the four MFPP devices consist of metallofullerene peapods.

A final remark in this section on *transport and magnetotransport in Dy metallofullerene peapods at 4.2 K* concerns a further metallofullerene peapod sample named MFPP5 in the following [Obe06]. To our knowledge, this is the first metallofullerene peapod transport sample, on which transport measurements including output and transfer characteristics have been carried out and which is proven to contain filled nanotubes indeed. The results obtained for MFPP5 are summarized in figure 7.9. A standard AFM image of MFPP5 taken at ambient conditions is displayed in figure 7.9a, followed by a high-resolution transmission electron micrograph of a section of MFPP5 in figure 7.9b, which was taken after underetching the sample according to the procedure described in chapter 4.7.1. The TEM micrograph shows that MFPP5 is a bundle consisting of three SWNTs with two nanotubes being regularly filled with $Dy@C_{82}$ endohedral metallofullerenes and the third tube being empty. The output and transfer characteristics of MFPP5 at $T = 4.2$ K are given in figure 7.9c,d, telling that MFPP5 is a p-type semiconductor. This is in contrast to the publications [Chi01, Shi02] that claim that a metallofullerene peapod should behave as a metal [Chi01] or as an ambipolar semiconductor [Shi02] at $T = 4.2$ K (cp. chapter 3.3).
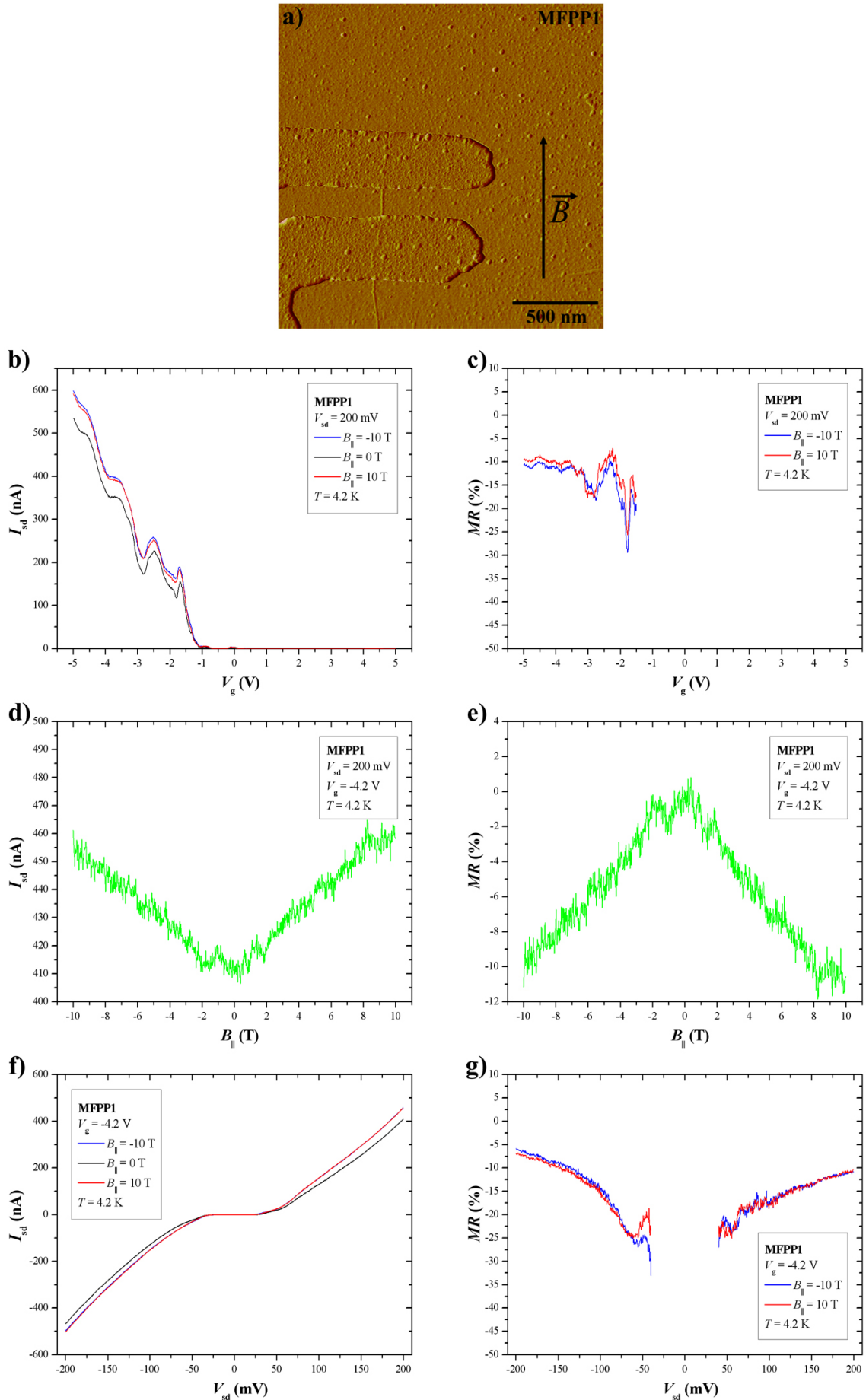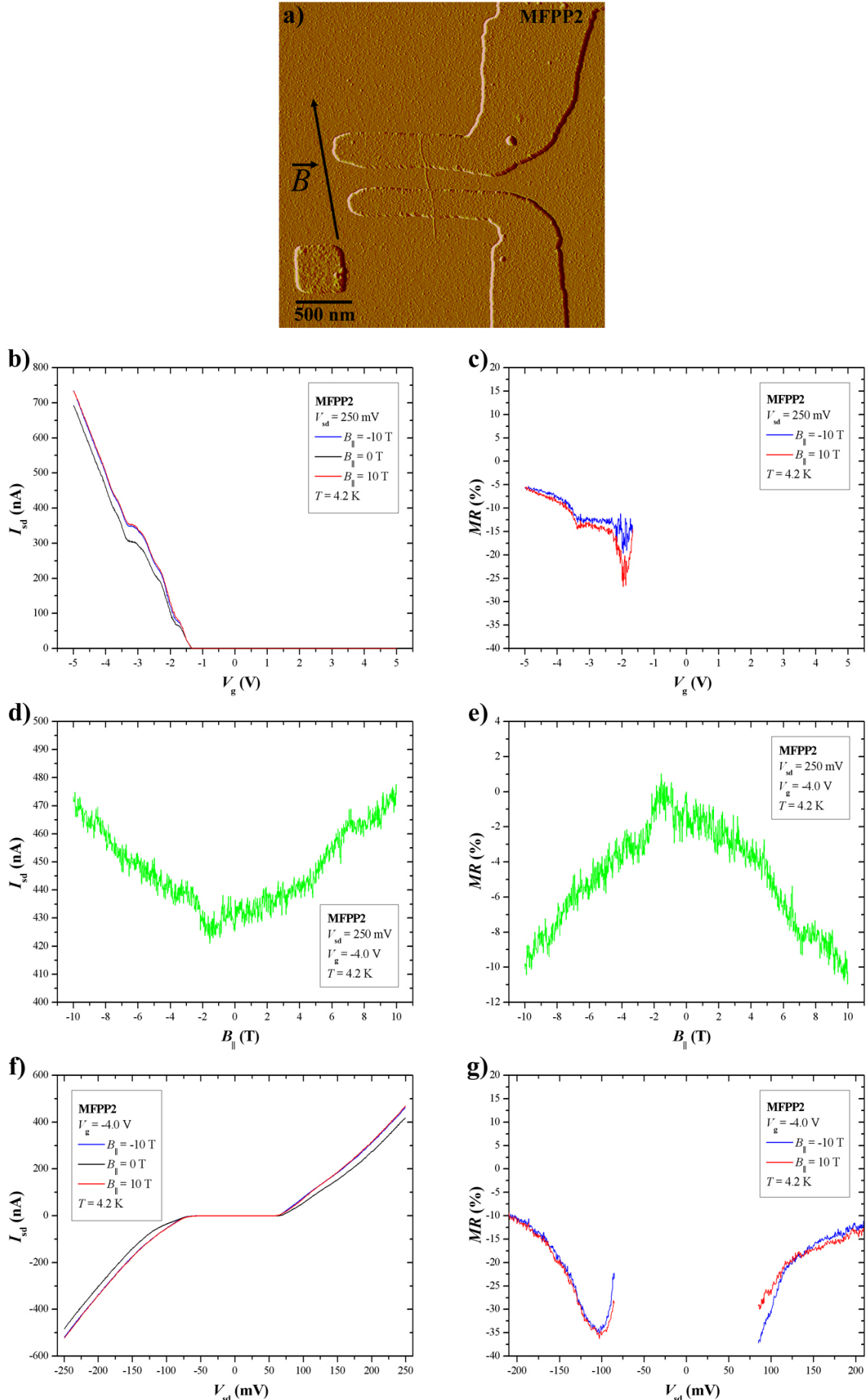
Fig. 7.1: 2-probe magnetotransport measurements performed on sample MFPP1 at 4.2 K with the magnetic field $B_{\parallel}$ parallel to the tube axis. **a)** Magnetic field orientation. **b),d),f)** I_{sd} as function of V_g, $B_{\parallel}$ and V_{sd}. **c),e),g)** Magnetoresistance data corresponding to **b),d),f)**.
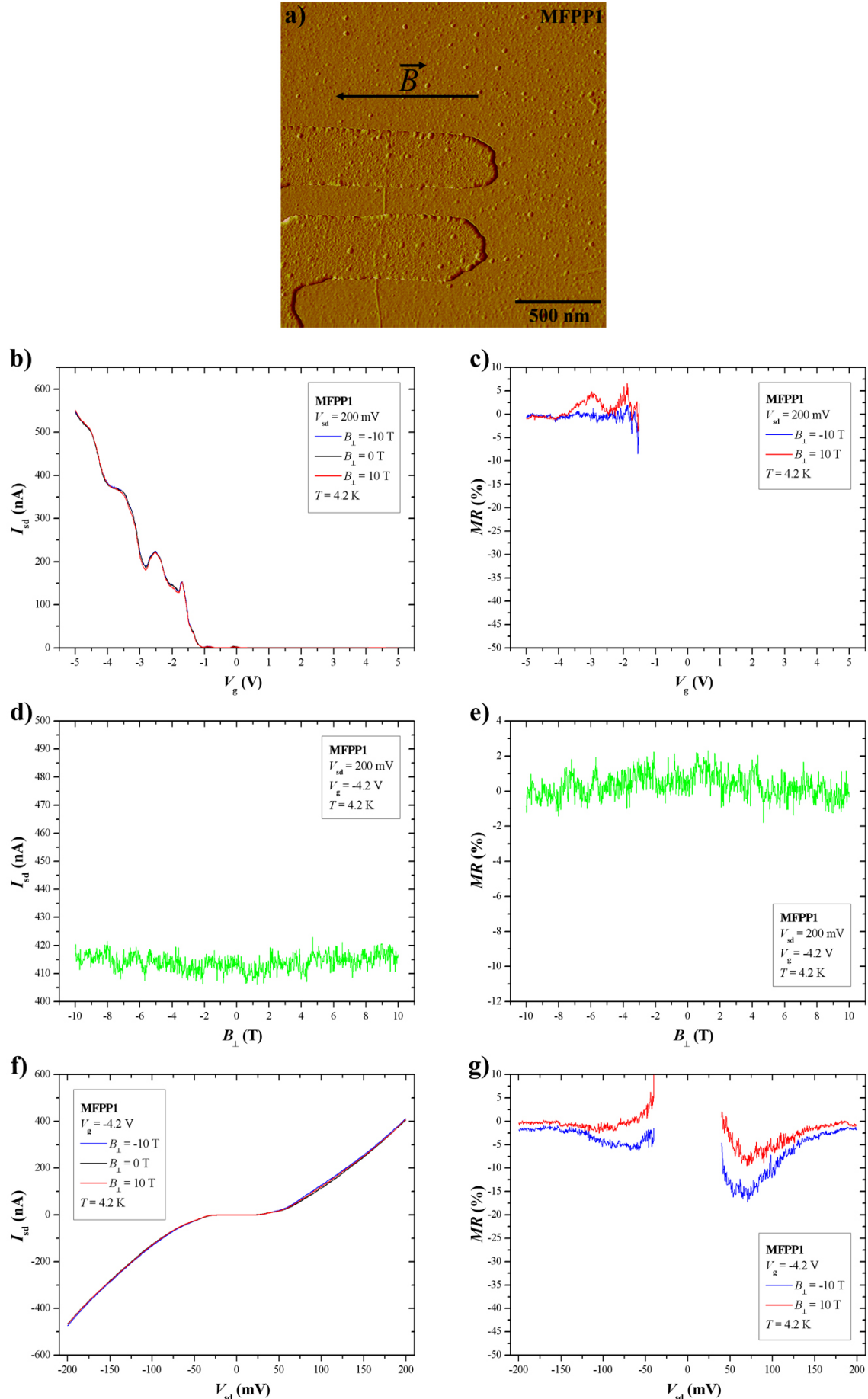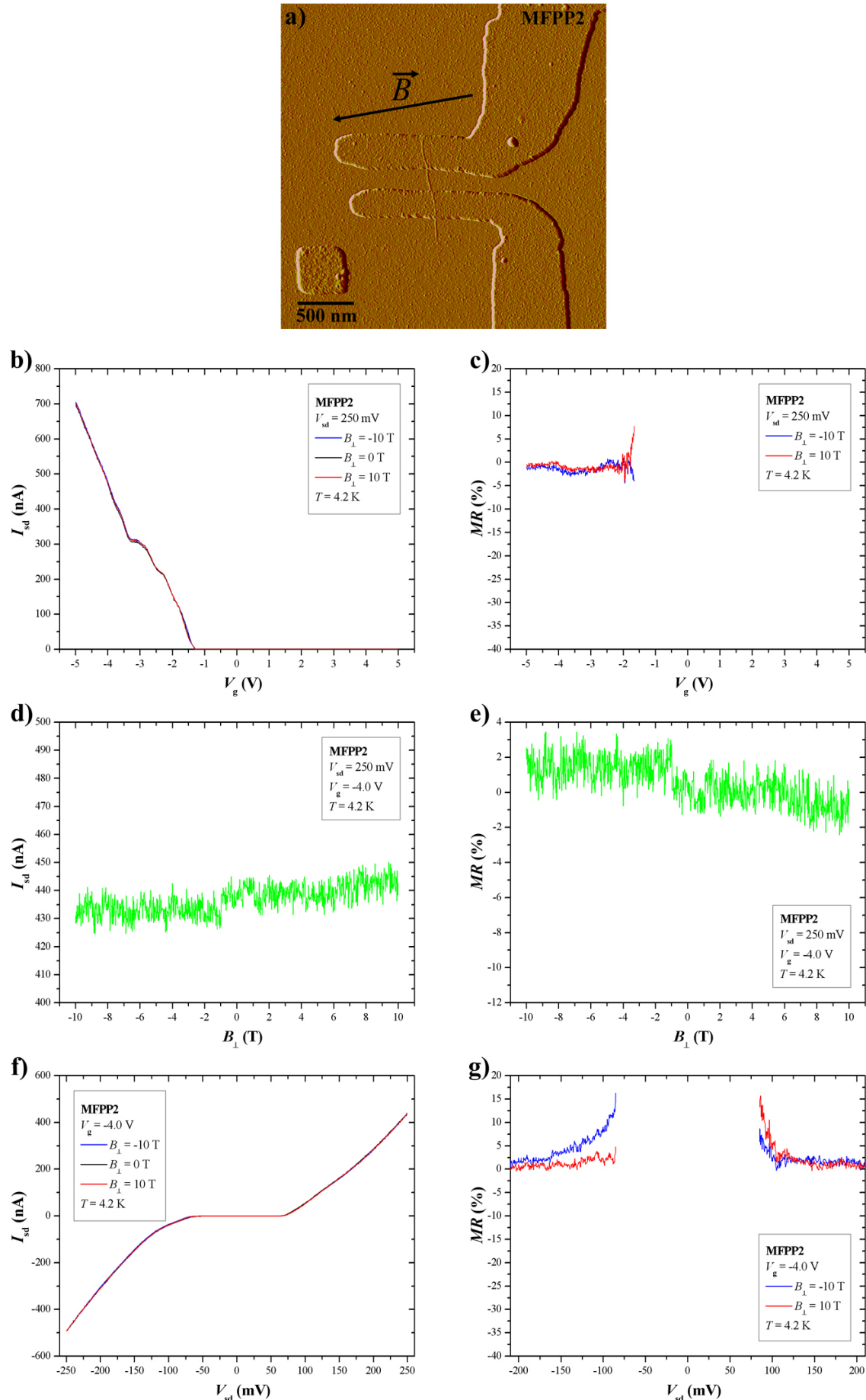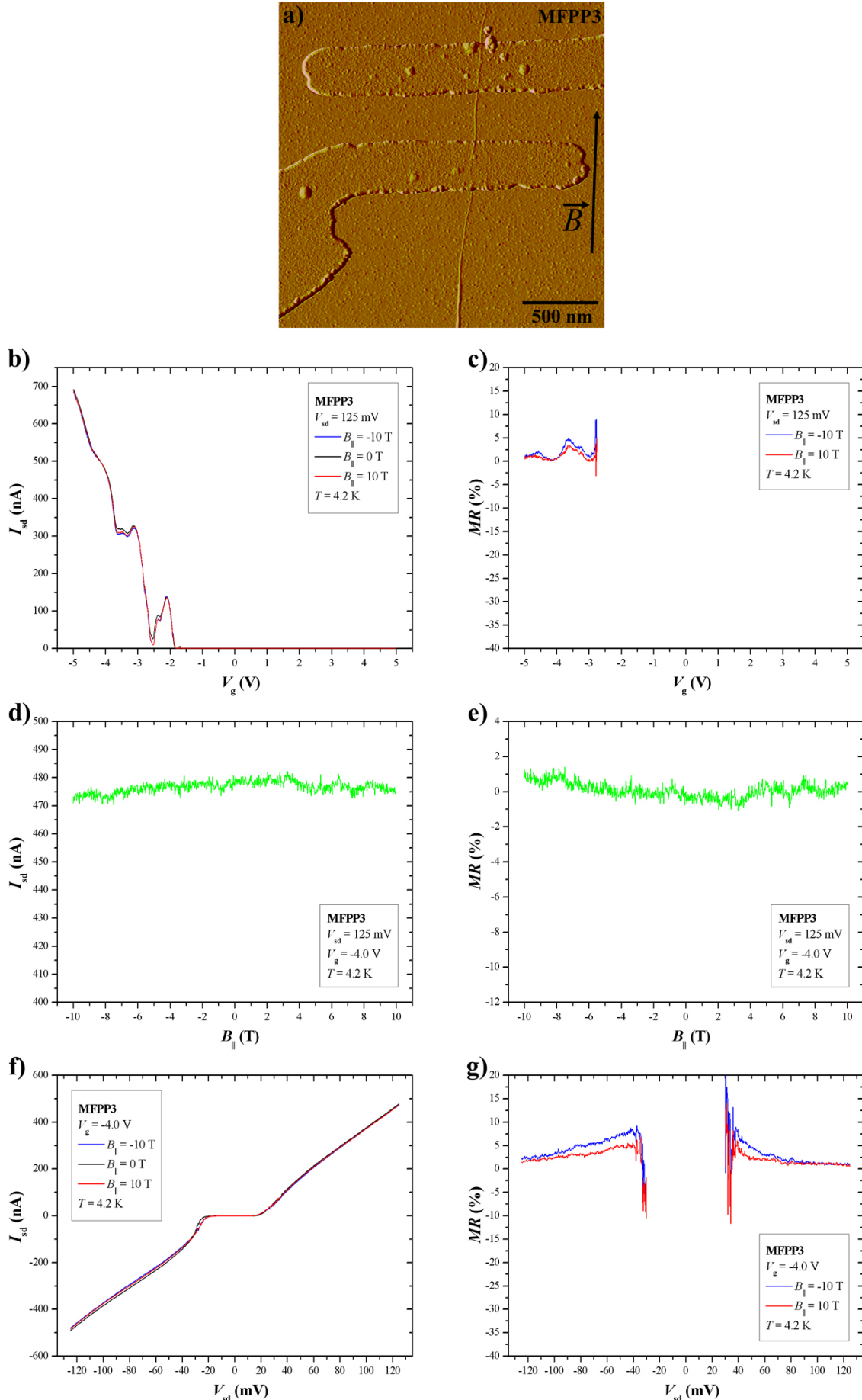
Fig. 7.2: 2-probe magnetotransport measurements performed on sample MFPP1 at 4.2 K with the magnetic field $B_\perp$ perpendicular to the tube axis. **a)** Magnetic field orientation. **b),d),f)** I_{sd} as function of V_g, $B_\perp$ and V_{sd}. **c),e),g)** Magnetoresistance data corresponding to **b),d),f)**.
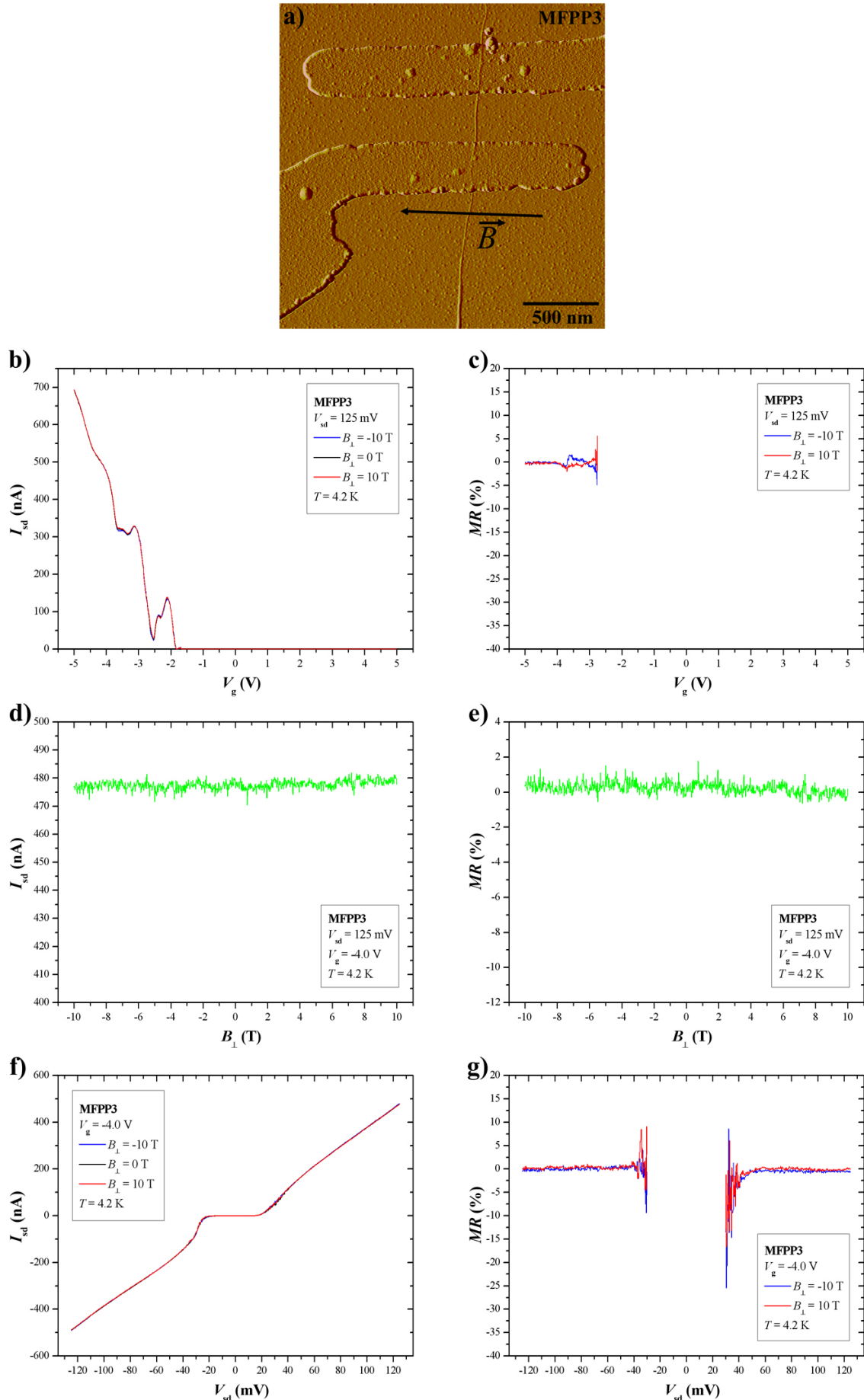
Fig. 7.3: 2-probe magnetotransport measurements performed on sample MFPP2 at 4.2 K with the magnetic field $B_\parallel$ parallel to the tube axis. **a)** Magnetic field orientation. **b),d),f)** I_{sd} as function of V_g, $B_\parallel$ and V_{sd}. **c),e),g)** Magnetoresistance data corresponding to **b),d),f)**.
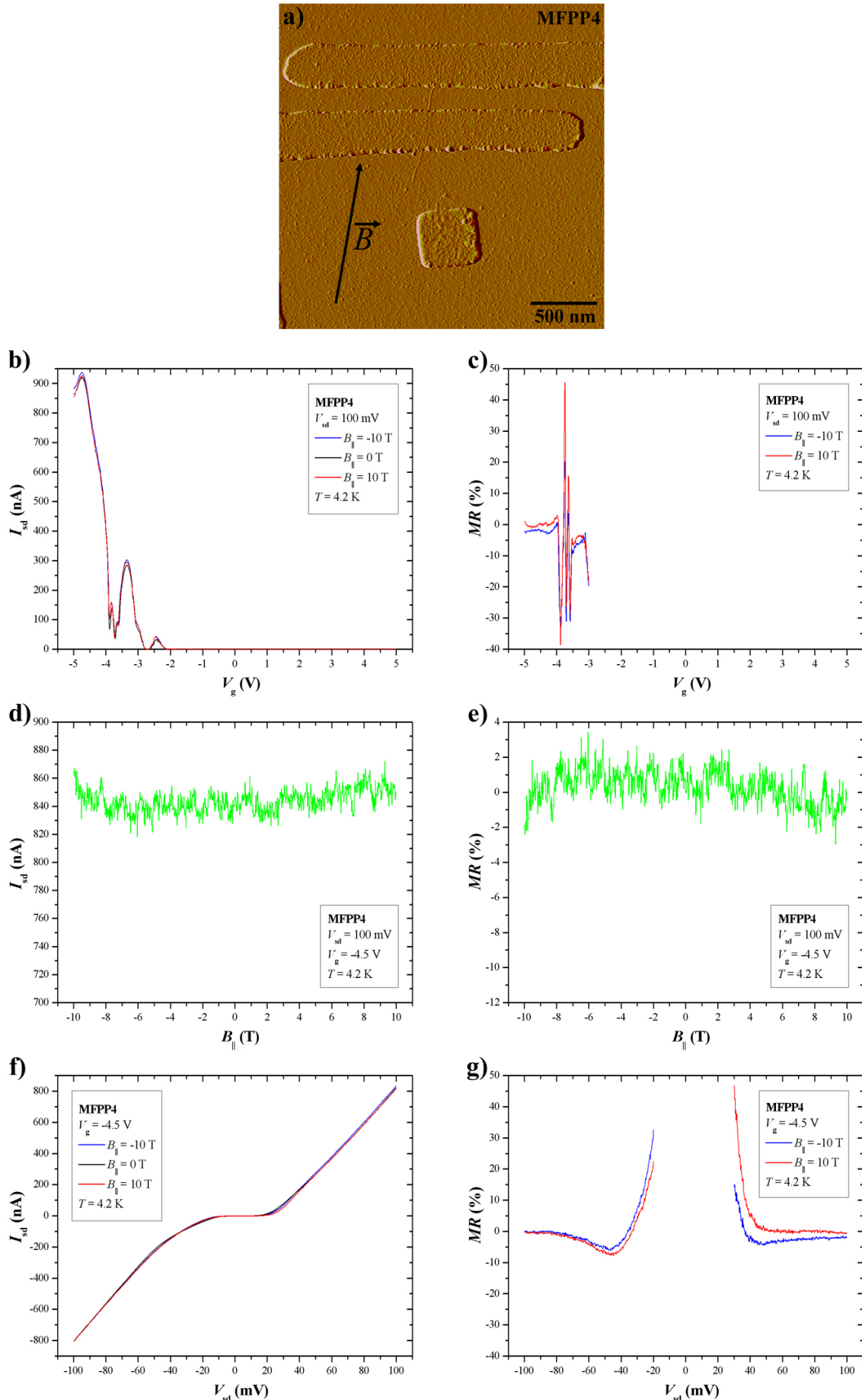
Fig. 7.4: 2-probe magnetotransport measurements performed on sample MFPP2 at 4.2 K with the magnetic field $B_\perp$ perpendicular to the tube axis. **a)** Magnetic field orientation. **b),d),f)** I_{sd} as function of V_g, $B_\perp$ and V_{sd}. **c),e),g)** Magnetoresistance data corresponding to **b),d),f)**.

Fig. 7.5: 2-probe magnetotransport measurements performed on sample MFPP3 at 4.2 K with the magnetic field $B_\parallel$ parallel to the tube axis. **a)** Magnetic field orientation. **b),d),f)** I_{sd} as function of V_g, $B_\parallel$ and V_{sd}. **c),e),g)** Magnetoresistance data corresponding to **b),d),f)**.
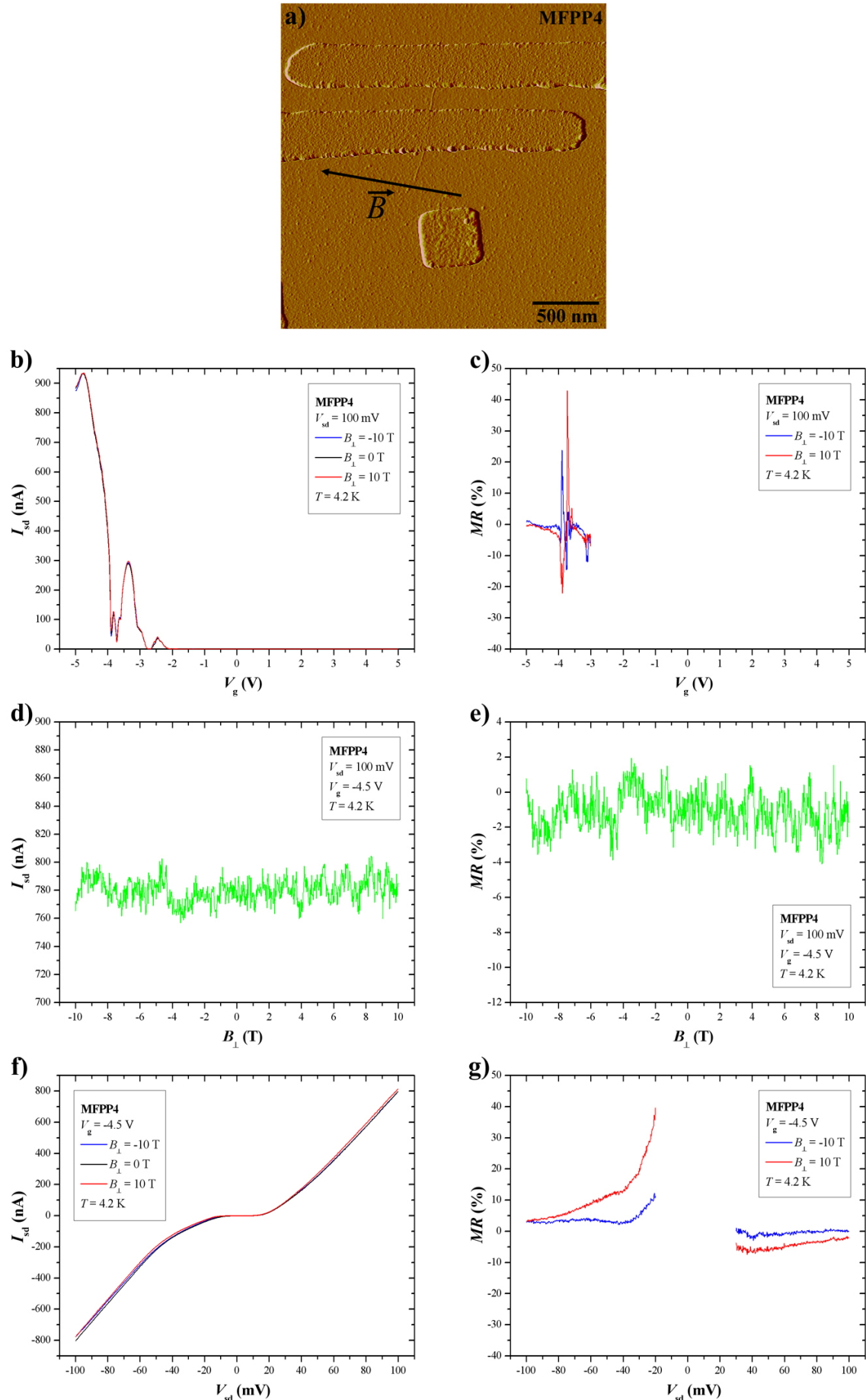
Fig. 7.6: 2-probe magnetotransport measurements performed on sample MFPP3 at 4.2 K with the magnetic field $B_\perp$ perpendicular to the tube axis. **a)** Magnetic field orientation. **b),d),f)** I_{sd} as function of V_g, $B_\perp$ and V_{sd}. **c),e),g)** Magnetoresistance data corresponding to **b),d),f)**.

Fig. 7.7: 2-probe magnetotransport measurements performed on sample MFPP4 at 4.2 K with the magnetic field $B_\parallel$ parallel to the tube axis. **a)** Magnetic field orientation. **b),d),f)** I_{sd} as function of V_g, $B_\parallel$ and V_{sd}. **c),e),g)** Magnetoresistance data corresponding to **b),d),f)**.
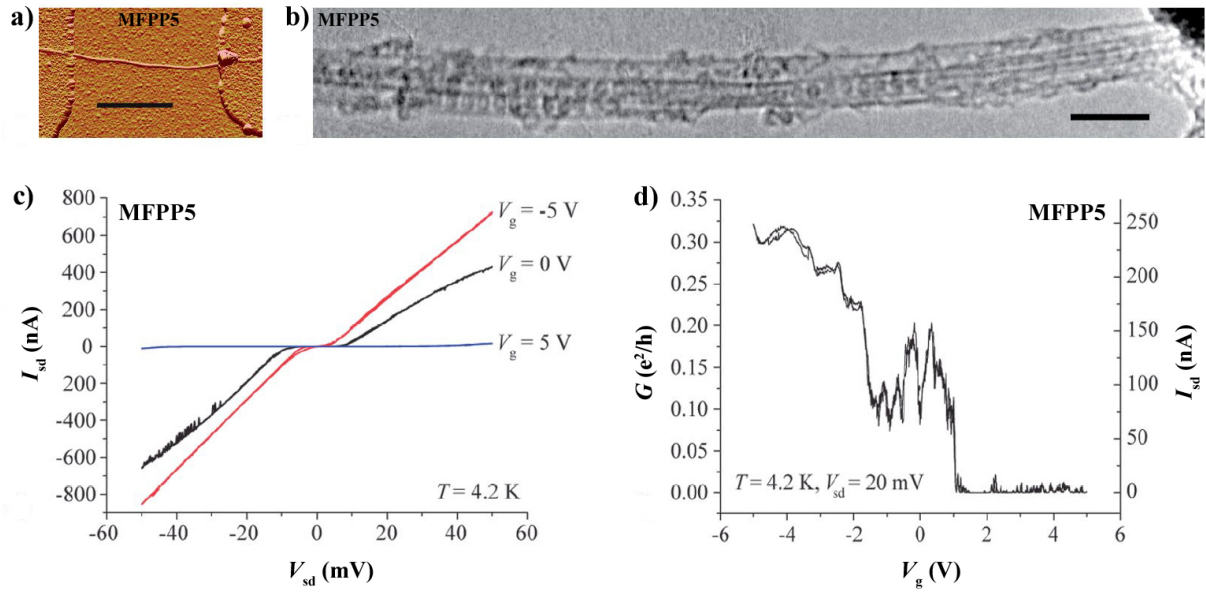
Fig. 7.8: 2-probe magnetotransport measurements performed on sample MFPP4 at 4.2 K with the magnetic field $B_\perp$ perpendicular to the tube axis. **a)** Magnetic field orientation. **b),d),f)** I_{sd} as function of V_g, $B_\perp$ and V_{sd}. **c),e),g)** Magnetoresistance data corresponding to **b),d),f)**.

Fig. 7.9: Structural and electrical characterisation of sample MFPP5 [Obe06]. **a)** Standard AFM image of MFPP5 taken at ambient conditions. Scale bar: 400 nm. **b)** High-resolution TEM micrograph of a section of MFPP5 taken with a Philips CM200 TEM at 120 kV after underetching the sample (cp. chapter 4.7.1). Scale bar: 5 nm. MFPP5 is a bundle of three nanotubes where two tubes are filled with $Dy@C_{82}$ metallofullerenes and one nanotube is empty. **c)** Output characteristics $I_{sd}(V_{sd})$ of MFPP5 at $V_g = -5, 0, 5$ V and $T = 4.2$ K. **d)** Transfer characteristics $I_{sd}(V_g)$ of sample MFPP5 at $V_{sd} = 20$ mV and $T = 4.2$ K, showing that MFPP5 is a p-type semiconductor. To our knowledge, sample MFPP5 is the first metallofullerene peapod sample which electronic transport measurements including the $I_{sd}(V_g)$ characteristics have been performed on and which has been proven to contain metallofullerene peapods indeed.

7.2   Magnetotransport in Dy metallofullerene peapods in the Coulomb blockade regime

Three further metallofullerene peapod devices, MFPP6, MFPP7 and MFPP8, were investigated by transport and magnetotransport measurements in the regime of *Coulomb blockade and few-electron tunneling* at $T = 4.2$ K. The samples MFPP7 and MFPP8 were measured before the possibility of rotating a sample in situ to adjust different magnetic field orientations was available (chapter 4.6), so there is only transport data at $B = 0$ T including diamond plots for MFPP7 and MFPP8.

In contrast to MFPP7 and MFPP8, the whole set of magnetotransport measurements in the Coulomb blockade regime as done on the samples SWNT1 and SWNT2 (cp. chapter 6.2) was carried out for metallofullerene peapod sample MFPP6. A standard AFM scan of MFPP6 is shown in figure 7.10a, followed by the sequence of Coulomb blockade peaks of the differential conductance dI_{sd}/dV_{sd} as a function of the gate voltage V_g in figure 7.10b, the diamond plot $dI_{sd}/dV_{sd}(V_{sd}, V_g)$ for MFPP6 in figure 7.10c and finally the 3-dimensional graph with the current I_{sd} through MFPP6 plotted vs. the bias and the gate voltage in figure 7.10d. All data in figures 7.10b-d have been recorded for $T = 4.2$ K and $B = 0$ T. The lower section of the diamond plot looks blurred, maybe due to influences of the ambience of the conducting channel, e.g. adsorbates or debris between the metal contacts and the nanotube surface, however, the capacitances characterizing MFPP6 as a quantum dot could be obtained using the upper, clean part of the diamond plot in figure 7.10c. The following values could be calculated for MFPP6 in the same way as described in chapter 6.2: $C_{s,MFPP6} = 1.0$ aF, $C_{d,MFPP6} = 2.0$ aF, $C_{g,MFPP6} = 0.7$ aF, $C_{\Sigma,MFPP6} = 3.7$ aF, $E_{C,MFPP6} = 21.6$ meV and $\beta_{MFPP6} = 0.2$.

The variations of the Coulomb blockade oscillations of MFPP6 due to applied parallel and perpendicular magnetic fields $B_\parallel$ and $B_\perp$ are displayed in figures 7.11 and 7.12, which are organized in the same way as the corresponding figures showing the respective data for SWNT1 and SWNT2 in chapter 6.2. For a magnetic field $B_\perp$ oriented perpendicularly to the axis of MFPP6, there is some modification of the Coulomb peak height (Figs. 7.11b,d,f), which is more pronounced as for the SWNTs, however it is accompanied by strong noise, the origin of which is unclear. The positions of the Coulomb blockade peaks with respect to the gate voltage V_g do not change noticeably with the applied perpendicular magnetic field $B_\perp$ (Fig. 7.12b). This is a similar behaviour as observed for the SWNT devices SWNT1 and SWNT2 (Figs. 6.8b and 6.11b). After the external magnetic field has been changed to parallel configuration, strong undulations of the differential conductance Coulomb blockade peaks appear (Fig. 7.11a,c,e) together with distinct shifts of the Coulomb blockade peak positions with respect to V_g at different values of $B_\parallel$ (Fig. 7.12a), which we assign to *diamagnetic shifts* and *Zeeman shifts* as described in chapter 6.2. In summary, MFPP6 behaves quite similarly to SWNT1 and SWNT2 in the regime of *Coulomb blockade and few-electron tunneling*, with the only difference that

for different values of $B_\perp$ there is some pronounced modulation of the Coulomb blockade peak height in combination with strong noise, however, the accompanying peak shifts (supposed to be small in this case) were not observed within our experimental resolution, maybe because the shifts were not larger than the peak widths. It is hard to estimate, whether this stronger peak modulation and the respective noise could be connected with a metallofullerene filling or might rather be due to e.g. adsorbates or debris in close vicinity to the conducting channel of MFPP6. So far, high-resolution AFM in order to check the filling status of sample MFPP6 has not yet been carried out, again - as for the samples MFPP1 to MFPP4 - due to the large amount of time needed for this imaging method.

To conclude this sub-chapter on metallofullerene peapod sample behaviour in the regime of *Coulomb blockade and few-electron tunneling*, the transport results received for the samples MFPP7 and MFPP8 shall be presented now. After the transport measurements, MFPP7 was intended to be underetched and subsequently imaged by high-resolution TEM, however, it was destructed throughout the underetching process, so it is unknown, whether MFPP7 was a metallofullerene peapod or not. A standard AFM image of MFPP7 is shown in figure 7.13a. The very regular and highly reproducible Coulomb blockade oscillations of the differential conductance $\mathrm{d}I_\mathrm{sd}/\mathrm{d}V_\mathrm{sd}$ are plotted vs. the gate voltage V_g in figure 7.13b. The complete diamond plot $\mathrm{d}I_\mathrm{sd}/\mathrm{d}V_\mathrm{sd}(V_\mathrm{sd}, V_\mathrm{g})$ confirms the excellent behaviour of sample MFPP7 as a single-electron transistor, a manifold of excited states is visible as parallel lines to the diamond boundaries (Fig. 7.13c). This diamond plot quality of a SWNT based quantum dot (well comparable to [Jar04]) is hard to achieve at $T = 4.2$ K, since often distortions by the close surroundings of the conducting channel inhibit observability of the spectrum of excited states. Finally, figure 7.13d depicts the current I_sd through the MFPP7 device as function of the gate voltage V_g and the bias voltage V_sd in a 3-dimensional plot. The special feature of MFPP7 is the extraordinary quality of its diamond plot, however, it is not associated with the possible filling of the nanotube with Dy@C$_{82}$ metallofullerenes.

Device MFPP8 (Fig. 7.14a) has been prepared following the same routine (cp. chapter 4.3) as for the other metallofullerene peapod samples MFPP1 to MFPP7, the transport results of which have been described within this chapter. However, MFPP8 has been proven by high-resolution transmission electron microscopy at least not to be filled completely (Fig. 7.14b), maybe it is even completely empty[†]. The output characteristics $I_\mathrm{sd}(V_\mathrm{sd})$ in figure 7.14c and the transfer characteristics $I_\mathrm{sd}(V_\mathrm{g})$ in figure 7.14d, both taken at $T = 4.2$ K, indicate that MFPP8 is an ambipolar semiconductor. The differential conductance diamond plot in figure 7.14e spans across the bandgap from hole to electron conduction and exhibits several irregularities such as overlapping diamonds and an elevated noise level

---

[†]High-resolution TEM can only be done for the sections of the freestanding carbon nanotube in close vicinity to the mechanically stabilizing metal contacts. The other parts of the nanotube, especially the one in the middle of the gap between the contacts, are thermally excited and vibrating resulting in a blurred image due to the lack of a proper focus adjustment. That is why the filling status of the middle segment of MFPP8 is unknown, whereas high-resolution TEM clearly shows that the parts of MFPP8 in the vicinity of the electrical contacts are empty.
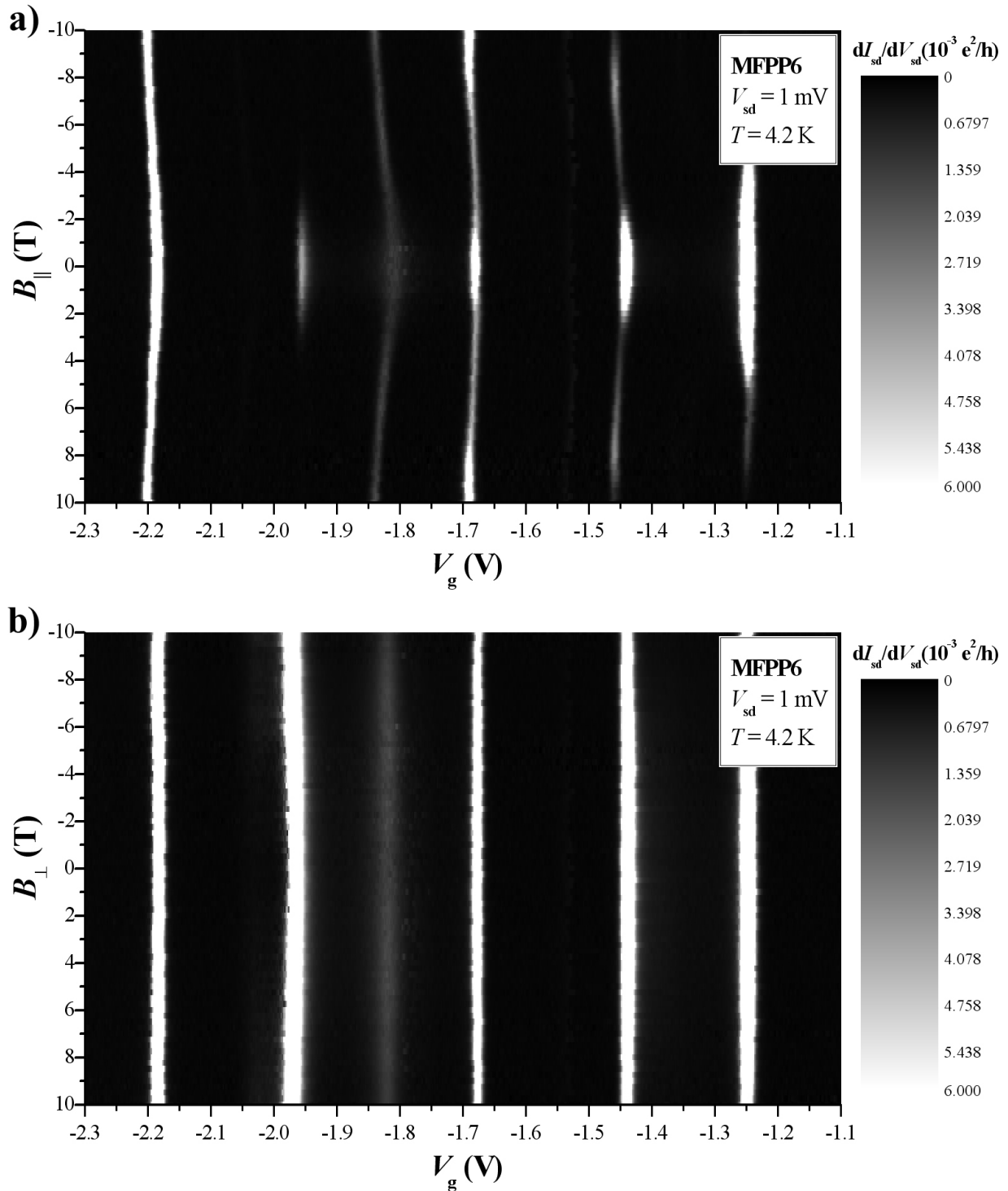
which one might attribute to a filling of the nanotube with metallofullerenes - if not knowing better due to the TEM imaging. In this way, sample MFPP8 is a suitable example that despite of a high overall ratio of 70 to 90 % nanotubes filled with fullerenes (cp. chapter 4.3), individual carbon nanotubes can be empty and an imaging method as high-resolution TEM or AFM is an appropriate tool to guarantee the claimed sample status/geometry [Obe06].
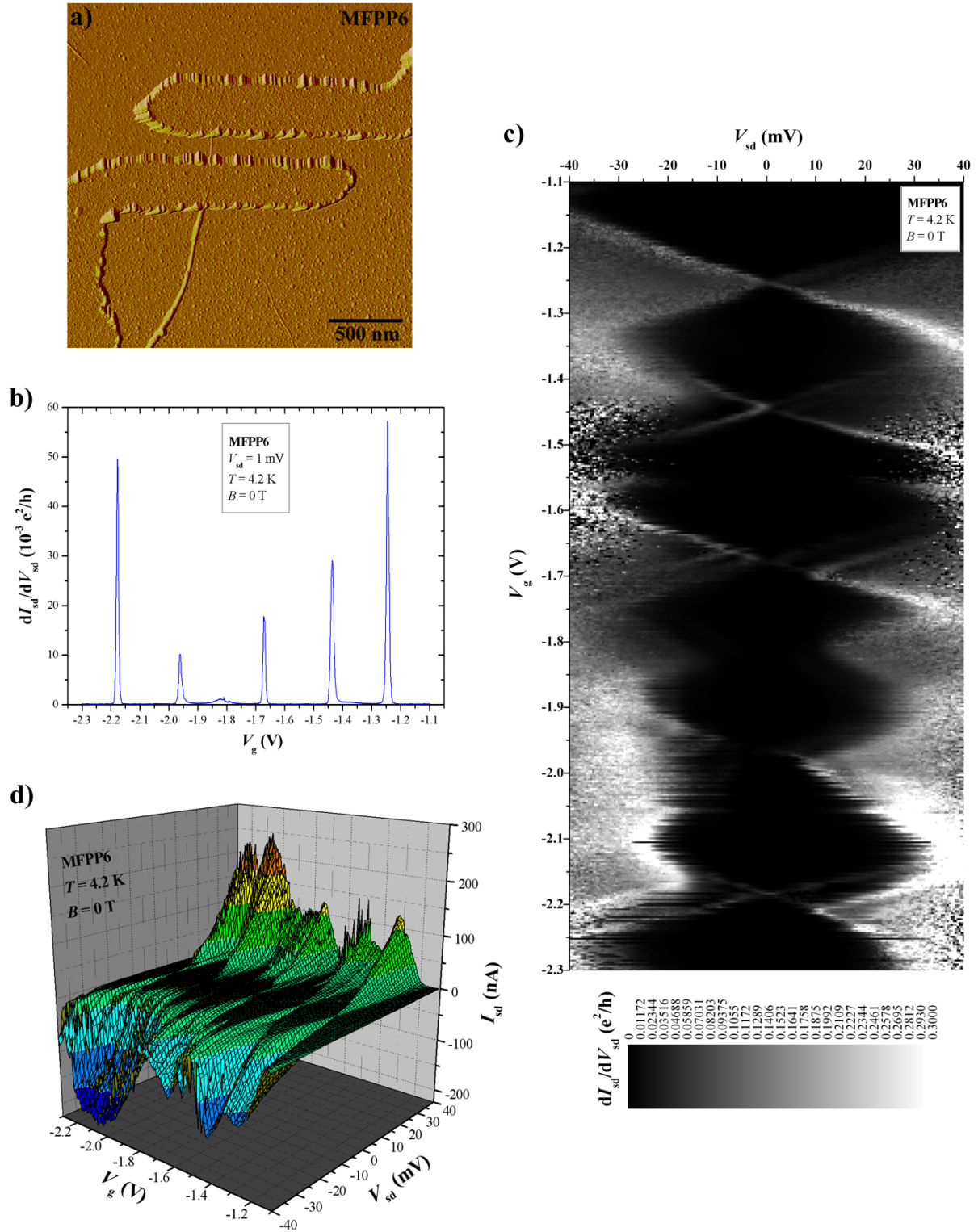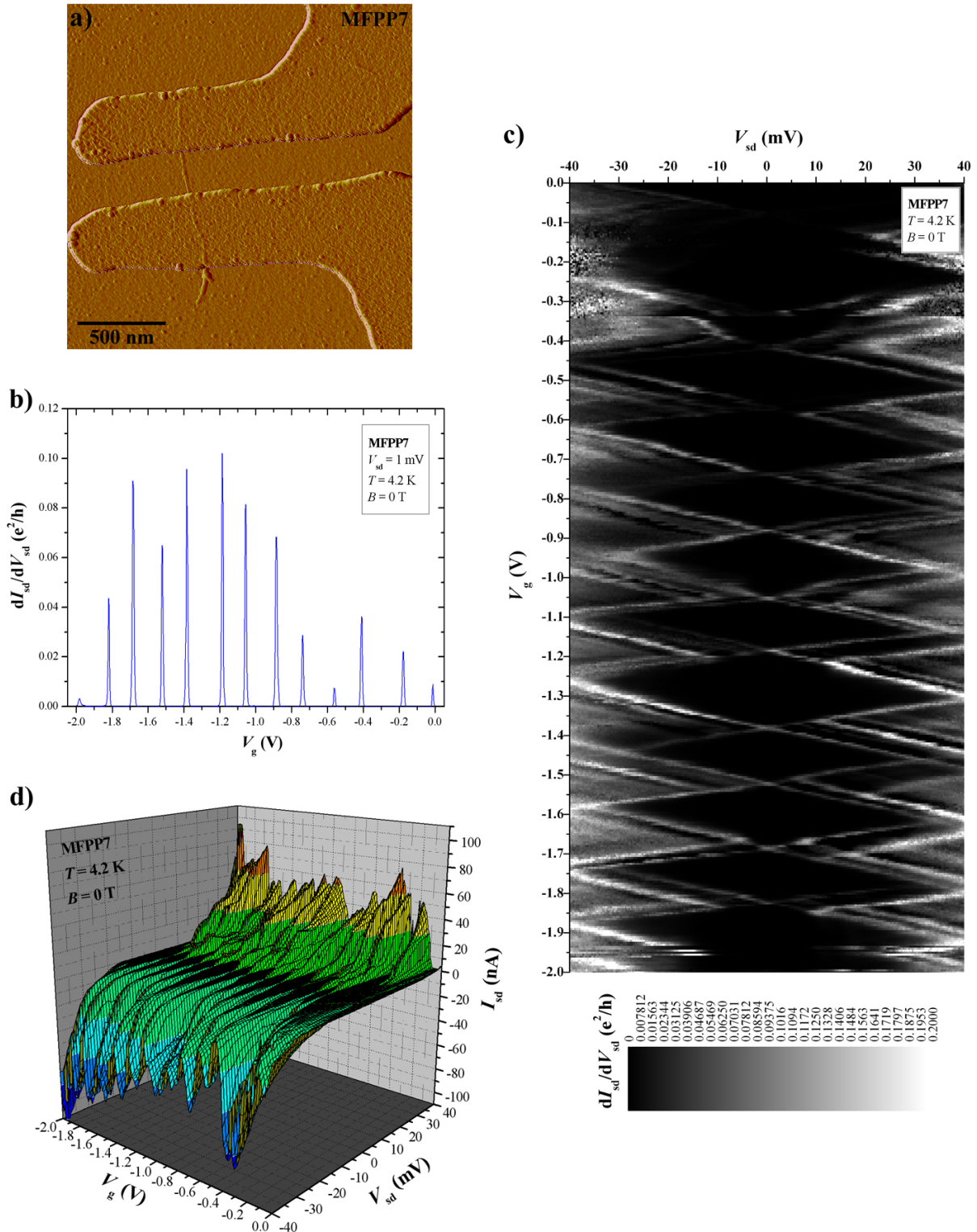
Fig. 7.10: a) Standard AFM image (taken at ambient conditions) of device MFPP6 after providing the metal source and drain contacts. **b)** Coulomb blockade oscillations of the differential conductance dI_{sd}/dV_{sd} of sample MFPP6 plotted vs. the applied gate voltage V_g at $V_{sd} = 1$ mV, $T = 4.2$ K and $B = 0$ T. **c)** Diamond plot of MFPP6, i.e. dI_{sd}/dV_{sd} as a function of the bias voltage V_{sd} and the gate voltage V_g at $T = 4.2$ K and $B = 0$ T. **d)** 3-dimensional graph of the current I_{sd} through device MFPP6 in the regime of Coulomb blockade and few-electron tunneling as a function of V_{sd} and V_g at $T = 4.2$ K and $B = 0$ T.
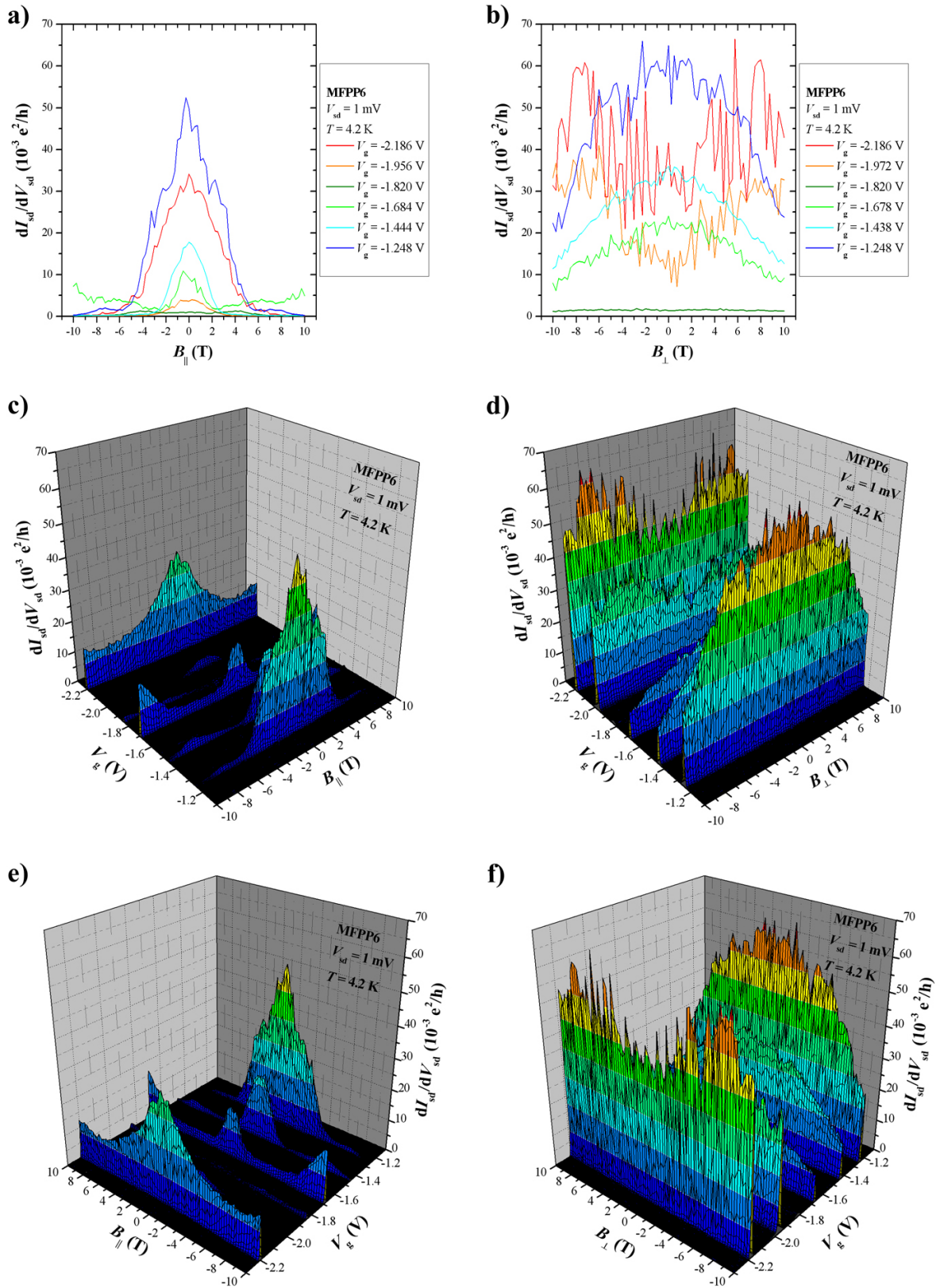
Fig. 7.11: Development of the Coulomb blockade peaks of device MFPP6 with applied magnetic field $B_\parallel$ parallel to the axis of SWNT1 (left column) or $B_\perp$ perpendicular to the axis of SWNT1 (right column) at $V_{sd} = 1$ mV and $T = 4.2$ K. **a),b)** Differential conductance dI_{sd}/dV_{sd} as a function of the **a)** parallel magnetic field $B_\parallel$ or the **b)** perpendicular magnetic field $B_\perp$ for different fixed gate voltages V_g. **c),d),e),f)** 3-dimensional plots of the differential conductance dI_{sd}/dV_{sd} as function of the gate voltage V_g and the **c),e)** parallel magnetic field $B_\parallel$ or the **d),f)** perpendicular magnetic field $B_\perp$ from different perspectives.

a)

b)

Fig. 7.12: Presentation of the differential conductance dI_{sd}/dV_{sd} of MFPP6 at $V_{sd} = 1$ mV and $T = 4.2$ K as function of the gate voltage V_g and the **a)** parallel magnetic field $B_\parallel$ or the **b)** perpendicular magnetic field $B_\perp$ as greyscale plots, in order to evaluate shifts of the Coulomb blockade peaks along the gate voltage axis induced by the magnetic field. The greyscale plots are based on the same datasets as used for figure 7.11.

Fig. 7.13: a) Standard AFM image (taken at ambient conditions) of device MFPP7 after providing the metal source and drain contacts. **b)** Coulomb blockade oscillations of the differential conductance $\mathrm{d}I_{\mathrm{sd}}/\mathrm{d}V_{\mathrm{sd}}$ of sample MFPP7 plotted vs. the applied gate voltage V_{g} at $V_{\mathrm{sd}} = 1$ mV, $T = 4.2$ K and $B = 0$ T. **c)** Diamond plot of MFPP7, i.e. $\mathrm{d}I_{\mathrm{sd}}/\mathrm{d}V_{\mathrm{sd}}$ as a function of the bias voltage V_{sd} and the gate voltage V_{g} at $T = 4.2$ K and $B = 0$ T. **d)** 3-dimensional graph of the current I_{sd} through device MFPP7 in the regime of Coulomb blockade and few-electron tunneling as a function of V_{sd} and V_{g} at $T = 4.2$ K and $B = 0$ T.
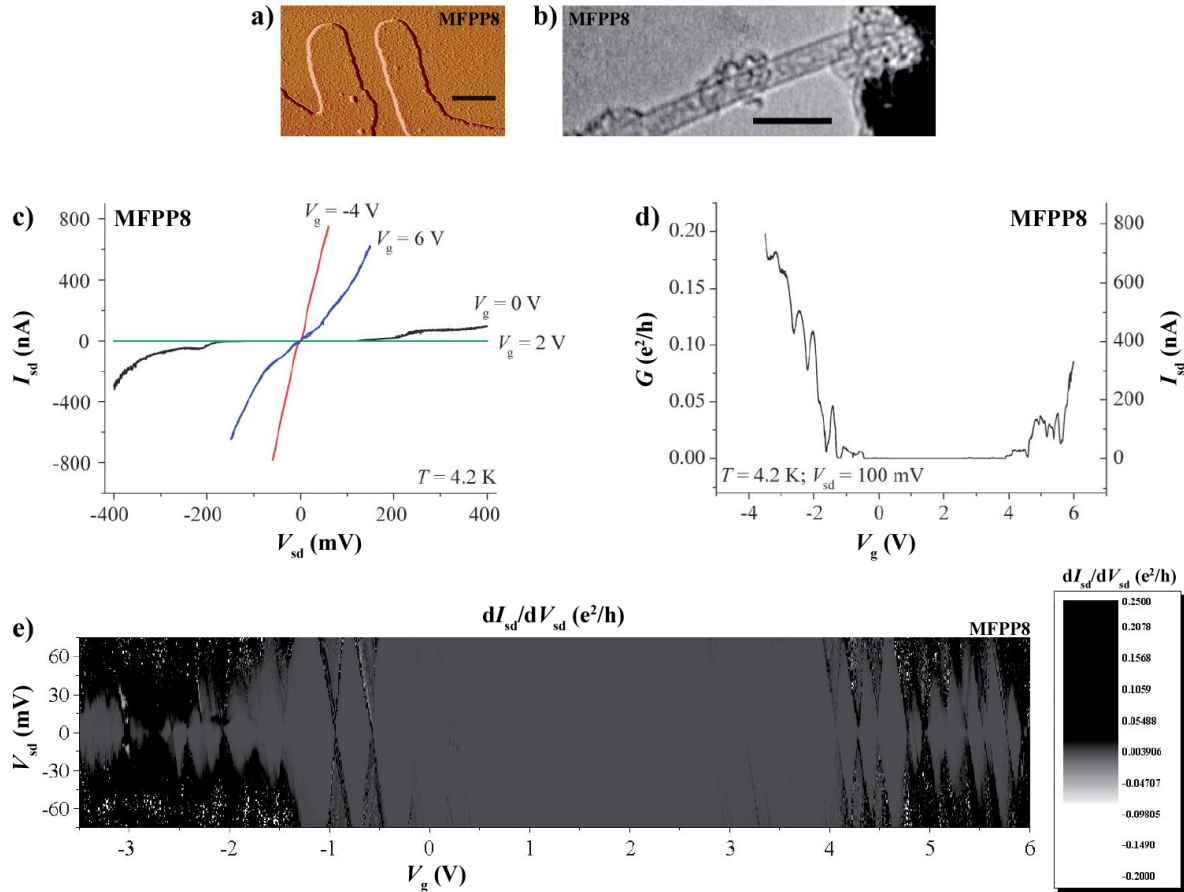
Fig. 7.14: Structural and electrical characterisation of sample MFPP8 [Obe06]. **a)** Standard AFM image of MFPP8 taken at ambient conditions. Scale bar: 400 nm. **b)** High-resolution TEM micrograph of a section of MFPP8 taken with a Philips CM200 TEM at 120 kV after underetching the sample (cp. chapter 4.7.1). Scale bar: 5 nm. Despite of the filling procedure described in chapter 4.3, MFPP8 is a single SWNT not or only partially filled with $Dy@C_{82}$ metallofullerenes. **c)** Output characteristics $I_{sd}(V_{sd})$ of MFPP8 at $V_g = -4, 0, 2, 6$ V and $T = 4.2$ K. **d)** Transfer characteristics $I_{sd}(V_g)$ of sample MFPP8 at $V_{sd} = 100$ mV and $T = 4.2$ K, showing that MFPP8 is an *ambipolar* semiconductor, i.e. both hole and electron conduction are accessible by adjusting the gate voltage V_g correspondingly. **e)** Differential conductance dI_{sd}/dV_{sd} of MFPP8 as function of the bias voltage V_{sd} and the gate voltage V_g at $T = 4.2$ K spanning across the bandgap from hole to electron conduction and exhibiting Coulomb blockade diamonds on either side.

7.3 Temperature dependence of electrical transport in Dy metallofullerene peapods

Further 2-probe transport investigations carried out on the metallofullerene peapod samples MFPP1 to MFPP4 are measurements of the output characteristics $I_{sd}(V_{sd})$ and the transfer characteristics $I_{sd}(V_g)$ at three different temperatures $T = 4.2$ K, $T = 80/85/86$ K and $T = 291/292$ K in analogy to the temperature dependent measurements done on the samples SWNT1 and SWNT2 in chapter 6.3. The transfer characteristics $I_{sd}(V_g)$ of MFPP1 to MFPP4 are displayed in figures 7.15a, 7.16a, 7.17a and 7.18a, the corresponding output characteristics $I_{sd}(V_{sd})$ in figures 7.15b, 7.16b, 7.17b and 7.18b. The overall principle behaviour of MFPP1 to MFPP4 at the three different temperatures resembles very much the one of the SWNT samples. As the samples SWNT1 and SWNT2, all metallofullerene peapod devices are p-type semiconductors at all three temperatures.
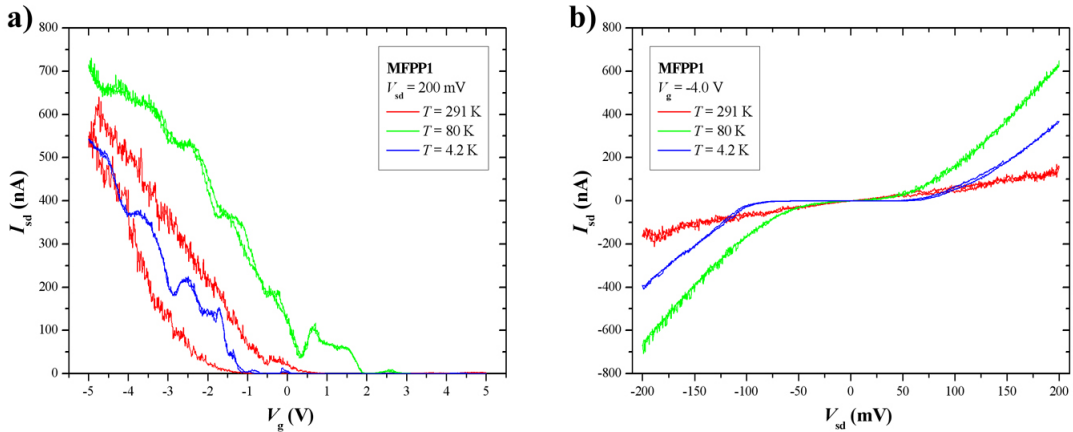
Fig. 7.15: Temperature dependence of 2-probe transport performed on the sample MFPP1. **a)** Transfer characteristics $I_{sd}(V_g)$ at $V_{sd} = 200$ mV and $T = 4.2$ K, 80 K, 291 K. **b)** Output characteristics $I_{sd}(V_{sd})$ at $V_g = $ -4.0 V and $T = 4.2$ K, 80 K, 291 K.
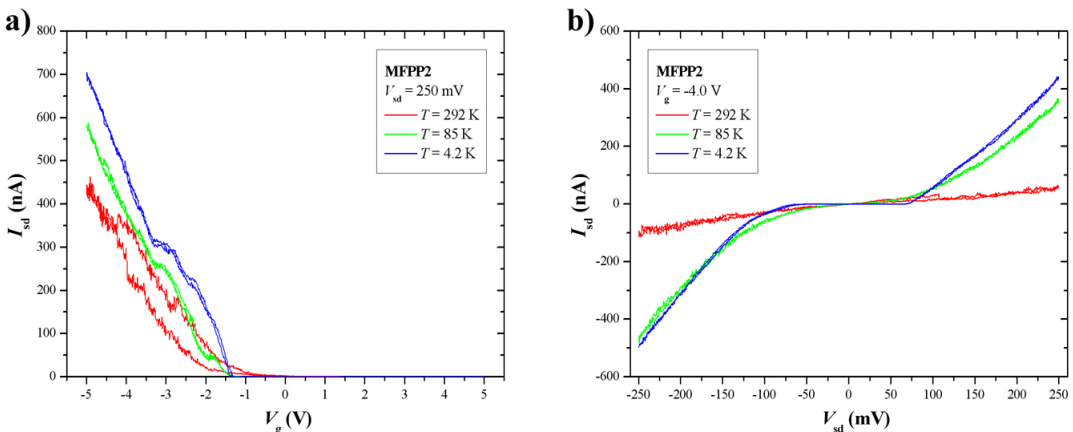
Fig. 7.16: Temperature dependence of 2-probe transport done on sample MFPP2. **a)** Transfer characteristics $I_{sd}(V_g)$ at $V_{sd} = 250$ mV and $T = 4.2$ K, 85 K, 292 K. **b)** Output characteristics $I_{sd}(V_{sd})$ at $V_g = $ -4.0 V and $T = 4.2$ K, 85 K, 292 K.
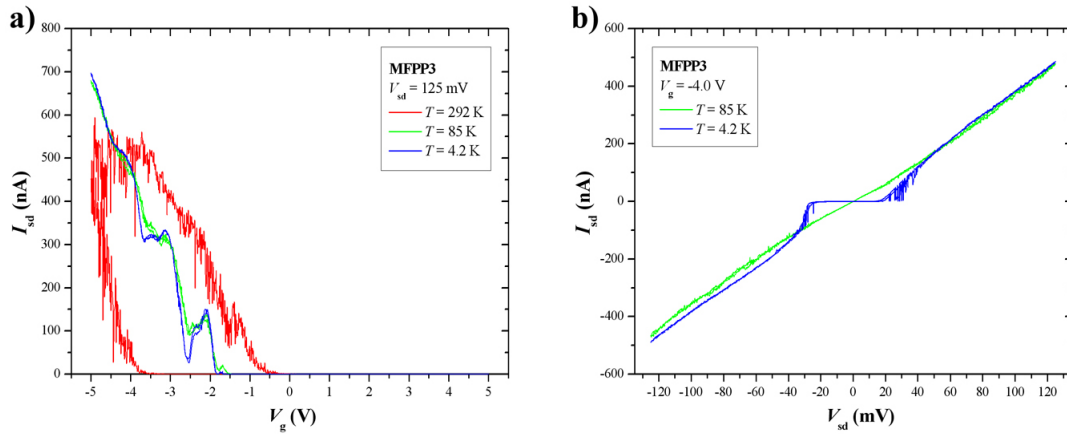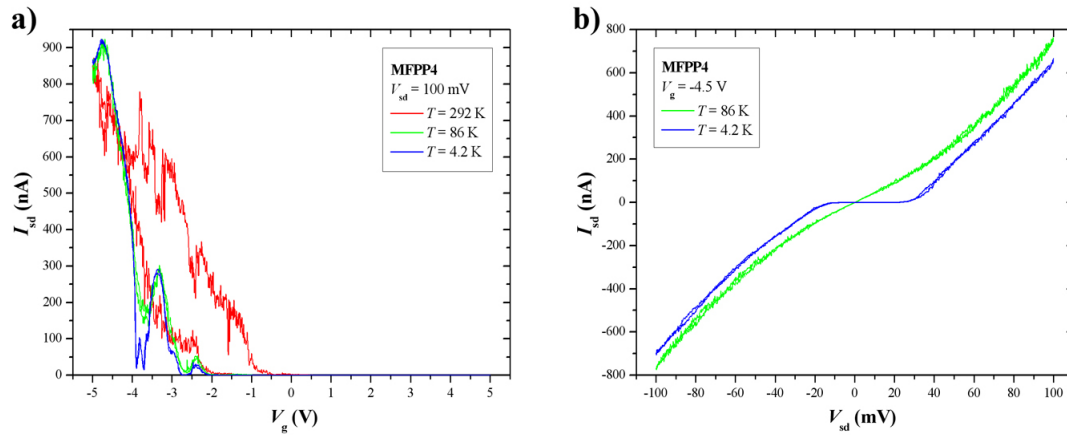
Fig. 7.17: Temperature dependence of 2-probe transport performed on the sample MFPP3. **a)** Transfer characteristics $I_{sd}(V_g)$ at $V_{sd} = 125$ mV and $T = 4.2$ K, 85 K, 292 K. **b)** Output characteristics $I_{sd}(V_{sd})$ at $V_g = -4.0$ V and $T = 4.2$ K, 85 K.

Fig. 7.18: Temperature dependence of 2-probe transport done on sample MFPP4. **a)** Transfer characteristics $I_{sd}(V_g)$ at $V_{sd} = 100$ mV and $T = 4.2$ K, 86 K, 292 K. **b)** Output characteristics $I_{sd}(V_{sd})$ at $V_g = -4.5$ V and $T = 4.2$ K, 86 K.

Similarly to the case of SWNTs, the $I_{sd}(V_g)$ curves become highly hysteretic and noisy at room temperature and the barriers in the $I_{sd}(V_{sd})$ graphs at low bias voltages vanish for elevated temperatures. There are differences amongst MFPP1 to MFPP4 regarding the relative conductance changes when changing the temperature, e.g. the $I_{sd}(V_g)$ curve for $T = 80$ K of MFPP1 is above the one for $T = 4.2$ K, which is opposite for MFPP2. However, these are details which likely depend on the contact and ambience properties, but not on the nanotube filling.

The most important points concerning the temperature dependent 2-probe measurements on the metallofullerene peapod samples MFPP1 to MFPP4 are firstly that *no* change of the type of conductance from p-type to n-type semiconducting to metallic behaviour with decreasing temperature from room temperature to 4.2 K is observed as postulated in [Chi01] (cp. chapter 3.3). Secondly, the MFPP samples do *not* behave as ambipolar semiconductors due to bandgap narrowing by the insertion of metallofullerenes as claimed in [Shi02] (cp. chapter 3.3). At this point it has to be stated that in principle *every*

semiconductor is an ambipolar semiconductor, the only question is whether by tuning the gate voltage one can reach the other conduction type before severe gate leakage sets in. Moreover, *ambipolar conduction* is *no* inherent property of metallofullerene peapods as claimed by [Shi02] since it is seen for empty (or eventually partially filled, see last footnote) SWNTs as well [Bab03, Jar04, Obe06] (Fig. 7.14). The bundle MFPP5, which was confirmed to contain two metallofullerene peapods out of three nanotubes in the bundle, is a p-type semiconductor at low temperature, which is also not in agreement with [Chi01, Shi02]. Four further metallofullerene samples which have not been presented here, exhibited p-type semiconducting behaviour at $T = 4.2$ K as well. In conclusion, the observations of [Chi01, Shi02] are not confirmed by the transport results gained within this project.

7.4   Summary of electrical transport in Dy metallofullerene peapods

Electrical transport and magnetotransport investigations have been performed on four metallofullerene peapod devices MFPP1 to MFPP4 in 2-probe transistor configuration at $T = 4.2$ K. All four samples behave as p-type semiconductors between 4.2 K and room temperature, which is also true for another four metallofullerene devices measured additionally but not presented here and which is not in agreement with earlier publications on metallofullerene peapod transport [Chi01, Shi02]. Furthermore, the statement that metallofullerene peapods behave as p-type semiconductors is supported by sample MFPP5, which to our knwoledge is the first metallofullerene peapod sample which is proven to contain metallofullerene peapods indeed. Obviously, the conduction type of the host tube is of relevance as well when discussing whether a metallofullerene peapod is a p-type, a n-type, an ambipolar semiconductor or a metal. Our results indicate, that a metallofullerene peapod need not necessarily be a metal [Chi01] or an ambipolar semiconductor [Shi02] at 4.2 K. When a magnetic field is applied along or perpendicularly to the axes of MFPP1 to MFPP4 in the *high-current regime*, i.e. I_{sd} is several 100 nA, two samples (MFPP1 and MFPP2) behave similarly as SWNT1, they show pronounced negative magnetoresistance with $MR \approx$ -8 to -12 % for $B_{\parallel}$, but no significant magnetoresistive effect for $B_{\perp}$. In contrast, the responses of the other two samples MFPP3 and MFPP4 upon the application of a parallel or perpendicular magnetic field are negligible for either magnetic field orientation (as in the case of SWNT2). In summary, the results of the transport and magnetotransport investigations on MFPP1 to MFPP4 are well comparable to the ones acquired for empty SWNTs. Thus, we conclude that the measured electrical properties of the metallofullerene peapods rather depend on the host single-walled carbon nanotubes than on the tube filling. Following the theory by E. L. Ivchenko and B. Spivak [Ivc02], MFPP1 and MFPP2 should have chiral host SWNTs, in contrast the ones of MFPP3 and MFPP4 should be achiral.

One further metallofullerene peapod sample MFPP6 showed Coulomb blockade behaviour

and was investigated in the regime of *Coulomb blockade and few-electron tunneling*. Its general behaviour with and without magnetic field applied is comparable to the one of empty nanotubes as well, i.e. the filling does not seem to be of relevance in this regime either.

The metallic and ambipolar behaviour of metallofullerene peapods at $T = 4.2$ K claimed in [Chi01] and [Shi02], respectively, could not be confirmed in our measurements.

Note that due to the high-resolution AFM being a very time-intensive imaging method, it was not possible to scan the metallofullerene peapod samples MFPP1 to MFPP4 and MFPP6 within the project time.

7.5   AFM imaging of metallofullerene peapods with atomic resolution

Imaging such complex hybrid structures as metallofullerene peapods by means of atomic resolution AFM might answer two sorts of questions: the first category of questions comprises the questions arising from fundamental scientific interest, e.g. the intriguing question how the topography of a metallofullerene peapod might look like at the atomic scale. One might ask as well, whether one could see the *peas in the pod*, i.e. a kind of periodic undulation pattern due to the fullerene filling if the host carbon nanotube is narrow enough. Another question might be if energy can be transferred to such a hybrid system, since there should be inner degrees of freedom, e.g. the possibility for the encapsulated fullerenes to resonate. The second kind of questions would be more practically oriented, namely, whether it is possible to use the technique of the atomic resolution AFM to differentiate between empty SWNTs and metallofullerene peapods in a non-invasive way, whether one might be able to obtain the structural indices (n, m) of the host nanotubes and maybe the number of tubes in a bundle and their precise diameters. These are questions being of great experimental relevance in the framework of this project, since transport and magnetotransport data gain relevance enormously if one is able to tell the detailed structure of the object one has perfomed electrical measurements on.

In a cooperation with M. Ashino and R. Wiesendanger (University of Hamburg) both sorts of questions were addressed experimentally. The AFM equipment and the underlying technology has been briefly introduced in chapter 4.7.2.

The results of dynamic high-resolution atomic force microscopy on empty SWNTs and $(Dy@C_{82})@SWNT$ metallofullerene peapods are displayed in figure 7.19: on the left, upper side (Figs. 7.19a-d), topography images are shown, whereas the corresponding, simultaneously acquired ΔE energy dissipation maps (Figs. 7.19e-h) are plotted on the right, lower side. The images in figures 7.19a,e belong to an empty SWNT with a diameter of 1.30 ± 0.05 nm, the images in figures 7.19b,f, figures 7.19c,g and figures 7.19d,h have been
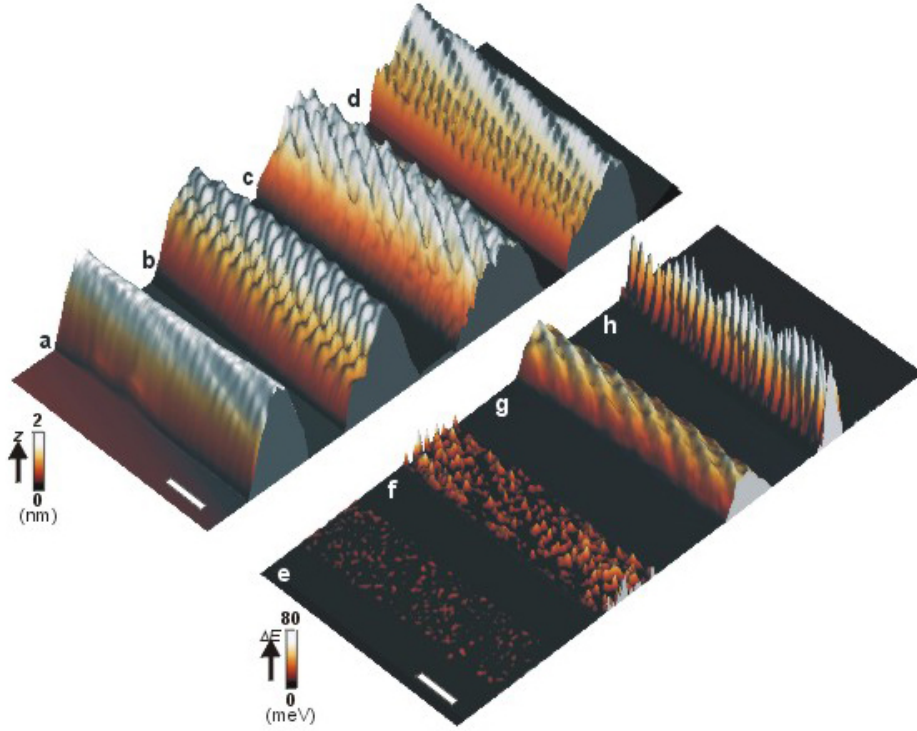
Fig. 7.19: Results obtained by dynamic, atomic resolution AFM. Scale bars: 1 nm. (a,e), (b,f), (c,g) and (d,h) each were recorded simultaneously. **a)** Topography of an empty SWNT with a diameter of 1.30 ± 0.05 nm. **b)-d)** Topography images of (Dy@C$_{82}$)@SWNT metallofullerene peapods with the following diameters: b) 1.62 ± 0.05 nm, c) 1.50 ± 0.05 nm and d) 1.30 ± 0.05 nm. **e)** ΔE energy dissipation image of an empty SWNT with a diameter of 1.30 ± 0.05 nm. **f)-h)** ΔE energy dissipation images of (Dy@C$_{82}$)@SWNT metallofullerene peapods with the following diameters: b) 1.62 ± 0.05 nm, c) 1.50 ± 0.05 nm and d) 1.30 ± 0.05 nm [As09b].

taken on (Dy@C$_{82}$)@SWNT metallofullerene peapods with diameters of 1.62 ± 0.05 nm, 1.50 ± 0.05 nm and 1.30 ± 0.05 nm, respectively. The topography of the empty SWNT in figure 7.19a exhibits atomic features in conjunction with a superimposed helical structure. Based on the helical angle and the apparent height of the nanotube [As09b], the structural indices could be determined to be (13,6) [Ash06]. Above areas of stronger curvature, the resolution is decreased, probably due to multiple tip apex sample interactions. Basically, the topographies of large diameter metallofullerene peapods in figures 7.19b,c resemble very much the topography image of the empty SWNT, except of the fact that the atomic-scale contrasts of the (Dy@C$_{82}$)@SWNT metallofullerene peapods are much more pronounced, which could result from the lower curvature due to larger diameter and maybe from the filling with metallofullerenes. In contrast to the large diameter metallofullerene peapods, the topography image of the narrow (Dy@C$_{82}$)@SWNT structure in figure 7.19d differs significantly from that of the empty SWNT in figure 7.19a of the same diameter: for the 1.30 ± 0.05 nm metallofullerene peapod (Fig. 7.19d), a highly regular undulation along the host nanotube axis is observable, with an amplitude of $\Delta z = 56 \pm 5$ pm and

an axial periodicity Δx of 1.15 ± 0.05 nm, which closely matches the $(Dy@C_{82})@SWNT$ periodicity of 1.05 ± 0.05 nm received from high-resolution TEM [Ash08]. Therefore, we attribute this undulation of the nanotube sidewall in figure 7.19d to the filling of the nanotube with metallofullerenes. Such a sidewall undulation can not be observed for the metallofullerene peapods of larger diameter since in that case, the spacing between metallofullerenes and nanotube wall is too large for the tube sidewall to be bulged out.

In contrast, the ΔE energy dissipation maps (Figs. 7.19e,f,g,h) exhibit clear differences between an empty SWNT and metallofullerene peapods. For the empty SWNT (diameter: 1.30 ± 0.05 nm), due to the high elasticity of the SWNT [Ash08], the oscillation of the AFM cantilever is not damped during scanning the SWNT, which means that the respective engery dissipation signals are zero (Fig. 7.19e)[†]. However, strong energy dissipation signals (71 ± 5 meV) are observed for the 1.30 ± 0.05 nm metallofullerene peapod (Fig. 7.19h). As in the corresponding topography image in figure 7.19d, pronounced undulated features are obtained, pointing to the fact that energy dissipation peaks at the sites the metallofullerenes reside within the host nanotube. We assign the energy dissipation of the $(Dy@C_{82})@SWNT$ metallofullerene peapods to excitation of internal degrees of freedom such as rocking the fullerenes or tumbling of the metal atoms inside. Increasing the diameter of the metallofullerene peapod host nanotube to 1.50 ± 0.05 nm, the magnitude of the average energy dissipation drops to 30 ± 6 meV (Fig. 7.19g), for a host nanotube diameter of 1.62 ± 0.05 nm, the average energy dissiptaion is only 7.9 ± 3.0 meV (Fig. 7.19f). Furthermore the undulation features of the energy dissipation vanish when increasing the metallofullerene host nanotube diameter (Figs. 7.19f,g). This may be related to the fact that the metallofullerenes excited by the resonating AFM tip are less confined along the tube axis in large diameter peapod systems and thus the sharp ΔE peaks acquired for narrow diameter tubes could be flattened out for larger host nanotube diameters. The origin of decreasing energy transfer with increasing metallofullerene peapod host nanotube diameter is assigned to a worse coupling between the AFM tip apex and the large diameter metallofullerene peapod. Figure 7.20 [As09b] plots the average ΔE energy dissipation versus metallofullerene peapod diameter. Obviously, the energy dissipation behaves as a linear function of the peapod diameter.

The answers to the scientific questions raised at the beginning of this chapter have been given throughout the text. Now, theoretical investigations are under way, in order to gain further understanding which internal degrees of the $(Dy@C_{82})@SWNT$ metallofullerene peapods are excited for which host nanotube diameters and to come up with a theory based fitting curve for figure 7.20.

As for the practical applicability, the high-resolution AFM investigations have proven their capability to differentiate between empty SWNTs and metallofullerene peapods through the energy dissipation of the peapods as a sufficient criterion in the host nanotube diameter

---

[†]the very small contrast in figure 7.19e is noise only
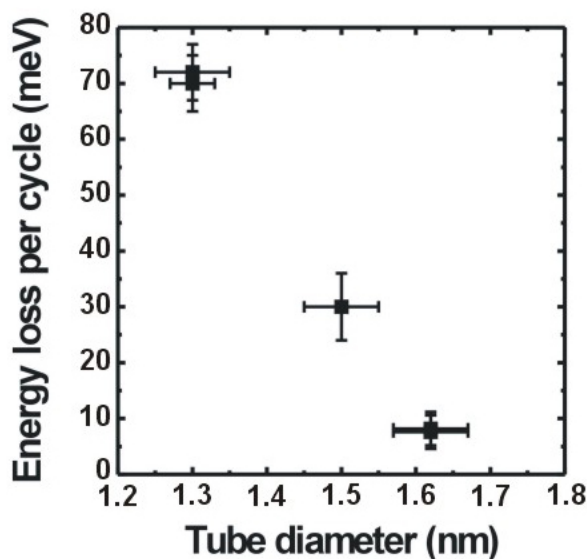
Fig. 7.20: Relationship between the average energy dissipation ΔE of a $(Dy@C_{82})$@SWNT metallofullerene peapod and the respective peapod diameter. The average energy dissipation drops with increasing metallofullerene peapod diameter. Five $(Dy@C_{82})$@SWNT systems have been picked up here, while several ten further peapods exhibited almost identical features. The metallofullerene peapod diameters have been extracted from atomically resolved dynamic AFM images (cp. Figs. 7.19a-d) [As09b].

range up to approx. 1.65 nm [Ash08, As09b]. Furthermore dynamic high-resolution AFM is able to tell atomic-scale structural features of the SWNT [Ash04] and the possibility to obtain helicities and structural indices (n, m) is given. So this non-destructive technique is the method of choice for combinatorial studies on SWNTs and metallofullerene peapods, even though it is very time-consuming.

7.6 Metallic nanocluster formation from a Dy metallofullerene peapod

From a chemist's point of view, a single-walled carbon nanotube is a very stable, inert molecule offering a considerably large inner space which might serve as a reaction chamber well isolated from the surroundings. Having filled such a *miniature reactor vessel* with potential reactants as $Dy@C_{82}$ endohedral metallofullerenes, one might try to externally trigger a chemical reaction between these metallofullerenes, e.g. by putting $(Dy@C_{82})$@SWNT metallofullerene peapods into a high-resolution transmission electron microscope and shine the electron beam onto the specimen. However, one has to be careful regarding the proper choice of the energy of the triggering electron beam: if the beam energy is above the knock-on damage for carbon-carbon bonds, the reactants will be severly damaged by the electron beam, dangling bonds will be created, which will dominate the dynamics of the system. A realistic chemical reaction can only be accomplished if the conditions are as mild as possible, i.e. the beam energy should be below the knock-on damage for C-C bonds. In this case, only thermal excitation of the heavy Dy atoms by

the electron beam remains which may be regarded as a proper external trigger for a chemical reaction. Since SWNTs are excellent thermal conductors, heating effects of the host carbon nanotubes may be neglected as long as a good thermal connection to the rest of the sample is ensured.

An ultimate challenge of chemistry is the stepwise understanding and tracing of a reaction process with high resolution in space and time. This defines two important requirements for the TEM which shall be used for such an experiment: it should have atomic resolution, which for the moment[†] can be realized best utilizing a spherical aberration (c_s) corrected TEM, and it should have a high image capture rate to follow the reaction process in real time.

This experiment with the described experimental setup was realized in a cooperation together with A. Chuvilin, U. Kaiser (University of Ulm) and A. N. Khlobystov (University of Nottingham) [Chu09]. (Dy@C_{82})@SWNT metallofullerene peapods were investigated by a c_s corrected, atomic-resolution transmission electron microscope at 80 kV accelerating voltage, which is below the C-C knock-on damage. Figure 7.21 displays a time sequence of a Dy metallofullerene peapod section together with the corresponding schematic illustration of the ongoing processes. In figure 7.21a_1,a_2 there are two intact Dy@C_{82} endohedral metallofullerenes, which can break open in the vicinity of the Dy atoms (Fig. 7.21b_1,b_2). The right Dy atom leaves its cage (Fig. 7.21c_1,c_2) and joins the other Dy atom in the left C_{82} fullerene (Fig. 7.21d_1,d_2). Subsequently the pair of Dy atoms manages to weaken and break the bonds of the left fullerene from its inner space (Fig. 7.21e_1,e_2,f_1,f_2). Studying this process reveals the importance of the Dy atoms as catalysts. There can be two ways how the Dy atoms might weaken and break covalent carbon-carbon bonds: firstly, the kinetic energy of the incident electrons transferred to the Dy atom might be further transferred to the carbon atoms facilitating the C-C bond rupture. Secondly, it is known that Dy atoms with an oxidation state of 2+ or 0 act catalytically on nearby π electron systems, i.e. they weaken C-C bonds in carbon hexagons for example. The original oxidation state of Dy in the Dy@C_{82} fullerene is 3+, since each Dy atom transfers 3 electrons to the fullerene cage (cp. chapter 2.3) [Shi00, Kit07], however, the Dy^{3+} ions can be reduced by the incident electron beam to become neutral Dy atoms.

After all Dy@C_{82} metallofullerenes have been ruptured by the impact of the Dy atoms, the fullerene cages coalesce by saturating dangling carbon bonds. One important observation is that - unlike for thermally induced formation of an inner tube - the inner nanotube formed by coalesced fullerenes is structurally imperfect, since the structural transformations stop as soon as the Dy atoms have left the fullerene cages. With the fullerenes being coalesced, the Dy atoms can freely move within the outer SWNT and start to form a metal cluster as depicted in figure 7.22a_1,a_2. Because the Dy atoms are continuously tumbling and moving, the metal cluster is highly dynamic (Fig. 7.22b_1,b_2,c_1,c_2). As soon as the

---

[†]until there is a fully aberration corrected TEM

cluster reaches a critical size of about 7 Dy atoms, it weakens the C-C bonds of the host SWNT, induces a kink in its sidewall (Fig. 7.22d_1,d_2) and finally breaks the SWNT in two parts (Fig. 7.22e_1,e_2). Short time after being ruptured apart, the two newly formed nanotube ends form carbon caps again (Fig. 7.22f_1,f_2). Despite of this rupturing event, the Dy metal cluster stays closely together throughout the whole observed period. The distances between each two Dy atoms are below 4 Å suggesting metallic bonds or Dy atoms connected by bridging carbon atoms.

This is the first time that a formation of a metallic cluster via one-by-one coalescence of metal atoms has been observed in real time with atomic resolution [Chu09].
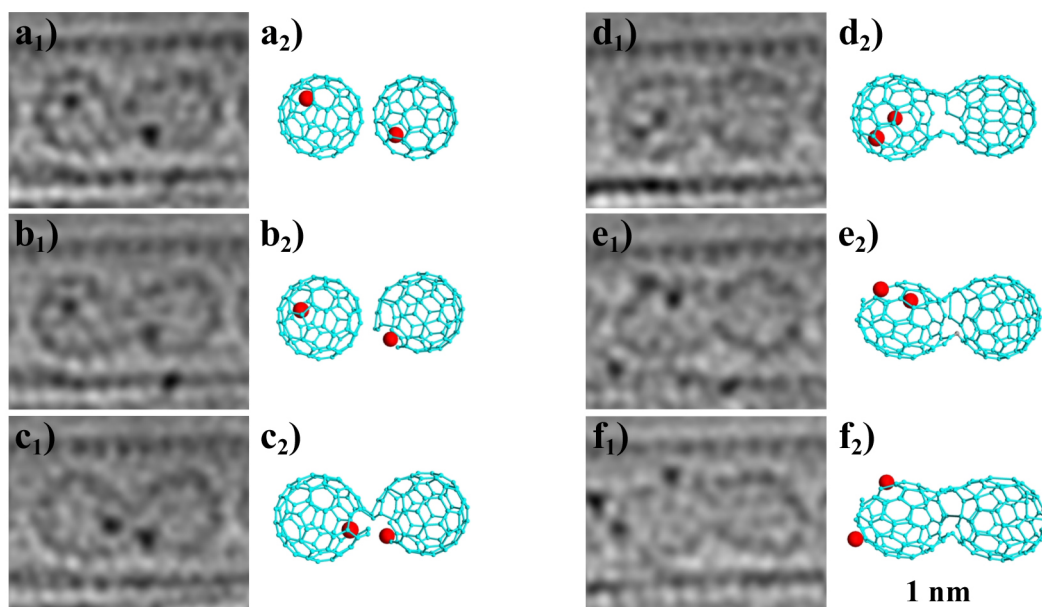
Fig. 7.21: Left columns: Atomic-resolution, spherical aberration (c_s) corrected transmission electron microscopy at 80 kV accelerating voltage of a metallofullerene peapod segment as a series in time. **Right columns:** Corresponding schematic illustration sequence. Carbon-carbon bonds of a_1),a_2) initially intact fullerenes b_1),b_2) are weakened and break in close vicinity to Dy atoms acting as catalysts. c_1),c_2) The right Dy atom finally leaves its fullerene cage, d_1),d_2) joins the other Dy in the left fullerene and e_1),e_2),f_1),f_2) both Dy atoms acting together break open the left C_{82} fullerene cage from its inner hollow space [Chu09].
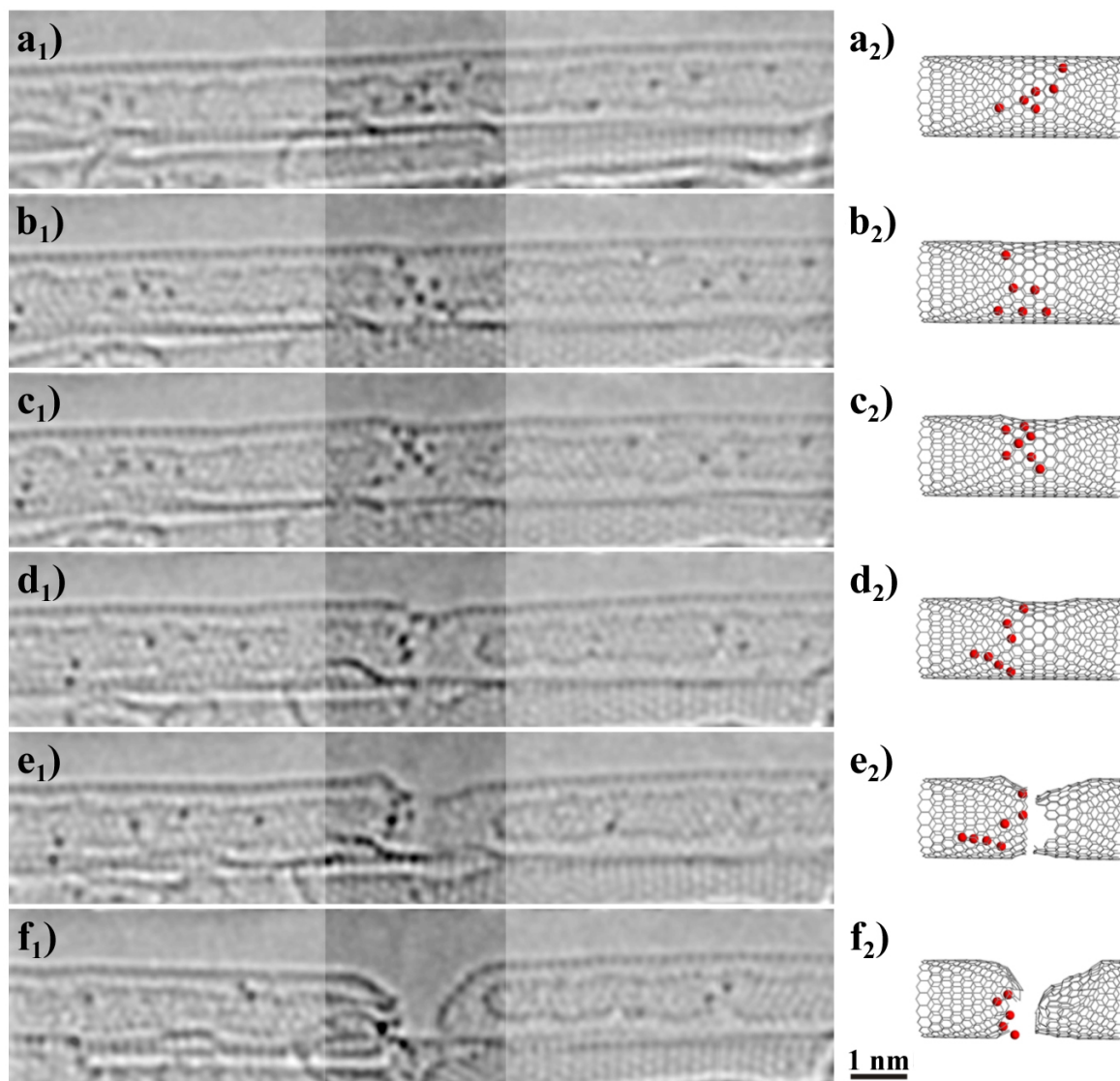
Fig. 7.22: Left column: Atomic-resolution, spherical aberration (c_s) corrected transmission electron microscopy at 80 kV accelerating voltage of a metallofullerene peapod segment as a series in time. **Right column:** Schematic illustration sequence corresponding to the highlighted part of the left column. After all the fullerene cages coalesced, the Dy atoms are free to move within the inner space of the host carbon nanotube and $\mathbf{a_1}),\mathbf{a_2})$ start to form a metal cluster. $\mathbf{b_1}),\mathbf{b_2}),\mathbf{c_1}),\mathbf{c_2})$ Since the Dy atoms continue to tumble and move, the metal cluster is highly dynamic. $\mathbf{d_1}),\mathbf{d_2})$ When the cluster has reached a critical size of about 7 Dy atoms, it acts on the upper sidewall of the host SWNT and induces a kink. $\mathbf{e_1}),\mathbf{e_2})$ After intensive interaction with the Dy cluster, the SWNT is ruptured apart at the former kink position. $\mathbf{f_1}),\mathbf{f_2})$ Shortly after the SWNT sidewalls are broken, the dangling carbon bonds form covalent bonds again, the two SWNT ends are instantaneously capped [Chu09].

8. Summary

One distinctive feature of carbon is its capability to form allotropes in zero, one, two and three dimensions, which arises from the different possible hybridizations of its valence electron orbitals. In recent years, novel low-dimensional and nanoscale carbon modifications of extraordinary physical properties have been found by researchers. The main focus of this thesis is to study several prominent novel carbon nanomaterials, namely graphene mono- and bilayers, single-walled carbon nanotubes (SWNTs) and single-walled carbon nanotubes encapsulating linearly aligned magnetic $Dy@C_{82}$ endohedral metallofullerenes [Hua00] ($\rightarrow$ *metallofullerene peapods*) with respect to their electronic behaviour at low temperatures, especially in the case of externally applied magnetic fields of different orientations.

Before addressing the actual experimental results, it shall be mentioned that one important objective which was pursued within this project was to combine (magneto-)transport studies with structural investigations on the same nanoscale object revealing the geometry of the sample characterized electronically before and allowing to draw the correct conclusions from the transport results. For the combinatorial imaging, we applied high-resolution TEM as well as high-resolution AFM and could gain some impact [Mey04, Obe06, Ash08] in the community since only very few groups carry out these - according to our opinion - essential cross-checks.

Quantum Hall effect measurements on graphene mono- and bilayers first published in November 2005 could be reproduced within this project. Using as-cleaved flakes without further precautions as SiO_2 surface treatment, etching of the flakes into hallbar structures and annealing to evaporate adsorbates often results in low quality quantum Hall effect signatures especially for bilayers which can be partially compensated by high magnetic fields of up to 18 T. The shape of the graphene flake edges seems to have major influence on the quantum Hall effect features. Meanwhile reproducible graphene sample quality is possible if using the methods mentioned above. 2-probe magnetotransport measurements on graphene mono- and bilayers showed the expected Hall effect signatures for magnetic fields perpendicularly aligned to the flakes. As anticipated, no significant magnetoresistance was observed for in-plane magnetic fields. Raman spectroscopy was used successfully to differentiate between one and two layers of graphene.

In contrast to graphene flakes, significant 2-probe magnetoresistance can occur for a single-walled carbon nanotube modeled as a graphene sheet rolled up to form a seamless cylinder. The theory by E. L. Ivchenko and B. Spivak [Ivc02] states that the coupling of the orbital momentum of the electrons around the circumference of a chiral SWNT with the linear electron momentum along the SWNT axis leads to a current density increasing linearly

with the axially aligned magnetic field $B_\parallel$, i.e. there is negative magnetoresistance in this case. In contrast, there is no effect if the magnetic field is perpendicularly aligned towards the axis of a chiral SWNT or if the SWNT is achiral. Detailed magnetotransport measurements on SWNT devices showed both type of behaviours, however successfully performed high-resolution AFM imaging revealed the device with the strong magnetoresistance (approx. -8 to -14 %) to be a bundle of SWNTs where the SWNTs seem to be twisted around each other. The second device without response to the magnetic field independent of its orientation was confirmed to be an individual SWNT, however it could not be told whether it is chiral or achiral due to adsorbates on the tube. In conclusion, we interpret the magnetotransport measurements in this high-current regime (I_{sd} several 100 nA) as follows: the individual SWNT not showing magnetoresistance at any magnetic field orientation is an achiral SWNT according to [Ivc02], whereas the SWNT bundle exhibits the significant magnetoresistance for parallel magnetic field either because one chiral SWNT is dominating the transport within the bundle according to [Ivc02] or due to the electrons following the twist of the SWNTs around each other in the bundle and creating a magnetic moment which interacts with the external magnetic field. Further high-resolution AFM studies are envisaged on these SWNT samples to gain more structural information. A suggested experimental way to clarify whether the observed negative magnetoresistance of approx. -8 to -14 % for an axially aligned magnetic field is due to the twist within the bundle or can be seen for individual SWNTs as well, is to start a new series of combined experiments (magnetotransport plus high-resolution AFM) on chemical vapor deposition (CVD) SWNT material which is known to consist of individual SWNTs predominantly.

Complementary magnetotransport measurements on the same SWNT devices have been carried out for the regime of *Coulomb blockade and few-electron tunneling*. In this case, both SWNT devices exhibit strong undulations of the differential conductance Coulomb blockade peak heights for different values of the parallel magnetic field $B_\parallel$. These undulations are accompanied by shifts of the Coulomb blockade peak positions along the gate voltage direction. We attribute these two effects to *diamagnetic* and *Zeeman energy shifts* of the SWNT states: ground states and respective excited states move towards each other with increasing parallel magnetic fields, where the weighting of their contributions to the overall coupling is being changed continuously resulting in the observed undulation patterns of the differential conductance Coulomb blockade peak heights (cp. chapter 6.2). For perpendicular magnetic fields $B_\perp$, both effects are negligible, probably as a consequence of the impossibility to induce circumferential diamagnetic moments in the SWNTs at this magnetic field orientation. The height undulations of the Coulomb blockade peaks and the corresponding shifts along the gate voltage direction have been observed for GaAs based quantum dots [Wei94, Wei05], however we are not aware of similar results published for SWNT transistors yet.

According to our knowledge, it is the first time that comprehensive magnetotransport measurements as described above have been carried out on an SWNT sample character-

ized by high-resolution imaging.

Similar 2-probe magnetotransport investigations were done on four metallofullerene pea-pod samples. For two out of the four samples, significant 2-probe magnetoresistance has been observed ($MR \approx$ -8 to -12 %) for parallel magnetic fields in the *high-current regime*, the effect vanished upon application of perpendicular magnetic fields on the same metallofullerene peapods. For the other two metallofullerene peapod devices, no magnetoresistive effect became apparent for either magnetic field orientation. In general, the data of the metallofullerene peapod samples are well comparable to the SWNT data. We attribute the occurence of the strong negative magnetoresistance rather to the host tubes being chiral according to [Ivc02] than to the effect of a potential filling with endohedral metallofullerenes. The other two peapod samples would have achiral host SWNTs according to this explanation.

The 2-probe magnetotransport measurements on a metallofullerene peapod sample in the *Coulomb blockade and few-electron tunneling regime* resulted in qualitatively similar results as for the SWNT samples. Again, we think that the host tube dominates the physical effects rather than the eventual filling with metallofullerenes.

The output characteristics $I_{sd}(V_{sd})$ and transfer characteristics $I_{sd}(V_g)$ of eight metallofullerene peapod samples were recorded at $T = 4.2$ K, $T \approx 80$ K and $T \approx 290$ K. For all temperatures, the metallofullerene peapods behave as p-type semiconductors, which does not confirm earlier studies that claim metallic [Chi01] and ambipolar behaviour of metallofullerene peapods [Shi02], respectively. These two studies do not come up with structural investigations. One metallofullerene peapod sample, which we confirmed to contain two filled SWNTs and one empty SWNT, is p-type semiconducting at $T = 4.2$ K as well.

Due to time restrictions we were not able to realize the time-intensive high-resolution AFM imaging on the metallofullerene peapod transport samples in order to detect whether the samples comprise SWNTs filled with metallofullerenes indeed. These measurements are envisaged for the future. However, a method to differentiate between empty SWNTs and metallofullerene peapods by non-invasive, high-resolution AFM was successfully developed in the project time (cp. chapter 7.5). Within these atomic resolution AFM studies, it was recognized that narrow host SWNTs of 1.3 nm diameter exhibit topography undulations if metallofullerenes are inserted, whereas these height undulations obviously vanish for large diameter host SWNTs (diameter approx. 1.6 nm) (Figs. 7.19b,c,d). Furthermore, energy transfer from the oscillating AFM cantilever to the metallofullerene hybrid system was detected (Figs. 7.19f,g,h), which is not seen for empty SWNTs (Fig. 7.19e). This energy is going into internal degrees of freedom and excites e.g. vibrations or tumbling motions of the metallofullerenes. The energy dissipation scales inversely proportional with the host SWNT diameter (Fig. 7.20) and is the suffient criterion to distinguish a metallofullerene peapod from an empty SWNT which does not exhibit any energy dissipation effects.

Finally, a side-project on high-resolution transmission electron microscopy resulted in the first real-time, atomic resolution observation of a metallic cluster formation through one-by-one coalescence of metal atoms (cp. chapter 7.6).

A. Appendix

A.1   Diagram of ViDi 1.70, mode 13

As highlighted in chapter 4.6.1, in this appendix the diagram, i.e. the source code of measurement mode 13 of the data acquisition software *ViDi 1.70* developed within this PhD project, shall be discussed in more detail. All 33 measurement modes of the *ViDi* software work in a similar way, thus for basic understanding of the *ViDi* functionality it is sufficient to look at the diagram of one representative measurement mode.

Measurement mode 13 records the channel current I_{sd} at fixed V_{sd} as a function of the gate voltage V_g and the magnetic field B. After each V_g loop, the magnetic field B is stepwise increased from B_{min} to B_{max} (or decreased from B_{max} to B_{min}).

LabView, the programming language used to develop the *ViDi* software, is a graphical programming language, i.e. the whole source code is presented in a graphical way. For instance, while-, if-, case- or for-loops are presented by various kinds of frames, subroutines are displayed as small squares and variables/constants are transmitted by wires of different colors representing the type of variable. For the sake of clarity, only the main diagram will be described in detail, not all the included subroutines.

The total diagram of measurement mode 13 is divided into 10 figures A.1 to A.10, which are to be viewed sequentially to follow the operation of the measurement.

Within the lower box in figures A.1 and A.2 various variables are set to initial values. Left of this box in figure A.1 a small cluster of three elements is defined, which is the so-called error cluster. It consists of a boolean value, a number and a string, with the boolean value telling whether an error has occured and the number/string being the respective error number and description. In the beginning, this cluster is set to *no error*, meaning to {F,0,-} (Fig. A.1). The error cluster will be piped through all functions and subroutines in the software, as soon as an error occurs, this cluster will be changed and the software will be halted. The large upper box in figures A.1 and A.2 merges all user input variables, i.e. V_{sd}, I_{sd}, V_g, B and further values to one large data cluster which is easy to address and to modify. Before the data cluster is transferred to further functions, V_{sd}, V_g and I_{sd} values (which are entered by the user in mV and nA) are recalculated into V and A values (Fig. A.2). The lower box in figures A.2 and A.3 defines a cluster of properties of the data input boxes, which is used to passivate user input boxes which are not active in the respective measurement mode and to activate all input boxes after the run.

The first subroutine to be performed is *all 2400in ok???* (Fig. A.2), which checks whether

all input values for the Keithley 2400 source units fulfill requirements like being in the set range or being an integer multiple of the minimum value which can be set. Note, that this subroutine - as many other of the subroutines which will follow - gets the data cluster and the error cluster as input values, which are fed into the small subroutine square symbol from the left hand side. It passes both clusters on to the next subroutine *Init Syst* (Fig. A.2) adjusting the Keithley 2400 units to appropriate initial settings. The subsequent box embodies an if-loop (Fig. A.2) executed only if Quicksweep = 0, i.e. if Quicksweep is turned off. In this case the subroutine *Init Data File 1-2* generates the file in which later on the data will be saved. Furthermore within the box structure included in the if-loop, the user input boxes which are not needed in mode 13 are passivated.

Before entering the lengthy box in figures A.3 and A.4, the Lakeshore 332 temperature controller and the Oxford PS 120 magnet power supply are initialized by the subroutines *332 start* and *PS120 init*. The subsequent, lengthy box puts the magnet power supply to the proper initial conditions and sets its magnetic field rate in T/min.

The central part of the software is included in the big box extending from figure A.4 to A.7. Indeed, it is not only one big box but a nested structure consisting of 6 boxes, meaning loop structures, plus several smaller loops. The outer box is an if structure, it is only entered if so far no error has occurred, i.e. if status is false. The second box, a case structure, is only entered if Quicksweep = 0, i.e. turned off. The third box, a further case loop, is evaluating the number of the sweep mode, which lasts from 0 to 32 corresponding to the measurement modes 1 to 33. In the present case, the active measurement mode is 13, i.e. the corresponding sweep mode is 12 (Fig. A.6). Having passed the boundary of the third box in figure A.4 with the values {status,Quicksweep,sweep mode}={false,0,12} (Fig. A.4), one enters the central part for measurement mode 13. First of all, the subroutine *is low < up???* verifies that the lower voltage/current values specified by the user indeed are smaller than the upper ones. This is followed by a check, whether the specified number of steps between the lower and the upper values indeed is larger zero (subroutine ♯*steps > 0??*). The next two subroutines *B♯steps&size* and *V♯steps&size* compute proper values for the number of steps and their size for the magnetic field and the gate voltage sweep and overwrite the corresponding user input data if necessary. The following subroutine *Init Data File 2-2* opens the file generated above and adds the file header containing all user input data. Subsequentially, the source-drain voltage V_{sd} and the gate voltage V_g are adjusted to lower Vsd and 0.00 respectively by double execution of the subroutine *Sweep Volt.*. Before entering/after leaving this voltage adjustment procedure, the boolean variable Adjust VsdIsdVg is set to true/false (Figs. A.4, A.5), which makes the LED *Adjusting Vsd, Isd or Vg* on the front panel (Fig. 4.20) flash during the voltage adjustment. The small, dark grey box positioned in the top area along the edges of figures A.4 and A.5 serves for computation of the total number of steps to be carried out throughout this measurement mode. The total number of steps is needed at different positions in order to calculate the up-to-date progress which is displayed in the progress bar at the left hand

side of the front panel in figure 4.20.

In figure A.5 the while-loop labelled **LOOP A** is entered. This is the loop which sweeps the magnetic field from $B_{\min}$ to $B_{\max}$ or from $B_{\max}$ to $B_{\min}$. Depending whether the variable BAscDesc is true or false (see left hand side of figure A.5), the upper or lower user input B value is transferred as starting value into **LOOP A** together with the B step size. The coloured symbols along the left part of the frame of **LOOP A** (Fig. A.5), which display small arrows pointing downwards, indicate, that the first value (when entering the loop) is taken from the left hand side, whereas all the other values for later loop cycles are transferred from the symbol with the arrow pointing upwards at the end of the respective loop (cp. orange, pink and blue arrow symbols at the end of **LOOP A** in figure. A.5). The subroutine *goto B* transfers the target B value to the magnet power-supply whereas the following while-loop reads the current magnetic field repeatedly (every 500 ms) as long as it differs from the target value. During the runtime of the while-loop, the process time displayed on the front panel (Fig. 4.20) is being updated and the *Adjusting B* LED of the front panel is being kept lighted. If the variable Delay B is larger 0, the program is delayed by the corresponding time by the subroutine *.seq wait(ms)* after having set the correct magnetic field value.

LOOP B, the while-loop responsible for sweeping the gate voltage V_{g}, is entered on the left hand side in figure A.6. The first subroutine in **LOOP B** along the error cluster line is the subroutine *set V-src. Intstp.*, which allows to set the desired gate voltage V_{g} for this loop cycle. The very first gate voltage to be set is $V_{\mathrm{g}} = 0$. Further V_{g} values for later loop cycles are transferred from the end of **LOOP B** (cp. Fig. A.7) via the orange symbol with the arrow pointing downwards at the beginning of **LOOP B** to the subroutine *set V-src. Intstp.*. If desired, the new gate voltage can be adjusted not in one, but in several steps (called *intersteps*, this feature was mainly introduced for V_{sd} adjustments to reduce noise when measuring differential conductances by lock-in amplifiers). The gate voltage V_{g} which has been set is passed further towards **LOOP C** (orange line in figure A.6 labelled Vg). After setting the gate voltage, the user specified gate voltage delay is inserted by the subroutine *.seq wait(ms)*, moreover *rd. leak curr.* reads the leakage current I_{g} through the gate oxide and *read V src* reads the source-drain voltage V_{sd}. As one can see in the top left corner of **LOOP B**, $j = i + 1$ is the current loop index for **LOOP B** with $j = \{1, 2, 3, ...\}$. The functions within the grey box below the subroutines along the error cluster line in **LOOP B** (Fig. A.6) compute the gate voltage V_{g}^{j+1} to be set at the beginning of the $(j + 1)^{\mathrm{st}}$ execution of **LOOP B** as well as the sign of the gate voltage change needed to calculate V_{g}^{j+2} from V_{g}^{j+1}. The grey box depicts the situation for the case that V_{g} is swept in an ascending way, i.e. from 0 to $V_{\mathrm{g,max}}$ to $V_{\mathrm{g,min}}$ and back to 0. The input values for the grey box are n_pos (lowest blue line), n_neg (2nd blue line from bottom), n (3rd blue line from bottom), loop index j (4th blue line from bottom), the boolean variable VgAscDesc (green line), the sign for changing the gate voltage for the next execution of **LOOP B** (5th blue line from bottom), the absolute value of the gate voltage step size (lower orange

line) and the up-to-date gate voltage V_g^j of the current loop execution (upper orange line). n_pos/n_neg is the number of steps between 0 and $V_{g,max}/V_{g,min}$. If $n\_pos \leq j < n\_pos+n$, the sign of the gate voltage change from V_g^{j+1} to V_g^{j+2} is negative, otherwise it is positive. Both output values of the grey box, i.e. the gate voltage V_g^{j+1} for the next **LOOP B** execution (orange line) and the sign of the gate voltage change from V_g^{j+1} to V_g^{j+2} (blue line), are fed in the arrow up symbols (orange and blue) at the end of **LOOP B** (Fig. A.7) and then transferred to the respective arrow down symbols at the entry of **LOOP B** in figure A.6.

Within the while-loop **LOOP C** (Fig. A.6) all values which are to be read in this measurement mode are acquired by the subroutine *Read 2000* reading data from the multimeters. In mode 13, the values to be read are the channel current I_{sd} and - if desired - the voltage V_d (corresponding to the voltage read by the upper digital multimeter in figure 4.21) and the differential conductance dI/dV_{sd} (phase and out-of-phase channel). Moreover the temperature data is read out the temperature controller. All these values are added to the corresponding data arrays. In the case that each data point should be measured only once, **LOOP C** is only executed once and the arrays are consisting of one element each. If the user wishes to repeatedly measure the data points and average at the end, **LOOP C** is carried out multiple times and the data arrays comprise several elements. After the last execution, the data arrays are transmitted further from the arrow-up symbols at the right handside of the box representing **LOOP C** together with the values for the source-drain voltage V_{sd} and the gate voltage V_g, which are constant and thus saved as small squares at the right borderline of **LOOP C**.

Re-entering **LOOP B** in figure A.7, the data arrays from **LOOP C** are used to calculate the respective mean values and standard deviations within the sub-VI symbolized by the bright yellow squares. Thereafter, the mean values and the corresponding standard deviations, furthermore the number n of the data point, the magnetic field B, the process time t and the gate leakage current I_g are transferred into an array of 29 elements which is appended to the data file. Thus, each line in the data file corresponds to one measured data point including all important parameters. The data sequence in each line is: 1. n, 2. V_{sd}, 3. $errV_{sd}$, 4. V_d, 5. $errV_d$, 6. V_g, 7. I_{sd}, 8. $errI_{sd}$, 9. dI/dV_{sd} (ph), 10. $errdI/dV_{sd}$ (ph), 11. R, 12. $errR$, 13. B, 14. T_{cer}, 15. $errT_{cer}$, 16. T_{pth}, 17. $errT_{pth}$, 18. t, 19. I_g, 20. dI/dV_{sd} (oph), 21. $errdI/dV_{sd}$ (oph), 22. V_{xx} (ph), 23. $errV_{xx}$ (ph), 24. V_{xx} (oph), 25. $errV_{xx}$ (oph), 26. V_{xy} (ph), 27. $errV_{xy}$ (ph), 28. V_{xy} (oph), 29. $errV_{xy}$ (oph). Finally, the graphs $I_{sd}(V_g)$ and $T_{cer}(t)$ (if activated, also $dI/dV_{sd}(V_g)$) are updated within this second part of **LOOP B**.

By ramping down both the gate voltage V_g and the source drain voltage V_{sd} to zero, the following second section of **LOOP A** (Fig. A.7) finalizes the central part of the *ViDi* software.

If the magnetic field was activated for the measurement and intended to be set back to 0 after measuring, the first nested loop structure in figure A.8 sweeps the magnetic field to zero. In all other cases, this loop structure is ignored. Final file operations are carried out in the next loop structure split between figures A.8 and A.9: if an error has occurred throughout the run or the user has aborted the software manually, an accordant text message is appended to the data file, subsequently the data file (in all cases) is closed.

Prior to entering the last frame (Figs. A.9, A.10), in which essentially all the input boxes are enabled for the next run (the ones not needed for the current run had been deactivated and greyed out), the subroutine *all syst local* sets back all measurement devices from remote to local operation (Fig. A.9). After execution of the last frame, the program is ended by evaluation and output of the error status.
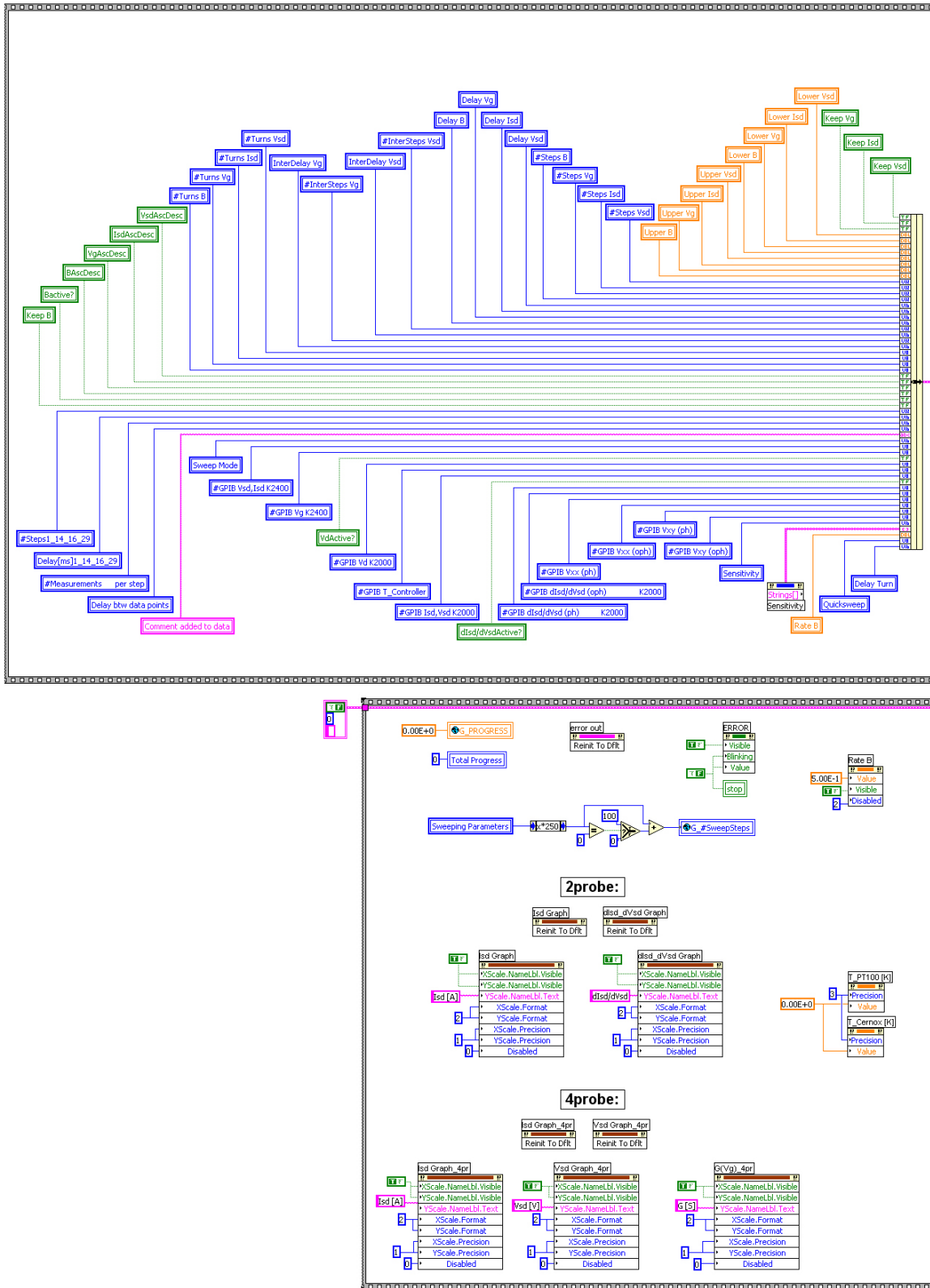
Fig. A.1: Diagram of the data acquisition software ViDi 1.70, measurement mode 13. 1$^{\text{st}}$ out of 10 sections.
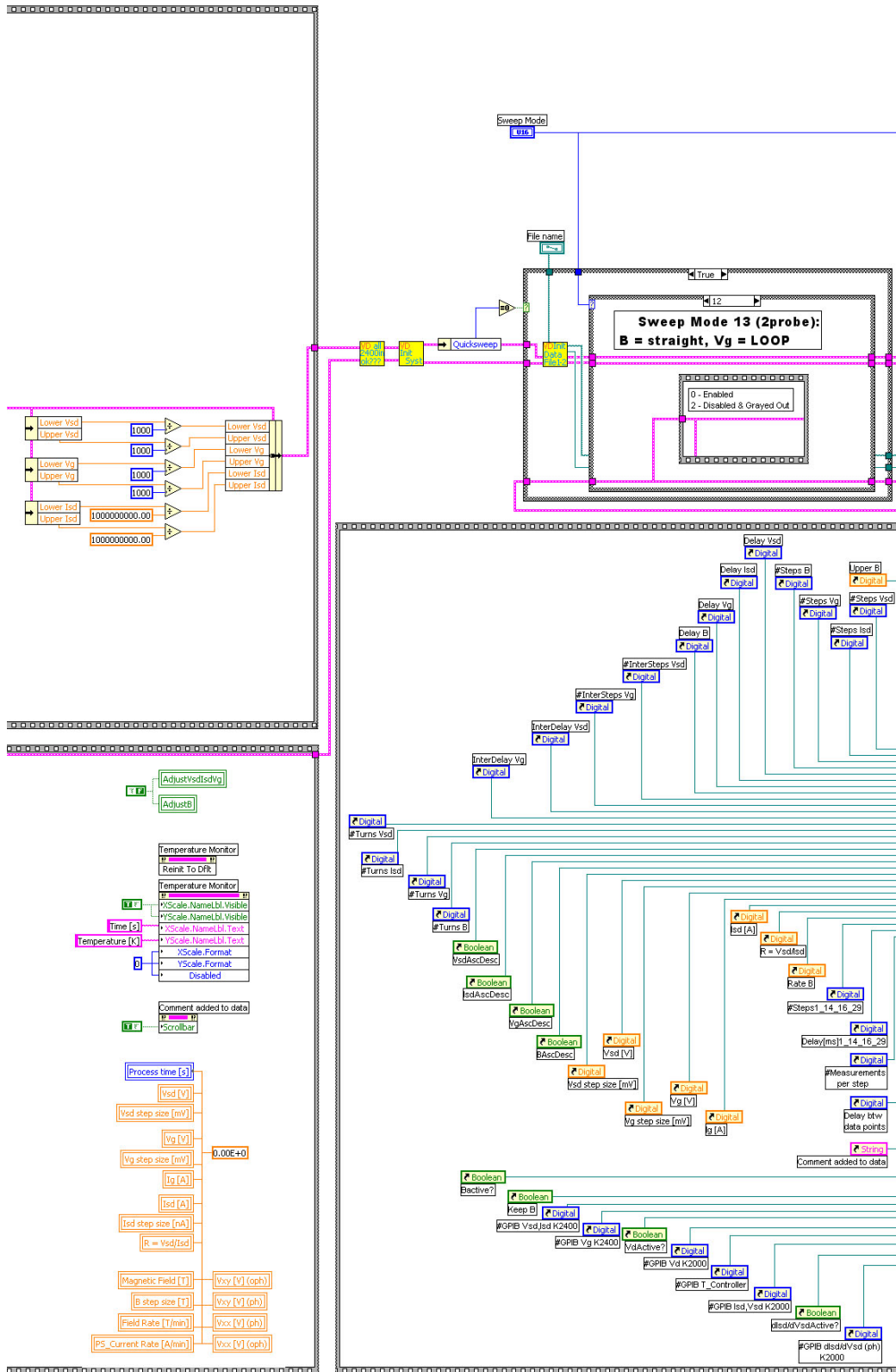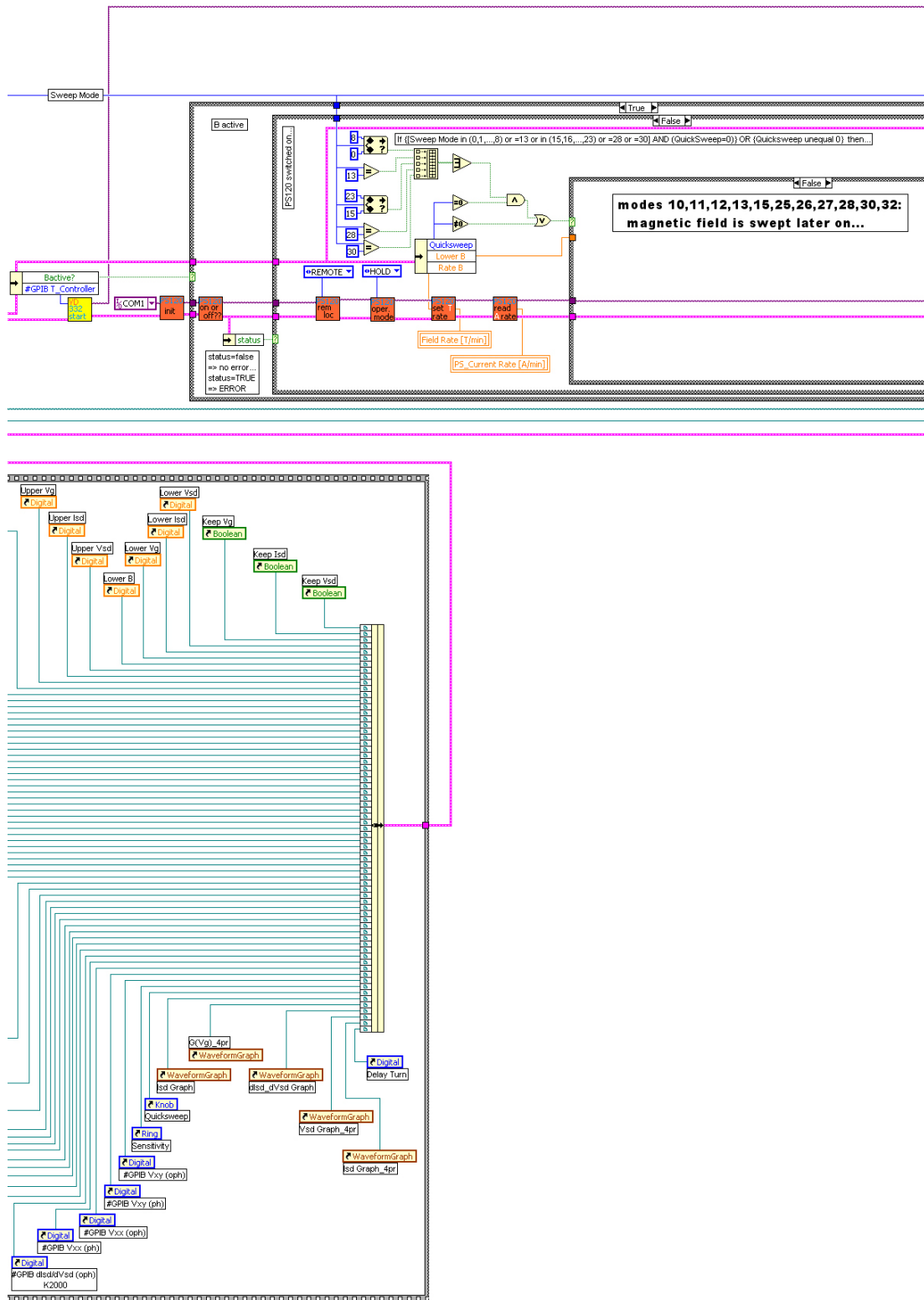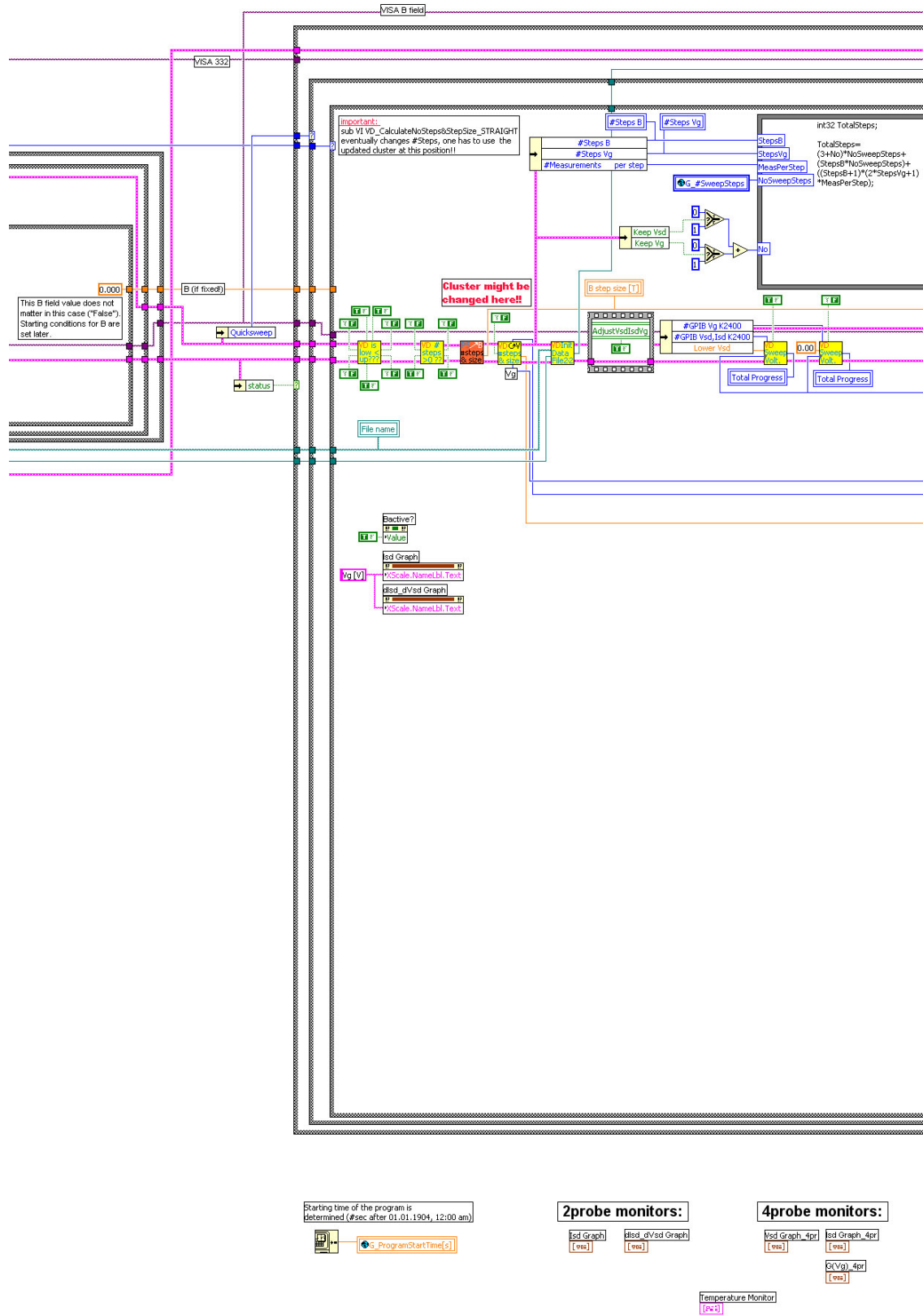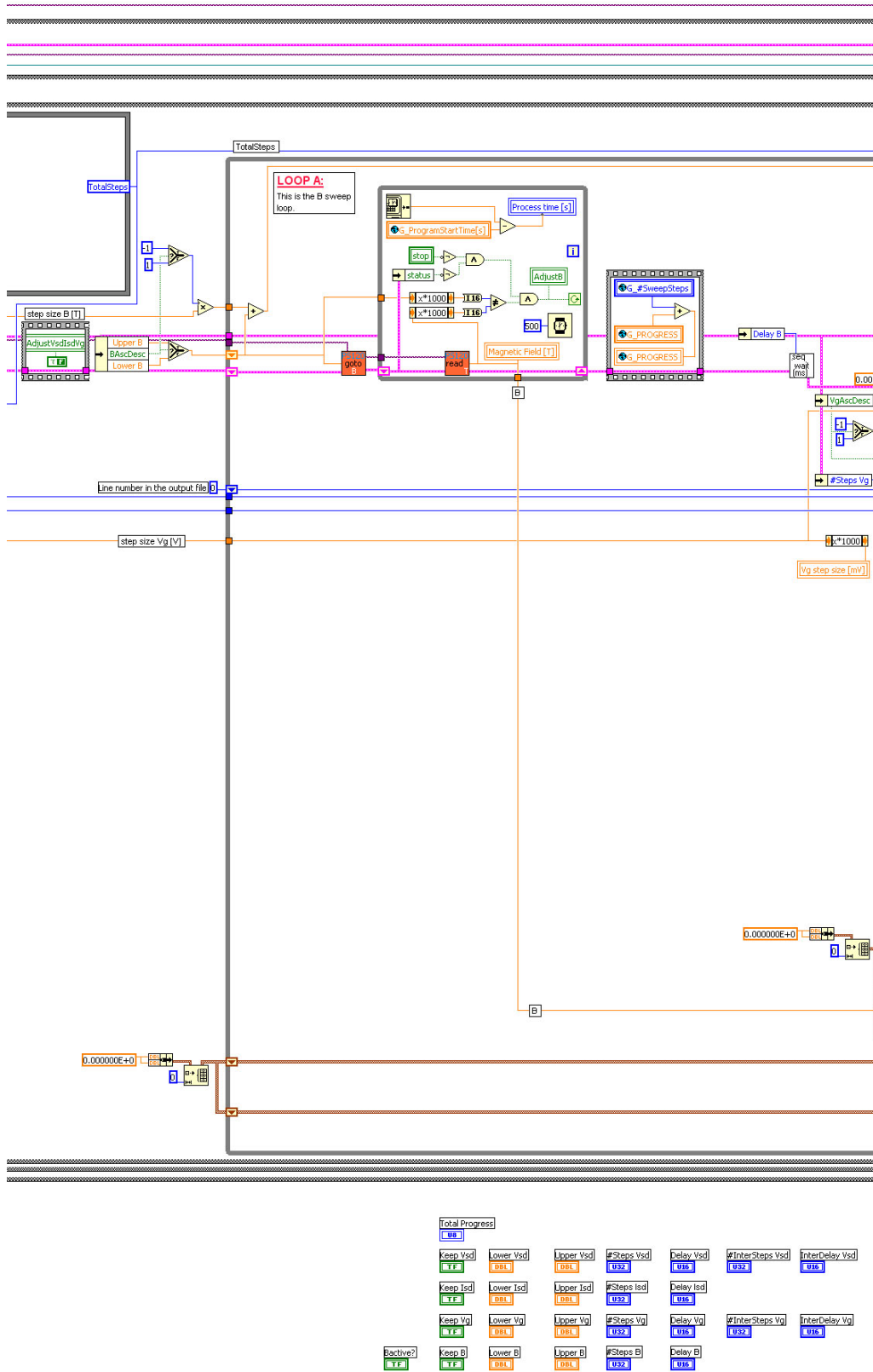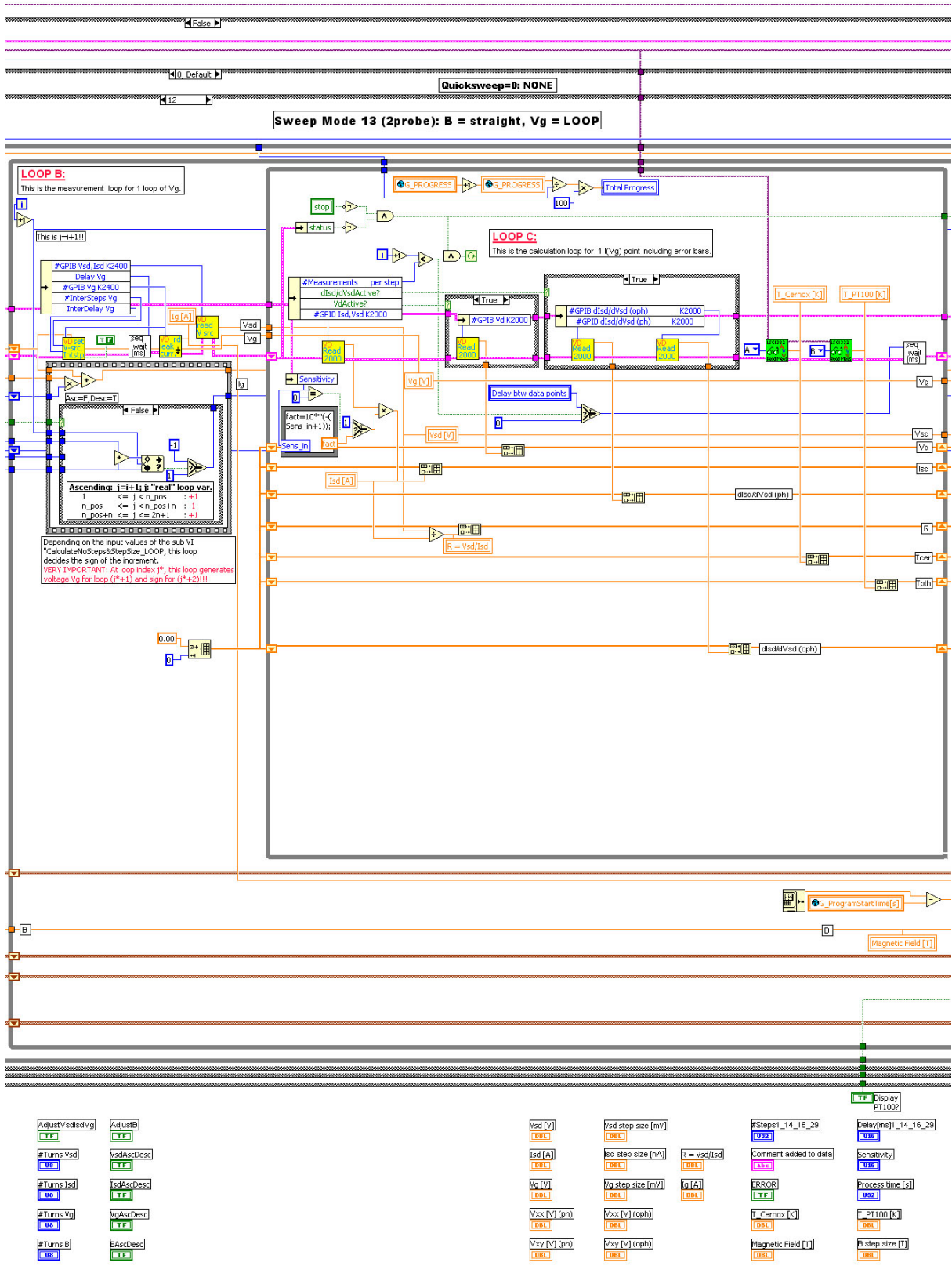
Fig. A.2: Diagram of the data acquisition software ViDi 1.70, measurement mode 13. 2nd out of 10 sections.

Fig. A.3: Diagram of the data acquisition software ViDi 1.70, measurement mode 13. 3$^{\text{rd}}$ out of 10 sections.

Fig. A.4: Diagram of the data acquisition software ViDi 1.70, measurement mode 13. 4$^{\text{th}}$ out of 10 sections.
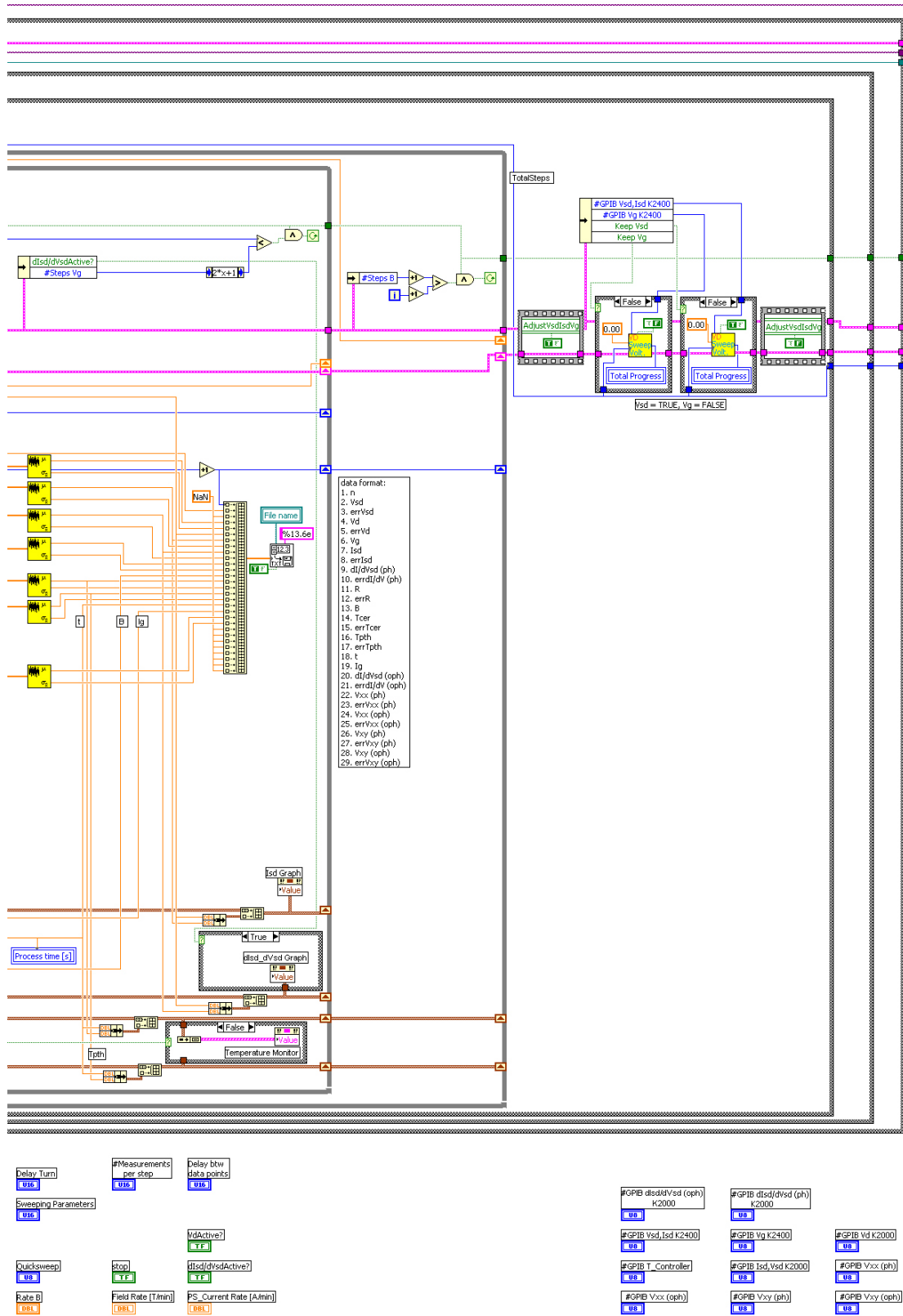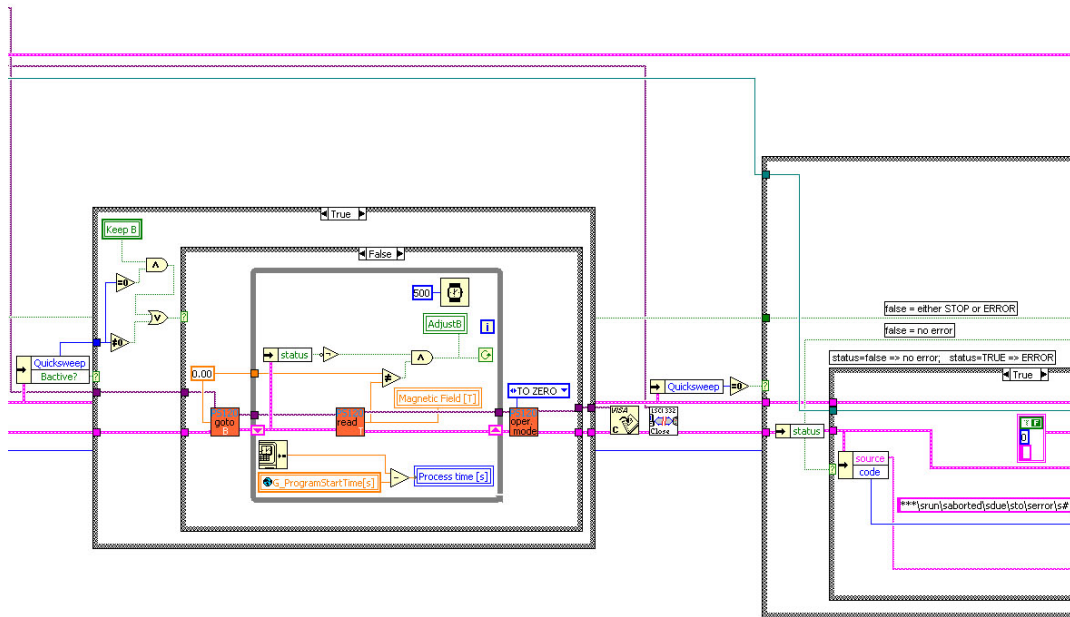
Fig. A.5: Diagram of the data acquisition software ViDi 1.70, measurement mode 13. 5th out of 10 sections.

Fig. A.6: Diagram of the data acquisition software ViDi 1.70, measurement mode 13. 6$^{\text{th}}$ out of 10 sections.
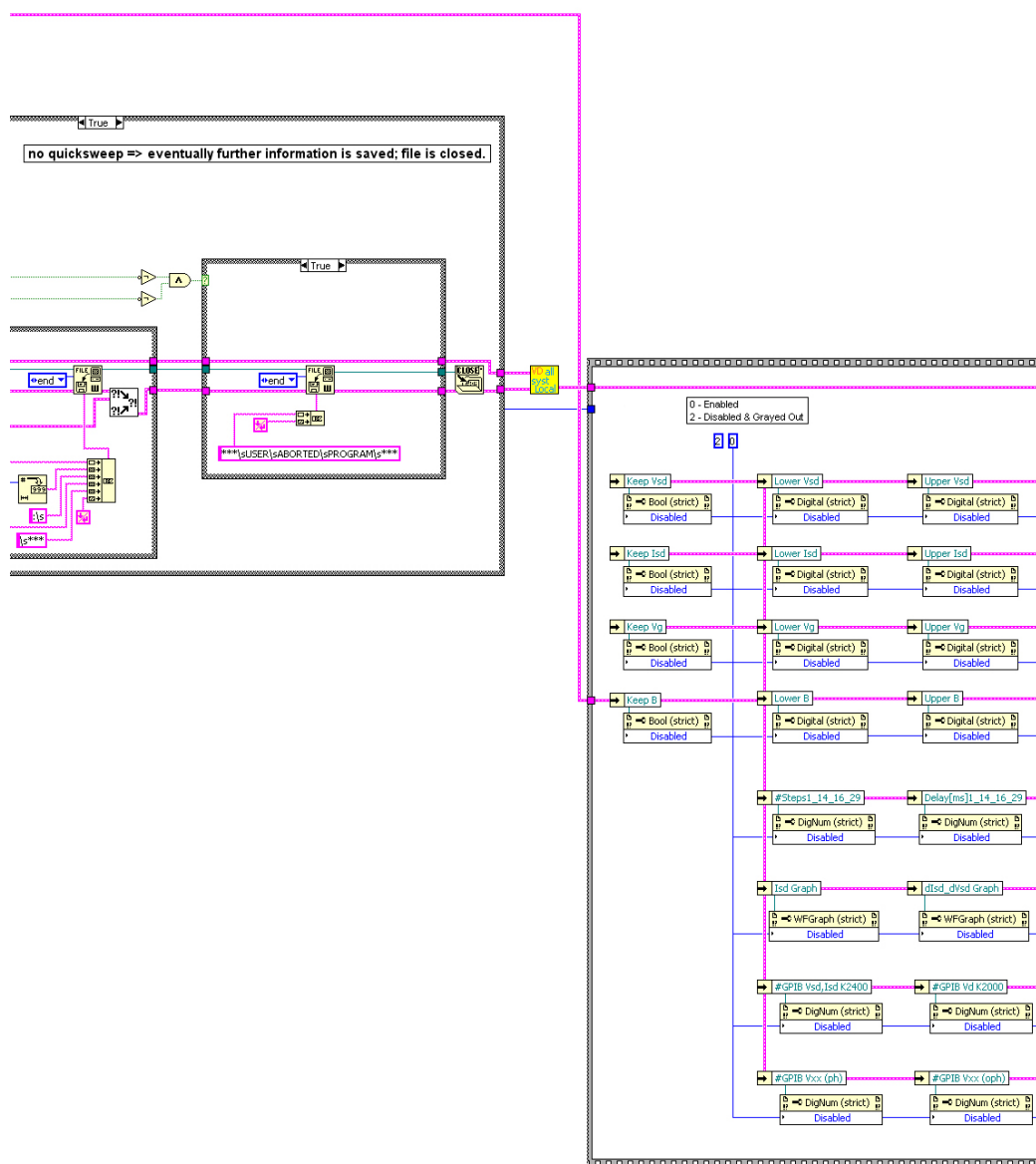
Fig. A.7: Diagram of the data acquisition software ViDi 1.70, measurement mode 13. 7th out of 10 sections.

Fig. A.8: Diagram of the data acquisition software ViDi 1.70, measurement mode 13. 8th out of 10 sections.

Fig. A.9: Diagram of the data acquisition software ViDi 1.70, measurement mode 13. 9th out
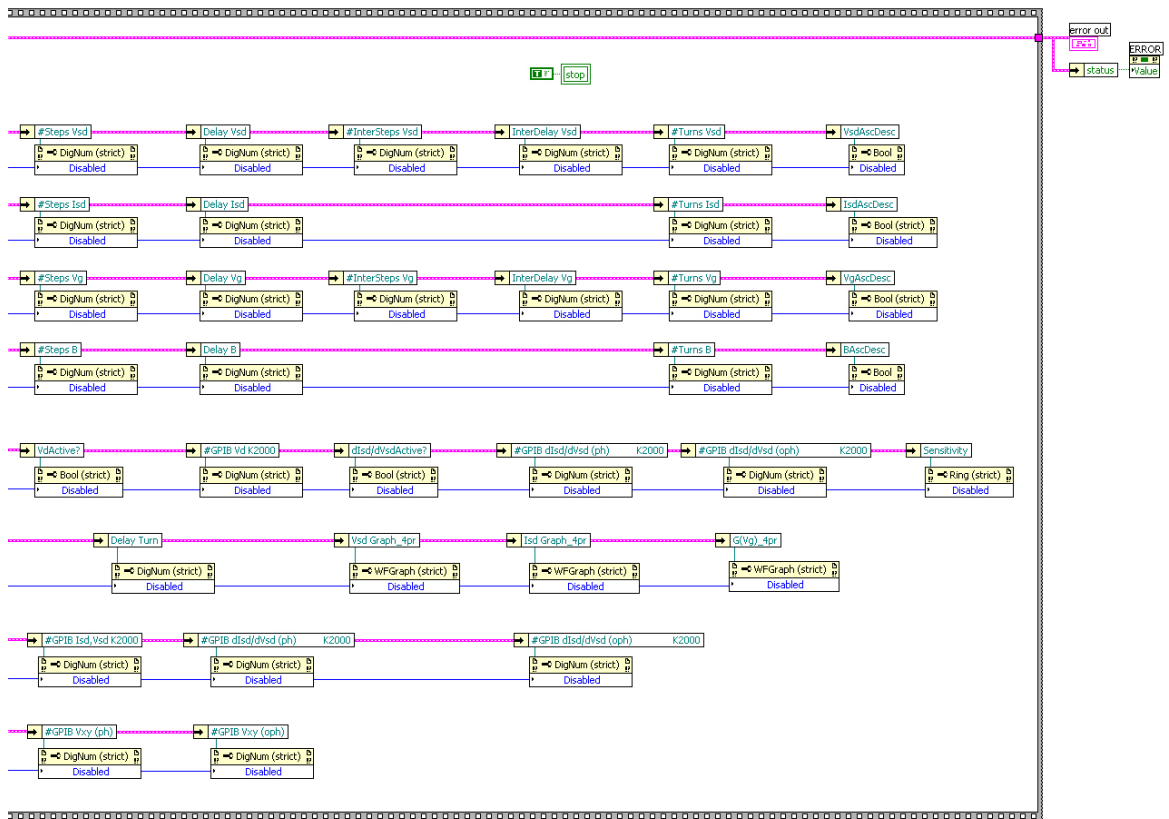of 10 sections.

Fig. A.10: Diagram of the data acquisition software ViDi 1.70, measurement mode 13. 10th out of 10 sections.

Bibliography

[Abe07] D. S. L. Abergel, A. Russell, V. I. Fal'ko, *Appl. Phys. Lett.* **91**, 063125 (2007).

[Ahl01] E. Ahlswede, P. Weitz, J. Weis, K. von Klitzing, K. Eberl, *Physica B* **298**, 562 (2001).

[Ahl02] E. Ahlswede, J. Weis, K. von Klitzing, K. Eberl, *Physica E* **12**, 165 (2002).

[Aji93] H. Ajiki, T. Ando, *J. Phys. Soc. Jpn.* **62**, 1255 (1993).

[Aji96] H. Ajiki, T. Ando, *J. Phys. Soc. Jpn.* **65**, 505 (1996).

[Alb91] T. R. Albrecht, P. Grütter, D. Horne, D. Rugar, *J. Appl. Phys.* **69**, 668 (1991).

[All98] W. Allers, A. Schwarz, U. D. Schwarz, R. Wiesendanger, *Rev. Sci. Instrum.* **69**, 221 (1998).

[App02] J. Appenzeller, J. Knoch, V. Derycke, R. Martel, S. Wind, Ph. Avouris, *Phys. Rev. Lett.* **89**, 126801 (2002).

[Ash04] M. Ashino, A. Schwarz, T. Behnke, R. Wiesendanger, *Phys. Rev. Lett.* **93**, 136101 (2004).

[Ash06] M. Ashino, R. Wiesendanger, *Jpn. J. Appl. Phys.* **45**, 2286 (2006).

[Ash08] M. Ashino, D. Obergfell, M. Haluška, S. Yang, A. N. Khlobystov, S. Roth, R. Wiesendanger, *Nature Nanotech.* **3**, 337 (2008).

[As09a] M. Ashino, D. Obergfell, M. Haluška, S. Yang, A. N. Khlobystov, S. Roth, R. Wiesendanger, *Nanotechnology* **20**, *accepted* (2009).

[As09b] M. Ashino, R. Wiesendanger, A. N. Khlobystov, S. Berber, D. Tomanek, *submitted* (2009).

[Bab03] B. Babić, M. Iqbal, C. Schönenberger, *Nanotechnology* **14**, 327 (2003).

[Bad05] C. E. Baddour, C. Briens, *Internat. J. Chem. React. Engin.* **3**, R3 (2005).

[Be93a] D. S. Bethune, C. H. Kiang, M. S. de Vries, G. Gorman, R. Savoy, J. Vazquez, R. Beyers, *Nature* **363**, 605 (1993).

[Be93b] D. S. Bethune, R. D. Johnson, J. R. Salem, M. S. de Vries, C. S. Yannoni, *Nature* **366**, 123 (1993).

[Bee07] C. W. J. Beenakker, arXiv: 0710.3848v1 (2007).

[Ber06] C. Berger, Z. Song, X. Li, X. Wu, N. Brown, C. Naud, D. Mayou, T. Li, J. Hass, A. N. Marchenkov, E. H. Conrad, P. N. First, W. A. de Heer, *Science* **312**, 1191 (2006).

[Bla62] L. C. F. Blackman, A. R. Ubbelohde, *Proc. Roy. Soc.* **A266**, 20 (1962).

[Bla07] P. Blake, E. W. Hill, A. H. Castro Neto, K. S. Novoselov, D. Jiang, R. Yang, T. J. Booth, A. K. Geim, *Appl. Phys. Lett.* **91**, 063124 (2007).

[Bol08] K. I. Bolotin, K. J. Sikes, Z. Jiang, M. Klima, G. Fudenberg, J. Hone, P. Kim, H. L. Stormer, *arXiv*, 0802.2389v2 (2008).

[Bri07] J. van den Brink, *Nature Nanotech.* **2**, 199 (2007).

[Bue88] M. Büttiker, *Phys. Rev. B* **38**, 9375 (1988).

[Cas99] A. M. Cassell, N. R. Franklin, T. W. Tombler, E. M. Chan, J. Han, H. Dai, *J. Am. Chem. Soc.* **121**, 7975 (1999).

[Cha06] B. Chandra, R. Caldwell, M. Huang, L. Huang, M. Y. Sfeir, S. P. O'Brien, T. F. Heinz, J. Hone, *phys. stat. sol. (b)* **243**, 3359 (2006).

[Cha07] J.-C. Charlier, X. Blase, S. Roche, *Rev. Mod. Phys.* **79**, 677 (2007).

[Che00] J. Che, T. Çağin, W. A. Goddard III, *Nanotechnology* **11**, 65 (2000).

[Che07] Z. Chen, Y.-M. Lin, M. J. Rooks, Ph. Avouris, *Physica E* **40**, 228 (2007).

[Chi01] P. W. Chiu, G. Gu, G. T. Kim, G. Philipp, S. Roth, S. F. Yang, S. Yang, *Appl. Phys. Lett.* **79**, 3845 (2001).

[Chk92] D. B. Chklovskii, B. I. Shklovskii, L. I. Glazman, *Phys. Rev. B* **46**, 4026 (1992).

[Chu09] A. Chuvilin, A. N. Khlobystov, D. Obergfell, M. Haluška, S. Yang, S. Roth, U. Kaiser, *to be published* (2009).

[Con07] M. A. Contreras, T. Barnes, J. van de Lagemaat, G. Rumbles, T. J. Coutts, C. Weeks, P. Glatkowski, I. Levitsky, J. Peltola, D. A. Britz, *J. Phys. Chem. C* **111**, 14045 (2007).

[Cot06] A. Cottet, T. Kontos, S. Sahoo, H. T. Man, M.-S. Choi, W. Belzig, C. Bruder, A. F. Morpurgo, C. Schönenberger, *Semicond. Sci. Technol.* **21**, S78 (2006).

[Dai02] H. Dai, *Acc. Chem. Res.* **35**, 1035 (2002).

[Dat95] S. Datta, *Electronic Transport in Mesoscopic Systems*, Cambridge University Press, Cambridge (1995).

[DPG06] cp. http://www.pro-physik.de/Phy/leadArticle.do?laid=8628
         [German Physical Society, DPG (2006)].

[Dre93] M. S. Dresselhaus, G. Dresselhaus, P. C. Eklund, *J. Mater. Res.* **8**, 2054 (1993).

[Dre04] M. S. Dresselhaus, G. Dresselhaus, J. C. Charlier, E. Hernández, *Phil. Trans. R. Soc. Lond. A* **362**, 2065 (2004).

[Dre05] M. S. Dresselhaus, G. Dresselhaus, R. Saito, A. Jorio, *Physics Reports* **409**, 47 (2005).

[Fan99] S. Fan, M. G. Chapline, N. R. Franklin, T. W. Tombler, A. M. Cassell, H. Dai, *Science* **283**, 512 (1999).

[Fed07] G. Fedorov, A. Tselev, D. Jiménez, S. Latil, N. G. Kalugin, P. Barbara, D. Smirnov, S. Roche, *Nano Lett.* **7**, 960 (2007).

[Fer06] A. C. Ferrari, J. C. Meyer, V. Scardaci, C. Casiraghi, M. Lazzeri, F. Mauri, S. Piscanec, D. Jiang, K. S. Novoselov, S. Roth, A. K. Geim, *Phys. Rev. Lett.* **97**, 187401 (2006).

[Fra00] N. R. Franklin, H. Dai, *Adv. Mater.* **12**, No. 12, 890 (2000).

[Fra06] cp. http://www.teg.fraunhofer.de/arbeitsgebiete/materialien/composites [Fraunhofer TEG, Stuttgart, Germany (2006)].

[Fre01] M. Freitag, M. Radosavljević, Y. Zhou, A. T. Johnson, W. F. Smith, *Appl. Phys. Lett.* **79**, 3326 (2001).

[Fuj05] M. Fujii, X. Zhang, H. Xie, H. Ago, K. Takahashi, T. Ikuta, H. Abe, T. Shimizu, *Phys. Rev. Lett.* **95**, 065502 (2005).

[Gei07] A. K. Geim, K. S. Novoselov, *Nature Materials* **6**, 183 (2007).

[Gol03] D. Golberg, M. Mitome, K. Kurashima, Y. Bando, *J. Electron Microsc.* **52**, 111 (2003).

[Gr05a] A. P. Graham, G. S. Duesberg, W. Hoenlein, F. Kreupl, M. Liebau, R. Martin, B. Rajasekharan, W. Pamler, R. Seidel, W. Steinhoegl, E. Unger, *Appl. Phys. A* **80**, 1141 (2005).

[Gr05b] A. P. Graham, G. S. Duesberg, R. V. Seidel, M. Liebau, E. Unger, W. Pamler, F. Kreupl, W. Hoenlein, *small* **1** 382 (2005).

[Gue03] K. Güven, R. R. Gerhardts, *Phys. Rev. B* **67**, 115327 (2003).

[Hal05] M. Haluška, V. Skákalová, D. Carroll, S. Roth, *Electronic Properties of Novel Nanostructures, AIP Conference Proceedings* **786**, 87 (2005).

[Hal06] M. Haluška, M. Hulman, B. Hornbostel, J. Čech, V. Skákalová, S. Roth, *phys. stat. sol. (b)* **243**, 3042 (2006).

[Hal07] M. Haluška, D. Obergfell, J. C. Meyer, G. Scalia, G. Ulbricht, B. Krauss, D. H. Chae, T. Lohmann, M. Lebert, M. Kaempgen, M. Hulman, J. Smet, S. Roth, K. von Klitzing, *phys. stat. sol. (b)* **244**, 4143 (2007).

[Han07] M. Y. Han, B. Özyilmaz, Y. Zhang, P. Kim, *Phys. Rev. Lett.* **98**, 206805 (2007).

[Hau93] R. J. Haug, *Semicond. Sci. Technol.* **8**, 131 (1993).

[Hei02] S. Heinze, J. Tersoff, R. Martel, V. Derycke, J. Appenzeller, Ph. Avouris, *Phys. Rev. Lett.* **89**, 106801 (2002).

[Hoe02] W. Hoenlein, *Jpn. J. Appl. Phys.* **41**, 4370 (2002).

[Hoe06] W. Hoenlein, G. S. Duesberg, A. P. Graham, F. Kreupl, M. Liebau, W. Pamler, R. Seidel, E. Unger, *Microelectr. Engin.* **83**, 619 (2006).

[Hua00] H. Huang, S. Yang, X. Zhang, *J. Phys. Chem. B* **104**, 1473 (2000).

[Hun03] U. T. Hunger, *Elektrischer Transport in Bündeln aus einwandigen Kohlenstoff-Nanoröhrchen mit semitransmissiven Kontakten*, PhD thesis, Technical University of Aachen (2003).

[Hun07] S. Hunklinger, *Festkörperphysik*, Oldenbourg-Verlag, München (2007).

[Iij91] S. Iijima, *Nature* **354**, 56 (1991).

[Iij93] S. Iijima, T. Ichihashi, *Nature* **363**, 603 (1993).

[Itk03] M. E. Itkis, D. E. Perea, S. Niyogi, S. M. Rickard, M. A. Hamon, H. Hu, B. Zhao, R. C. Haddon, *Nano Lett.* **3**, 309 (2003).

[Ivc02] E. L. Ivchenko, B. Spivak, *Phys. Rev. B* **66**, 155404 (2002).

[Jar04] P. Jarillo-Herrero, S. Sapmaz, C. Dekker, L. P. Kouwenhoven, H. S. J. van der Zant, *Nature* **429**, 389 (2004).

[Jor03] A. Jorio, M. A. Pimenta, A. G. Souza Filho, R. Saito, G. Dresselhaus, M. S. Dresselhaus, *New Journal of Physics* **5**, 139.1-139.17 (2003).

[Jou97] C. Journet, W.K. Maser, P. Bernier, A. Loiseau, M. Lamy de la Chapelle, S. Lefrant, P. Deniard, R. Lee, J.E. Fischer, *Nature* **388**, 756 (1997).

[Kan97] C. L. Kane, E. J. Mele, *Phys. Rev. Lett.* **78**, 1932 (1997).

[Kas99] A. Y. Kasumov, R. Deblock, M. Kociak, B. Reulet, H. Bouchiat, I. I. Khodos, Y. B. Gorbatov, V. T. Volkov, C. Journet, M. Burkhard, *Science* **284**, 1508 (1999).

[Kat00] H. Kataura, Y. Kumazawa, Y. Maniwa, Y. Ohtsuka, R. Sen, S. Suzuki, Y. Achiba, *Carbon* **38**, 1691 (2000).

[Kia98] C.-H. Kiang, W. A. Goddard III, R. Beyers, J. R. Salem, D. S. Bethune, *J. Phys. Chem.* **98**, 6612 (1994).

[Kia00] C.-H. Kiang, *J. Phys. Chem. A* **104**, 2454 (2000).

[Kim05] T. Kim, J.-M. Zuo, E. A. Olson, I. Petrov, *Appl. Phys. Lett.* **87**, 173108 (2005).

[Kit06] R. Kitaura, H. Shinohara, *Chem. Asian J.* **1**, 646 (2006).

[Kit07] R. Kitaura, H. Shinohara, *Jpn. J. Appl. Phys.* **46**, 881 (2007).

[Khl06] private discussion with A. N. Khlobystov, University of Nottingham, 2006.

[Khl07] private discussion with A. N. Khlobystov, University of Nottingham, 2007.

[Khl08] private discussion with A. N. Khlobystov, University of Nottingham, 2008.

[Koc02] M. Kociak, K. Suenaga, K. Hirahara, Y. Saito, T. Nakahira, S. Iijima, *Phys. Rev. Lett.* **89**, 155501 (2002).

[Kra90] W. Krätschmer, L. D. Lamb, K. Fostiropoulos, D. R. Huffman, *Nature* **347**, 354 (1990).

[Kri06] I. V. Krive, R. I. Shekhter, M. Jonson, *Low Temp. Phys.* **32**, 887 (2006).

[Kro85] H. W. Kroto, J. R. Heath, S. C. O'Brien, R. F. Curl, R. E. Smalley, *Nature* **318**, 162 (1985).

[Laf08] private discussion with M. Lafkioti, Max Planck Institute for Solid State Research, 2008.

[Lee02] J. Lee, H. Kim, S.-J. Kahng, G. Kim, Y.-W. Son, J. Ihm, H. Kato, Z. W. Wang, T. Okazaki, H. Shinohara, Y. Kuk, *Nature* **415**, 1005 (2002).

[Lie94] K. Lier, R. R. Gerhardts, *Phys. Rev. B* **50**, 7757 (1994).

[Mar98] R. Martel, T. Schmidt, H. R. Shea, T. Hertel, Ph. Avouris, *Appl. Phys. Lett.* **73**, 2447 (1998).

[McK93] B. A. McKinnon, T. C. Choy, *Aust. J. Phys.* **46**, 601 (1993).

[Mey04] J. C. Meyer, D. Obergfell, S. Roth, S. Yang, S. F. Yang, *Appl. Phys. Lett.* **85**, 2911 (2004).

[Mey06] J. C. Meyer, *Structure and Properties of Carbon Nanotubes*, PhD thesis, University of Tübingen (2006).

[Mey07] J. C. Meyer, A. K. Geim, M. I. Katsnelson, K. S. Novoselov, T. J. Booth, S. Roth, *Nature* **446**, 60 (2007).

[Mey08] J. C. Meyer, C. O. Girit, M. F. Crommie, A. Zettl, *Nature* **454**, 319 (2008).

[Moo62] A. W. Moore, A. R. Ubbelohde, D. A. Young, *Brit. J. Appl. Phys.* **13**, 393 (1962).

[Mor08] S. V. Morozov, K. S. Novoselov, M. I. Katsnelson, F. Schedin, D. C. Elias, J. A. Jaszczak, A. K. Geim, *Phys. Rev. Lett.* **100**, 016602 (2008).

[Na93a] S. Nagase, K. Kobayashi, *Chem. Phys. Lett.* **201**, 475 (1993).

[Na93b] S. Nagase, K. Kobayashi, *Chem. Phys. Lett.* **214**, 57 (1993).

[Nag96] S. Nagase, K. Kobayashi, T. Akasaka, *Bull. Chem. Soc. Jpn.* **69**, 2131 (1996).

[Nak02] T. Nakanishi, A. Bachtold, C. Dekker, *Phys. Rev. B* **66**, 073307 (2002).

[Net07] A. H. C. Neto, F. Guinea, N. M. R. Peres, K. S. Novoselov, A. K. Geim, arXiv: 0709.1163v1 (2007).

[Nil06] J. A. Nilsson, A. H. Castro Neto, F. Guinea, N. M. R. Peres, *Phys. Rev. Lett.* **97**, 266801 (2006).

[NME07] Editorial, *Nature materials* **6**, 169 (2007).

[Nom07] K. Nomura, A. H. MacDonald, *Phys. Rev. Lett.* **98**, 076602 (2007).

[No05a] K. S. Novoselov, D. Jiang, F. Schedin, T. J. Booth, V. V. Khotkevich, S. V. Morozov, A. K. Geim, *Proc. Natl. Acad. Sci. USA* **102**, 10451 (2005).

[No05b] K. S. Novoselov, A. K. Geim, S. V. Morozov, D. Jiang, M. I. Katsnelson, I. V. Grigorieva, S. V. Dubonos, A. A. Firsov, *Nature* **438**, 197 (2005).

[Nov06] K. S. Novoselov, E. McCann, S. V. Morozov, V. I. Fal'ko, M. I. Katsnelson, U. Zeitler, D. Jiang, F. Schedin, A. K. Geim, *Nature Physics* **2**, 177 (2006).

[Nov07] K. S. Novoselov, Z. Jiang, Y. Zhang, S. V. Morozov, H. L. Stormer, U. Zeitler, J. C. Maan, G. S. Boebinger, P. Kim, A. K. Geim, *Science* **315**, 1379 (2007).

[Obe06] D. Obergfell, J. C. Meyer, M. Haluška, A. N. Khlobystov, S. Yang, L. Fan, D. Liu, S. Roth, *phys. stat. sol. (b)* **243**, 3430 (2006).

[OCo02] M. J. O'Connell, S. M. Bachilo, C. B. Huffman, V. C. Moore, M. S. Strano, E. H. Haroz, K. L. Rialon, P. J. Boul, W. H. Noon, C. Kittrell, J. Ma, R. H. Hauge, R. B. Weisman, R. E. Smalley, *Science* **297**, 593 (2002).

[Par06] B. Partoens, F. M. Peeters, *Phys. Rev. B* **74**, 075404 (2006).

[Rei04] S. Reich, C. Thomsen, J. Maultzsch, *Carbon Nanotubes - Basic Concepts and Physical Properties*, WILEY-VCH, Weinheim (2004).

[Rob07] J. Robertson, *materials today* **10**, 36 (2007).

[Rot04] S. Roth, D. Carroll, *One-Dimensional Metals*, WILEY-VCH, Weinheim (2004).

[Rot07] S. Roth, *Stuttgart-Korea lectures* (04.09. - 04.12.2007).

[Rot08] private discussion with S. Roth, Max Planck Institute for Solid State Research, 2008.

[Row06] M. W. Rowell, M. A. Topinka, M. D. McGehee, H.-J. Prall, G. Dennler, N. S. Sariciftci, L. Hu, G. Gruner, *Appl. Phys. Lett.* **88**, 233506 (2006).

[Sag04] M. Sagnes, J.-M. Broto, B. Raquet, C. Vieu, V. Conedera, P. Dubreuil, T. Ondaruhu, Ch. Laurent, E. Flahaut, *Microelectron. Eng.* **73-74**, 689 (2004).

[Sai94] R. Saito, G. Dresselhaus, M. S. Dresselhaus, *Phys. Rev. B* **50**, 14698 (1994).

[Sai96] R. Saito, G. Dresselhaus, M. S. Dresselhaus, *Phys. Rev. B* **53**, 10408 (1996).

[Sai98] R. Saito, G. Dresselhaus, M. S. Dresselhaus, *Physical Properties of Carbon Nanotubes*, Imperial College Press, London (1998).

[Sai00] Y. Saito, Y. Tani, A. Kasuya, *Phys. Chem. B* **104**, 2495 (2000).

[Sam03] Ge. G. Samsonidze, R. Saito, A. Jorio, M. A. Pimenta, A. G. Souza Filho, A. Grüneis, G. Dresselhaus, M. S. Dresselhaus, *J. Nanosci. Nanotechnol.* **3**, 431 (2003).

[Set00] A. A. Setlur, S. P. Doherty, J. Y. Dai, R. P. H. Chang, *Appl. Phys. Lett.* **76**, 3008 (2000).

[Shi00] H. Shinohara, *Rep. Prog. Phys.* **63**, 843 (2000).

[Shi02] T. Shimada, T. Okazaki, R. Taniguchi, T. Sugai, H. Shinohara, K. Suenaga, Y. Ohno, S. Mizuno, S. Kishimoto, T. Mizutani, *Appl. Phys. Lett.* **81**, 4067 (2002).

[Sid04] A. Siddiki, R. R. Gerhardts, *Phys. Rev. B* **70**, 195335 (2004).

[Smi98] B. W. Smith, M. Monthioux, D. E. Luzzi, *Nature* **396**, 323 (1998).

[Sze07] S. M. Sze, Kwok K. Ng, *Physics of Semiconductor Devices*, John Wiley & Sons, Hoboken, New Jersey (2007).

[Tan98] S. J. Tans, A. R. M. Verschueren, C. Dekker, *Nature* **393**, 49 (1998).

[Tan07] Y.-W. Tan, Y. Zhang, K. Bolotin, Y. Zhao, S. Adam, E. H. Hwang, S. Das Sarma, H. L. Stormer, P. Kim, *Phys. Rev. Lett.* **99**, 246803 (2007).

[The96] A. Thess, R. Lee, P. Nikolaev, H. Dai, P. Petit, J. Robert, C. Xu, Y. H. Lee, S. G. Kim, A. G. Rinzler, D. T. Colbert, G. E. Scuseria, D. Tománek, J. E. Fischer, R. E. Smalley, *Science* **273**, 483 (1996).

[Ulb03] H. Ulbricht, G. Moos, T. Hertel, *Phys. Rev. Lett.* **90**, 095501 (2003).

[Ulb08] private discussion with Gerhard Ulbricht, Max Planck Institute for Solid State Research, 2008.

[Vas07] P. Ya. Vasilyev, N. V. Kamanina, *Techn. Phys. Lett.* **33**, 764 (2007).

[vKl80] K. von Klitzing, G. Dorda, M. Pepper, *Phys. Rev. Lett.* **45**, 494 (1980).

[vKl84] K. von Klitzing, *Physica* **126 B**, 242 (1984).

[vKl86] K. von Klitzing, *Rev. Mod. Phys.* **58**, 519 (1986).

[vKl05] K. von Klitzing, R. Gerhardts, J. Weis, *Physik Journal* **4**, 37 (2005).

[We00a] P. Weitz, E. Ahlswede, J. Weis, K. von Klitzing, K. Eberl, *Applied Surface Science* **157**, 349 (2000).

[We00b] P. Weitz, E. Ahlswede, J. Weis, K. von Klitzing, K. Eberl, *Physica E* **6**, 247 (2000).

[We05] J. Wei, M. Shimogawa, Z. Wang, I. Radu, R. Dormaier, D. H. Cobden, *Phys. Rev. Lett.* **95**, 256601 (2005).

[Wei94] J. Weis, R. J. Haug, K. von Klitzing, K. Ploog, *Surface Science* **305**, 664 (1994).

[Wei02] J. Weis, *Electrical Transport Through Quantum Dot Systems*, Habilitation thesis, University of Stuttgart (2002).

[Wei05] J. Weis, *Lect. Notes Phys.* **658**, 87 (2005).

[WoS07] Number of articles mentioning nanotubes within the titles or abstracts in the specified year: 11 (1992), 66 (1993), 143 (1994), 185 (1995), 258 (1996), 367 (1997), 549 (1998), 801 (1999), 1167 (2000), 1623 (2001), 2499 (2002), 3307 (2003), 4533 (2004), 5738 (2005), 7014 (2006), 8141 (2007). Total number of articles (in the specified year) covered by the Science Citation Index (SCI) as a rough measure for the growth of scientific literature: 722400 (1992), 763500 (1993), 803400 (1994), 860400 (1995), 902100 (1996), 939000 (1997), 948900 (1998), 977700 (1999), 989700 (2000), 981000 (2001), 1031400 (2002), 1076700 (2003), 1142700 (2004), 1210200 (2005), 1266900 (2006), 1261500 (2007). Source: Thomson/ISI Web of Science (WoS).

[Yan03] S. F. Yang, *Ultrathin Films of Metallofullerenes: Preparation, Characterization and Photoelectrochemical Applications*, PhD thesis, The Hong Kong University of Science and Technology (2003).

[Yan07] Y. Yan, M. B. Chan-Park, Q. Zhang, *small* **3**, 24 (2007).

[Yoo05] M. Yoon, S. Berber, D. Tománek, *Phys. Rev. B* **71**, 155406 (2005).

[Yoo07] D. Yoon, S.-J. Kang, J.-B. Choi, Y.-J. Kim, S. Baik, *J. Nanosci. Nanotechnol.* **7**, 3727 (2007).

[Yos02] D. Yoshioka, *The Quantum Hall Effect*, Springer-Verlag, Berlin/Heidelberg (2002).

[Yu05] C. Yu, L. Shi, Z. Yao, D. Li, A. Majumdar, *Nano Lett.* **5**, 1842 (2005).

[Zha02] J. Zhao, J. Han, J. P. Lu, *Phys. Rev. B* **65**, 193401 (2002).

[Zha05] Y. Zhang, Y.-W. Tan, H. L. Stormer, P. Kim, *Nature* **438**, 201 (2005).

List of publications

Transmission electron microscopy and transistor characteristics of the same carbon nanotube, J. C. Meyer, **D. Obergfell**, S. Roth, S. Yang, S. F. Yang, *Appl. Phys. Lett.* **85**, 2911 (2004).

Fabrication of Single-Walled Carbon-Nanotube-Based Pressure Sensors, C. Stampfer, T. Helbling, **D. Obergfell**, B. Schöberle, M. K. Tripp, A. Jungen, S. Roth, V. M. Bright, C. Hierold, *Nano Lett.* **6**, 233 (2006).

Nano-Electromechanical Displacement Sensing Based on Single-Walled Carbon Nanotubes, C. Stampfer, A. Jungen, R. Lindermann, **D. Obergfell**, S. Roth, C. Hierold, *Nano Lett.* **6**, 1449 (2006).

Transport and TEM on dysprosium metallofullerene peapods, **D. Obergfell**, J. C. Meyer, M. Haluška, A. N. Khlobystov, S. Yang, L. Fan, D. Liu, S. Roth, *phys. stat. sol. (b)* **243**, 3430 (2006).

On the roughness of single- and bi-layer graphene membranes, J. C. Meyer, A. K. Geim, M. I. Katsnelson, K. S. Novoselov, **D. Obergfell**, S. Roth, C. Girit, A. Zettl, *Solid State Comm.* **143**, 101 (2007).

Investigation of the shift of Raman modes of graphene flakes, M. Haluška, **D. Obergfell**, J. C. Meyer, G. Scalia, G. Ulbricht, B. Krauss, D. H. Chae, T. Lohmann, M. Lebert, M. Kaempgen, M. Hulman, J. Smet, S. Roth, K. von Klitzing, *phys. stat. sol. (b)* **244**, 4143 (2007).

Atomically resolved mechanical response of individual metallofullerene molecules confined inside carbon nanotubes, M. Ashino, **D. Obergfell**, M. Haluška, S. Yang, A. N. Khlobystov, S. Roth, R. Wiesendanger, *Nature Nanotech.* **3**, 337 (2008).

Graphene-Metal Interface: Two-Terminal Resistance of Low-Mobility Graphene in High Magnetic Fields, V. Krstić, **D. Obergfell**, S. Hansel, G. L. J. A. Rikken, J. H. Blokland, M. S. Ferreira, S. Roth, *Nano Lett.* **8**, 1700 (2008).

Effects of Charge Impurities and Laser Energy on Raman Spectra of Graphene, M. Hulman, M. Haluška, G. Scalia, **D. Obergfell**, S. Roth, *Nano Lett.* **8**, 3594 (2008).

Atomic-resolution three-dimensional force and damping maps of carbon nanotube peapods, M. Ashino, **D. Obergfell**, M. Haluška, S. Yang, A. N. Khlobystov, S. Roth, R. Wiesendanger, *Nanotechnology* **20**, *accepted* (2009).

Real time observation of chemical reactions in carbon nanotubes at the atomic scale, A. Chuvilin, A. N. Khlobystov, **D. Obergfell**, M. Haluška, S. Yang, S. Roth, U. Kaiser, *to be published* (2009).

Acknowledgements

At first I would like to thank my academic supervisors Dr. Siegmar Roth, Prof. Dieter Kern and Prof. Klaus von Klitzing for their excellent support and supervision.

I deeply appreciated the scientific and social atmosphere within the von Klitzing department at the Max Planck Institute for Solid State Research in Stuttgart and I would like to thank all the department members for contributing to this unique atmosphere.

My special thanks go to my direct supervisor Dr. Siegmar Roth for always being there when needed, for supporting me and my work in various ways, for giving us PhD students such a lot of possibilities as active participation in numerous international conferences and in several international cooperations and finally for leading the *Synthetic Nanostructures group* in his way everybody knows who joined the 4C11 team for some while.

All my 4C11 colleagues and friends I would like to thank sincerely for turning the years at MPI-FKF into a great and unforgettable time, both on the scientific and on the social level: Dr. Viera Skákalová, Dr. Ursula Dettlaff, Dr. Miro Haluška, Dr. Po-Wen Chiu, Dr. Martti Kaempgen, Dr. Jannik Meyer, Dr. Björn Hornbostel, Dr. Giusy Scalia, Dr. Jan Lagerwall, Dr. Márcio Dias Lima, Mônica Jung de Andrade, Dr. Alberto Ansaldo, Dr. Melanie Kaliwoda, Serhat Sahakalkan, Viktor Siegle and Chen-Wei Liang. In detail, I thank Dr. Miro Haluška for preparing the non-magnetic SWNTs for metallofullerene encapsulation and for Raman investigations, Dr. Viera Skákalová for Raman measurements and for being a great long-term officemate, Dr. Jannik Meyer for the TEM investigations on freestanding SWNTs, metallofullerene peapods and graphene sheets, and my fellow PhD students Serhat, Viktor and Chen-Wei for helping me to keep the 3C11 cryostat cold and for being a nice team during the last years. Moreover I would like to thank Viktor Siegle for contributing to the *ViDi* measurement software by programming several basic communication sub-VIs.

Furthermore, I thank Prof. Werner Dietsche, Dr. Jürgen Weis and Dr. Jurgen Smet for discussions and especially for their generous hardware support.

Thanks as well to Dr. Gerhard Ulbricht and to Timm Lohmann for our common graphene activities.

I am very grateful to our technicians Monika Riek, Ulrike Waizmann, Achim Güth, Thomas Reindl, Manfred Schmid, Ingo Hagel, Steffen Wahl and Hans Riek for their help and support. Special thanks go to Ingo Hagel and Manfred Schmid for construct-